BULGARIAN CHEMICAL COMMUNICATIONS

Lysozyme crystal nucleation in solution layers

F.V. Hodzhaoglu, L.N. Stanoeva, C.N. Nanev*

Rostislaw Kaischew Institute of Physical Chemistry, Bulgarian Academy of Sciences, Acad. G. Bonchev Str. Bl.11,

1113 Sofia, Bulgaria

By using the classical approach of *separation in time* of nucleation and growth stages, protein crystal nucleation was investigated in thin protein solution layers confined between two glass plates of custom made quasi two-dimensional all-glass cells. Solution layer thickness was varied from 0.05 down to 0.01, 0.0065 and 0.002 cm. Two commercial samples of hen-egg-white lysozyme, HEWL, Seikagaku 6 times crystallized and Sigma 3 times crystallized, were used as model proteins. The number of HEWL crystal nuclei decreased with diminishing solution layer thickness but the crystal nuclei reduction was considerably lesser than proportional to solution layer diminish. Heterogeneous (on-glass) protein crystal nucleation was separated from bulk one in 0.05 cm solution layers, the corresponding nucleation rates being measured separately. Up to 80% of the crystal nuclei were formed heterogeneously, on the glass, from 0.05 cm protein solution layers of Seikagaku HEWL. On the contrary, only 10 to 13% of the nuclei were observed on glass under the same conditions in Sigma solution; bulk nucleated crystals represented the main crystal fraction in this case. A plausible explanation of the experimental results was suggested. It is that the bulk crystal nucleation occurs on rests of source biomaterial that are always present in the protein solutions. Moreover, they may be even more active nucleants than the glass.

Key words: protein crystal nucleation, thin protein solution layers, heterogeneous *vs.* homogeneous nucleation, crystal nucleants of biological origin.

INTRODUCTION

The big success of the Human Genome Project recently stimulates protein crystallography. Deeper understanding of the proteins bio-function requires knowledge of their exact molecular structure. X-ray diffraction is still the most frequently used technique for protein structure determination, sufficiently large and high quality protein crystals being needed. Nowadays it is generally anticipated that protein crystallization is the rate-determining step in the protein crystallography.

Spontaneous crystallization is usually practiced with proteins. Crystal nucleation is its first stage. Precise control over the rate of protein crystal nucleation is worth achieving because it fixes the number and determines the quality and final size of the crystals. Therefore we need to better understand all peculiarities of the crystal nucleation process with proteins.

The tendency to constantly decrease solution volumes is a general trend in protein crystallization. Using drop techniques this leads to capillary pressure effects, especially with the tiniest droplets.

For instance, the capillary pressure, P_c of 1μL droplet of protein solution in air is about 100 Pa, while that of 1nL droplet is ten times higher. Therefore such droplets evaporate very fast. To avoid evaporation, and its influence on the protein crystal nucleation and growth, oil is used [1]. Nevertheless, the effect of the capillary pressure remains. Besides, the surface to volume ratio is increased.

To shed light on these issues, series of experiments on the protein crystal nucleation were carried out by decreasing one dimension of the liquid phase, namely its thickness. Quasi two-dimensional protein solution layers of different thickness were confined between two glass plates of custom made all-glass cells. Separation in time of the nucleation and growth stages, i.e. the *classical double pulse approach*, was applied. To obtain additional information the amounts of substrate (on-glass) and bulk protein crystal fractions were measured separately in 0.05 cm cells. Crystal number-densities *vs.* nucleation time dependences were plotted and the stationary nucleation rates of HEWL crystals were measured. The results suggest the presence of bulk nucleants and stress on their role in protein crystal nucleation process. The impact of other factors on the protein crystal nucleation like natural convections, crystal

---
* To whom all correspondence should be sent.
E-mail: nanev@ipc.bas.bg;
Phone: (359-2) 8719306; Fax: (359-2) 971 26 88.

sedimentation, capillary pressure, etc. was considered as well.

Two commercial samples of hen-egg-white lysozyme, HEWL, Seikagaku and Sigma, were used in the investigation. The reason behind this approach is to establish also the role of the admixtures [2] that are present in every protein solution. In fact, a noticeable difference in the crystallization behavior of the two HEWL samples was observed.

EXPERIMENTAL

Experimental set-up

The investigations were performed with quasi-two-dimensional all-glass cells. For cell construction a pair of optical glass plates in disk form was welded in exactly parallel position. The HEWL crystals (Fig. 1) were nucleated and grown in thin solution layers confined in the gaps between the plates. The gaps were varied in a series of cells, from 0.05 down to 0.01, 0.0065 and 0.002 cm. These custom-made cells have small inside volumes. The cells allow excellent microscopic observation and easy cleaning.

The following protocol was used. Initially the cells were purified with a hot 5:1 sulfuric to nitric acid mixture, and than flushed by bi-distilled water (till it reached neutral pH). It turned out that this procedure was very important because it insured complete wetting, and filling of the whole cell. (Evidently, the precondition for a regular flow, and avoiding air bubble formation, is the complete wetting within the entire cell.)
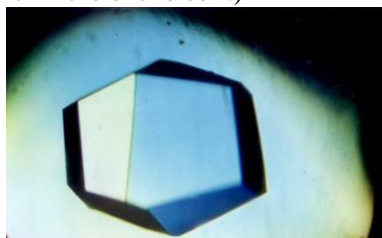

Fig. 1. Hen-egg-white lysozyme crystal, about 0.4 mm in size.

After drying the cell was loaded with HEWL solution that is metastable at room temperature, 20ºC. The solution metastability was proven in preliminary experiments – no crystals appeared at 20°C for a month or two. (Indeed, the existing crystals grew under these conditions.) Two commercial samples of HEWL, Seikagaku 6x crystallized and Sigma 3x crystallized (approx. 95% protein), were used without additional purification of the products. Aqueous solutions of 40 mg/ml protein at pH = 4.5 (50 mM acetate

buffer) and 0,43M NaCl as precipitant found application. At 20ºC the dimensionless super-saturation ($\triangle\mu = \ln (c/c_e)$) is approximately 1.0. The equilibrium state, when $\triangle\mu = 0$, is at 26ºC.

In the present study we performed series of parallel experiments on crystal nucleation and growth of HEWL using the whole set of crystallization cells. Besides the solution layer thickness however, other factors like natural convections, crystal sedimentation, capillary pressure, etc., may influence the protein crystal nucleation process. To shed light on these issues experiments with thicker, 0.05 cm quasi-2D-glass cells were performed initially. Taking advantage of a sharp-focus microscope, separation of substrate from the bulk crystal nucleation was achieved. We were able to distinguish between HEWL crystals growing on the upper glass plate, those in the solution bulk and the crystals on the bottom cell plate; simply, the microscope was focused on those particular levels. Note that this experimental approach was impossible with cells thinner than 0.05 cm because the crystals grown in thinner cells usually touch simultaneously both glass plates, and it was not clear where they were born.

The reasoning is simple. Focusing initially the microscope on the upper glass plate of a 0.05 cm glass cell we observed HEWL crystals growing there; evidently, those were truly heterogeneously nucleated crystals. The reason for this conclusion was that since the nuclei stuck to the glass plate strongly enough [3], they grew afterwards remaining on the same places. Thus, we counted the crystals on the upper glass plate separately and this was our *benchmark for the substrate type of heterogeneous nucleation*. Although several HEWL crystals were observed sometimes also in solution bulk, most of the crystals were found on the cell bottom. Therefore it was logical to assume that also sediment crystals were found on this particular place (because the number density of the crystals, which were nucleated truly heterogeneously onto the bottom glass plate, should not exceed this one observed for the upper glass plate).

### *Measurement of HEWL crystal nucleation rates*

The classical approach [4] which enables measurement of the nucleation rates experimentally, without ever actually seeing the nuclei themselves, was applied. This classical technique is very simple and reliable. However its proper fulfillment requires some experimental skills, e.g. see [5–7]. It requires strict separation in time of the nucleation and growth stages.

Practically, the crystallization experiment is divided into two periods (Fig. 2). During the nucleation period the crystals do only form. This is possible because crystal nucleation demands considerably higher supersaturation as compared to that which is sufficient for the subsequent crystal growth. By keeping the nucleation period relatively short (minutes), the nuclei do not have enough time to grow and to exhaust the overall supersaturation. Indeed, some of them which appeared very first could grow a little bit. Keeping the nucleation time sufficiently short, however, these clusters remained so small that they did not consume an appreciable amount of the protein; thus, they were unable to decrease substantially the overall protein concentration.

Note that excessively long nucleation times violate the principle of separation of the nucleation and growth stages. In such cases the nuclei that are born very first may deplete the local supersaturation, and even turn it to metastable condition. Thus, nucleus formation could be hindered in some zones around such crystals. In contrast, during short or moderate nucleation times the eventually appearing nucleation excluded zones will be very few and small and can not appreciably decrease the volume in which crystal nucleation takes place further. Also not too high supersaturations were used because otherwise it would be impossible to quantify the very large (sometimes countless) number of the grown crystals.

Being nanosized particles, the crystal nuclei are not visible under light microscope, like the so-called *image centers* in the photographic plates. In order to make them visible, after the expected nucleation onset the supersaturation is rapidly lowered below the threshold, which is necessary for crystal nucleation (Fig. 2). Being now in the so-called metastable zone, the system is unable to produce further nuclei. During this second (growth) stage only the existing nuclei grow to microscopically visible crystals. (Picturesquely speaking, the invisible nuclei are "developed", like the image centers in the photographic plates.) Purposely, the growth stage is set as long as necessary, usually several days. Finally, the number density of crystals, **n** is determined and by plotting **n** *vs* the nucleation time, **t** the stationary nucleation rate **I** is obtained from the linear part of the curve. Historically the classical principle of separation in time of the nucleation and growth stages has been applied in studying crystallization of glasses, formation of droplets, electrochemical nucleation of

metal crystals, etc. Protein crystal nucleation has been studied as well [5-7].
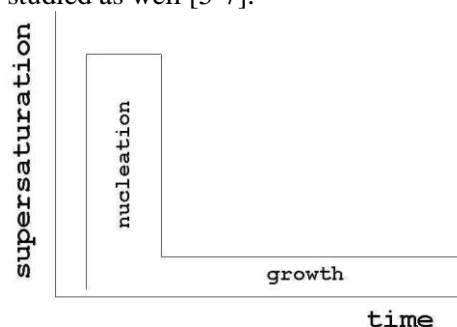
Fig. 2. Schematic representation of the classical principle of separation in time of the nucleation and growth stages.

For creating relatively fast supersaturation changes, thermal jumps were used in the present study because lysozyme exhibits strong temperature dependent solubility, perhaps the strongest for a protein. Although the classical technique is sometimes also called "double-pulse method", a term that comes historically from the electrochemical nucleation of metal crystals, it is obvious that with any temperature change, both cooling and heating, the system requires certain time to respond to that change. In order to shorten this period we chose water cooling for our samples because the thermal conductivity of water is more than 20 times higher than that of the air (and the glass possesses a relatively good thermal conductivity, a little bit higher than that of water).

Lysozyme exhibits normal temperature-dependent solubility, i.e. it decreases with temperature drop. Therefore the sufficiently high supersaturation that is necessary for crystal nucleation was established by sudden temperature decrease. To evoke crystal nucleation we set the temperature of our samples at 10°C because HEWL solubility at this temperature is known, 5 mg/ml [8]. At this conditions the dimensionless supersaturation ($\triangle\mu = \ln (c/c_e)$) is approximately 2.1. Another important benefit of our experimental setup was used. The imposing of rapid temperature shift was achieved using water baths. We simply immersed the whole cell with the protein solution directly in water of temperature 10°C. In fact, we measured with our quasi-2D-glass cells that water cooling was 2 to 3 times faster than air cooling (Fig. 3); purposely a thermoprobe was inserted directly in the cell. The solution in the cell was tempered from metastability temperature of 20°C to 10°C for about 15 s (Fig. 3). Keeping in mind this fact, and in order to diminish the experimental error, we chose nucleation time of minimum 5 min

363
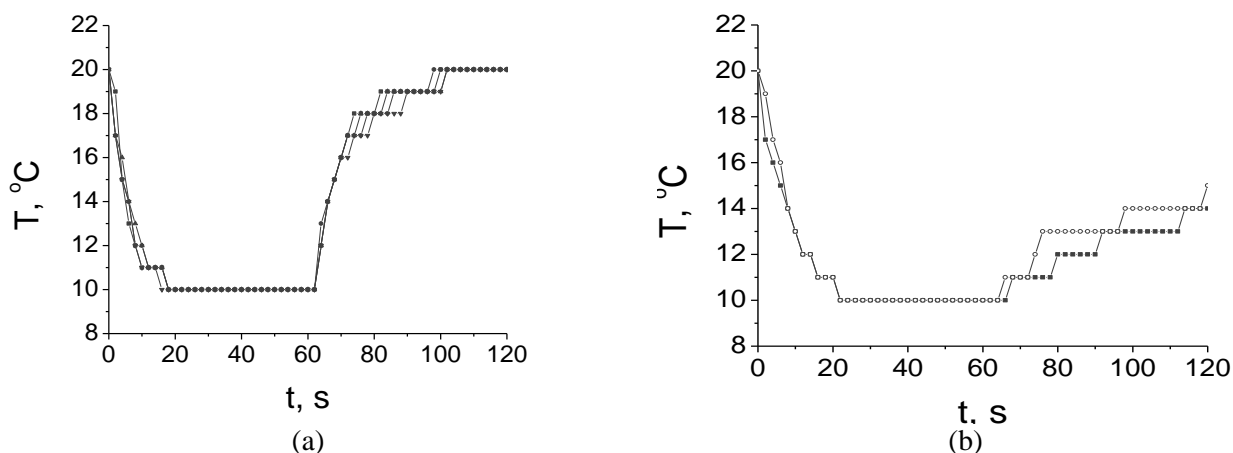
Fig. 3. Temperature ($T^{\circ}C$) changes depending on time (t, s) by two ways of cooling: a) water bath cooling and reheating; b) water bath cooling and air reheating. (Data of several measurements are superimposed.)

(i.e. 20 times longer than thermal transition time), but maximum of 120 min.

After the chosen nucleation time elapsed the supersaturation was sharply decreased to metastability level, the cell was re-heated to 20°C for about 15 s (Fig. 3 a). Under this condition the existing super-critically sized clusters grew to visible sizes, were counted, and the numbers plotted depending on the nucleation time, etc. Special attention was paid in our investigation to the optimization of the second (growth) "pulse" because, evidently, it was not sufficient only to prevent the appearance of new nuclei; it was also necessary to avoid any nuclei loss due to dissolution. Therefore, to properly choose the growth temperature, the growth of HEWL crystals was scrutinized in preliminary experiments, performed at a series of temperatures. While secondary nucleation was observed at 18°C we found that at 22°C the crystals were dissolved. Therefore, during the second (growth) "pulse" the cell with the protein solution was re-heated to 20°C and this temperature was maintained, at least overnight, but preferably for several days, till one week, till the crystals grew to microscopically visible sizes.

Having the advantage of being a direct method, the thermal variant of the classical approach also shows some drawbacks. It is reasonable to think that during the very beginning of the first stage (cooling) the nucleation rate *progressively* increases, till it reaches the stationary rate; and *vice versa*, it is quieting down relatively slowly during re-heating to 20°C. (Thus, although transient, some additional and uncontrolled nucleation takes place for 15 s, during the reheating to 20°C.) The theoretical analysis of these effects is not simple. Fortunately, they should be small, oppositely directed, and it is logical to assume that they nearly cancel each other. Because an inherent scatter of the experimental data is typical due to the stochastic character of the crystal nucleation process the inaccuracy should be below the measurement accuracy. Therefore we repeated the measurements many times and averaged the results.

RESULTS AND DISCUSSION

Applying a typical for the protein crystal nucleation supersaturation c/c_e = 800% (c and c_e being the actual and equilibrium protein concentrations, respectively) to a solution of 40 mg/ml HEWL at 10°C, a quantitative study was performed on protein crystal nucleation; the thermal variant of the classical double-pulse method was utilized. Investigations were carried out with quasi-two-dimensional glass cells by varying solution layer thickness δ, 0.05, 0.01, 0.0065 and 0.002 cm; identical solutions were loaded in all cells. It was already mentioned that in cells thinner than 0.05 cm the HEWL crystals usually touched both glass plates, so that it was not clear where they arose. Therefore the total (on glass substrate plus bulk) number **N** of the HEWL crystals nucleated and grown **per unit visible cell area** was plotted *vs*. the nucleation time **t**, Fig. 4 a, b. Linear dependences of different slopes were observed initially, and then plateaus appeared. A definite time-lag was observed only with Seikagaku HEWL but not with Sigma HEWL (Fig. 4 a, b).

Note the constantly decreasing slopes of the linear parts of the curves in Fig. 4 with decreasing layer thickness from 0.05 cm downwards, and especially the abrupt drop of **N**/cm^{2*} *vs*. **t** with Seikagaku solution below 0.05 cm layer thickness, Fig. 4 b. The decreases are power functions for Sigma HEWL, while the dependence is almost linear with Seikagaku HEWL (Fig. 5).

(a) (b)
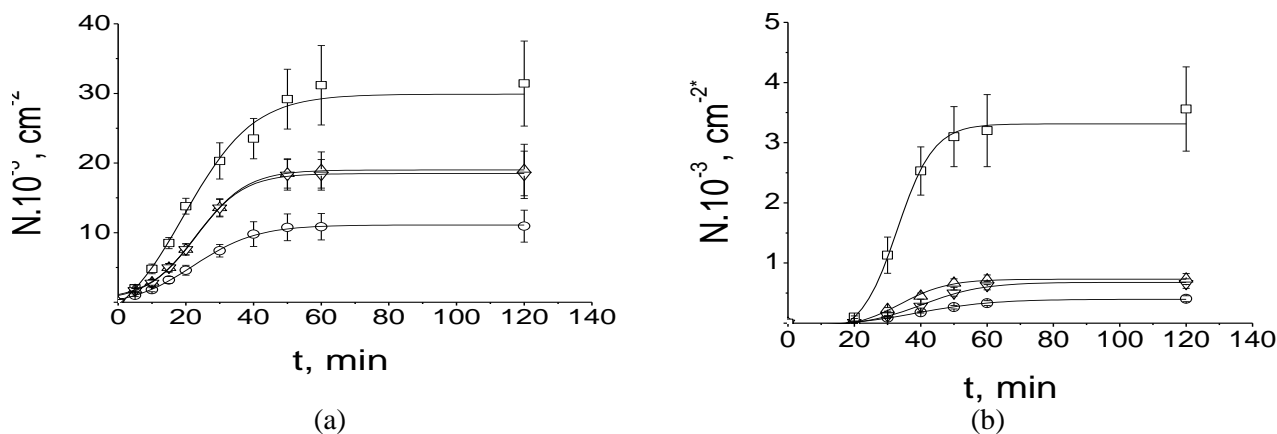
Fig. 4. Number densities **N**/cm^{2*} (the asterisk indicates that N is per unit visible cell area) of HEWL crystals *vs* nucleation time, t, min and solution layer thickness δ: □ - 0.05 cm, Δ - 0.01 cm, ∇ - 0.0065 cm, ○ - 0.002 cm; a – Sigma, b – Seikagaku (the sizes of the marks in Fig. 4 b that differ from □ reflect the error bar sizes).

(a) (b)
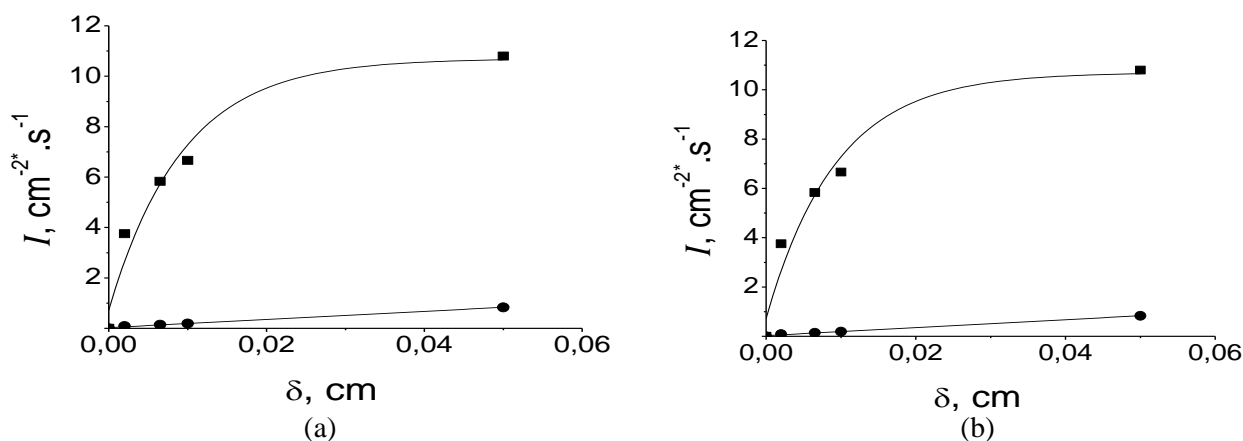
Fig. 5. a. Slopes (*I*) of the linear parts of the curves in Fig. 4 *vs.* solution layer thickness (δ); b. maximum crystal number densities, N$_{plato}$/cm^{2*} (the asterisk indicates that N$_{plato}$ is per unit visible cell area) *vs.* solution layer thickness δ. ■ – Sigma, ● – Seikagaku.

The differences in the plateau levels of Sigma and Seikagaku substances in Fig. 4 also deserve attention. They rise systematically with the decrease in solution layer thickness. Changing the thickness from 0.05 cm downwards to 0.002 cm the plateau levels decreased about three times with Sigma HEWL, while the decrease with Seikagaku HEWL was more than 8 times. Note however that nucleants' amount should decrease proportionally to the decrease in solution volume, which is equal to the solution layer thickness, i.e. 25 times. Besides, comparing the data for the two sorts of HEWL one can see that, despite the same crystallization conditions, the total number densities for Sigma HEWL crystals at the plateau regions on Fig. 4 a are about (and more than) one order of magnitude larger compared to Seikagaku HEWL crystals in Fig. 4 b.

The results obtained during the investigation with decreasing solution layer thickness put questions about the possible reasons for these peculiarities. For instance, the solubility of two lysozyme sorts may slightly differ giving impact on supersaturation, despite the same crystallization conditions. Factors like natural convection, which was observed in the 0.05 cm cells and which was almost fully suppressed in the thinner ones, especially in the 0.002 cm cells should be considered. In contrast, crystal sedimentation which could be thought as another factor hardly plays any virtual role in the crystal nucleation process. The sedimentation velocity of HEWL crystals that are much larger than the nucleus was estimated from solution viscosity and density. It was found that 1 μm^3 crystals should sediment in the 0.05 cm cells for about 85 min; indeed, growing larger the crystals sediment sooner.

365

Still another factor may be the capillary pressure, P_c which has to act, especially in the thinnest two-dimensional glass cells. In fact it is known that hydrostatic pressures, up to 100 MPa augment HEWL solubility [9 – 14], thus decreasing the supersaturation. Moreover, the reason to consider the role of the capillary pressure was a peculiarity that was observed by filling those cells. In contrast to the 0.05 cm cell, inside the 0.002 cm cell the liquid was climbing up even when the latter was situated in a vertical position: we observed that the air-solution interface in the cell rose very quickly (note that two air-solution interfaces do exist at the cell inlets). The capillary pressure, P_c, which in the case under consideration is **negative**, was calculated by means of Young–Laplace equation:

$$P_c = \gamma \left(1/r_1 + 1/r_2\right) \qquad (1)$$

where γ is solution's surface tension, r_1 and r_2 being the two principal radii of curvature.

With $\gamma = (3{,}5 \pm 0{,}2) \cdot 10^{-2}$ Nm^{-1}, measured with our working solution, and $r_1 = 0.001$ cm, $P_c \approx 3.5$ kPa was calculated for the 0.002 cm cell, while $P_c \approx$ 0.14 kPa was obtained for the 0.05 cm cell. Thus, it turns out that in the case under consideration P_c hardly plays any role because it is too small.

Still another factor was already mentioned, namely the presence of bulk nucleants. To shed light on the issue, the glass substrate HEWL crystal nucleation was distinguished from the bulk one in the same experiment, using 0.05 cm quasi-2D-glass cells (see above). Keeping the same supersaturation, $c/c_e = 800\%$ the number densities, **n**, of nucleated HEWL crystals *vs.* nucleation time, **t**, were plotted separately for glass substrate nucleation, Fig. 6 a ($\mathbf{n}_{glass}$ is the number density for the upper glass plate only, which is the same for the bottom plate) and bulk nucleation (Fig. 6 b, $\mathbf{n}_{bulk}$); 83 experiments were carried out for the plots in Fig. 6. Linear parts of different slopes were observed on the curves in Fig. 6 a and b; plateaus appeared in all four cases as well. A time-lag, which is most obvious for the bulk crystal nucleation of Seikagaku HEWL (Fig. 6 b) has to be emphasized as well.

(a)

(b)
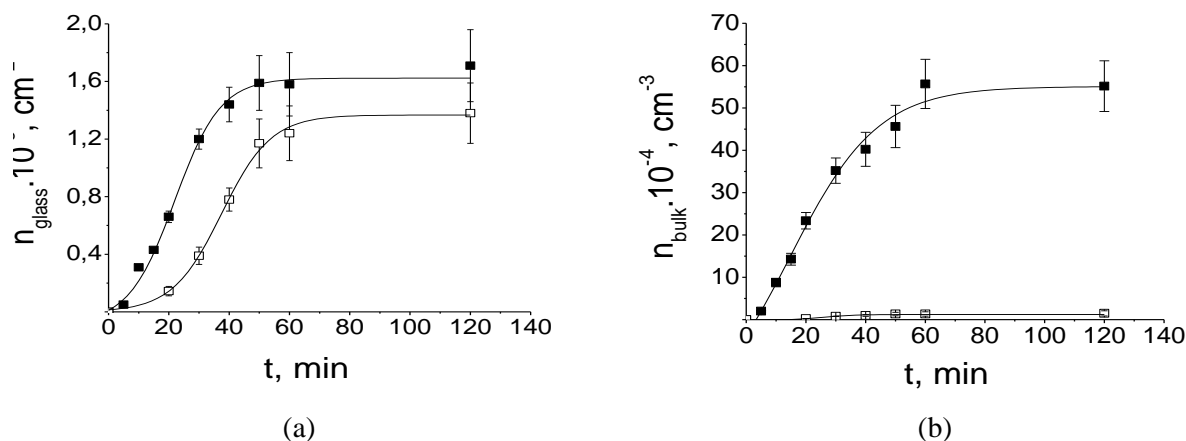
Fig. 6 a, b. Number densities, n *vs.* nucleation time, t of: (a) on-glass nucleated, and (b) bulk nucleated HEWL crystals. ■ – Sigma HEWL, □ – Seikagaku HEWL (the size of the mark □ in Fig. 6 b approximately coincides with the size of the error bars).
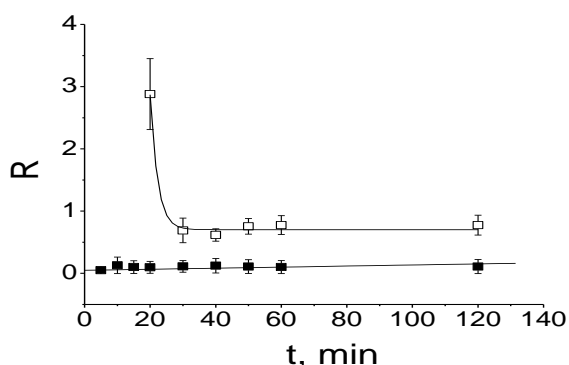
Fig. 6c. Ratio R *vs.* time, t; ■ – Sigma HEWL, □ – Seikagaku HEWL.

The relation between the substrate *vs.* bulk HEWL crystal nucleation can be established quantitatively from Fig. 6 a, b. For instance, the linear parts of the curves show that 65 to 72% (and 76 to 79% in the plateau regions) of the crystals nucleated of Seikagaku HEWL were born heterogeneously on glass substrate. In contrast, very small amount (only about 13%, by 10 min nucleation time, and 11%, by 120 min nucleation time) of Sigma HEWL nucleated crystals were found on the upper and bottom glass plates of the cell; bulk nucleated crystals represented the main crystal fraction (Fig. 6 b). It should be emphasized however that the comparison holds true for this

particular system only. The reason is that HEWL crystals arose on the glass support from a very thin (adjacent) solution volume, as compared to the much voluminous solution bulk. Despite this fact the comparison is instructive enough. It shows that the HEWL crystals nucleated on glass substrate prevailed strongly with Seikagaku solution while just the opposite effect was observed with Sigma HEWL, where the bulk nucleation prevailed. Note that this is a highly unexpected result because it is well known that heterogeneous crystal nucleation is easier [15].

Indeed, nucleation place does not determine explicitly the manner of nucleus formation. Although born in solution bulk some (or may be even all?) nuclei, especially in Sigma HEWL, may be formed on foreign particles that served as nucleants, for example other protein species, non-crystalline protein aggregates or traces of non-protein biomacromolecular impurities. Thus, the striking result seen in Fig. 6b may be explained in a sense that the nucleants in the bulk of Seikagaku's solution are less active or/and smaller in number than those in Sigma's one.

Although our SDS-PAGE didn't show any difference in the impurities' content of Sigma and Seikagaku HEWL it is known that foreign substances are always present in any protein solution, e.g. [16, 17] and may act as nucleants. Actually, Rosenberger has shown by SDS-PAGE the difference in impurity levels between Sigma and Seikagaku lysozymes. While in the two sorts proteins with molecular weight (MW) of about 25 kDa have been detected, the Sigma ones contain extra 40, 50 and 75 kDa proteins [18]. In fact, a simple estimation has shown that only the active nucleants should be below the detection limit of SDS-PAGE. The estimation was based on the (maximum) crystal number densities in the Sigma HEWL plateau region of Fig. 6b, and under the suggestion that all bulk crystals have nucleated on nucleants. Thus, we estimated that the total number of crystal nucleants in our SDS-PAGE trials should not exceed 30 active nucleant particles.

Also ratios, R, of the number of HEWL crystals nucleated on substrate (on both upper and bottom glass plates of the cell) *vs.* HEWL crystals nucleated in solution bulk are plotted in Fig. 6 c depending on the nucleation time for the same system. Fig. 6 c shows that while the Sigma R-value remains almost constant or increases very slowly with the nucleation time, the R-value of Seikagaku solution drops drastically (between 20 and 30 min nucleation time) and afterwards

becomes also constant. An explanation may be that some active centers on glass are exhausted. (Indeed, glass may have also some spots that promote HEWL crystals nucleation but in such a case crystals had to arise constantly on the same place, which was not observed.) Another explanation may be that rests of source biomaterial may be adsorbed randomly on the glass and can serve as especially active nucleants. Last but not least the nucleants in Seikagaku solution may act more sluggish, i.e. they may be less active than those in Sigma solution.

Both heterogeneous and bulk crystal nucleation rates were measured separately (at the given supersaturation, $c/c_e = 800\%$) from the linear parts of the curves in Fig. 6a and Fig. 6b. The slopes of the linear parts in $\mathbf{n}$ *vs.* $\mathbf{t}$ plots in Fig. 6 a render $I_{heter} = 0.9$ nuclei.cm^{-2}s^{-1} for Sigma HEWL and $I_{heter} = 0.6$ nuclei.cm^{-2}s^{-1}, for Seikagaku HEWL. So, the heterogeneous on glass crystal nucleation rates of the two protein samples do not differ substantially. In contrast, the bulk nucleation rates calculated from Fig. 6b, $I_{bulk} = 167$ nuclei.cm^{-3}s^{-1} for the Sigma sample and $I_{bulk} = 4$ nuclei.cm^{-3}s^{-1} for the Seikagaku sample differ more than 40 times. A plausible explanation of the latter result, and the time-lag in Fig. 6b as well, may be given again with the presence of some foreign particles and their different activity as nucleants.

Table 1. Heterogeneously on glass, n_{glass} being the crystal number density for the upper glass plate only, and bulk, n_{bulk} number densities of HEWL crystals, nucleated in 0.05 cm cell, when the former are nearly the same for both protein samples. (The small differences in the percentages of the on glass and bulk nucleated HEWL crystals as compared with the data extracted from Fig. 6 a, b are due to the fortuitous character of the nucleation process).

HEWL	$n_{glass}.10^{-3}$, cm^{-2}	$n_{bulk}.10^{-4}$, cm^{-3}
Sigma	1.47	54.36
(3x)	1.59	55.66
Seikagaku (6x)	1.43	1.62
	1.55	1.04

Interestingly, in separate experiments (some of those shown in the plateau region in Fig. 6 a), it was observed that the number densities n_{glass} of heterogeneously nucleated crystals were the same for both Sigma HEWL and Seikagaku HEWL, while the volume fraction was from 30 to 50 times smaller in the latter case, Table 1. This fact may be considered as a crucial (although indirect) evidence for the important role of the foreign nucleants in the process of protein crystal nucleation. Moreover, on the basis of the experimental results it is logical to assume that the most (and most active) nucleants

had been removed from Seikagaku HEWL as a result of its crystallization performed 6 times in contrast to those in the 3 times crystallized HEWL from Sigma.

CONCLUSION

It seems that the experiments performed with quasi-two-dimensional protein solution layers of different thickness put more questions than can be answered. Some light was shed by investigations on HEWL crystallization in 0.05 cm quasi-two dimensional cells. The similar substrate nucleation of two lysozyme sorts indicates that glass is poor a nucleant for crystallization of lysozyme and likely of other proteins. The comparison between bulk nucleated lysozyme crystals suggests that impurities in protein substances are a very significant source of heterogeneous nucleation centers. Evidently, the glass substrate is not as good nucleant for protein crystals as those impurity particles [16-18]. It is logical to assume that due to the similar nature the adhesion of the protein crystals to such particles should be stronger than to the glass. A stringent argument in favour of such explanation is the fact that horsehair [19] and human hair [20] induce crystal nucleation of some proteins. But due to the inherent fortuitous character of the nucleation process the data that are presently available do not allow a final conclusion. Moreover, the picture may be additionally dimmed due to the presence of differently active nucleants.

REFERENCES

1. N.E. Chayen, *Structure*, **5**, 1269 (1997).
2. D.-C. Yin, N.I. Wakayama, H.-M. Lu, Y.-J. Ye, H.-S. Li, H.-M. Luo, Y. Inatomi, *Cryst. Res. and Technol.*, **43**, 447 (2008).
3. C.N. Nanev, I. Dimitrov, D. Tsekova, *Cryst. Res. & Technol.*, **41**, 505 (2006).
4. G.Tammann, in: Aggregatzustaende, Die Zustandsaenderungen der Materie in Abhaengigkeit von Druck und Temperatur, Second Edition, von Leopold Voss, Leipzig, 1923, p. 222.
5. D. Tsekova, S. Dimitrova, C. N. Nanev, *J. Cryst.Growth,* **196**, 226 (1999).
6. O. Galkin, P.G. Vekilov, *J. Phys. Chem.*, **B 103**, 10965 (1999).
7. O. Galkin, P.G. Vekilov, *J. Am. Chem. Soc.*, **122**, 156 (2000).
8. A. Kadowaki, I. Yoshizaki, L. Rong, H. Komatsu, O. Odawara, S. Yoda, *J. Synchrotron Rad.*, **11**, 38 (2004).
9. B. Lorber, G. Jenner, R. Giege, *J. Crystal Growth*, **158**, 103 (1996).
10. G. Sazaki, K. Kurihara, T. Nakada, S. Miyashita, H. Komatsu, *J. Crystal Growth*, **169**, 355 (1996).
11. K.J. Takano, H. Harigae, Y. Kawamura, M. Ataka, *J. Crystal Growth*, **171**, 554 (1997).
12. J.N. Webb, R.Y. Waghmare, J.F. Carpenter, C.E. Glatz, T.W. Randolph, *J. Crystal Growth*, **205**, 563 (1999).
13. Y. Suzuki, S. Miyashita, G. Sazaki, T. Nakada, T. Sawada, H. Komatsu, *J. Crystal Growth*, **208**, 638 (2000).
14. Y. Suzuki, T. Sawada, S. Miyashita, H. Komatsu, G. Sazaki, T. Nakada, *J. Crystal Growth*, **209**, 1018 (2000).
15. W. Ostwald, *Z. Physik. Chemie*, **22**, 302 (1897).
16. F. Rosenberger, P. G. Vekilov, M. Muschol, B. R. Thomas, *J. Crystal Growth*, **168**, 1 (1996).
17. F. Rosenberger, E. J. Meehan, *J. Crystal Growth*, **90**, 74 (1988).
18. F. Rosenberger, *J. Crystal Growth*, **166**, 40 (1996).
19. A. D'Arcy, A. MacSweeney, A. Haber, *Acta Cryst.*, **D 59**, 1343 (2003).
20. D.G. Georgieva, M.E. Kuil, T.H. Oosterkamp, H.W. Zandbergen, J.P. Abrahams, *Acta Cryst.*, **D 63**, 564 (2007).

ЗАРОДИШООБРАЗУВАНЕ НА ЛИЗОЗИМ В ТЪНКИ КВАЗИДВУМЕРНИ КРИСТАЛИЗАЦИОННИ СИСТЕМИ

Ф. В. Ходжаоглу, Л. Н. Станоева, Хр. Н. Нанев

Институт по физикохимия "Акад. Ростислав Каишев", Българска академия на науките, блок 11, 1113 София, България

(Резюме)

Изследвана е кристализацията на моделния белтък лизозим в стъклени квазидвумерни клетки чрез прилагане на класическия двойно-импулсен метод на разделяне по време на етапите на зародишообразуване и кристален растеж. Дебелината на разтвора между стъклените плоскости беше точно задавана чрез използване на набор от работни клетки с разстояние между стъклените дискове от 0.05, 0.01, 0.0065 до 0.002 cm. За целите на изследването бяха използвани две различни белтъчни субстанции на кокоши яйчен лизозим (HEWL), по-скъпият белтък на фирмата Seikagaku (6x прекристализиран) и този на фирмата Sigma (3x прекристализиран). Експерименталните резултати показват, че броят на лизозимните кристални зародиши, образувани и нараснали в едни и същи изходни разтвори, но с различна дебелина, е непропорционален на дебелината на разтвора. Чрез оптично наблюдение на най-дебелите клетки (0,05 см) бяха измерени както скоростта на хетерогенно зараждане на белтъчните кристали върху стъклената подложка, така и скоростта на обемно зародишообразуване. При използвани едни и същи кристализационни параметри, двете белтъчни субстанции показаха различно кристализационно поведение. Приблизително 80% от кристалите на лизозим от Seikagaku 6x бяха образувани хетерогенно, докато дялът на същата кристална фракция при Sigma беше от 10 до 13%. При втората субстанция, броят на белтъчните кристали, образувани в обема, значително надвишаваше този на хетерогенните. Причина за това може да бъде различната степен на пречистване на използваните белтъци. Вероятно, кристалните лизозимни зародиши са се образували с участието на активни примесни частици, които винаги съпътстват и най-високо пречистените белтъци, но при Sigma 3x те са в значително по-голямо количество. Счита се, че чуждите биологични частици са по-активни нуклеанти в сравнение със стъклената подложка.

Comparison of different kinetic models for adsorption of heavy metals onto activated carbon from apricot stones

I. Tsibranska, E. Hristova

Department of Chemical Engineering, University of Chemical Technology and Metallurgy, 8 Kl. Ohridski Blvd.,

1756 Sofia, Bulgaria

In this work single and four-component adsorption kinetics was studied for removal of Pb^{2+}, Cd^{2+}, Cu^{2+} and Zn^{2+} from aqueous solutions with activated carbon from apricot stones. The adsorption equilibrium was calculated by the Langmuir model for single- and multi-component systems. Comparison of three kinetic models for internal diffusion control was performed. The steep initial part of the kinetic curve was accounted for by an intercept term in the linear representation of the models of Weber and Morris, Boyd and the moment method. The Weber and Morris model was found to correlate best with the experimental data. The intraparticle diffusion coefficients for the individual ions are in the range $1-3 \times 10^{-8} cm^2/s$. Similar results were obtained by the moment method applied to homogeneous solid phase diffusion control. Lower values of the kinetic parameters were obtained in four-component solutions. The calculated summary diffusion coefficient in the multi-component system is close to that obtained for single-component solutions with the same total initial ion concentration.

Keywords: adsorption kinetics; diffusion coefficient, active carbon, heavy metals

INTRODUCTION

The kinetic study has the important practical task to determine the degree of utilization of the adsorption capacity as a function of the time of contact between the liquid and the solid. Therefore, different models are used to fit the obtained kinetic curves in order to define the rate parameters and explain the mechanism of mass transfer. Most studies dealing with heavy metals adsorption on low-cost adsorbents use the statistical approach of the best-fit model that compares the correlation coefficients of models with different physical background and applies as a criterion the acceptable description of the whole kinetic curve or as large part of it as possible. Kinetic investigations with activated carbons usually apply first-order [1,3–10,12] and second-order reaction models [1,5–7,9,10]. For porous sorbents as activated carbons, however, diffusional effects may be quite important and the physical meaning of the evaluated rate constants has to be consequently determined in order to get insight into the transfer mechanism. Usually comparison with other mass transfer models [6,11,12,24] is performed, like the Boyd model [1,5,7,13] and the intraparticle diffusion model of Morris and Weber [1-5,9–12]. The

moment method is less used, because of its original limitation to systems with linear equilibrium. Its application to batch adsorption uptake curves with nonlinear isotherms [15] enhances the scope of its utilization, including the adsorption of heavy metals [16, 17]. The obtained rate constant is related to the traditional mathematical models used for describing solid phase mass transfer, like the linear driving force model, the homogeneous solid phase or the pore diffusion model, as well as to more complicated structures like biporous sorbents [16].

The *Weber and Morris model* or intraparticle diffusion model is of major interest because the internal diffusion determines the adsorption rate in most of the liquid systems. Eq. (1) is a general representation of the kinetics, where the intercept is related to the mass transfer across the boundary layer and the expected value of the exponent is 0.5 (for Fickian diffusion and plate geometry).

$$q = k_{in} t^n + c \qquad (1)$$

Both processes are generally observed for adsorption kinetics on activated carbons – the external mass transfer from the solution to the liquid-solid interface and the diffusion of the adsorbed species inside the porous particle. The Weber and Morris model (eq. 2) describes the time evolution of the concentration in adsorbed state, where the rate constant (k_{in}) is obtained from the plot of q versus $t^{0.5}$ and is related to the respective

---

* To whom all correspondence should be sent:
E-mail: e.hristova@abv.bg

intraparticle diffusion coefficient (D) according to eq.(3).

$$q = k_{in} t^{0.5} \qquad (2)$$

$$k_{in} = 6 \frac{q_0}{R} \sqrt{\frac{D}{\pi}} \qquad (3)$$

The different mechanisms of mass transfer are manifested as different slopes in the linear plot of q versus $t^{0.5}$, obtained by piecewise linear regression. They correspond to different consecutive stages of mass transport with decreasing rate: external mass transfer and intraparticle diffusion in the macro-, meso- and microporous structure of the adsorbent [5].

The *Boyd's model* is often used to obtain insight into the mechanism of the adsorption kinetics. Originally proposed for intraparticle diffusion in a spherical particle, it is better known as the Boyd's film-diffusion model. When applied to external mass transfer, it supposes a linear dependence through the origin between $F = \frac{q}{q_e}$ (the fractional approach to equilibrium) and t (time): $\ln(1 - F) = kt$. Here k denotes the external mass transfer coefficient.

The general solution of the model, applied to solid phase control, is:

$$F = 1 - \frac{6}{\pi^2} \sum_{n=1}^{\infty} \frac{1}{n^2} \exp\left(-n^2 B t\right), \qquad (4)$$

where the rate coefficient B is related to the effective diffusion coefficient (D_{eff}) and the particle radius as $B = \pi^2 D_{eff}/R^2$.

By applying Fourier transform, the relation between the fractional approach to equilibrium F and the rate coefficient B is written as:

$$Bt = \left(\sqrt{\pi} - \sqrt{\pi - (\pi^2 F / 3)}\right)^2 \text{ for } F < 0.85 \quad (5a)$$

and $Bt = -0.498 - \ln(1 - F)$ for F>0.85 (5b)

The linear plot between the time and the right side of the above expressions, $f\ (F)$, is used to evaluate the rate parameter B. The observance of an intercept is an indication for the effect of a second mass transfer mechanism (external mass transfer).

The method of moments

The main idea of the method is to connect the Laplace transform solution of the mass balance equations with the statistical characteristics of the corresponding concentration curves. The time

evolution of the liquid phase concentration is given by the mass balance equation:

$$\frac{dc}{dt} = -\beta \frac{dq}{dt}, \qquad (6)$$

where β denotes the solid-liquid ratio $\beta = V_e/V_l$.

The dimensionless representation of eq. (6) is: $\frac{d\bar{c}}{dt} = -\beta K \frac{d\bar{q}}{dt}$. Equilibrium is suggested between the final solid and liquid phase concentrations, denoted by the slope of the isotherm $K = \frac{q_e}{c_e}$. The change in the solid phase concentration is described according to the model of mass transfer:

For the linear driving force model $\frac{dq}{dt} = k_s (q_e - q)$, where the rate constant k_s is defined as the solid phase mass transfer coefficient [s^{-1}]. The solution for the solid phase concentration in this case is:

$$\frac{q}{q_e} = \left[1 - \exp\left(-\frac{t}{\mu_1'}\right)\right] \qquad (7a)$$

or in dimensionless form:

$$\ln(1 - \frac{q}{q_e}) = -\frac{t}{\mu_1'} \qquad (7b)$$

Here the first absolute moment of the uptake curve is inversely proportional to the rate constant $k_s = \frac{1}{\mu_1'}$. This solution is formally identical to that for a first-order reaction model $\ln(q_e - q) = \ln q_e - k_1 t$.

b) For the homogeneous solid phase diffusion model the change in the volume averaged solid phase concentration is due to diffusion flux across the boundary ($r = R$):

$$\frac{dq}{dt} = \frac{3}{R} D_a \frac{q}{\partial r}\bigg|_{r=R} \qquad (8)$$

Here a denotes the local adsorbed concentration. Fick diffusion is supposed inside the spherical particle:

$$\frac{dq}{dt} = \frac{D_a}{r^2} \frac{\partial}{\partial r}\left(r^2 \frac{\partial q}{\partial r}\right) \qquad (9)$$

The relation between the moment of the uptake curve (μ_1') and the diffusion coefficient (D_a) is given as:

$$\mu_1' = \frac{R^2}{(1 + \beta K)15 D_a} \qquad (10)$$

Relations for other diffusion models are given in [16] and [17]. The equilibrium parameter K was originally defined for a linear isotherm. It was later shown that it may be treated as the local slope of the isotherm at the equilibrium concentration c_e [17].

Despite the large number of articles concerning the adsorption of heavy metals on low cost adsorbents, very few of them are dealing with the multi-component kinetic behaviour of such systems. In the case of adsorption on activated carbon from apricot stones (ACAS) only single component kinetics for batch removal of chromium [14] and gold ions [23] is reported. The authors [14] compare different kinetic models with the results being in favour of the pseudo first-order reaction model.

The aim of the present paper was to investigate the adsorption kinetics of Pb^{2+}, Cd^{2+}, Cu^{2+} and Zn^{2+} on ACAS in single- and four-component solutions. Three kinetic models for solid phase diffusion control were discussed and compared in order to obtain the rate parameters of the adsorption process, based on the microporous nature of the activated carbon and the suggested ion exchange mechanism [18].

EXPERIMENTAL

Single and four-component solutions containing $Pb(NO_3)_2$, $CdCl_2$, $ZnSO_4 \times 7H_2O$ and $CuSO_4 \times 5H_2O$ with total concentration of about 1.5 mmol/l were used in the kinetic experiments. ACAS, supplied by the Institute of Organic Chemistry, Bulgarian Academy of Sciences, was used, whose properties and adsorption equilibrium were reported earlier [18]. The kinetic curves were obtained by several parallel runs with different contact times. The other experimental conditions were: particle size 1.8 mm; mass of dry solid 0.5 g (M_s); volume of metal ion solution 50 ml (V_l). The liquid phase concentration $c(t)$ was measured by atomic absorption spectrometry (Perkin-Elmer 5000). The solid phase concentration $q(t)$ was calculated from the mass balance: $V_l(c_0 - c) = M_s q$, where c_o is the initial concentration in the solution, mmol/l.

RESULTS AND DISCUSSON
Single component adsorption kinetics

Figs.1a) to d) present the kinetic curves for the individual ions in dimensionless coordinates: q/q_e *vs.* time. The equilibrium value q_e was calculated
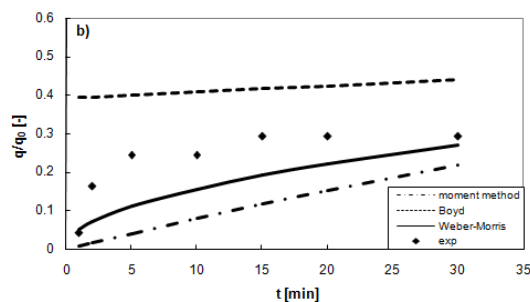
Fig.1a. Dimensionless experimental and calculated kinetics for Pb^{2+}.
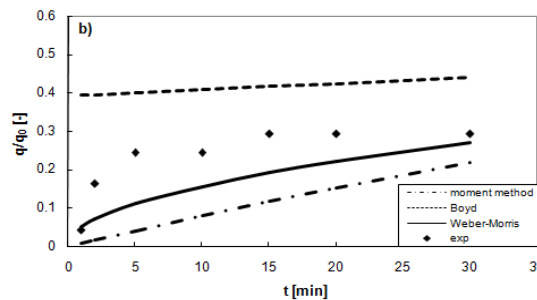

Fig.1b. Dimensionless experimental and calculated kinetics for Cd^{2+}.
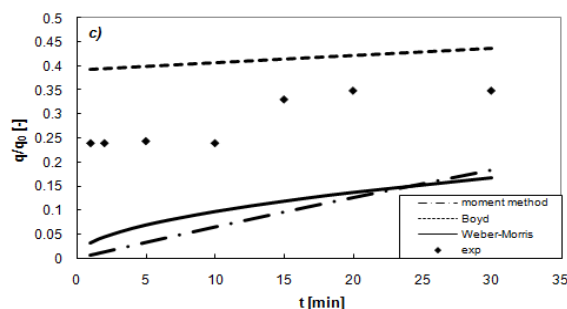

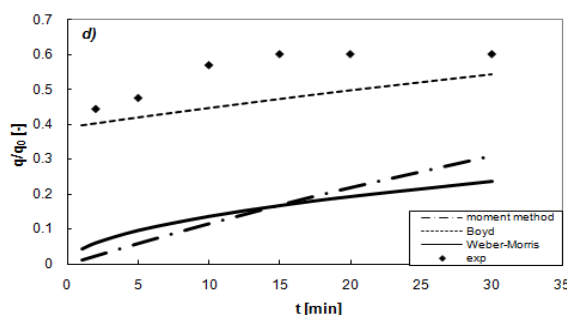**Fig.1c**. Dimensionless experimental and calculated kinetics for Cu^{2+}.

Fig.1d. Dimensionless experimental and calculated kinetics for Zn^{2+}.

by the Langmuir isotherm [18], whose equilibrium parameters (q_m and b) are shown in Table 1. The slope of the isotherm (K) is determined at the equilibrium concentration c_e, which was calculated by the mass balance in the liquid phase:

$$V_l(c_0 - c_e) = M_s(q_e - q_0) = M_s q_e = M_s \frac{q_m b c_e}{1 + b c_e} \qquad (11)$$

Table 1. Equilibrium parameters and conditions for the individual ions in single-component solutions

Ion	q_m [mmol/g]	b [l/mmol]	c_0 [mmol/l]	q_e [mmol/g]	K [-]	S [-]
Pb	0.0762	11.534	1.544	0.0692	81.09	0.092
Cu	0.1222	5.774	1.26	0.0858	210.26	0.298
Cd	0.01196	1.203	1.245	0.0549	78.55	0.543
Zn	0.0935	1.064	1.485	0.0482	48.15	0.484

Table 2. Rate parameters for the individual ions in single-component solutions

Ion	Method of moments				Boyd's model		Weber and Morris model		
	k_s [min^{-1}]	$D_a \times 10^8$ [cm^2/s]	R^2	B [min^{-1}]	$D_{eff} \cdot \times 10^8$ [cm^2/s]	R^2	k_{in} [mmol/gmin$^{-1/2}$]	$D \times 10^8$ [cm^2/s]	R^2
Pb^{2+}	0.0126	6.262	0.680	0.0072	9.86	0.69	0.0035	3.01	0.74
Cd^{2+}	0.0082	4.135	0.59	0.0027	3.69	0.70	0.0027	2.84	0.73
Cu^{2+}	0.0067	1.944	0.81	0.0031	4.245	0.82	0.0026	1.08	0.79
Zn^{2+}	0.0124	8.424	0.70	0.0096	13.15	0.71	0.0021	2.23	0.83

Only experimental values for the initial concentrations (c_o) were necessary in this case. The final equilibrium values were predicted by the isotherm. This approach is also useful for situations when the plateau of the kinetic curve is not reached or is poorly defined. The parameter $S = \dfrac{1}{1+bC_0}$ in Table 1 characterizes the nonlinearity of the isotherm ($S=1$ applies for a linear isotherm, $S=0$ – for a rectangular one). It is close to the highly favourable (rectangular) isotherm for Pb^{2+}, as can be seen in Table 1. For the other three ions the values of S correspond to different nonlinearity (0.3-0.5), far from the linear case.

1. Morris and Weber model

The experimental kinetics of Pb^{2+}, Cd^{2+}, Cu^{2+}, and Zn^{2+} adsorption on ACAS is characterized by a sharp increase in the adsorbed concentration during the first 1-2 min, followed by a lower uptake rate, which can be described by the Weber and Morris model in the form of eq. (1): $q = k_{in}t^{0.5} + c$. The kinetic curve, in fact, exhibits a different initial slope (dotted line in Fig. 2) and the intercept c is an extrapolation of its second linear 'diffusion' part to the ordinate (solid line in Fig. 2). The initial part is connected to faster mass transfer through the boundary layer and/or adsorption on the solid surface, followed by slow diffusion inside the particles. The obtained rate constants k_{in} are shown in Table 2, as well as the intraparticle diffusion coefficients D calculated by eq. (3). The values obtained for k_{in} are in the order reported in the literature for adsorption on low-cost activated carbons from plant materials. Depending on the initial concentration of lead ions, values of $k_{in} =$
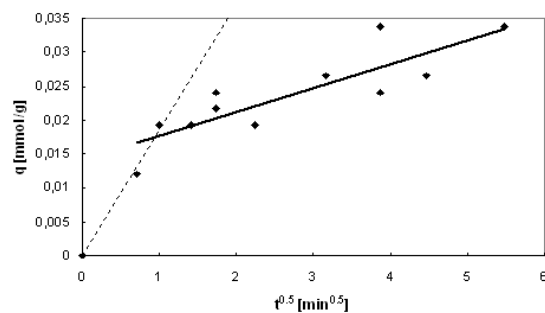
Fig.2. Morris and Weber linear plot for lead ions in single-component solution

$0.2 \div 1.85$ mg/g·min$^{-1/2}$ were found in [1]. They correspond to the $k_{in,Pb}$ presented in Table 2, if recalculated in the dimensions of [1], i.e. 0.724 mg/g min$^{-1/2}$. The Morris and Weber model gives values of k_{in} in the range 0.83-5.94 mg/g min$^{-1/2}$ for lead adsorption on palm shell-based activated carbon [5]. Kinetic data for Cr^{2+} adsorption on ACAS are reported in [14] for comparable experimental conditions (pH=3, d=1.6 mm, c_o=1-2 mmol/l). In the authors' representation - percentage of ion adsorption *vs* time [h], the results for k_{in} in Table 2 should be: Cd^{2+}-37.5, Pb^{2+}-39.68, Zn^{2+}-33.86 and Cu^{2+}=23.17 h$^{-1/2}$, i.e. of the same order as those, reported in [14] (33.5 - 37.3 h$^{-1/2}$). The obtained intraparticle diffusion coefficients (Table 2) are in the range 1-3·10^{-8} cm^2/s, which is physically reasonable for internal diffusion. The comparison with the coefficients of molecular diffusion also supports the conclusion for a rate limiting internal diffusion mechanism. The reported values for molecular diffusion of free ions in aqueous solutions are in the order of 10^{-6} cm^2/s (Pb^{2+}- 9.5·10^{-6} cm^2/s, Cd^{2+} - 6.52-7.2 ·10^{-6} cm^2/s, Cu^{2+} - 6.47-7.3·10^{-6} cm^2/s, Zn^{2+} - 6.37-7.2·10^{-6} cm^2/s [19-22]).

2. Boyd's model

A linear representation in coordinates $\left(\sqrt{\pi}-\sqrt{\pi-(\pi^2 F/3)}\right)^2$ *vs t* was used to obtain the kinetic parameter B and the respective effective diffusion coefficient. As can be seen from Table 2, the D_{eff} values are higher ($3.7 \cdot 10^{-8} - 1.3 \cdot 10^{-7}$ cm²/s) than those, obtained with the Morris and Weber model. Similar results are reported in [1], where $D_{eff,Pb}$ is about three times higher ($3.1 \cdot 10^{-7}$ cm²/s). Our values for B are about one order of magnitude lower than those, reported in [5] for the film diffusion model and lower or comparable to those, obtained in [13] (0.013–0.014 min^{-1}), where pore diffusion inside the particles was found to play an important role. The correlation coefficients are generally lower, except for Cu^{2+}. The presence of an intercept shows that diffusion is not the only observed mechanism of transfer.

3. The moment method-application

The nth absolute moment of a concentration curve $c(t)$ is defined as:

$$\mu'_n = \frac{1}{\mu_0} \int_0^{\infty} t^n \frac{d^j c}{dt^j} dt \qquad (12)$$

where: $j=1$ for an uptake curve obtained from batch experiment; $\mu'_0 = \int_0^{\infty} \frac{d^j c}{dt^j} dt = c_0$ and c_o is the initial concentration.

μ'_1 can be calculated directly from the experimental kinetic curve for analysis of the adsorption rate. When the plateau of this curve was not reached or was poorly defined, the solution of the LDF model was used. Eq. (7a) applies for batch type experiment. Its linearized form (eq. 7b) in coordinates $\ln(1-\frac{q}{q_e})$ *vs t* gives the value of μ'_1 and the corresponding solid phase mass transfer coefficient ($k_s = \frac{1}{\mu'_1}$). Linear regression with intercept was used again to separate the initial part of the kinetic curve from the subsequent linear one. Results for k_s are shown in Table 2. These values can also be compared to the reported rate constants for a first order reaction model, as the rate expressions are identical. The obtained values are in line with the reported ones in the literature for lead adsorption on low-cost activated carbons: 0.0151–0.0161 min^{-1} [13], 0.0117–0.127 min^{-1} [5].

The kinetic curves for the different ions gave k_s values in a close variation range of 0.007 to 0.013, which was also observed for Pb^{2+}, Cu^{2+}, Cd^{2+} and Zn^{2+} adsorption on activated carbons [24, 25]. Despite the lower correlation coefficients, the calculated diffusion coefficients were in the same order (10^{-8} cm²/s) as those, obtained by the other two models.

Figs. 1a) to d) present the comparison of the results from the calculation of the slopes of the kinetic curves by utilizing the different models. The calculations were done according to eq. 2, 4 and 7a. In order to better visualize the results, the intercepts of the calculated linear regression equations were not included in Fig.1, which explains the displacement of the calculated curves from the experimental data. These intercepts were explained by the initial fast mass transfer through the liquid film around the particle and they were easily accounted for by a diffusion model with an appropriate boundary condition:

$$-D_a \frac{\partial q}{\partial r}\bigg|_{r=R} = k_f \left(c\big|_{r=R} - c\right) \qquad (13)$$

Here k_f denotes the external mass transfer coefficient [m/s]. Simplified models like Morris and Weber, Boyd and the moment method usually suggest a first order boundary condition $\left(c\big|_{r=R} = c\right)$, i.e. no mass transfer resistance across the liquid film. As can be seen in Fig.1, the moment method gives similar results as the Morris and Weber model, which is to be expected, as they have similar theoretical background. The analysis of the results in Table 2 and Fig. 1 leads to the conclusion that the best description of the kinetic data is provided by the Morris and Weber model. The correlation coefficients with this model are higher and the scatter of the diffusion coefficients is less pronounced, which is in agreement with the similar time evolution of the experimental data obtained for the different ions.

Multi-component adsorption kinetics

The experimental kinetic curves for the individual ions in a four-component solution are shown in Fig. 3. Dimensionless solid phase concentrations q/q_e are used. The equilibrium value q_e was calculated by the extended Langmuir model for multi-component adsorption:

$$q_{e,i} = \frac{q_{m_i} b_i c_{e,i}}{1 + \sum_{i=1}^{N} b_j c_{e,j}} \qquad (14)$$

Here c_{ej} is the concentration of the ith ion in the solution; q_{mi} and b_j are single-component isotherm parameters, as they are shown in Table 1. Table 3 shows the equilibrium characteristics for the multi-component kinetic runs. Initial liquid phase concentrations are presented together with the calculated q_{ej} and the slope of the isotherm (K_i) for the respective ions at equilibrium concentration $c_{e,i}$. The latter was calculated by the mass balance in the liquid phase:

$$V_l\left(c_{0,i} - c_{e,i}\right) = M_s q_{e,i} = M_s \frac{q_{m,i} b_i c_{e,i}}{1 + \sum_{j=1}^{4} b_j c_{e,j}} \qquad (15)$$

where $\sum_{1}^{4} b_j c_{e,j} = const$ for each kinetic experiment. The rearrangement of eq. (15) gives:

$$c_{e,i} = \frac{c_{0,i}}{\left(\dfrac{\beta q_{m,i} b_i}{1 + const} + 1\right)} \qquad (15a)$$

where $\beta = \frac{M_s}{V_l}$. Further summation on i=1 to 4 gives $\sum_{1}^{4} b_i c_{e,i} = const = \sum_{1}^{4} \dfrac{b_i c_{0,i}}{\left(\dfrac{\beta q_{m,i} b_i}{1 + const} + 1\right)}$,

where the unknown parameter is the constant ($\sum_{1}^{4} b_i c_{e,i}$); $c_{o,i}$ is the measured initial concentration in the solution. The equilibrium liquid phase concentrations $c_{e,i}$ were calculated by eq. (15a). For the initial concentrations shown in Table 3, the value of

$$\frac{1}{1 + \sum_{j=1}^{4} b_j c_{e,j}}$$

was evaluated to 0.385. Table 3 also presents the summary adsorption in the four-component system, which can be compared to the q_e values in Table 1 with approximately the same initial loading.

Table 3. Equilibrium parameters and conditions for the individual ions in 4-component solution

Ion	c_0 [mmol/l]	q_e [mmol/g]	K [-]
Pb^{2+}	0.081	0.006	338.4
Cu^{2+}	0.403	0.0294	271.4
Cd^{2+}	0.436	0.0155	55.3
Zn^{2+}	0.566	0.0157	38.3
Sum	1.485	0.0666	45.0
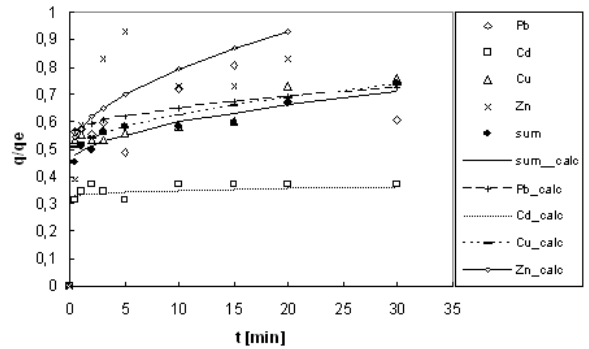
Fig. 3. Dimensionless experimental and calculated kinetic curves in four-component solution.
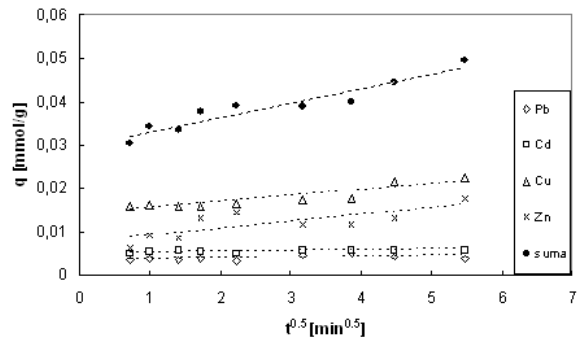
Fig. 4. Morris and Weber linear plots for the individual ions in four-component solution.

The individual ions exhibit similar kinetic behaviour, as can be seen from the dimensionless representation in Fig. 3. The Cu^{2+} data practically coincide with the summary adsorption curve in a multi-component solution. Stronger deviation is obtained for the Cd^{2+} ions, where much slower kinetics was observed. Fig. 4 illustrates the Morris and Weber plots of the multi-component kinetic data. The calculated rate parameters are shown in Table 4.

Table 4. Rate parameters for the individual ions in 4-component solution

Ion	Morris-Weber			Boyd		
	k_{in} [mmol/gmin$^{1/2}$]	$D \cdot \times 10^8$ [cm^2/s]	R^2	B [min^{-1}]	$D \cdot \times 10^7$ [cm^2/s]	R^2
Pb	0.0002	1.215	0.27	0.0101	1.383	0.15
Cd	0.0001	0.049	0.42	0.0012	0.16	0.37
Cu	0.0014	2.668	0.83	0.0206	2.82	0.899
Zn	0.0016	1.228	0.59	0.0284	3.89	0.11
Sum	0.0033	2.872	0.90	0.0180	2.47	0.922

The results with Boyd's model are analogous to those, observed in single-component solutions. Lower correlation coefficients and up to one order of magnitude higher diffusion coefficients were calculated (10^{-7}cm^2/s), compared to the Morris and Weber model. The k_{in} values in the 4-component solution were lower, as can be seen from the comparison of the results in Tables 4 and 2. The difference between the individual diffusion coefficients D is more pronounced. This can be explained by the competition of the diffusing ions in the multi-component system, but also by errors coming from the calculated equilibrium, which was predicted and not directly measured from the plateau of the experimental curve. Best correlation was obtained for the summary adsorption kinetics, as well as for Cu^{2+}, which was best adsorbed in the multi-component system [18]. The summary diffusion coefficient was practically the same as that, obtained for single-component adsorption with the same initial loading. Comparison of the experimental kinetic curves with the calculations of the Morris and Weber model (Eq. 2), including the intercept term, is shown in Fig. 4. Despite the scatter of the experimental points and the low correlation coefficients, the observed agreement is satisfactory.

CONCLUSIONS

The adsorption kinetics of Pb^{2+}, Cd^{2+}, Cu^{2+} and Zn^{2+} in single- and four-component aqueous solutions with activated carbon from apricot stones was successfully described by the model of Weber and Morris. The intraparticle diffusion coefficients for the individual ions are in the range of 1 to 3×10^{-8} cm^2/s, which is reasonable for the case of internal diffusion control. These values give a satisfactory description of the observed kinetics after the first 1–2 min. The initial part of the kinetic curves was described by the formal inclusion of an intercept term. A more detailed diffusion model including the appropriate boundary condition is needed to account for the combined effect of the external mass transfer and internal diffusion. Lower rate parameters were observed in the multi-component solutions. Despite the lower correlation coefficients in this case, the agreement between the experimental data and the kinetics calculated by the model of Morris and Weber was satisfactory. The moment method gave similar values for the rate of internal mass transfer and the respective diffusion coefficient. This result was expected, because of the similar physical background of the two models. The

obtained effective diffusion coefficients with the Boyd model were usually greater, but still in the range expected for internal diffusion control. Best correlation coefficients were obtained with the Morris and Weber model. The calculated summary diffusion coefficient in the 4-component solution was close to that obtained in single-component solutions for the same total initial concentration. No kinetic studies were found in the literature for adsorption of Pb^{2+}, Cd^{2+}, Cu^{2+} and Zn^{2+} on ACAS. The comparison with the reported rate parameters for other low-cost activated carbons in similar systems is encouraging for further investigation of the adsorption behaviour of ACAS in a fluidized bed column.

REFERENCES

1. J. Acharya, J. N. Sahu, C. R. Mohanty, B. C. Meikap, *Chem. Eng. J.*, **149,** 249 (2009).
2. G. Karthikeyan, S. Sivailango, *E-Journal of Chemistry*, **5** (4), 666 (2008),
3. N. Kannan, T. Veemaraj, *E-Journal of Chemistry*, **6** (2), 247 (2009).
4. R. Ayyappan, A. Carmalin Sophia, K. Swaminathan, S. Sandhya, *Process Biochem.*, **40**, 1293 (2005).
5. M. K. Aroua, S. P. Leong, L. Y. Teo, C. Y. Yin, W. M. A. Wan Daud, *Bioresour. Technol.,* **99,** 5786 (2008).
6. E. Demirbas, N. Dizge, M.T. Sulak, M. Kobya, *Chem. Eng. J.*, **148,** 480, (2009).
7. K. Li, X. Wang, *Bioresour. Technol.*, **100,** 2810 (2009).
8. S. Gueu, B. Yao, G. Ado, *Int. J. Environ. Sci. Tech.*, **4** (1), 11 (2007)
9. M. Nadeema, A. Mahmood, S.A. Shahid, S.S. Shah, A.M. Khalid, G. McKay, *J. Hazard. Mater.*, **B138,** 604 (2006).
10. I. Kula, M.Ugmrlu, H. Karaoglu, A. Çelik, *Bioresour. Technol.*, **99,** 492 (2008).
11. D. Mohan, K. P. Singh, V. K. Singh, *J. Hazard. Mater.,* **152,** 1045 (2008)
12. M. Barkat, D. Nibou, S. Chegrouche, A. Mellah, *Chem. Eng. Process.*, **48,** 38 (2009).K.G. Sreejalekshmia, K. Anoop Krishnan, T.S. Anirudhan, *J. Hazard. Mater.,* **161,** 1506 (2009).
13. E. Demirbas, M. Kobya, E. Senturk, T. Ozkana, *Water SA*, **30** (4), 533 (2004).
14. G. J. Siri, M. A. Galan, B. J. McCoy, *Comput. Chem. Eng.*, **13** (6), 661 (1989).
15. M. Kostova, I. Tsibranska, S. Nenov, *J. Univ. Chem. Technol. Met. (Sofia),* **38** (1), 79 (2003).
16. J. Yener, T. Kopac, G. Dogu, T. Dogu, *Chem. Eng. J.,* **144,** 400 (2008).
17. I. Tsibranska, E. Hristova, *Compt. rend. Acad. bulg. Sci.,* **64** (6), 831 (2011).
18. K. Furukawa, Y. Takahasui, *Chemosphere*, **73**, 1272 (2008).

19. Ch. W. Cheung, Ch. K. Chan, J. F. Porter, A. McKay, *Environ. Sci. Technol.*, **35,** 1511 (2001).
20. V.J.P. Vilar, C.M.S. Botelho, R. A.R. Boaventura**,** *Chem. Eng. J.,* **138**, 249 (2008).
21. Sh. Scally, W. Davison, H. Zhang, *Anal. Chim. Acta*, **558**, 222 (2006).

22. M. Soleimani, T. Kaghazchi, *Bioresour. Technol.*, **99,** 5374 (2008).
23. M. Guo, G. Qiu, W. Song, *Waste Management*, **30** (2), 308 (2010).
M. Madhava Rao, D.K. Ramana, K. Seshaiah, M.C. Wang, S.W. Chang Chien, *J. Hazard. Mater.,* **166,** 1006 (2009).

СРАВНЕНИЕ НА РАЗЛИЧНИ КИНЕТИЧНИ МОДЕЛИ ПРИ АДСОРБЦИЯ НА МЕТАЛНИ ЙОНИ С АКТИВЕН ВЪГЛЕН ОТ КАЙСИЕВИ ЧЕРУПКИ

И. Цибранска, Е. Христова

Химикотехнологичен и металургичен университет, бул. „Климент Охридски" № 8, София 1756

(Резюме)

В тази работа е изследвана кинетиката на едно- и четири-компонентна адсобция на Pb^{2+}, Cd^{2+}, Cu^{2+} и Zn^{2+} йони от водни разтвори с активен въглен от кайсиеви черупки. За описание на едно и многокомпонентно равновесие е използван моделът на Лангмюир. Направено е сравнение на три кинетички модела за вътрешно дифузионен контрол. Първоначалната стръмна част на кинетичната крива бе определена от отреза на линейното представяне на моделите на Вебер и Морис, Бойд и моментния метод. Най-добро съвпадение с експерименталните данни са получени с модела на Вебер и Морис. Коефициентите на вътрешна дифузия за отделните йони са в диапазона $1\text{-}3 \cdot 10^{-8} cm^2/s$. Подобни резултати са получени и при използване на моментния метод. Получени са по-ниски стойности на кинетичните параметри за четирикомпонентен разтвор. Стойността на сумарният дифузионен коефициент за многокомпонентна система е близък до този получен за еднокомпонентен разтвор със същата концентрация.

Mechanochemical synthesis and photocatalytic properties of zinc titanates[♦]

R. Iordanova[1], A. Bachvarova-Nedelcheva[1*], Y. Dimitriev[2], Tz. Iliev[3]

[1] Institute of General and Inorganic Chemistry, Bulgarian Academy of Sciences, 1113 Sofia, Bulgaria
[2] University of Chemical Technology and Metallurgy, 8 Kl. Ohridski blvd.,
1756 Sofia, Bulgaria
[3] Geological Institute, Bulgarian Academy of Sciences, 1113 Sofia, Bulgaria

A mixture consisting of both cubic $ZnTiO_3$ and Zn_2TiO_4 was synthesized by ball milling at room temperature. A stoichiometric mixture of nano ZnO and TiO_2 powders in a 1:1 molar ratio was subjected to intense mechanical treatment in air using a planetary ball mill (Fritsch – Premium line – Pulverisette No. 7) for a period from 5 to 120 min. The phase formation and the structural transformation were followed by X-ray phase analysis and IR spectroscopy. The synthesis of the zinc titanates started after 30 min and finished after 45 min milling time at a high speed (1000 rpm). The agglomeration tendency and the crystal size of the obtained powders were determined by scanning electron microscopy. The photocatalytic activity of the samples was investigated by degradation of a model aqueous solution of malachite green (MG) upon UV-irradiation.

Key words: $ZnTiO_3$, mechanochemical activation, photocatalytic properties.

INTRODUCTION

Zinc titanates are attractive materials owing to their various applications as paints, pigments, thermistors, sorbents, microwave dielectrics, dielectric resonators, catalysts, etc. [1-6]. Several compounds are known to exist in the $ZnO-TiO_2$ system: Zn_2TiO_4 congruently melting above 1500^0C; $ZnTiO_3$ stable up to 945^0C and $Zn_2Ti_3O_8$ which was found later [1, 7]. Both zinc titanates ($ZnTiO_3$ and Zn_2TiO_4) are electroceramic materials with interesting dielectrical properties and low sintering temperatures [8, 9]. There are several methods for preparing $ZnTiO_3$ powders, generally focused on conventional solid state reactions [1, 10], mechanochemical activation [11, 12], precipitation [13, 14] and several variants of the sol-gel technique [1, 10, 15-18]. The attempts to synthesize pure $ZnTiO_3$ by thermal treatment of ZnO/TiO_2 mixtures are generally unsuccessful because this titanate decomposes at high temperatures ($\sim 950^0C$). According to the review analysis, up to now $ZnTiO_3$ phase was always obtained simultaneously with Zn_2TiO_4 using the mechanochemical activation method [11, 12]. High energy ball milling was applied on the $ZnO-TiO_2$ system in order to obtain the most stable Zn_2TiO_4 phase [19-21]. It was established that intensive

milling conditions favor the formation of low temperature titanate forms. Very recently, Labus *et al.* [12] established coexistence of $ZnTiO_3$, Zn_2TiO_4 and TiO_2 (rutile) in a low temperature region below 945^0C for the composition with stoichiometric ratio 1:1. Generally, the mechanochemical activation of crystalline solids performed in high-energy mills becomes a very useful method to control the reactivity in the solid state [22]. Moreover, the milling conditions were limited up to 400-500 rpm, which did not exhaust the possibilities for synthesis by this method. Up to now the influence of the dispersity of the used precursors was not studied in the literature. For this reason, the study of new routes of synthesis of zinc titanates needs to be explored. That is why we were motivated to continue the investigations in the binary system $ZnO-TiO_2$ using high energy ball milling in order to control the process of synthesis.

The purpose of the present work was to study and to verify the behavior of the $ZnO-TiO_2$ system under new experimental conditions of mechanochemical activation of nano oxides (ZnO, <100 nm and TiO_2, < 25 nm) in order to obtain zinc titanates.

EXPERIMENTAL PROCEDURE

Nanopowders of zinc oxide (Sigma-Aldrich,

---

*To whom all correspondence should be sent:
E-mail: albenadb@svr.igic.bas.bg

<100 nm) and titanium oxide (anatase) (Sigma-Aldrich, < 25 nm) were used as starting materials.

The initial mixture of ZnO and TiO$_2$ in a molar ratio 1:1 was subjected to intensive mechanochemical activation in a planetary ball mill (Fritsch–Premium line–Pulverisette 7). The milling speed was 1000 rpm. Stainless steel vials and balls of 5 mm diameter were used. The balls:powder weight ratio was 10:1 and the milling time - from 5 to 60 min.

The phase and structural transformations were monitored by X-ray diffraction (XRD) and infrared (IR) spectroscopy. Powder XRD patterns were registered with a Bruker D8 Advance diffractometer using Cu Kα radiation in the range from 10 to 80^0. The thermal behavior of the powders was examined by differential thermal analysis (LABSYS^{TM} EVO apparatus). Infrared spectra were registered in the range 1200-400 cm^{-1} on a Nicolet-320 FTIR spectrometer using the KBr pellet technique. Morphologies and crystallite sizes of the obtained samples were characterized by scanning electron microscopy (JEOL Superprobe 733). The photocatalytic activity of the powder was studied using malachite green (MG) (Sigma-Aldrich) dye after subjecting it to UV-radiation. The UV irradiation was carryed out using an UV-lamp (Sylvania BLB, 18 W, $\lambda \sim 315–400$ nm). The aqueous solution of MG (150 mL, 5 ppm) containing 0.1 g of the prepared powder was placed in a vessel. Before photodegradation, an adsorption-desorption equilibrium state was established by ultrasonic and mechanical stirring for 10 min. Volumes of 3 mL were taken from the solution at given time intervals and separated through centrifugation (5000 rpm, 5 min). Then the concentration of MG in the solution was determined with a Jenway 6400 spectrophotometer.

RESULTS AND DISCUSSION

The X-ray diffraction patterns of the samples obtained are presented in Fig. 1. The diffraction lines of the obtained products ZnTiO$_3$ and Zn$_2$TiO$_4$ were indexed using JCPDS database. The interaction between the initial oxides started after 15 min and completed after 45 min milling time. On the diffractogram pattern for the milling time of 30 min, reflection characteristics for both cubic ZnTiO$_3$ (JCPDS 39-0190) and Zn$_2$TiO$_4$ (JCPDS 77-scanning electron microscopy (JEOL Superprobe 733). The photocatalytic activity of the powder was 0014) occurred. It is seen that after 15 min a small amount of FeTiO$_3$ (JCPDS 75-0519) appeared in the X-ray diffraction pattern. The prolongation of the mechanochemical treatment up to 120 min at the same milling speed did not lead to a change in the XRD patterns of the samples. Obviously, this high milling speed is decisive for the rapid synthesis. The presence of TiO$_2$ (rutile) was not established in our study in contrast to Labus *et al.* [12], which did not achieve a complete synthesis.
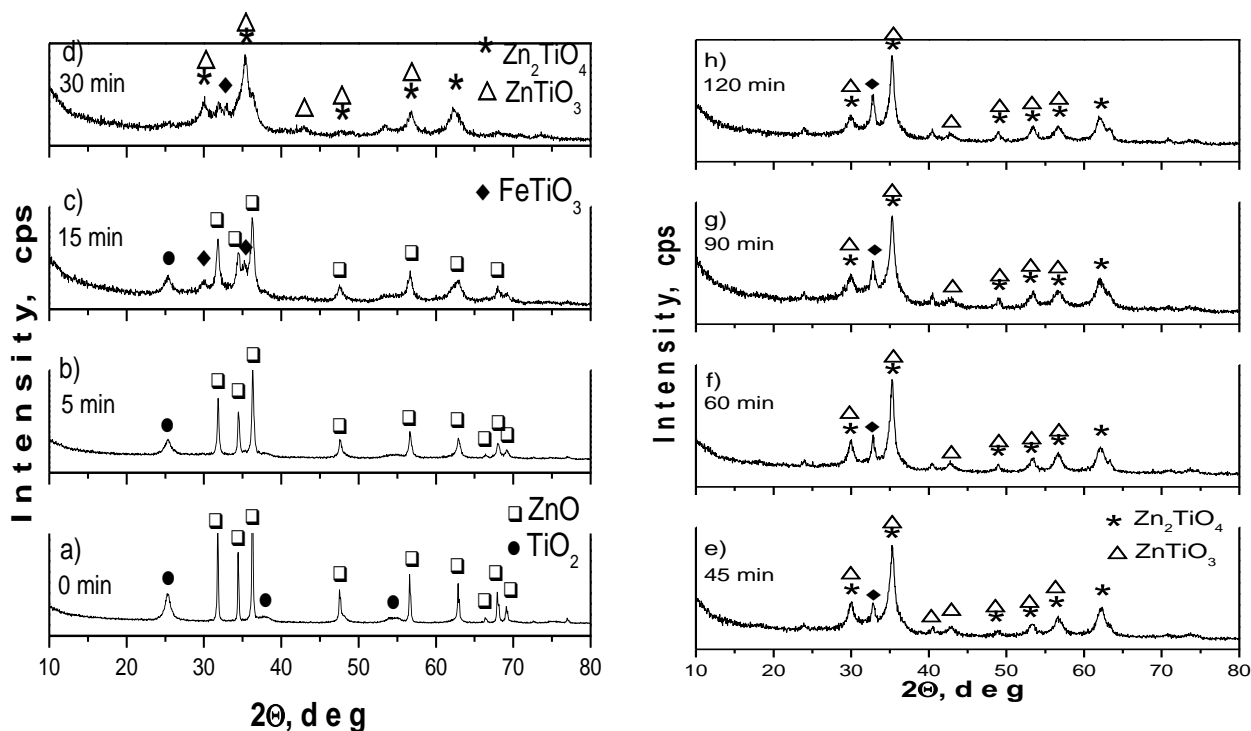
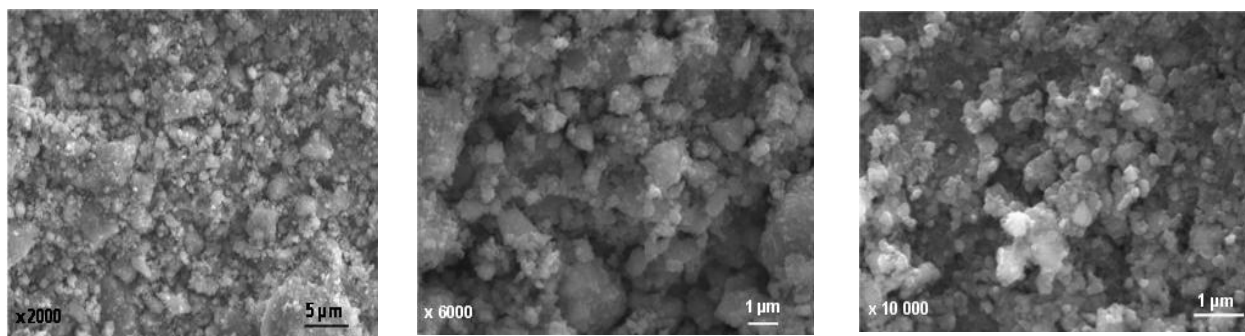**Fig. 1**. XRD patterns of the mixture at different milling time

Fig. 2. SEM images of the obtained powders after 60 min milling time at different magnifications.
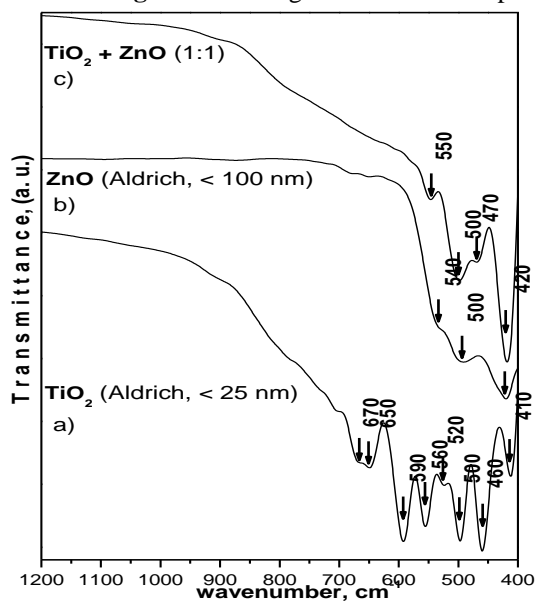

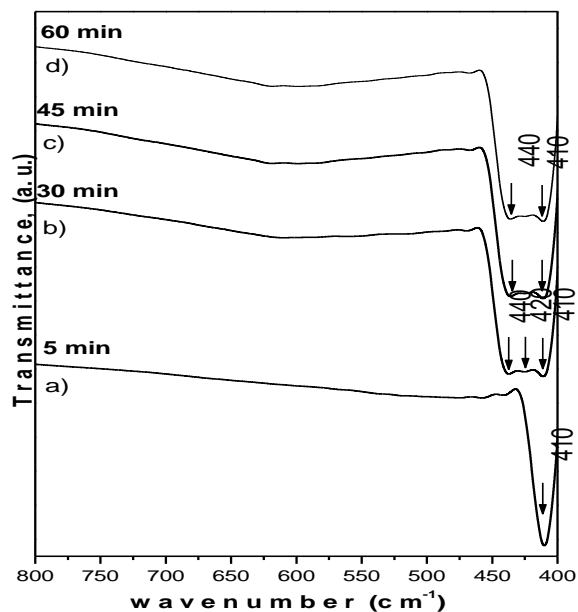**Fig. 3.** IR spectra of the mixture at different milling time

Fig. 4. IR spectra of TiO_2, ZnO and mixture of ZnO and TiO_2

Our results differ from those in the literature owing to the higher activity of the powders and the more intensive mechanochemical activation. Thereby, the selected experimental conditions in this study provided completeness of the zinc titanates synthesis. For comparison, similar results were obtained by Labus *et al.* [12] after 80 min milling time and by Qian *et al.* [23] – after 10 hours milling time. The average crystalline size of the obtained powders calculated from the broadening of the diffraction line using Sherrer's equation is about 60-70 nm. The morphology and particle size of the powders obtained after 60 min milling time are presented in Fig. 2. The SEM results showed that the obtained product consisted of agglomerates with average size below 1 μm.

IR spectroscopy was used to confirm the synthesis of the crystalline material. The absorption bands of the pure oxides TiO_2 (bands at 670, 650, 590-480 and 410 cm^{-1}) and of ZnO (bands at 540, 500 and 420 cm^{-1}) are shown in Fig. 3, while Fig. 4

presents the IR spectra of the mixtures after different milling times. As it is seen the IR spectrum of the mixture after 5 min milling time is different from the IR spectrum of the mixture without mechanochemical activation because the bands corresponding to TiO_2 disappeared (Fig. 3c). One band only, at 410 cm^{-1}, is observed that could be assigned to the vibration of ZnO polyhedra [24-26] and this may be an indication of the beginning of the chemical reaction (Fig. 4). It is well known that the bands corresponding to ZnO_n polyhedra are in this absorption range. This peculiarity was not found in the X-ray diffraction patterns, where the diffraction lines of the starting materials were found, but the strongest peak of TiO_2 decreased (Fig. 1b). At 30 min milling time new bands appeared in the same spectral range (about 440 and 420 cm^{-1}) which pointed to the continuation of the synthesis. Between 30 min and 45 min milling time the IR spectra changed which could be related to the synthesis of crystalline phases. According to

380

some authors [1, 27], the appearance of the bands about 450-440 cm^{-1} could be related to the Ti-O stretching vibrations in ZnTiO$_3$.
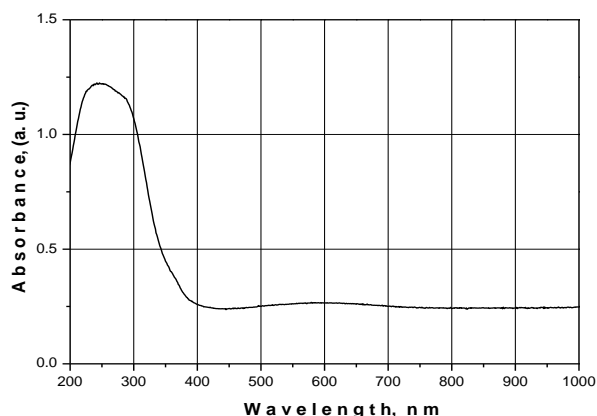
Fig. 5. UV-VIS spectrum of ZnTiO$_3$ powder obtained by mechanochemical activation
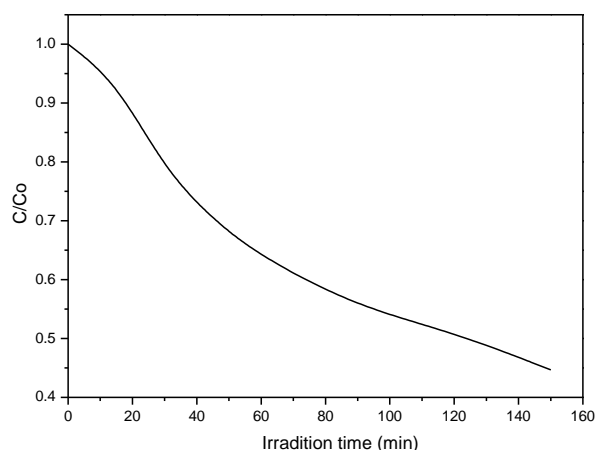
Fig. 6. Photocatalytic degradation of Malachite Green (MG) by ZnTiO$_3$ powder

The UV-Vis spectrum of the sample obtained after 60 min milling time is shown in Fig. 5. As it is seen the obtained powder is highly transparent in the visible region. The UV-Vis spectrum shows that the absorption edge starts at about 240 nm. Fig. 6 shows the temporal evolution of the concentration (C/C_0) of MG, where C_0 and C represent the initial equilibrium concentration and the reaction concentration of MG, respectively. The photodegradation of MG was completed in 150 min and it was compatible to the photocatalytic activity of ZnO and TiO$_2$ [26, 28] (Fig. 6).

CONCLUSIONS

A mixture of both cubic ZnTiO$_3$ and Zn$_2$TiO$_4$ was successfully prepared under new experimental conditions: 45 min milling time and milling speed of 1000 rpm. The mechanochemically obtained mixture of zinc titanates displays photocatalytic activity towards the degradation of malachite green

after 150 min irradiation time. The UV-Vis spectrum shows that the obtained sample is transparent in the visible range of the spectrum.

REFERENCES

1. O. Yamaguchi, M. Morimi, H. Kawabata, *et al.*, *J. Amer. Ceram. Soc.*, **70,** 97 (1987).
2. A. Baumgrate, R. Blachnik, *J. Alloys Compd.*, **210**, 75 (1994).
3. Z. Chen, A. Derking, W. Kot, M. Dijk, *J. Catal.*, **161**, 730 (1996).
4. H. Kim, S. Nahm, J. Byun, *J. Am. Ceram. Soc.*, **82**, 3476 (1999).
5. H. Kim, J. Byun, Y. Kim, *Mater. Res. Bull.*, **33**, 963 (1998).
6. S.F. Wang, M. Lu, F. Gu, C. Song, D. Xu *et al.*, *Inorg. Chem. Commun.*, **6**, 185 (2003).
7. F.H. Dulin, D.E. Rase, *J. Amer. Ceram. Soc.*, **43**, 12 (1960).
8. H. T. Kim, J. D. Byun, Y. Kim, *Mater. Res. Bull.*, **33**, 963 (1998).
9. H. T. Kim, S. H. Kim, J. D. Byun *et al.*, *J. Amer. Ceram. Soc.,* **82**, 3043 (1999).
10. Y. Chang, Y.H. Chang, I.G. Chen *et al.*, *Ceram. Intern.*, **30**, 2183 (2004).
11. P. Botta, E. F. Aglietti, J. Porto Lopez, *J. Mater. Sci.*, **39**, 5195 (2004).
12. N. Labuss, N. Obradovic, T. Sreckovic, *Sci. and Sintering*, **37**, 115 (2005).
13. H. W. Yao, R.B. Feng, *Mining Safety Environ. Protect.*, **28**, 20 (2001).
14. R. P. Gupta, S.K. Gangwal, S. Jain, US Patent N 5,714,431 (1998).
15. C. Li, Y. Bando, M. Nakamura, N. Kimizuka *et al.*, *Mater. Res. Bull.*, **35,** 351 (2000).
16. Y.L. Chai, Y.S. Chang, G.J. Chen, Y.J. Hsiao, *Mater. Res. Bull.*, **43**, 1066 (2008).
17. X. Xing, J. Luo, G. Liu, L. Qiao, J. Meng, *J. Amer. Ceram. Soc.*, **89**, 1125 (2006).
18. S.F. Wang, F. Gu, M.K. Lu *et al.*, *Mater. Res. Bull.*, **38**, 1283 (2003).
19. S. K. Manik, P. Bose, S. K. Pradhan, Mater. *Chem Phys.*, **82**, 837 (2003).
20. S. K. Manik, S. K., Pradhan, *Physica E*, **33**, 69 (2006)
21. T. Sreckovic, N. Labus, N. Obradovic, Lj. Zivkovic, *Mater. Sci. Forum*, **543-454**, 435 (2004).
22. C. Suryanarayana, E. Ivanov, V. Boldyrev, *Mater. Sci. Eng.*, **A304-306**, 151 (2001).
23. D. Qian, L. Gerward, J. Jiang, *J. Mater. Sci.*, **39**, 5389 (2004).
24. M. Mancheva, R. Iordanova, Y. Dimitriev, *J. Alloys Compd.*, **509**, 15 (2011).

25. M. Andres-Verges, M. Martinez-Gallego, *J. Mater. Sci.*, **27**, 3756 (1992).

26. Y. Dimitriev, Y. Ivanova, A. Staneva, L. Alexandrov, M. Mancheva, R. Yordanova, C. Dushkin, N. Kaneva, C. Iliev, *J. Univ. Chem. Tech. Metall.*, **44**, 235 (2009).

27. B.G. Shabalin, *Mineral. Zh.*, **4**, 54 (1982).

28. A. Stoyanova, M. Sredkova, A. Bachvarova-Nedelcheva, R. Iordanova, Y. Dimitriev, H. Hitkova, Tz. Iliev, *Opt. Adv. Mater. - RC*, **4**, 2059 (2010).

МЕХАНОХИМИЧЕН СИНТЕЗ И ФОТОКАТАЛИТИЧНИ СВОЙСТВА НА ЦИНКОВИ ТИТАНАТИ

Р. Йорданова[1], А. Бъчварова-Неделчева[1*], Я. Димитриев[2] и Цв. Илиев[3]

[1] *Институт по обща и неорганична химия, Българска академия на науките, ул.“Акад. Г. Бончев”, бл. 11, 1113 София, България*

[2] *Химикотехнологичен и металургичен университет, бул. „Кл. Охридски” 8, 1756 София, България*

[3] *Геологически институт, Българска академия на науките, 1113 София, България*

(Резюме)

Смес, съдържаща кубичните форми на $ZnTiO_3$ и Zn_2TiO_4, е синтезирана по механохимичен път при стайна температура. Стехиометричната смес, съдържаща нано ZnO и TiO_2 прахове в моларно съотношение 1:1, е подложена на интензивна механична обработка на въздух в планетарна топкова мелница (Fritsch – Premium line – Pulverisette No. 7) за период от 5 до 120 мин. Фазообразуването и структурните трансформации са проследени чрез рентгенофазов анализ и ИЧ спектроскопия. Установено е, че синтезът на цинковите титанати започва след 30 мин и приключва след 45 мин механохимично третиране при висока скорост (1000 оборота). Тенденцията за агломериране и размерът на получените прахове са определени чрез СЕМ. Фотокаталитичната активност на образците е изследвана чрез разлагането на моделен разтвор на малахитово зелено (MG) под влияние на УВ лъчение.

The marvellous Marcus equation

V Jagannadham*, R. Sanjeev

Department of Chemistry, Osmania University, Hyderabad-500 007, India

Nitrobenzenes ($\mathbf{XC_6H_4NO_2}$) were reduced to their radical anions ($\mathbf{XC_6H_4NO_2^{\bullet-}}$) by eighteen different carbon centered radicals derived from formate and simple alcohols, and pyrimidine bases. These radicals were generated by pulse radiolysis in aqueous solution. Carbon dioxide radical anion ($\mathbf{CO_2^{\bullet-}}$) is taken as standard which reacts by direct electron transfer ("non-bonded" or "outer sphere") with nitrobenzenes. Reaction of α-hydroxy-iso-propyl radical with nitrobenzenes again proceeds by direct electron transfer ("non-bonded" or "outer sphere") and some radicals react via addition/electron transfer mechanism ("bonded" or "inner sphere") giving final products. And the reaction of some radicals stops at the stage of addition to give nitroxide type radicals $\mathbf{[(XC_6H_4N(O^\bullet)OR]}$ where R is alcohol or pyrimidine moiety on the micro second time scale. The addition/electron transfer mechanisms are well characterized by Marcus theory. All these results are rationalized on the basis of the magnitude of the slopes of Marcus plots established from Marcus theory of one electron transfer mechanisms.

Key words: Marcus Equation, Electron Transfer Reactions.

INTRODUCTION

The nature of electron transfer reactions in terms of energy considerations is nothing but an amalgamation of activation barrier ($\Delta G^{\neq}$) and thermodynamic driving force (ΔG^{o}). Hence for a thermo neutral reaction ($\Delta G^{o} = 0$) the activation barrier ($\Delta G^{\neq}$) itself is the intrinsic activation barrier (λ). Marcus equation is a successful treatise for treating kinetic data of electron transfer reactions to separate activation ($\Delta G^{\neq}$) and thermodynamic quantities (ΔG^{o}). Ever since the theory of electron transfer reactions is developed by Marcus [1], interest of kineticists for doing research in this direction has been the central point for understanding the "outer sphere" and "inner sphere" electron transfer reactions. The nomenclature of electron transfer reactions makes frequent use of the terms "outer sphere" and "inner sphere" electron transfer reflects the historical fact that the experimental studies of electron transfer between metal complexes have predominated very often. These terms refer to the structure of the transition states, "outer sphere" denoting that the inner coordination shells of the reacting complexes are left intact in the transition state as to the number and type of ligands originally present, and "inner sphere" meaning that the complexes share at least one ligand of their first coordination spheres in the

transition state. This bridging ligand perhaps provides a continuous pathway of good orbital overlap from metal ion to metal ion. But the notions of "outer sphere" and "inner sphere" mechanisms are not directly applicable to reactions with organic molecules as reacting partners, and hence the terms "non-bonded" and "bonded" have been introduced for electron transfer reactions taking place in organic molecules.
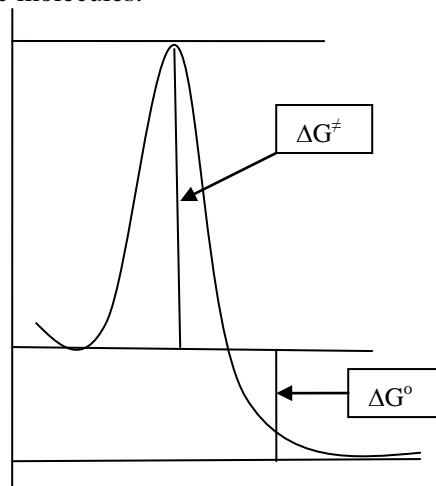
Many articles using the treatment of Marcus theory on several reactions have appeared in literature. These findings include the reactions between several redox pairs of metal ions [2-5], proton transfer at carbon [6-9] and at oxygen or nitrogen[7-10], H⁻ transfer [11], H• transfer [12], nucleophilic addition to carbonyl group [13,14], to carbocations [8, 15], and bimolecular nucleophilic

* To whom all correspondence should be sent:
E-mail: jagannadham1950@yahoo.com

aliphatic substitutions [16,17]. In the present article an attempt is made to distinguish between the "non-bonded" single electron transfer reaction from "bonded" single electron transfer reaction using the magnitudes of the slopes of Marcus plots in some free radical reactions where in nitrobenzenes are reduced to their radical anions by a variety of carbon centered radicals generated pulse radiolytically from formate, simple alcohols, and pyrimidine bases. To the author's knowledge this article may be first of its kind to apply Marcus treatment to electron transfer reactions involving radicals and molecules. The nature of electron transfer in these reactions was published [18, 21] based on the results obtained from ESR and time resolved experiments using pulse radiolysis spectroscopic and conductivity detection systems.

EXPERIMENTAL

All experimental details and the data used in this article are from the author's (VJ) work available in literature [18, 21].

DISCUSSION

Oxidation-reduction reactions involving the transfer of an electron between redox partners have been the subject of many kinetic studies. These redox reactions could be broadly classified in to two categories based on whether the transfer of electron involves ionic sphere or coordination sphere of the redox partners: and the two categories are (a) An outer-sphere electron transfer reaction and (b) An inner-sphere electron transfer reaction. In outer-sphere electron transfer reaction the metal ion retains its full coordination shell and there is a direct electron transfer from the reductant to the oxidant. The electron given by the reducing agent must be transferred from the primary bond system of one complex to that of the other. The essential feature of this mechanism is that there is no transfer of ligands between the reactants. Kinetically the rate of reaction is faster than the rate of substitution of ligands, or the ligand exchange or displacement is slower than electron transfer. And in an inner-sphere electron transfer reaction one of the reactants is labile. In reactions of this class, electron transfers are preceded by the substitution of coordination sphere of one of the ions, with the formation of bridged intermediate in which the two reactants are linked by a common ligand. In this case, ligand displacement is faster than electron transfer process.

These two examples are well explained [4] by a single reaction which involves both the reaction path ways by an example of oxidation of penta-cyanocobaltate (II) by penta-amminocobalt (III) complexes based on the only results of stoichiometry and kinetics.

$$Co^{II}(CN)_5^{3-} + Co^{III}(NH_3)X \xrightarrow{k_i} [(CN)_5Co^{II}-X-Co^{III}(NH_3)_5] \longrightarrow CO^{III}(CN)_5X$$

$$+CN^- \big\Vert K$$

$$Co^{II}(CN)_6^{4-} + CO^{III}(NH_3)_5X \xrightarrow{k_o} [(CN)_5Co^{II}(CN)(X)Co^{III}(NH_3)_5] \longrightarrow Co^{III}(CN)_6^{3-}$$
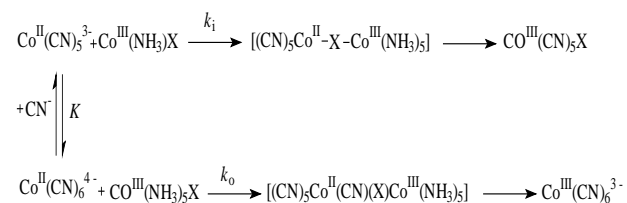
When $X = PO_4^{3-}, CO_3^{2-}, SO_4^{2-}, NH_3$, and OAc⁻ the reaction followed an outer sphere electron transfer route and when X = Cl⁻, N_3^-, NCS⁻ and OH⁻ the reaction followed an inner sphere electron transfer route.

We have probed in this article the possibility of using the magnitude of Marcus slopes to distinguish between outer sphere (non-bonded) electron transfer reactions and inner sphere (bonded) electron transfer reactions. A particularly promising opportunity thereby is afforded for the systematic examination of the choice between these two mechanisms.

Successful comparison and properties of electrochemical and chemical rate constants made by Marcus [3] led to arrive at the following equation after rewriting and several rearrangements:

$$\log k = -\log \frac{h}{k_B T} - \frac{\lambda}{4} + \frac{nF}{2 \bullet 2.303\, RT} E^\circ \qquad (1)$$

Where k is rate constant, h Planck constant, k_B the Boltzmann constant, λ is the intrinsic activation barrier, n the number electrons transferred from donor to acceptor, F the Faraday constant, R the gas constant, E° is the redox potential or the driving force and T is temperature in Kelvin scale. And this equation could be obtained as follows from Marcus equation:

According to Marcus [3] for a reaction with weak-overlap electron transfer or non-bonded electron transfer or for an outer sphere electron transfer, the following equation is obtained:

$$\Delta G^{\neq} = \frac{\lambda}{4} + \frac{w_R + w_P}{2} + \frac{\Delta G^\circ}{2} \qquad . (2)$$

Omitting the work terms [22] (w_R and w_P are the quantities of works required to bring the reactants together and for the removal of the products respectively) for proton transfer and electron transfer reactions between molecules or

ions and molecules or radicals and molecules, the final equation obtained was:

$$\Delta G^{\neq} = \frac{\lambda}{4} + \frac{\Delta G^{o}}{2} \qquad (3)$$

$\Delta G^{\neq}$ is the free energy of activation and ΔG^{o} is the standard free energy change for the process. Therefore for thermo neutral reactions ($\Delta G^{o} = 0$) $\Delta G^{\neq}$ is itself equal to one fourth of the λ which is the intrinsic activation barrier.

From transition state theory provided by Eyring:

$$k = \frac{k_{B}T}{h} e^{-\frac{\Delta G^{\neq}}{RT}} \qquad . (4)$$

And from electrochemistry for a driving force, the standard free energy change is given by the equation:

$$\Delta G^{o} = - n F E^{o} \qquad (5)$$

Taking logarithms of Eq.(4) and rearranging for $\Delta G^{\neq}$ we get

$$\Delta G^{\neq} = - 2.303 \log \frac{k h}{k_{B}T} \qquad (6)$$

Substituting the values of ΔG^{o} and $\Delta G^{\neq}$ in to Eq. (3) we get

$$- 2.303 \log \frac{k h}{k_{B}T} = \frac{\lambda}{4} - \frac{n F E^{o}}{2} \qquad (7)$$

Rearranging the Eq.(7) for log k we get

$$\log k = - \log \frac{h}{k_{B} T} - \frac{\lambda}{4} + \frac{n F}{2 \bullet 2.303 R T} E^{o} \qquad (8)$$

Hence for an outer sphere electron transfer (non-bonded) in a given homologous series of reaction, a plot of log k versus redox potential (E^{o}) should give a straight line with a slope equal to $\left(\frac{n F}{2 \bullet 2.303 R T} \right)$ and an intercept equal to $-\left(\log \frac{h}{k_{B} T} + \frac{\lambda}{4} \right)$. Substituting the constants in the quantity for the slope for one electron transfer reaction at 298 K (n = 1) yields **8.5 V^{-1}**. And from the intercept, again substituting the constants and at 298 K we get

$$\text{Intercept} = 13.21 - \frac{\lambda}{4} \qquad (9)$$

$$\text{Or} \quad \lambda = 4 \text{ X } (13.21 \text{ - Intercept}) \qquad (10)$$

As a specific example, the applicability of Eq.(8) is seen for the oxidation [5] of Fe(II)-tris-

(1,10-phenanthroline) complexes by Ce(IV) in H_2SO_4 medium at 298 K where in the two redox

$$Fe^{2+}(1,10\text{-phen}) + Ce(IV) \xrightarrow{k} Fe^{3+}(1,10\text{-phen}) + Ce(III$$
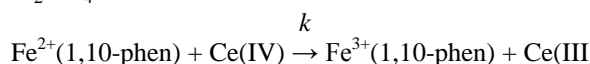
partners are inorganic species. A plot of (Fig. 1; R = 0.983) log k versus redox potentials of iron complexes was found to be linear with a slope of **7.9 V^{-1}** which is very close to **8.5 V^{-1}** as predicted by Eq. (8) for an outer sphere electron transfer mechanism. From the intercept the intrinsic activation barrier (λ) was found to be **– 1.4** kJ mole^{-1}. The negative sign of the intrinsic activation barrier is probably an indication of smooth electron transfer from Fe(II) to Ce(IV) with a weak overlap satisfying the so-called Frank-Condon restrictions. And the small magnitude or negligible value of the barrier may be understood that the reaction between Fe(II) and Ce(IV) is an example of a thermo neutral reaction.

Figure 1: Fe(II)(Phe)-Ce(IV) reaction: Plot of log k versus redox potential[a] of Fe(II) Phenonthroline complexes

slope = 7.9 V^{-1}
intercept = 13.6
R = 0.983
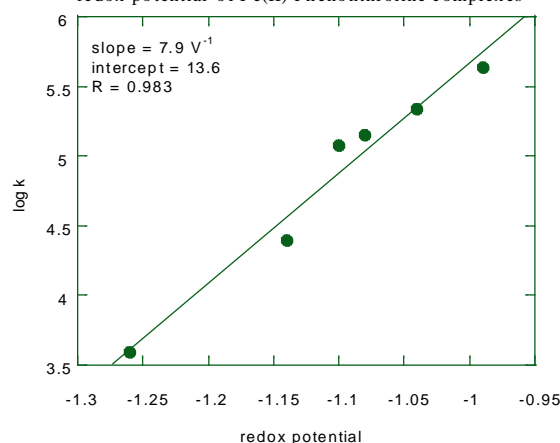
[a] reference 5.

The nature of electron transfer reactions in many organic reactions undergo extensive electronic reorganization and changes in bonding to reacting atoms differ with simple outer-sphere electron transfer reactions for which the Marcus theory was developed to explain. The intrinsic activation barrier for the electron transfer could be taken as a model for the reorganization of the solvent which can assist an optimal tunneling of electron from donor to acceptor.

The main object to discuss the application of Marcus equation to free radical reactions with nitroaromatic compounds is due to the fact that these compounds have widespread potential use in medicine and cancer therapy [23, 24]. There is direct proof that free-radical metabolites are involved in many applications and widespread interest in free-radical intermediates in the action of

several classes of medically important compounds. It is arguable that nitro compounds are the one class of drug in which direct proof of radical production in intact target organisms has been demonstrated [24] and in which the free-radical reaction almost certainly responsible for the therapeutic selectivity has been observed directly [24]. And redox properties control the rate and mode of electron transfer from donors to acceptors. The following are the several examples involving free radical reactions and are classified in to 'non-bonded" (outer-sphere) and "bonded" (inner-sphere) electron transfer mechanisms based on the magnitudes of the slopes of Marcus plots. And intrinsic activation barriers (λ) were also calculated and discussed for all the reactions.

All the radicals were produced pulse radiolytically in N_2O saturated aqueous solutions containing desired reactants. And these radicals were subjected to react with nitrobenzenes. All the kinetic data used in this article is from the author's (VJ's) work [18-21].

Carbon dioxide radical anion ($CO_2^{\bullet -}$ *)[18]:* The Marcus plot for the following reaction:
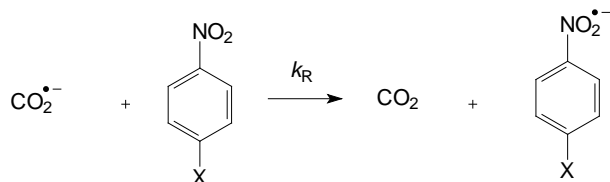
(rate constant is k_R $M^{-1} s^{-1}$)
was found to be linear (Fig. 2; R = 0.988) with a slope of **7.3 V^{-1}**, the value though not as close as the value of Fe(II) –Ce(IV) reaction to the value of **8.5 V^{-1}** predicted for an outer-sphere electron transfer reaction, cf. Eq. (8), but it may not be misunderstood that the reaction of carbon dioxide

radical anion with nitrobenzenes is not a "non-bonded" (outer-sphere) electron reaction. From the intercept of 11.8 the intrinsic activation barrier (λ) was found to be **5.7** kJ mol^{-1}. The radical anion $CO_2^{\bullet -}$ was quantitatively oxidized to CO_2 by nitrobenzene and which was confirmed by comparing the yield of $XC_6H_4NO_2^{\bullet -}$ with that of the quantity obtained by direct reaction of nitrobenzene with hydrated electron [18] (e_{aq}^-). Hence it is concluded that the reaction involves a smooth direct "non-bonded" electron transfer without under going any prime structural changes in the reactants and taken as standard for comparison of the rest of the reactions discussed in this article. The redox potentials of nitrobenzenes used in this figure and in subsequent figures are from reference 24, and for some nitrobenzenes they were calculated using the following equation:

$$E \cong -0.484 + 0.168 \; \sigma_P^-$$

Similar values of redox potentials were reported by S. Steenken [28].
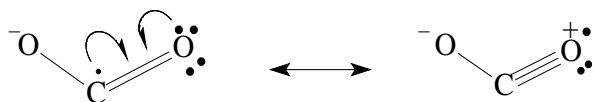
α-hydroxy-isopropyl radical [(CH₃)₂C•OH[18]:
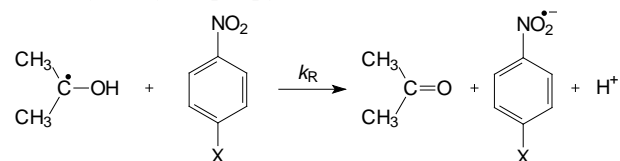
The plot of log k_R versus redox potential of nitrobenzenes was linear (Fig. 3: R = 0.962) with a slope of **1.6 V^{-1}** and intercept of 9.9. And this need not be misunderstood that whether the reaction will be proceeding through "bonded" or "non-bonded" electron transfer mechanism since the magnitude of the slope is not on Marcus scale. The α-hydroxy-isopropyl radical was quantitatively oxidized to acetone by nitrobenzenes and which was confirmed

Figure 2: log k_R versus E for the reaction of carbon dioxide radical anion and nitro benzenes

Figure 3: Plot of log k_R versus E for the reaction of iso-propanol radical with nitrobenzenes.
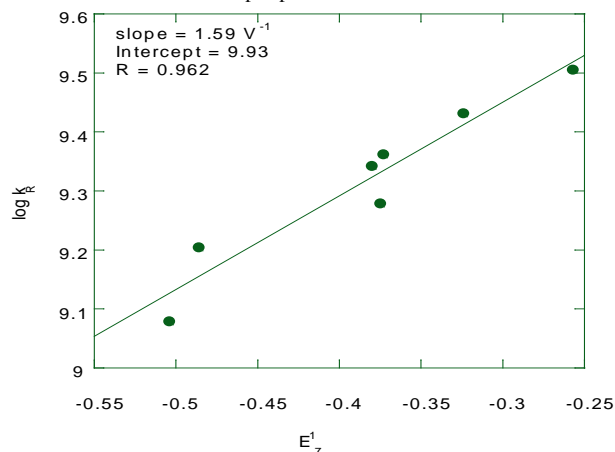
by comparing the yields of $\mathbf{XC_6H_4NO_2^{\bullet-}}$ with that of the quantity again obtained by direct reaction of nitrobenzene with hydrated electron [18] ($\mathbf{e_{aq}^-}$). And the yields of acetone were checked by GC by comparing with an authentic sample. Hence it is concluded that the reaction again with α-hydroxy-isopropyl radical involves a smooth direct "non-bonded" electron transfer. In fact the rate constants (k_R M^{-1} s^{-1}) of reaction of all nitrobenzenes studied for the oxidation of this radical was more or less look identical and are close to the rate constant (~ 5×10^9 M^{-1} s^{-1}) of a diffusion controlled reaction. The rate constants for the reaction of this radical were higher than those observed for the oxidation of carbon dioxide radical anion. Invoking reactivity-selectivity principle here that more reactive radical is less selective and less selective radical is more reactive. And this could be explained due to differences in stabilities of carbon dioxide radical anion ($\mathbf{CO_2^{\bullet-}}$) and α-hydroxy-isopropyl radical as shown in the following:

This kind of structure for α-hydroxy-isopropyl radical is not possible hence carbon dioxide radical anion is more stable than α-hydroxy-isopropyl radical hence more selective.

α-hydroxy-ethyl radical (CH₃CH•OH) [18]:
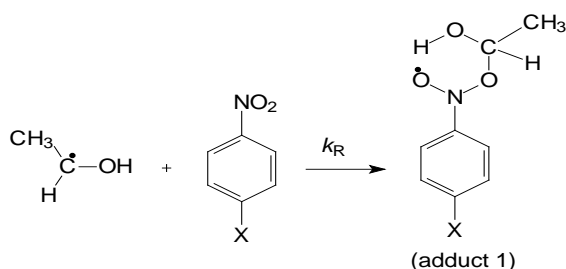
(adduct 1)

Figure 4: Plot of log k_R versus E for the reaction of ethanol radical with nitrobenzenes
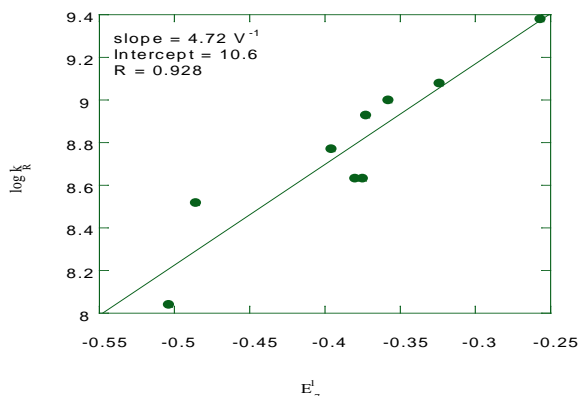
The reaction of this radical with nitrobenzenes underwent in two reaction channels [18]. One involves the formation of nitroxide radical (k_R mol^{-1} sec^{-1}) and the other (see later in the text) giving the radical anion, acetaldehyde and the proton (k_s s^{-1}). The plot (Fig. 4; R = 0.928) of log k_R versus redox potentials of nitrobenzenes was fairly linear with a slope of **4.7 V^{-1}** and with an intercept of 10.6. From the intercept, intrinsic activation barrier (λ) was found to be **10.4.**

α-hydroxy-methyl radical ($^\bullet CH_2OH$ [18]:
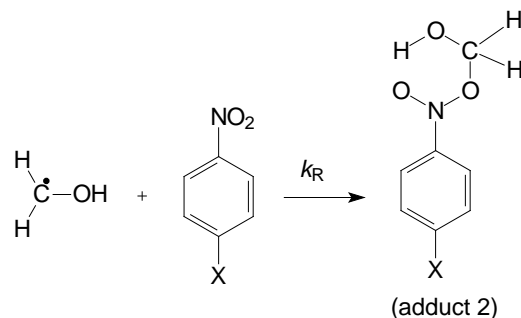
(adduct 2)

Figure 5: Plot of log k_R versus E for the reaction of methanol radical with nitrobenzenes
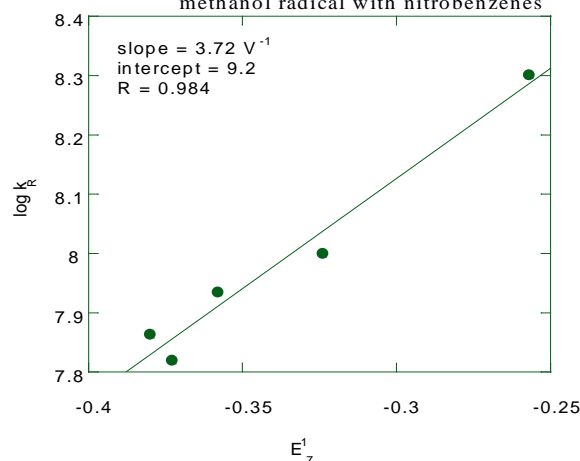
The reaction of this radical with nitrobenzenes ended up only with adduct formation unless the pH of the solution raised beyond 7 to give redox products [18]. The plot (Fig. 5; R = 0.984) of log k_R versus redox potentials of nitrobenzenes was linear with a slope of **3.72 V^{-1}** and with an intercept of 9.2. The value of intercept leads to 16 as intrinsic activation barrier (λ). This is again a clear indication that no electron transfer took place.

Reactions of 6-methyluracil-6-yl (6-MeU•), 6-methylcytosine-6-yl (6-MeC•), 6-methyl-di-hydrouracil-6-yl (6-MeDHU•) and 2-amino-4,6-dimetyluracil-6-yl (2-A-4,6-DMU•) radicals [20-21]:

(adduct 3)
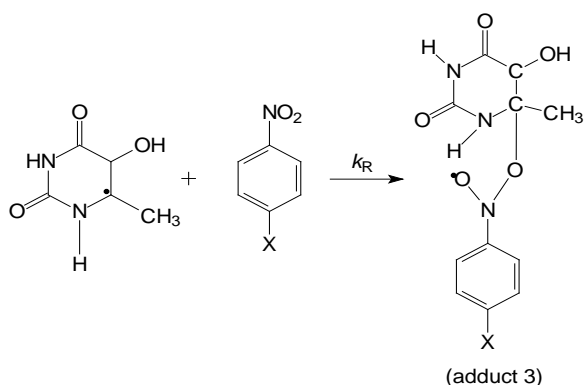
Figure 6: Plot of log k_R versus E for the reaction of 6-MeU radical with nitrobenzenes

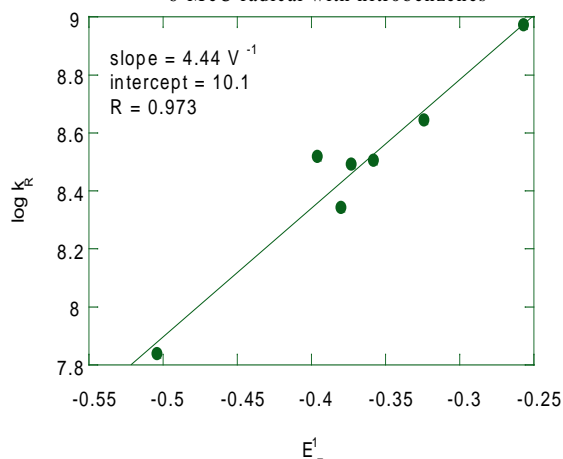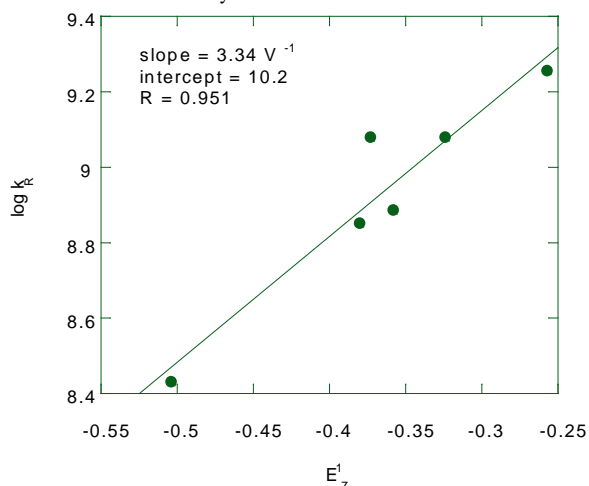Figure 7: Plot of log k_R versus E for the reaction of 6-Me Cytosine radical with nitrobenzenes

The Marcus plots for the reactions (k_R M^{-1} sec^{-1}) of these radicals with nitrobenzenes to give nitroxide type radicals yield the slopes and intercepts **4.44 V^{-1}** and 10.1 (6–MeU$^\bullet$: Fig 6, R = 0.973), **3.34 V^{-1}** and 10.2 (6-MeC$^\bullet$: Fig 7, R = 0.951), **1.45 V^{-1}** and 9.8 (6-MeDHU$^\bullet$: Fig 8, R = 0.914) and **4.95 V^{-1}** and 10.6 (2-A-4,6-DMU$^\bullet$: Fig 9, R = 0.999) respectively. The very low values of the Marcus slopes not close to **8.5 V^{-1}** are again an indication for the formation of the nitroxide type

adducts only and not for the electron transfer. The intrinsic activation barriers (λ) were found to be **12.4**, **12**, **13.6** and **10.4** respectively. Either it is surprise or accident but it is by experimental evidence that the very similar Marcus slopes of the

Figure 8: Plot of log k_R versus E for the reaction of 6-Me DHU radical with nitrobenzenes
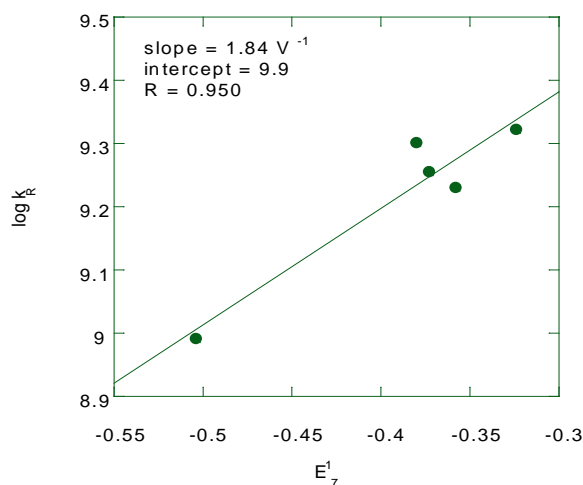
Figure 9: Plot of log k_R versus E for for the reaction of 2-A-4,6-DMU Radical
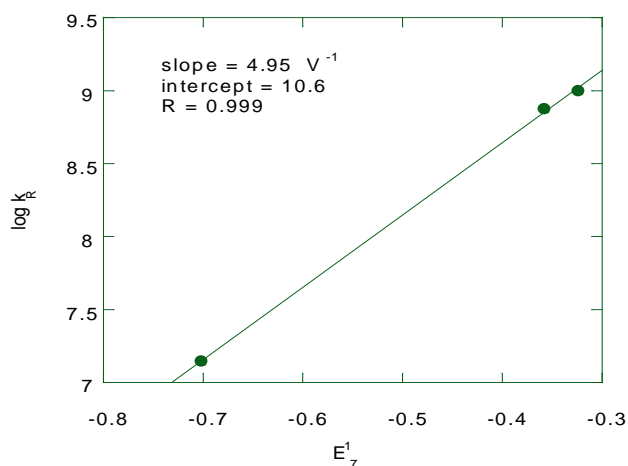
reactions of **isopropyl (1.59 V^{-1})** and **6-MeDHU$^\bullet$ (1.45 V^{-1})** radicals shows that the transition states of these two reactions resemble with each other on their way to products in spite of the fact that the two Marcus slopes are one for electron transfer and the other for adduct formation respectively. But before they go to products, the nature of the transition states could be understood as similar ones. This could be seen in the Scheme 1 shown in rectangles [25].

Hence isopropyl radical could be taken as a good model radical for understanding the reduction properties of 6-methyl substituted pyrimidine-6-yl radicals.
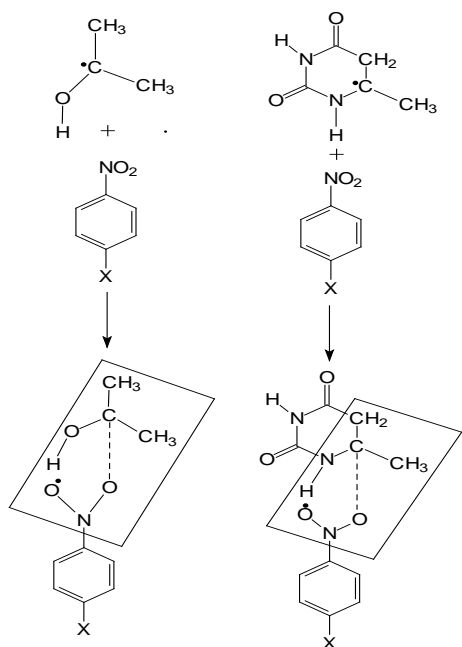
Scheme-1

Reactions of uracil-6-yl (U•), cytosine-6-yl (Cy•), and 1-methyl-uracil-6-yl (1-MeU•) radicals [19]

The reactions of these radicals with nitrobenzenes again ended up only with adduct formation unless the pH of the solution raised beyond 7 like in the case of **α-hydroxy-methyl radical (•CH₂OH)** to give redox products. The Marcus plots of log k_R versus redox potentials of nitrobenzenes were linear with slopes and
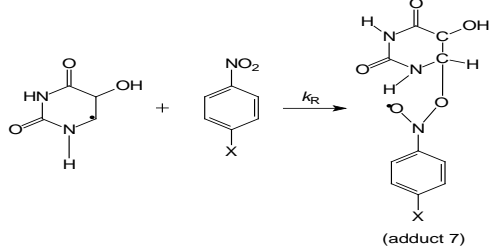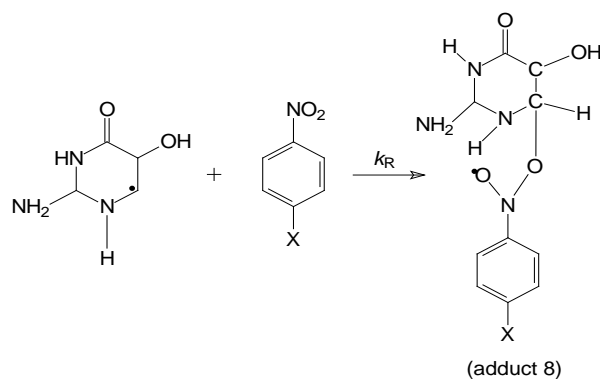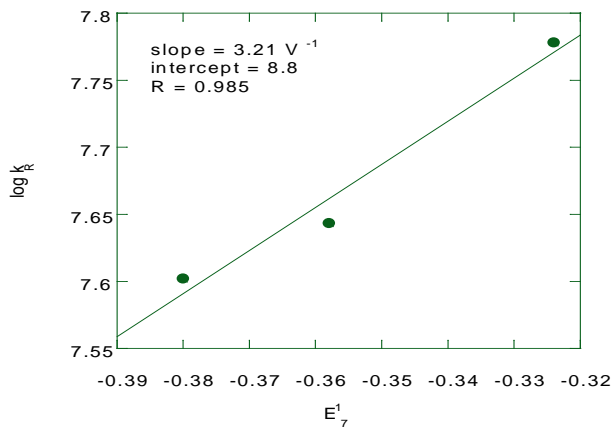

(adduct 7)

Figure 10: Plot of log k_R versus E for the reaction of uracil radical

(adduct 8)

Figure 11: Plot of log k_R vs E values for the reaction of Cytosine radical with nitrobenzenes.
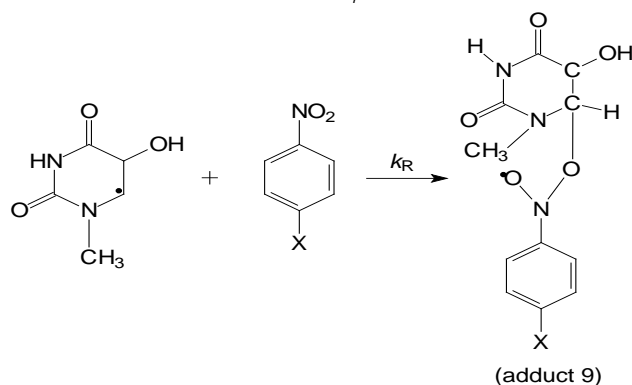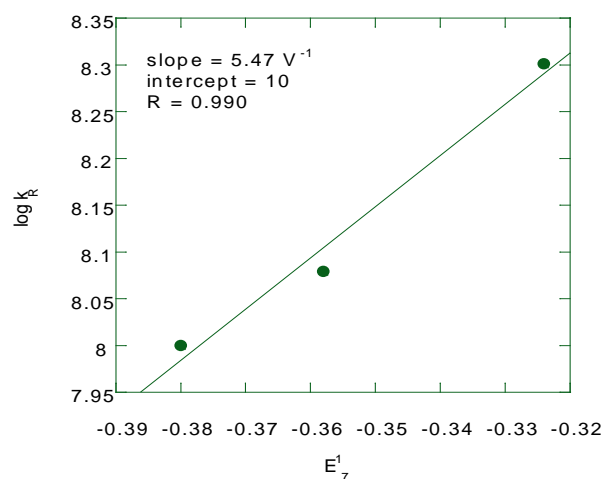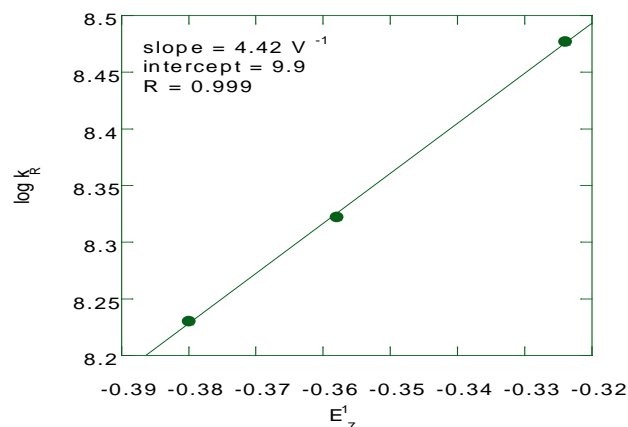

slope = 5.47 V⁻¹
intercept = 10
R = 0.990

(adduct 9)

Figure 12: Plot of log k_R vs E for the reaction of 1-MeUracil radical with nitrobenzenes

slope = 4.42 V⁻¹
intercept = 9.9
R = 0.999

389

intercepts of **3.21 V^{-1}** and 8.8 (**U$^•$**: Fig 10, R = 0.985), **5.47 V^{-1}** and 10 (**Cy$^•$**: Fig 11, R = 0.993), and **4.42 V^{-1}**, and 9.9 (**1-MeU$^•$**: Fig 12, R = 0.999) respectively. The values of intercepts lead to 17.6, 12.8 and 13.2 as intrinsic activation barriers (**λ).** This is again a clear indication that no electron transfer took place between these radicals and nitrobenzenes. And further from similar Marcus slopes of **3.7 V^{-1}** and **3.2 V^{-1}** for the reactions of $^•$CH$_2$OH and U$^•$ radicals respectively, it could be concluded that **α-hydroxy-methyl radical ($^•$CH$_2$OH)** may be understood as a good model radical for **pyrimidine-6-yl (U$^•$)** radicals as shown in Scheme 2.

Figure 13: Plot of log k$_s$ versus E for the reaction of ethanol radical with nitrobenzenes
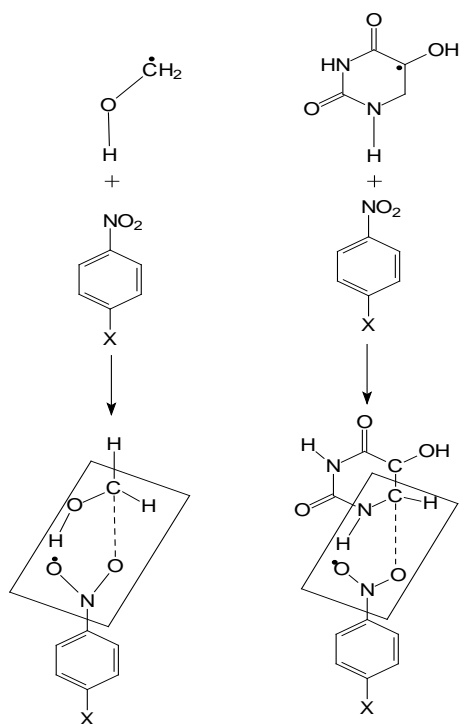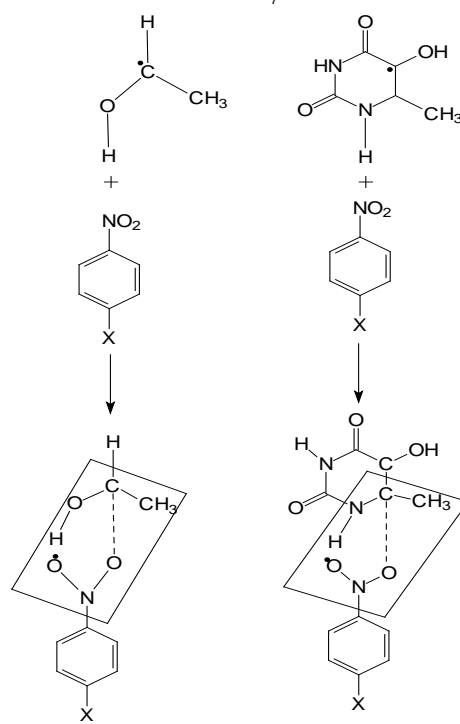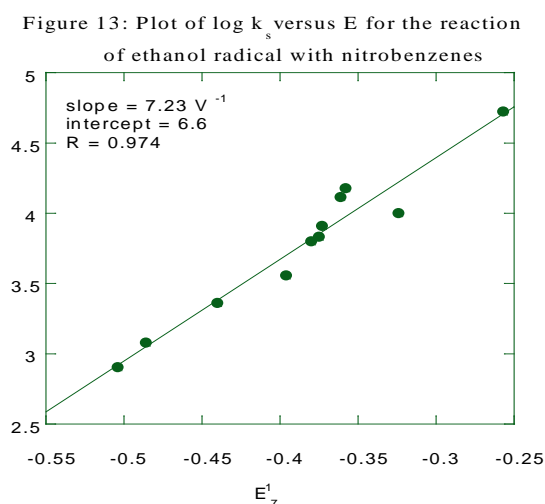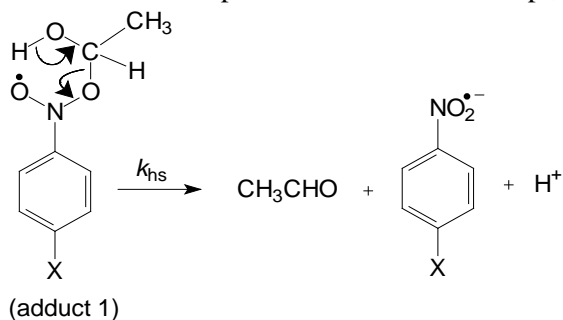

Scheme 2

The plot of log k_s versus redox potentials for the reaction of **α-hydroxy-ethyl radical** was found to be linear (Fig. 13; R = 0.974) with a slope of **7.2 V^{-1}** and with an intercept of 6.6. From the intercept,

(adduct 1)

Scheme 3

intrinsic activation barrier (**λ)** was found to be **26.4.** The very low Marcus slope of **4.7 V^{-1}** for the first step of the reaction is an indication of adduct formation and the not the smooth electron transfer and that of for the second step involving electron transfer is **7.2 V^{-1}** which is close to the value of **8.5 V^{-1}** as expected by Eq. (8). Hence the reaction is considered to be an example of addition/electron transfer reaction and from the similar slopes of **4.7 V^{-1}** and **4.4 V^{-1}** for the reactions of CH$_3$C$^•$HOH and 6-MeU$^•$ radicals respectively, it could be concluded that **α-hydroxy-ethyl radical (CH$_3$C$^•$HOH)** may be understood as a good model radical for **6-methyluracil-6-yl (6-MeU$^•$)** radicals as shown in Scheme 3.

(adduct 3)

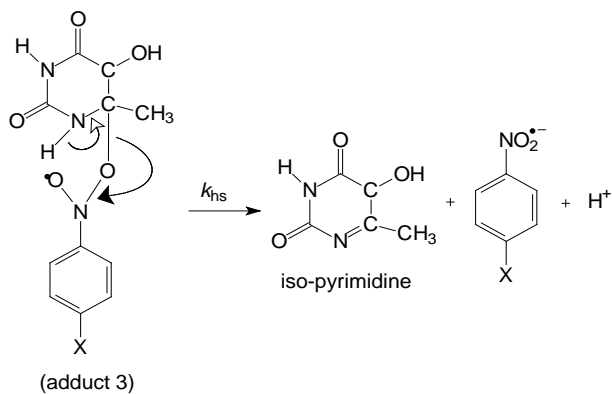Figure 14: Plot of log k_s versus E for the reaction of 6-Me Uracil radical with nitrobenzenes
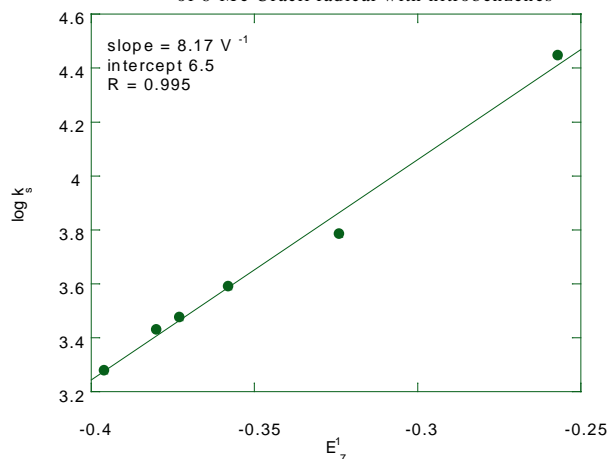
slope = 8.17 V^{-1}
intercept 6.5
R = 0.995

(adduct 5)

Figure 16: Plot of log k_s versus E for the reaction of 6-Me DHU radical with nitrobenzenes

slope = 6.97 V^{-1}
intercept = 7.4
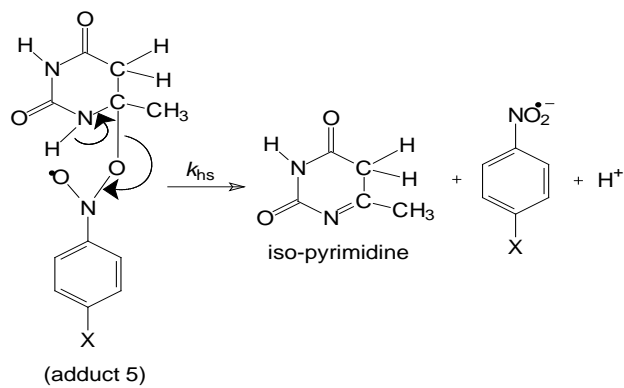R = 0.996

(adduct 4)

Figure 15: Plot of log k_s versus E for the reaction of 6-Me Cytosine radical with nitrobenzenes

slope = 6.65 V^{-1}
intercept = 6.5
R = 0.993

(adduct 6)

Figure 17: Plot of log k_s vs E for the reaction of 2-A-4,6-DMU radical with nitrobenzenes

slope = 4.2 V^{-1}
intercept = 7.3
R = 0.989
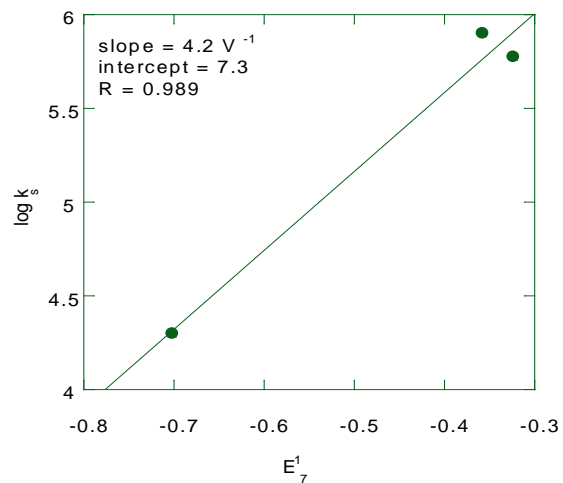
The Marcus plots for the heterolysis reactions (k_s s^{-1}) of the nitroxyl adducts of 6-methyluracil-6-yl (**6-MeU•**), 6-methylcytosine-6-yl (**6-MeC•**), 6-methyl-di-hydrouracil-6-yl (**6-MeDHU•**) and 2-amino-4,6-dimetyluracil-6-yl (**2-A-4,6-DMU•**) radicals to give radical anions and other oxidized products yield the slopes and intercepts **8.17 V^{-1}** and 6.5 (6-MeU•: Fig 14, R = 0.995), **6.65 V^{-1}** and 6.5 (6-MeC•: Fig 15, R = 0.993), **6.97 V^{-1}** and 7.4 (6-MeDHU•: Fig 16, R = 0.996) and **4.21 V^{-1}** and 7.3 (2-A-4,6-DMU•: Fig 17, R = 0.989) respectively. Again the Marcus slopes for the heterolysis reactions are in accordance with electron transfer concept (close to **8.5 V^{-1}**).

For the heterolysis step of adducts shown in Figures 13–17 the very similar Marcus slopes (except 2-A-4, 6-DMU•) and intrinsic activation barriers (Table 1) it may be further understood that these four adducts undergo heterolysis with similar transition states [25].

OH and 4-NBN is linear. The redox potentials of various alcohol radicals are from reference 26. But the reason for the very small Marcus slope (**0.27 V^{-1}**) in spite of "bonded" electron transfer is not understandable at present. It should have been some where close to **5** or **6 V^{-1}**. And from the value of the intercept 3.5, the intrinsic activation barrier (λ) was found to be 39 kJ mole^{-1} which is even more than the values (~23-27) that are observed for the other five adducts. And one more important observation is that with a particular given nitrobenzene, in this case with 4-nitroacetophenone (known as PNAP among radiation chemists) the Marcus plot (Fig 19, R = 0.986) for the formation of (k_R M^{-1} sec^{-1}) of nitroxyl adducts with various pyrimidine-6-yl radicals is linear with a slope of **1.0 V^{-1}**. And from the value of the intercept 7.8, the intrinsic

Where R = CH$_3$, C$_2$H$_5$, n-C$_3$H$_7$, i-C$_3$H$_7$, t-Bu, HOCH$_2$.

Uracil: R$_1$ = R$_2$ = R$_3$ = H and X = O

Thymine: R$_1$ = CH$_3$, R$_2$ = R$_3$ = H and X = O

1-MeUracil: R$_1$ = R$_3$ = H, R$_2$ = CH$_3$ and X = O

1,3-Di-Me-Uracil = R$_1$ = H, R$_2$ = R$_3$ = CH$_3$ and X = O
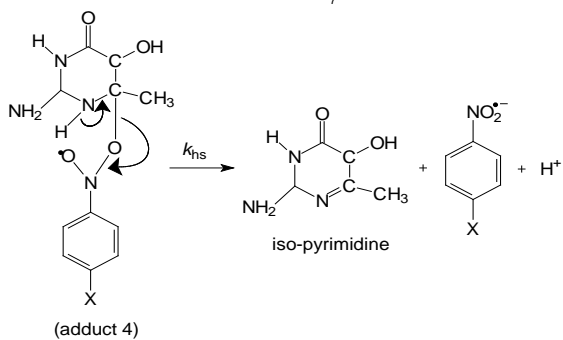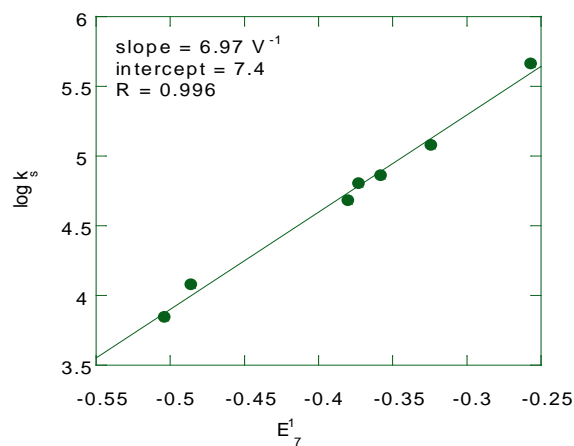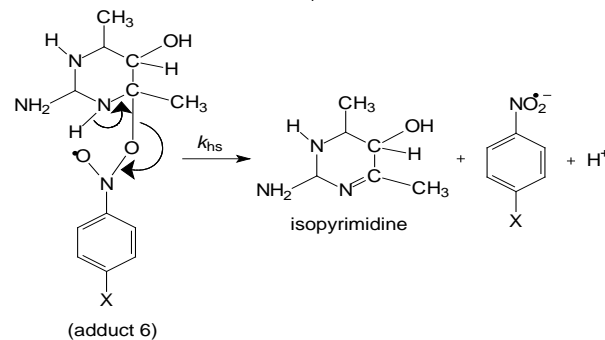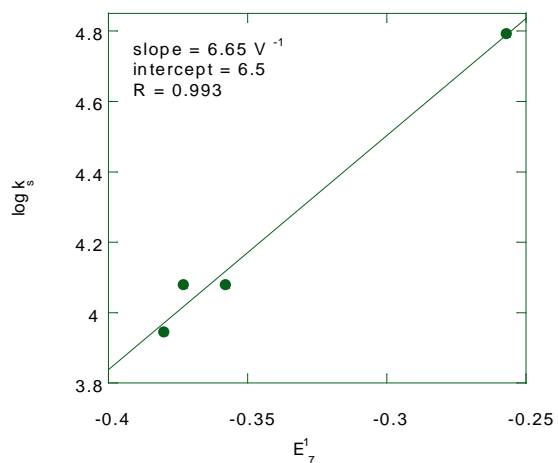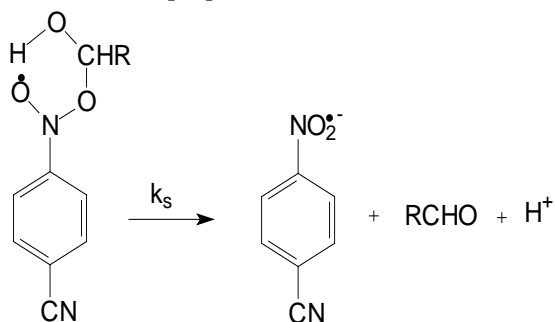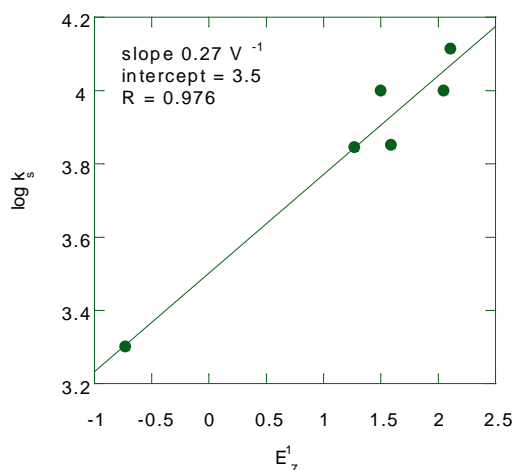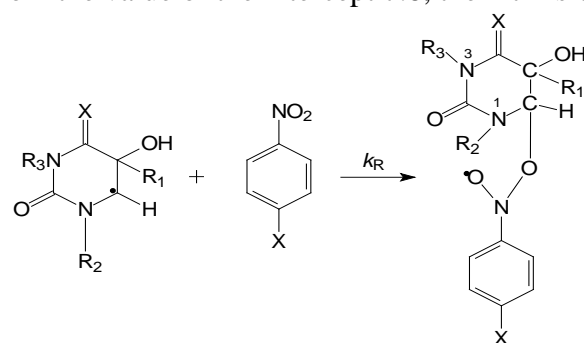
Cytosine: R$_1$ = R$_2$ = R$_3$ = H and X = NH

Figure 18: Plot of log k_s versus E for the reaction of alcohol radicals with 4-nitrobenzonitrile

Fig 19: Plot of log k_R versus redox potentials of pyrimidine bases and two alcohols 4-NAP

Another important and very striking observation is that with a particular given nitrobenzene, in this case with 4-nitrobenzonitrile (4-NBN) the Marcus plot (Fig 18, R = 0.976) for the heterolysis (k_s s^{-1}) of nitroxyl adducts formed with alcohol radicals having a methyl group α- to
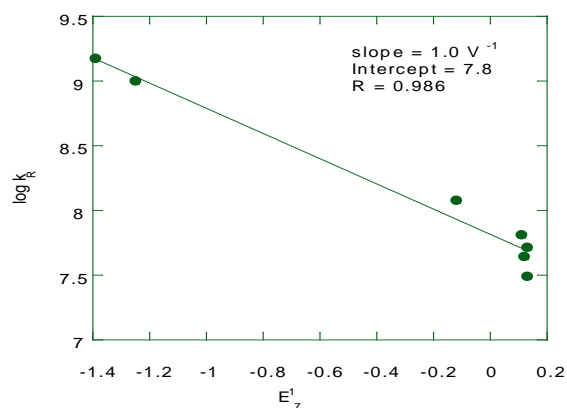
activation barrier (λ) was found to be 21.6 kJ mole^{-1}. The very small Marcus slope indicates that the reaction is only addition type and not electron transfer. The redox potentials of

Table 1. Summary of the data of Marcus slopes and intrinsic activation barriers.

Radical/reaction	Marcus slope (V^{-1})		Intrinsic activation barrier (λ) kJ mole^{-1}	
	For reaction (k_R M^{-1} sec^{-1})	For heterolysis (k_{hs} sec^{-1})	For reaction (k_R M^{-1} sec^{-1})	For heterolysis (k_{hs} sec^{-1})
Fe(II)*tris*-(1,10-phe)-Ce(IV) reaction[*] This reaction is taken as a reference reaction	7.9 (The expected value is 8.5 based on equation 8, see text)	–	– 1.4	–
$CO_2^{\bullet-}$	7.3	No heterolysis step	5.70	No heterolysis step
$(CH_3)_2C^{\bullet}OH$	1.6	No heterolysis step	13.2	No heterolysis step
$CH_3C^{\bullet}HOH$	4.7	7.2	10.4	26.4
$^{\bullet}CH_2OH$	3.7	No heterolysis step	16.0	No heterolysis step
6-MeU$^{\bullet}$	4.4	8.2	12.4	26.8
6-MeC$^{\bullet}$	3.3	6.7	12.0	26.8
6-MeDHU$^{\bullet}$	1.5	7.0	13.6	23.2
2-A-4,6-DMU$^{\bullet}$	5.0	4.2	10.4	23.6
U$^{\bullet}$	3.2	No heterolysis step	17.6	No heterolysis step
Cy$^{\bullet}$	5.5	No heterolysis step	12.8	No heterolysis step
1-MeU$^{\bullet}$	4.4	No heterolysis step	13.2	No heterolysis step

*reference 5.

various pyrimidine-6-yl radicals are from reference 27.

CONCLUDING REMARKS

The Marcus treatment (in the form of equation 8) is an excellent tool for identifying the "non-bonded" electron transfer reactions from "bonded" electron transfer reactions taking place in organic molecules.

And it is apparent that a radical with at least one methyl group α- to OH is essential for a reaction to undergo a "bonded" electron transfer reaction without which no electron transfer is observed. If there are two methyl groups (like the α-OH-*i*-propyl radical) in the radical α- to OH, the reaction undergoes exclusively by "non-bonded" electron transfer route and the Marcus slope was not close to **8.5 V⁻¹** as the reactions are close to diffusion controlled limit.

In the case of pyrimidine-6-yl radicals, it is essential that the radical should have a methyl group at 6 position of the pyrimidine for the reaction to go by addition ("bonded") and then by electron transfer mechanism.

REFERENCES:

1. R A Marcus, *J. Chem. Phys.*, **24**, 966 (1956).
2. R Campion, N Purdie, N Sutin, *J. Am. Chem. Soc.*, **85**, 3528 (1963).
3. R A Marcus, *J. Phys. Chem.*, **67**, 853, (1963).
4. J.P Candlin, J. Halpern, S. Nakamura, *J. Am. Chem. Soc.*, **85**, 2517 (1963).
5. G. Dulz,, N. Sutin, *Inorg. Chem.*, **2**, 917 (1963).
6. J.P Richard, K.B. Williams, *J. Am. Chem. Soc.*, **129**, 6952 (2007).
7. A.J. Kresge, *Chem. Soc. Revs.*, **2**, 475 (1973).
8. J.P Richard, T.L. Amyes, M.M. Toteva, *Acc. Chem. Res.* **34**, 981 (2001).
9. J.P. Guthrie, *J. Am. Chem. Soc.*, **119**, 1151 (1997).
10. R.A. Marcus, *J. Phys. Chem.*, **72**, 891 (1968).
11. D. Kim, I.S.H. Lee, and M. Maurice. Kreevoy, *J. Am. Chem. Soc.*, **112**, 1889 (1990)
12. A.S. Dneprovskii, and E.V. Eliseenkov, *J Org Chem USSR* **24**, 243 (1988)
13. J.P. Guthrie, V. Pitchko, *J Am Chem Soc*, **122**, 5520-28 (2000)
14. J.P. Guthrie, *J. Am. Chem. Soc.*, **122**, 5529 (2000).
15. J.P. Guthrie, V. Pitchko, *J. Phys. Org. Chem.*, **17**, 548 (2004).
16. W.J. Albery, M.M. Kreevoy, *Adv. Phy. Org. Chem.*, **16**, 87 (1978).
17. E.S. Lewis, D.C. Hu, *J. Am. Chem. Soc.*, **106**, 3292 (1984).
18. V. Jagannadham, S. Steenken, *J. Am.. Chem.. Soc.*, **106**, 6542 (1984).
19. S. Steenken, V. Jagannadham, *J. Am.. Chem.. Soc.*, **107**, 6818 (1985).

20. V. Jagannadham, S. Steenken, *J. Phys. Chem.*, **92**, 111 (1988).
21. V. Jagannadham, S. Steenken, *J. Am. Chem. Soc.*, **110**, 2188 (1988).
22. In Lennart Eberson, *Adv. Free Radical Biology & Medicine*, **1**, 19-90 (1985), pp. 28-29.
23. M.V. Ornaz, R.P. Mason, *J. Bio. Biochem.*, **264**, 12379 (1989).
24. P. Wardman, *Environ. Health Perspectives*, **64**, 309 (1985).
25. V. Jagannadham, *Chem. Education J. Japan*, **12** (1) (2009).
   http://chem.sci.utsunomiya-u.ac.jp/cejrnlE.html
26. H. A. Schwarz, R. W. Dodson, *J. Phys.. Chem.,* **93**, 409 (1989).
27. P.S. Raol, E. Hayon, *J. Am. Chem. Soc.*, **96**, 1295 (1974).
28. S. Steenken, *Landolt-Börnstein,* 1985, **vol. 13e**, p. 147.

ЧУДЕСНОТО УРАВНЕНИЕ НА МАРКУС

В. Джаганадхан, Р. Санджиив

Катедра по химия, Университет Османия, Хайдерабад-500 007, Индия

(Резюме)

Нитробензени ($XC_6H_4NO_2$) са редуцирани до радикални аниони ($\mathbf{XC_6H_4NO_2^{\bullet-}}$) чрез осемнадесет различни въглерод центрирани радикали, получени от формиат и прости алкохоли и пиримидиновите бази. Тези радикали са получени чрез импулсна радиолиза във воден разтвор. Радикалният анион на въглеродния диоксид ($\mathbf{CO_2^{\bullet-}}$) се приема като стандарт, който реагира чрез директен електронен пренос ("не-свързан" или "външна сфера") с нитробензени. Реакцията на радикала на α-хидрокси-изо-пропил с нитробензени също се извършва чрез директен електронен пренос ("не-свързан" или "външна сфера"), а някои радикали реагират чрез механизъм на добавяне/ електронен пренос ("свързан" или "вътрешна сфера") до получаване на крайни продукти. Реакцията на някои радикали спира на етапа на добавяне, за да даде нитроксиден тип радикали [($XC_6H_4N(O\bullet)OR$], където R е алкохолна или пиримидинова съставка на микро секундна времева скала. Механизмите на добавяне /електронен пренос са добре описани от теорията на Маркус. Всички тези резултати са рационализирани въз основа на ъгловия коефициент на графиките на Маркус, въведени от теорията на Маркус за механизмите на електронен пренос.

Synthesis and *in vitro* biological activity of *N*-(5-amino-2-methylphenyl)-4-(3-pyridyl)-2-pyrimidinamine derivatives

K. N. Mohana*, L. Mallesha

Department of Studies in Chemistry, University of Mysore, Manasagangotri, Mysore 570 006, India

A series of novel *N*-(5-amino-2-methylphenyl)-4-(3-pyridyl)-2-pyrimidinamine derivatives, **4(a-f)** were synthesized by the reaction of *N*-(5-amino-2-methylphenyl)-4-(3-pyridyl)-2-pyrimidinamine with various ketones in order to determine their *in vitro* antimicrobial activities against clinically isolated strains. The antioxidant activity was also determined by diphenylpicrylhydrazyl (DPPH) radical scavenging assay method. The chemical structures were confirmed by elemental analyses, UV-Vis, FT-IR and ^{1}H NMR spectral studies. The synthesized compounds **4b**, **4c** and **4e** showed moderate antimicrobial activity compared to standard drugs against bacterial and fungal strains tested. The compounds, **4b** and **4c** showed good antioxidant activity in diphenylpicrylhydrazyl (DPPH) radical-scavenging assay method.

Key words: *N*-(5-amino-2-methylphenyl)-4-(3-pyridyl)-2-pyrimidinamine, ketones, antimicrobials, antioxidant.

INTRODUCTION

Diseases caused by microbial infection are a serious menace to the health of human beings and often have connection to some other diseases, whenever the body system gets debilitated. Developing antimicrobial drugs and maintaining their potency, in opposition to resistance by different classes of microorganisms as well as a broad spectrum of antibacterial activity are some of the major concern of research in this area. The compounds containing an azomethine group (-C=N-) are important in elucidating the mechanism of transamination and racemisation reactions in biological systems [1, 2]. Due to the great flexibility and diverse structural aspects, a wide range of Schiff bases have been synthesized and their complexation behaviors have been studied [3]. They have been synthesized from a variety of compounds such as amino thiazoles, 2-hydroxy-1-napthalaniline, amino sugars, aromatic aldehydes, acetophenones, isatin, triazole ring, thiosemicarbazides, amino acids, pyrazolone, etc [4, 5]. Antibacterial, antifungal, antitumor and anticancer activities of some Schiff bases have been reported and they are active against a wide range of organisms [6, 7]. Antibacterial activity has been studied more than antifungal activity, because bacteria can achieve resistance to antibiotics

through biochemical and morphological modifications [8, 9]. Some Schiff bases bearing aryl groups or heterocyclic residues possess excellent biological activities have attracted the attention of many researchers in recent years [10-12].

The Schiff bases formed from aromatic aldehydes or aromatic ketones and their derivatives are quite stable. Many Schiff bases are known to be medicinally important and are used to design medicinal compounds [6, 13]. In recent years there has been an increased interest in the application of antioxidants to medical treatment. Information is constantly gathered linking the development of human diseases to oxidative stress. Free radicals play a role in the pathogenesis of chronic degenerative diseases including cancer, autoimmune, inflammatory, cardiovascular and neurodegenerative diseases and aging generally [14-17]. It is also known that oxidative stress can be induced by a wide range of environmental factors including UV stress, pathogen invasion, pesticide action and oxygen shortage [18]. Owing to these facts, synthetic and natural compounds with potential antioxidation activity are receiving increased attention in biological research, medicine and pharmacy [19, 20].

N-(5-amino-2-methylphenyl)-4-(3-pyridyl)-2-pyrimidinamine is an intermediate for the preparation of imatinib which is an anti-cancer agent, and it is currently marketed as Gleevec. It has also been found to be effective in the treatment of gastrointestinal stromal tumors (GISTs) [21]. This selective inhibition of Bcr-Abl kinase by

---

*To whom all correspondence should be sent:
E-mail: knmsvp@yahoo.com

imatinib has been a successful therapeutic strategy for chronic myeloid leukemia because of the high efficacy and mild side effects of this compound [22]. In connection with such studies, the present paper reports for the first time on the synthesis of *N*-(5-amino-2-methylphenyl)-4-(3-pyridyl)-2-pyrimidinamine derivatives, **4(a-f)** which are formed during the reaction of *N*-(5-amino-2-methylphenyl)-4-(3-pyridyl)-2-pyrimidinamine **(2)** with different ketones, **3(a-f)**. The synthesized compounds are characterized by elemental analyses and spectroscopy (UV-visible, FT-IR, ^{1}H NMR and ^{13}C NMR). Antimicrobial and antioxidant activities of compounds are reported and structural activity relationship is also discussed. On the basis of their activity, these derivatives are identified as viable for further studies.

CHEMISTRY

The target key intermediate, *N*-(5-amino-2-methylphenyl)-4-(3-pyridyl)-2-pyrimidinamine **(2)** was synthesized according to the reported procedure [23] by reacting with stannous chloride dihydrate (11.29 g, 50 mmol) in hydrochloric acid (30 ml) and cooled at 0 ºC. *N*-(2-methyl-5-nitrophenyl)-4-pyridin-3-yl-pyrimidin-2-ylamine **(1**, 3.69 g, 12 mmol) was added in portions while the suspension was vigorously stirred for 6 h. The mixture was then poured onto crushed ice, made alkaline with solid sodium hydroxide and extracted three times with ethyl acetate (100 ml). The combined organic phase was dried over anhydrous sodium sulphate and the filtrate was evaporated to dryness *in vacuo*. The residue was recrystallized from methanol.

EXPERIMENTAL

Materials and Methods

All solvents and reagents were purchased from Sigma Aldrich Chemicals Pvt Ltd. Melting range was determined by Veego Melting Point VMP III apparatus. Elemental analyses were recorded in DMSO on VarioMICRO superuser V1.3.2 Elementar. The UV-visible spectra were recorded on Analytikjena Specord 50 UV–Vis spectrophotometer with quartz cell of 1.0 cm path length. The FT-IR spectra were recorded using KBr discs on FT-IR Jasco 4100 infrared spectrophotometer and were quoted in cm^{-1}. NMR spectra were recorded on Bruker DMX 300 spectrometer (300 MHz for ^{1}H NMR and 100 MHz for ^{13}C NMR) using DMSO-d$_6$ as solvent and TMS as an internal standard.

General procedure for the synthesis of N-(5-amino-2-methylphenyl)-4-(3-pyridyl)-2-pyrimidinamine derivatives, 4(a-f)

Equimolar concentrations of different ketones, **3(a-f)** (0.01 mol) and *N*-(5-amino-2-methylphenyl)-4-(3-pyridyl)-2-pyrimidinamine (**2**, 0.01 mol) were stirred for 6-8 hr at room temperature using absolute ethanol (25 ml) and then 2-3 drops of concentrated sulfuric acid was added to the mixture. The progress of the reaction was followed by TLC until the reaction was complete. It was cooled to 0°C, the precipitate was filtered, washed with diethyl ether and the residue was recrystallized from ethanol.

4-Methyl-N^1-(1-phenylethylidene)-N^3-(4-(pyridin-3-yl)pyrimidin-2-yl)benzene-1,3-diamine (4a)

The general experimental procedure described above afforded **4a**, and the product obtained from *N*-(5-amino-2-methylphenyl)-4-(3-pyridyl)-2-pyrimidinamine (**2**) (2.78 g, 0.01 mol) and acetophenone (**3a**) (1.21 g, 0.01 mol). FT-IR *v*: 3179 (N–H), 3955 (Ar-H), 1619 (C=N), 1558 (C=C), 1078 (C-N). ^{1}H NMR δ: 9.67 (s, 1H, pyr-H), 9.23 (s, 1H, N-H), 8.91 (d, 1H, J = 3.4 Hz, pyr-H), 8.70 (d, 1H, J = 5.3 Hz, pyrimidine-H), 8.53 (d, 2H, J = 7.2 Hz, Ar-H), 7.54-7.51(m, 3H, Ar-H), 7.44 (d, 1H, J = 3.9 Hz, pyr-H), 7.33 (t, 1H, J = 7.3 Hz, pyr-H), 7.25 (d, 1H, J = 6.1 Hz, pyrimidine-H), 6.98 (d, 1H, J = 6.0 Hz, Ar-H), 6.95 (d, 1H, J = 8.8 Hz, Ar-H), 6.31 (s, 1H, Ar-H), 3.84 (s, 3H, CH$_3$), 2.49 (s, 3H, CH$_3$). Anal. Calcd. for C$_{24}$H$_{21}$N$_5$ (in %): C-75.97, H-5.58, N-18.46. Found C-75.71, H-5.60, N-18.21.

N^1-(1-(1H-indol-3-yl)ethylidene)-4-methyl-N^3-(4-(pyridin-3-yl)pyrimidin-2-yl)benzene-1,3-diamine (4b)

The general experimental procedure described above afforded **4b**, and the product obtained from *N*-(5-amino-2-methylphenyl)-4-(3-pyridyl)-2-pyrimidinamine (**2**) (2.78 g, 0.01 mol) and 1− (1H-indol-3-yl)ethanone (**3b**) (1.60 g, 0.01 mol). FT-IR *v*: 3181 (N-H), 3056 (Ar-H), 1628 (C=N), 1573 (C=C), 1077 (C-N). ^{1}H NMR δ: 9.68 (s, 1H, pyr-H), 9.30 (s, 1H, N-H), 9.21 (s, 1H, N-H), 8.90 (d, 1H, J = 3.1 Hz, pyr-H), 8.71 (d, 1H, J = 5.5 Hz, pyrimidine-H), 7.54-7.50 (m, 4H, Ar-H), 7.45 (d, 1H, J = 4.0 Hz, pyr-H), 7.33 (t, 1H, J = 7.1 Hz, pyr-H), 7.25 (d, 1H, J = 5.8 Hz, pyrimidine-H), 6.98

(d, 1H, J = 5.7 Hz, Ar-H), 6.94 (d, 1H, J = 7.6 Hz, Ar-H), 6.31 (s, 1H, Ar-H), 6.05 (s, 1H, pyrrole-H), 3.85 (s, 3H, CH$_3$), 2.5 (s, 3H, CH$_3$). Anal. Calcd. for C$_{26}$H$_{22}$N$_6$ (in %): C-74.62, H-5.30, N-20.08. Found C-74.81, H-5.50, N-20.21.

4-Methyl-N^1-(1-(pyridin-3-yl)ethylidene)-N^3-(4-(pyridin-3-yl)pyrimidin-2-yl)benzene-1,3-diamine (4c)

The general experimental procedure described above afforded **4c**, and the product obtained from *N*-(5-amino-2-methylphenyl)-4-(3-pyridyl)-2-pyrimidinamine (**2**) (2.78 g, 0.01 mol) and 1-(pyridin-3-yl)ethanone (**3c**) (1.22 g, 0.01 mol). FT–IR *v*: 3181 (N-H), 3056 (Ar-H), 1689 (C=N), 1574 (C=C), 1078 (C-N). ^{1}H NMR δ: 9.61 (s, 1H, pyr-H), 9.30 (s, 1H, N-H), 9.20 (s, 1H, pyr-H), 8.72 (d, 1H, J = 2.8 Hz, pyr-H), 8.67 (d, 1H, J = 3.1 Hz, pyr-H), 7.44 (d, 1H, J = 5.0 Hz, pyrimidine-H), 7.31 (d, 1H, J = 3.8 Hz, pyr-H), 7.24 (d, 1H, J = 3.5 Hz, pyr-H), 7.13 (t, 1H, J = 7.0 Hz, pyr-H), 7.08-7.06 (t, 1H, J = 7.3 Hz, pyr-H), 7.01 (d, 1H, J = 6.1 Hz, pyrimidine-H), 6.96 (d, 1H, J = 5.9 Hz, Ar-H), 6.87 (d, 1H, J = 7.2 Hz, Ar-H), 6.30 (s, 1H, Ar-H), 3.85 (s, 3H, CH$_3$), 2.5 (s, 3H, CH$_3$). Anal. Calcd. for C$_{23}$H$_{20}$N$_6$ (in %): C-72.61, H-5.30, N-22.09. Found C-72.42, H-5.23, N-22.21.

4-Methyl-N^1-(1-(naphthalen-2-yl)ethylidene)-N^3-(4-(pyridin-3-yl)pyrimidin-2-yl)benzene-1,3-diamine (4d)

The general experimental procedure described above afforded **4d**, and the product obtained from *N*-(5-amino-2-methylphenyl)-4-(3-pyridyl)-2-pyrimidinamine (**2**) (2.78 g, 0.01 mol) and 1-(naphthalen-2-yl)ethanone (**3d**) (1.71 g, 0.01 mol). FT-IR *v*: 3180 (N-H), 3057 (Ar-H), 1646 (C=N), 1572 (C=C), 1077 (C–N). ^{1}H NMR δ: 9.65 (s, 1H, pyr-H), 9.23 (s, 1H, N-H), 8.71 (d, 1H, J = 3.2 Hz, pyr-H), 8.58 (s, 1H, Ar-H), 8.53 (d, 1H, J = 7.3 Hz, Ar-H), 8.42 (d, 1H, J = 4.7 Hz, Ar-H), 7.54 (d, 1H, J = 5.1 Hz, pyrimidine-H), 7.43-7.4 (m, 4H, Ar-H), 7.38 (d, 1H, J = 3.4 Hz, pyr-H), 7.33 (t, 1H, J = 7.2 Hz, pyr-H), 7.25 (d, 1H, J = 6.4 Hz, pyrimidine-H), 6.98 (d, 1H, J = 5.7 Hz, Ar-H), 6.95 (d, 1H, J = 7.9 Hz, Ar-H), 6.31 (s, 1H, Ar-H), 3.85 (s, 3H, CH$_3$), 2.45 (s, 3H, CH$_3$). Anal. Calcd. for C$_{28}$H$_{23}$N$_5$ (in %): C-78.30, H-5.40, N-16.31. Found C-78.12, H-5.21, N-16.11.

4-Methyl-N^3-(4-(pyridin-3-yl)pyrimidin-2-yl)-N^1-(1-(pyridin-4-yl)ethylidene)benzene-1,3-diamine (4e)

The general experimental procedure described above afforded **4e**, and the product obtained from *N*-(5-amino-2-methylphenyl)-4-(3-pyridyl)-2-

pyrimidinamine (**2**) (2.78 g, 0.01 mol) and 1-(pyridin-4-yl)ethanone (**3e**) (1.22 g, 0.01 mol). FT-IR *v*: 3189 (N-H), 3056 (Ar-H), 1698 (C=N), 1572 (C=C), 1078 (C-N). ^{1}H NMR δ: 9.60 (s, 1H, pyr-H), 9.31 (s, 1H, N-H), 8.72 (d, 2H, J = 7.2 Hz, pyr-H), 8.67 (d, 1H, J = 3.0 Hz, pyr-H), 8.54 (d, 2H, J = 6.8 Hz, pyr-H), 7.45 (d, 1H, J = 5.3 Hz, pyrimidine-H), 7.31 (d, 1H, J = 3.1 Hz, pyr-H), 7.15 (t, 1H, J = 7.7 Hz, pyr-H), 7.05 (d, 1H, J = 6.2 Hz, pyrimidine-H), 6.95 (d, 1H, J = 5.3 Hz, Ar-H), 6.87 (d, 1H, J = 7.1 Hz, Ar-H), 6.31 (s, 1H, Ar-H), 3.84 (s, 3H, CH$_3$), 2.5 (s, 3H, CH$_3$). Anal. Calcd. for C$_{23}$H$_{20}$N$_6$ (in %): C-72.61, H-5.30, N-22.09. Found C-72.82, H-5.01, N-22.28.

3-(1-(3-(4-(Pyridin-3-yl)pyrimidin-2-ylamino)-4-methylphenylimino)ethyl)benzonitrile (4f)

The general experimental procedure described above afforded **4f**, and the product obtained from *N*-(5-amino-2-methylphenyl)-4-(3-pyridyl)-2-pyrimidinamine (**2**) (2.78 g, 0.01 mol) and 3-acetylbenzonitrile (**3f**) (1.46 g, 0.01 mol). FT-IR *v*: 3168 (N-H), 3056 (Ar-H), 2243 (C≡N), 1689 (C=N), 1574 (C=C), 1079 (C-N). ^{1}H NMR δ: 9.67 (s, 1H, pyr-H), 9.21 (s, 1H, N-H), 8.71 (d, 1H, J = 3.3 Hz, pyr-H), 8.53 (d, 1H, J = 7.1 Hz, Ar-H), 7.43 (d, 1H, J = 5.2 Hz, pyrimidine-H), 7.35 (s, 1H, Ar-H), 7.54 (d, 1H, J = 4.5 Hz, Ar-H), 7.51 (d, 1H, J = 7.1 Hz, Ar-H), 7.45 (d, 1H, J = 3.4 Hz, pyr-H), 7.33 (t, 1H, J = 7.1 Hz, pyr-H), 7.25 (d, 1H, J = 6.3 Hz, pyrimidine-H), 6.97 (d, 1H, J = 5.1 Hz, Ar-H), 6.95 (d, 1H, J = 7.3 Hz, Ar-H), 6.32 (s, 1H, Ar-H), 3.85 (s, 3H, CH$_3$), 2.46 (s, 3H, CH$_3$). Anal. Calcd. for C$_{25}$H$_{20}$N$_6$ (in %): C-74.24, H-4.98, N-20.78. Found C-74.13, H-4.81, N-20.51.
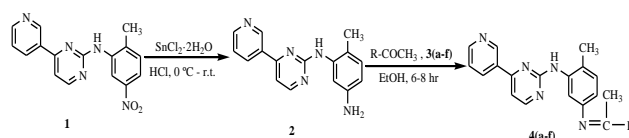
Scheme 1

ANTIBACTERIAL ASSAY

Antibacterial activity of the synthesized compounds was determined against Gram-positive bacteria (*Bacillus subtilis*, *Staphylococcus aureus*) and Gram-negative bacteria (*Xanthomonas malvacearum* and *Escherichia coli*) in DMF by disc diffusion method on nutrient agar medium [24]. The sterile medium (Nutrient Agar medium, 15 ml) in each Petri plates was uniformly smeared with cultures of Gram-positive and Gram-negative bacteria. Sterile discs of 6 mm diameter (Hi-Media) were made in each of the Petri plates, to which 50 µL (concentration was 1 mg/ml, i.e., 50 µg/disc) of

the different synthesized compounds were added. The treatments also included 50 µl of DMF and streptomycin as negative and positive control for comparison. Each compound was assessed in triplicate. The plates were incubated overnight at 25 ± 2 ºC and then the inhibition zones were measured in millimeters.

ANTIFUNGAL ASSAY

The synthesized compounds were screened for their antifungal activity against *Fusarium oxysporum* and *Aspergillus niger* in DMF by poisoned food technique [25]. Potato Dextrose Agar (PDA) media was prepared and about 15 ml of PDA was poured into each petri plate and allowed to solidify. 5 mm disc of seven days old culture of the test fungi was placed at the center of the petri plates and incubated at 26 °C for 7 days. After incubation the percentage inhibition was measured, and three replicates were maintained for each treatment. Activity of each compound was compared with standard drugs. All of the synthesized compounds were tested (at the dosage of 500 µl of the novel compounds in Petri plate, where concentration was 0.1 mg/ml) by poisoned food technique.

DPPH RADICAL SCAVENGING ASSAY

The free radical scavenging activity of the synthesized compounds was studied *in vitro* by 1, 1-diphenyl-2-picrylhydrazyl (DPPH) assay method [26]. Stock solution of the drug was diluted to different concentrations in the range of 100–200 µg/ml in methanol. Methanolic solution of the synthesized compounds (2 ml) was added to 0.003% (w/v) methanol solution of DPPH (1 ml). The mixture was shaken vigorously and allowed to stand for 30 min. Then absorbance at 517 nm was determined and the percentage of scavenging activity was calculated. Ascorbic acid was used as a reference compound. All tests and analyses were done in duplicate and the results were averaged. The inhibition ratio (*I* %) of the tested compounds was calculated according to the following equation:

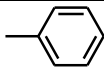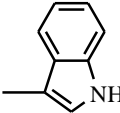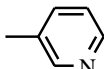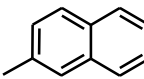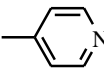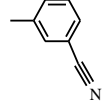$$I \% = (Ac\text{-}As) / Ac \times 100$$

where *Ac* is the absorbance of the control and *As* is the absorbance of the sample.

RESULTS AND DISCUSSION

In this work, the novel *N*-(5-amino-2-methylphenyl)-4-(3-pyridyl)-2-pyrimidinamine derivatives **4(a–f)** were synthesized by the method summarized in Scheme 1. Compounds were purified by recrystalization using ethanol. The

chemical structures and physical data of all the synthesized compounds are tabulated in Table 1.

Table1. Chemical structure of the synthesized compounds

Compound	R	Yield (%)	M.P. (°C)	UV-visible (λ_{max})
4a		74	128-130	480
4b		71	154-156	495
4c		68	158-160	505
4d		68	151-153	498
4e		72	159-161	507
4f		70	152-154	510

The elemental analyses data showed good agreement between the experimentally determined values and the theoretically calculated values within the limits of permissible error. The synthesized compounds are stable in air, soluble in DMSO and DMF. The elemental analyses data confirm the stoichiometry and hence the molecular formula of the synthesized compounds. The electronic absorption spectra of synthesized compounds show new bands and appearance of longer wavelength absorption band in the visible region in UV-visible spectrum owing to confirms the formation of synthesized compounds.

The absence of NH_2 and C=O absorption bands in the IR spectra confirmed that the synthesized compounds **4(a–f)** were obtained via condensation. However the changes in integral intensities and band widths, especially of the bands originating from NH_2 stretching vibrations didn't show in products. The absorptions around 3000 cm^{-1} in compounds **4(a–f)** confirm the aromatic C-H stretching vibrations, and the appearance of a medium to strong absorption bands above 1600 cm^{-1} due to a stretching vibration of the azomethine (C=N) bond formation in synthesized compounds.

The proton spectral data agree with respect to the number of protons and their chemical shifts with the proposed structures. The proton spectral data agree with respect to the number of protons and their chemical shifts with the proposed structures. The proton spectral data of the

intermediate, *N*-(5-amino-2-methylphenyl)-4-(3-pyridyl)-2-pyrimidinamine (**2**) shows resonance at δ 5.52 ppm (s, 2H, -NH$_2$). In all the synthesized compounds **4** (**a–f**) the above resonances disappeared and additional resonances were observed, which confirmed the condensation between the amino group and carbonyl group.

To provide further evidence for the synthesized compounds, ^{13}C NMR spectra were recorded. The peaks at 164.23 - 164.01 ppm due to azomethine carbon atoms, which were not present in the starting materials. The strong signals at δ 151.04 – 108.32 ppm indicate the presence of aromatic carbons.

The antibacterial activity of compounds **4(a-f)** were evaluated and compared with streptomycin as standard drug. The compounds **4b**, **4c** and **4e** have shown moderate antibacterial activity against four pathogenic bacterial strains among the six compounds screened. Compared with streptomycin the compound **4f** showed less inhibitory activity against *B. subtilis* and *S. aureus*. Among the compounds **2** and **4(a–f)** the antibacterial inhibitory activity follows the order **4b** > **4e** > **4c** > **4d** > **4a** > **4f** > **2** against tested four pathogenic bacterial strains.

The antifungal activity of compounds **4(a-f)** were evaluated and compared with nystatin as standard. All the compounds do not show antifungal activity against *A. niger*. The compound **4b** showed moderate activity against *F. oxysporum*. Compared with nystatin the compounds **4c** and **4e** showed moderate inhibitory activity against *F. oxysporum*. It is evident from the results that most of the compounds are moderately active and few are weakly active. Among the compounds **2** and **4(a–f)** showed inhibitory activity in the order **4b** > **4e** > **4c** > **4d** > **4a** > **4f** > **2** against *F. oxysporum*. Antimicrobial screening results of the tested compounds are shown in Table **2**.

Antioxidant activity results of the tested compounds are shown in Table **3**. As antioxidants donate protons to DPPH radicals, the absorption decreases. The decrease in absorption is taken as a measure of the extent of radical scavenging. Free radical scavenging capacities of the compounds, measured by DPPH assay, are shown in Figure 1. Compound, **2** showed weak antioxidant activity (48.7 %) compared to standard ascorbic acid (99.3 %) at 200 µg/ml. Compounds **4b** and **4c** showed good antioxidant activity (68.5 % and 63.7 %) at

**Table 2.** Antibacterial and antifungal activities of compounds

Compound	Zone of inhibition in diameter (mm)				% inhibition
	B. subtilis	*S. aureus*	*X. malvacearum*	*E. coli*	*F. oxysporum*
2	-	-	-	-	24.5
4a	10	09	-	-	38.2
4b	11	11	08	09	55.7
4c	11	11	08	08	47.6
4d	10	09	-	-	41.2
4e	11	11	08	09	54.1
4f	09	08	-	-	29.8
Streptomycin	18	21	13	14	-
Nystatin	-	-	-	-	90

- Denotes very low antibacterial activity (Zone of inhibition < 7 mm)

Table 3. Results of DPPH radical scavenging assay

Compound	Scavenging effect, (%)			IC$_{50}$ (µg/ml)
	100 µg/ml	150µg/ml	200 µg/ml	
2	28.4	39.3	48.7	-·
4a	30.8	40.1	49.2	-·
4b	46.8	56.4	68.5	114
4c	42.7	53.1	63.7	134
4d	34.5	42.7	51.0	196
4e	39.8	46.4	53.3	180
4f	37.1	44.6	52.5	185
Ascorbic acid	74.1	86.4	99.3	8.6

·No IC$_{50}$ value even at higher concentration i.e., at 200 µg/ml
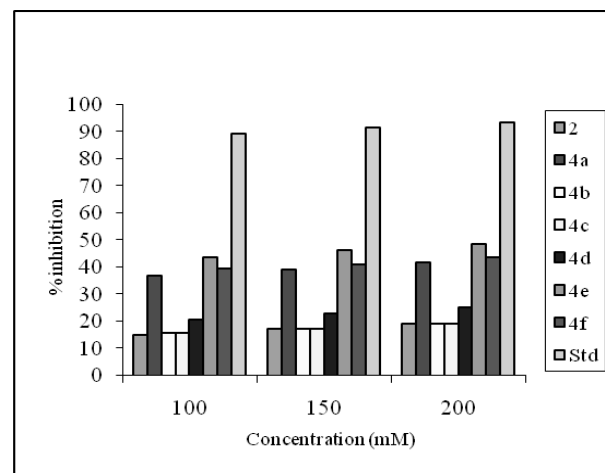
Fig. 1 DPPH scavenging activity of different concentrations of compounds, **2** and **4(a- f)**.

200 µg/ml. The increased DPPH radical scavenging activity of all the newly synthesized compounds is as follows: **4b** > **4c** > **4e** > **4f** > **4d** > **4a** > **2**.

CONCLUSION

In conclusion, a series of novel *N*-(5-amino-2-methylphenyl)-4-(3-pyridyl)-2-pyrimidinamine derivatives **4(a–f)** were synthesized in good yield, characterized by different spectral studies and their antimicrobial and antioxidant activities have been

evaluated. Compounds **4b**, **4c** and **4e** demonstrated moderate inhibition against bacterial and fungal strains tested. The antioxidant activity revealed that compounds **4b** and **4c** are good antioxidant activity. On the basis of their activity, these derivatives were identified as viable for further studies.

REFERENCES

1. K.Y. Lau, A. Mayr, K. K. Cheung, *Inorg. Chim. Acta.*, **285**, 223 (1999).
2. A.S. Shawali, N. M. S. Harb, K. O. Badahdah, *J. Heterocyclic Chem.*, **22**, 1397 (1985).
3. N. Raman, V. Muthuraj, S. Ravichandran, A. Kulandaisamy, *Proc. Indian Acad. Sci.* (*Chem. Sci.*), **115**, 161 (2003).
4. S.K. Sridhar, A. Ramesh, *Indian Journal of Chemistry - Section B Organic and Medicinal Chemistry*, **41**, 668 (2002).
5. P. Przybylski, B. Brzezinski, *Biopolymers*, **67**, 61 (2002).
6. F.M. Abdel-Gawad, Y. M. Issa, S. M. Abd-Alhamid, *Egypt. J. Pharm. Sci.*, **34**, 219 (1993)
7. N. Sari, S. Arslan, E. Logoglu, I. Sariyan, *G. U. J. Sci.*, **16,** 283 (2003).
8. V. Opletalova, J. Hartl, A. Patel, K. Palát Jr., V. Buchta, *Farmaco*, **57**, 135 (2002).
9. M. Biava, R. Fioravanti, G. C. Porretta, G. Sleite, D. Deidda, G. Lampis, R. Pompei, *Farmaco*, **54**, 721 (1999).
10. E. Haddock, W. J. Hopwood, (Shell Int. Res. Maatsch. B. V.), GB 2,078,212, (1982).
11. B.S. Holla, B. S. Rao, K. Shridhara, P. M. Akberali, *Farmaco*, **55**, 338 (2000).
12. V.K. Chadha, N. S. Ranwa, P. K. Dadheech, K. Pawan, *J. Phytol. Res.*, **11**, 201 (1998).
13. R. Capdeville, E. Buchdunger, J. Zimmermann, A. Matter, *Nat. Rev. Drug. Discov.*, **1**, 493 (2002).
14. I. Cantuti-Castelvetri, B. Shukitt-Hale, J. A. Joseph, *Int. J. Dev. Neurosci.*, **18**, 367 (2000).
15. Y.J. Surh, K.S. Chun, H.H. Cha, S.S. Han, Y.S. Keum, K. K. Park, S. S. Lee, *Mutat Res.*, 243 (2001).
16. J. Vaya, M. Aviram, *Curr. Med. Chem.*, **1**, 99 (2001).
17. O. I. Aruoma, *Mutat. Res.*, **523**, 9 (2003).
18. O. Blokhina, E. Virolainen, K.V. Fagerstedt, *Ann. Bot.*, **91**, 179 (2003).
19. O.I. Aruoma, *Food Chem. Toxicol.*, **32**, 671 (1994).
20. P.C.H. Hollman, M.B. Katan, *Food Chem. Toxicol.*, **37**, 937 (1999).
21. M. Kalaycio, *Curr. Hematol. Rep.*, **3**, 37 (2004).
22. K. Peggs, S. Mackinnon, *N. Engl. J. Med.*, **348**, 1048 (2003).
23. S. Chang, S. L. Yin, J. Wang, Y. K. Jing, J. H. Dong, *Molecules*, 14, 4166 (2009).
24. A.W. Bauer, W. M. Kirby, J. C. Sherris, M. Turck, *Am. J. Clin.Pathol,.* 45, 493 (1966).
25. S. Satish, D. C. Mohana, M. P. Raghavendra, K. A. Raveesha, *J. Agri. Techn.*, 3, 109 (2007).
26. M.H. Shih, F. Y. Ke, *Bioorg. Med. Chem.*, 12, 4633 (2004).

СИНТЕЗ И *IN VITRO* БИОЛОГИЧНА АКТИВНОСТ НА N-(5-АМИНО-2-МЕТИЛФЕНИЛ)-4-(3-ПИРИДИЛ)-2-ПИРАМИДИНАМИНОВИ ПРОИЗВОДНИ

К. Н. Мохана*, Л. Малеша

Департамент за изследвания по химия в Университета на Мисор, Манасагангготри, Мисор 570 006, Индия

(Резюме)

Серия от нови N-(5-амино-2-метилфенил)-4-(3-пиридил)-2-пиримидинаминови производни, **4(a-f)** са синтезирани чрез реакция на N-(5-амино-2-метилфенил)-4-(3- пиридил)-2-пиримидинамин с различни кетони, за да се определи тяхната *in vitro* антимикробна активност срещу клинично изолирани щамове. Антиоксидантната активност също се определя чрез анализ по метода на улавяне на свободните радикали дифенилпикрилхидразил (DPPH) Химическите структури са потвърдени от елементен анализ, UV-Vis, FT-IR и ^{1}H NMR спектрални изследвания. Синтезираните съединения, **4b, 4c и 4d** показват умерена антимикробна активност в сравнение със стандартните лекарства, тествани срещу бактериални и гъбични щамове. Съединенията **4b** и **4c** показват добра антиоксидантна активност при изпитване по метода на улавяне на свободните радикали дифенилпикрилхидразил (DPPH).

Forced convection corrosion of steel equipments in the water layer present in crude oil

S .A. Nosier, Y.A. Alhamed

Department of Chemical and Materials Engineering, Faculty of Engineering, King Abdulaziz University, Kingdom of Saudi Arabia

The present study addresses the relationship between the presence of some salts in crude oil and the corrosion of metallic equipments in the context of the petroleum refining industry. The rate of corrosion of iron in water containing $CaCl_2$ and $MgCl_2$ with concentrations similar to those in the water present in crude oil before desalting was measured by the weight loss technique. The variables investigated were $CaCl_2$ concentration, $MgCl_2$ concentration, operating temperature and angular speed of rotation. It was found that the rate of corrosion increases with increasing $MgCl_2$ and $CaCl_2$ concentrations up to a certain level, after which it remains almost constant. Increasing the angular speed of rotation favors the rate of corrosion. The rate of corrosion was found to increase with temperature according to the Arrhenius equation with activation energy of 8.64 and 5.16 kcal/ mol for $MgCl_2$ and $CaCl_2$ respectively, which denotes that the corrosion of steel in both $MgCl_2$ and $CaCl_2$ solutions is a diffusion-controlled reaction under the operating conditions.

Key Words: Crude oil, desalting, steel corrosion, diffusion-controlled reaction

INTRODUCTION

Crude oil contains water, inorganic salts, suspended solids, and water–soluble salts of trace metals. During the first step of refinery treatment, crude oil is normally desalted to remove species such as chloride which deactivate the refinery catalysts and cause further corrosion of distillation columns [1–4]. Calcium and magnesium chlorides ($CaCl_2$ and $MgCl_2$) are frequently found in crude oil; the presence of these compounds in crude oil can cause several problems in the refining processes.

Hydrochloric acid is not present in crude oil, but it may be produced during distillation by the hydrolysis of chloride salts, particularly magnesium chloride and calcium chloride, that are present in the brine found in crude oils. The presence of hydrochloric acid leads to the so-called acid corrosion that occurs in vapor lines, condensers, coolers, and rundown lines, particularly at points where water accumulates, such as valves in horizontal lines. The corrosive effect of dilute hydrochloric acid at the temperature maintained in the distillation equipment cannot be satisfactorily sustained by common materials.

Steel equipments suffer severe corrosion attack in water containing electrolytes. The rate of corrosion depends, among other factors, upon the concentration of oxygen and the motion of water. Stainless steel undergoes severe damage in water containing chlorides [5], where pitting corrosion and stress corrosion cracking take place.

The aim of the present work was to study the rate of steel corrosion in salt-containing water simulating the water present in crude oil. Crude oil usually contains some water – dissolved salts such as $CaCl_2$ and $MgCl_2$ [6]. Before processing crude oil in the distillation tower, the water should be removed first by a process known as dehydration and desalting [7, 8]. Early water removal from crude oil minimizes corrosion of process equipment such as pumps, heat exchangers, distillation towers and condensers. On the other hand, the equipment used for handling water that has been separated from the oil can suffer from severe corrosion depending upon the salt content of water.

EXPERIMENTAL TECHNIQUE

The experimental set-up used in the present study is shown in Fig.1. It consists of a 2 dm^3 cylindrical glass container of 11.9 cm diameter and 18 cm height. The container was fitted with a variable speed motor. The impeller was an iron rod of 1 cm diameter and 3 cm height. The iron rod was centered on a stainless steel shaft of 0.7 cm

---

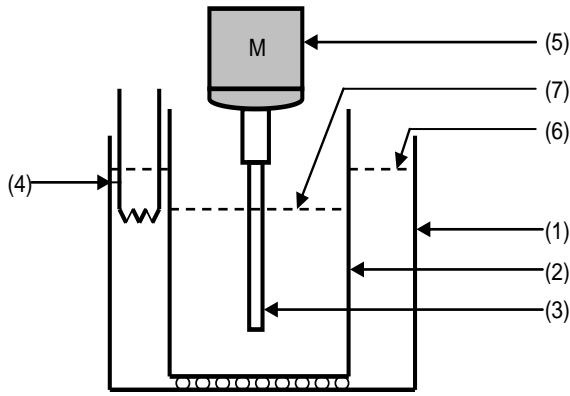* To whom all correspondence should be sent:
 E-mail: Snosier@kau.edu.sa

Figure (1): Experimental apparatus. 1- Rectangular water bath; 2- Cylindrical glass container; 3- Iron rod; 4- Thermostat; 5- Variable speed motor; 6- Water level; 7- Electrolyte level.

diameter and 15 cm length at a distance of 4 cm from the vessel bottom. The stainless steel shaft was isolated with epoxy resin. The rotation speed of the motor was controlled by means of a varic and measured by an optical tachometer. Care was taken to avoid vibration and eccentric motion. The cylindrical glass container and its contents were immersed in a rectangular water bath to control the temperature. Before each run, the iron rod was degreased in trichloroethylene, and oxides were mechanically removed with emery paper. The sample (iron rod) was washed under running water, dried with alcohol and ether, and then accurately weighed. 1 dm^3 of fresh $CaCl_2$ or $MgCl_2$ solution was introduced into the cylindrical vessel provided that the iron rod was completely immersed in the solution at various speeds of rotation. Corrosion was allowed to take place for a period of 30 min, after which the iron rod was washed under running water, dried and reweighed. The rate of corrosion was calculated by the formula:

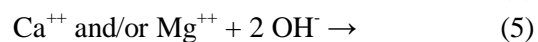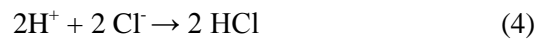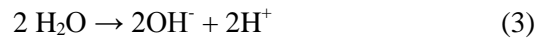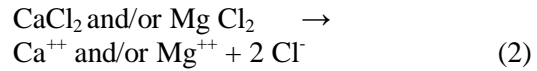$$r = \frac{\Delta W}{[A * t]} \qquad (1)$$

Where:

r = rate of corrosion in g /cm^2.s, ΔW = weight loss in gram, A = surface area of iron rod in cm^2 and t = time in seconds.

Experiments were carried out over the temperature range 30 - 45°C for $CaCl_2$ and 30 - 40°C for $MgCl_2$. The solution concentration ranged from 0.5 to 10 g/dm^3 for both $CaCl_2$ and $MgCl_2$. The angular speed of rotation ranged from 94.25 to 136.14 and from 107.82 to 281.73 rad/sec for $CaCl_2$ and $MgCl_2$ respectively. All solutions were prepared using A.R. grade chemicals and distilled water.

RESULTS AND DISCUSSION

The effect of $CaCl_2$ and $MgCl_2$ concentrations on the rate of steel corrosion at different angular speeds of rotation is shown in Figs. 2-a and b, respectively. The rate of corrosion increased with increasing $CaCl_2$ and $MgCl_2$ concentrations up to a certain level and remained almost constant with further increase in salt concentration. This may be attributed to the hydrolysis of $CaCl_2$ and $MgCl_2$ [9] according to the following equations:

$CaCl_2$ and/or $Mg Cl_2$ $\rightarrow$
Ca^{++} and/or Mg^{++} + 2 Cl^- $\qquad (2)$

$2 H_2O \rightarrow 2OH^- + 2H^+$ $\qquad (3)$

$2H^+ + 2 Cl^- \rightarrow 2 HCl$ $\qquad (4)$

Ca^{++} and/or Mg^{++} + 2 $OH^- \rightarrow$ $\qquad (5)$
$Ca (OH)_2$ and/or $Mg (OH)_2$

The overall hydrolysis reaction for $CaCl_2$ and $MgCl_2$ is:

$CaCl_2$ and/ or $MgCl_2$ + 2 $H_2O \rightarrow$
$Ca (OH)_2$ and/or $Mg (OH)_2$ + 2 HCl $\qquad (6)$
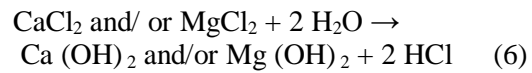
Figure (2-a): Effect of $MgCl_2$ concentration on the rate of corrosion at different angular speed of rotation
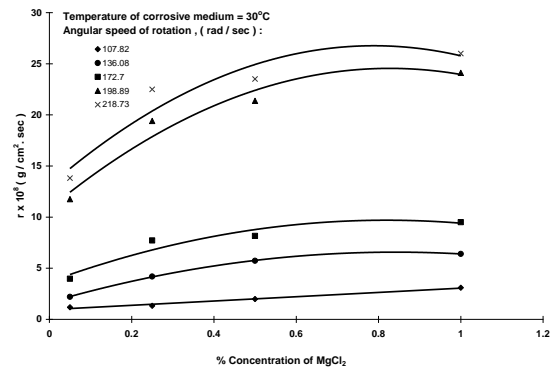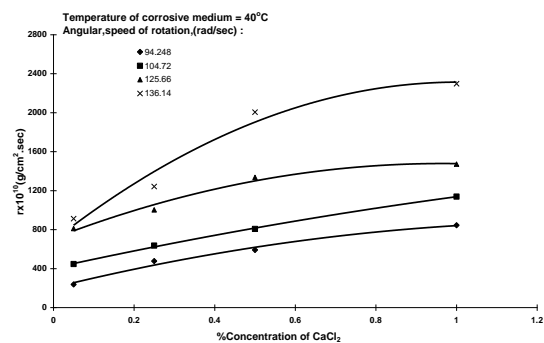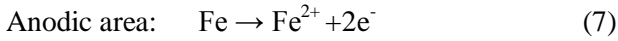

Figure (2-b): Effect of $CaCl_2$ concentration on the rate of corrosion at different angular speed of rotation

As a result of the above hydrolysis reaction, the solution becomes acidic, and the higher the salt concentration, the higher is the acidity of the solution. The acidity favors the rate of corrosion as a result of:

1. The increase in solution conductivity due to the presence of the highly mobile H^+, which (in accordance with Faraday's law) leads to an increase in the corrosion rate.
2. The presence of relatively high H^+ concentration leads to H_2 evolution at the cathode in addition to oxygen reduction. That means, under the present conditions, O_2 reduction takes place at the cathode simultaneously with H_2 evolution, according to the following reactions [2,3,4]:

Anodic area: $\quad Fe \rightarrow Fe^{2+} + 2e^-$ $\qquad$ (7)

Cathodic area:

$1/2\ O_2 + H_2O + 2\ e^- \rightarrow 2OH^-$ $\qquad$ (8)

$2\ H^+ + 2\ e^- \rightarrow H_2$ $\qquad$ (9)

The fact that the corrosion rate remained almost constant at relatively high $CaCl_2$ or $MgCl_2$
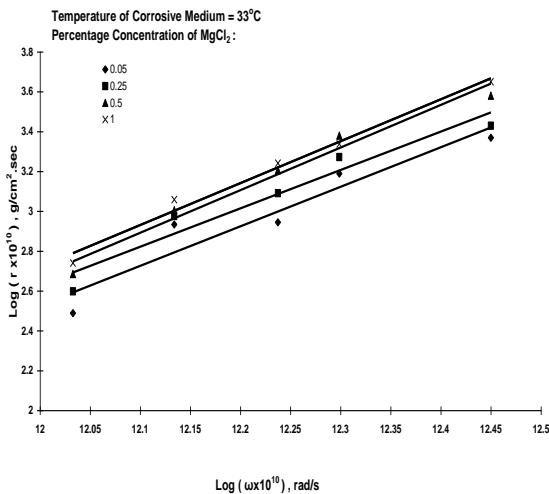
Figure (3-a): Effect of angular speed of rotation on the rate of corrosion at different $MgCl_2$ concentration
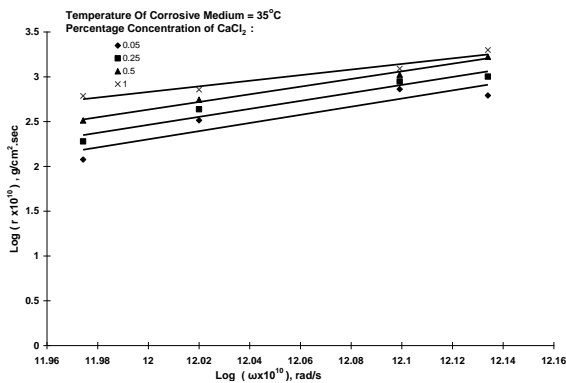
Figure (3-b): Effect of angular speed of rotation on the rate of corrosion at different $CaCl_2$ concentration

concentrations may be due to balanced opposing effects, e.g., higher salt concentrations suppress the solubility of dissolved O_2 in the solution. This is known as the "salting out" effect [6, 10]. Also,

oxygen depletion results in a decrease in the rate of corrosion [11, 12]. Additionally, it is possible that Ca^{++} or Mg^{++} may inhibit the rate of corrosion to some extent by combining with OH^- formed at the cathode to deposit an inert film of $Ca\ (OH)_2$ or $Mg\ (OH)_2$ in the cathodic areas, thereby decreasing the effective area exposed, with a consequent decrease in the rate of steel corrosion [6,10,13]. It seems that the above retarding effects balanced the enhancing effect arising from the increase in solution conductivity at high $CaCl_2$ or $MgCl_2$ concentrations.

The data shown in Figs. 3-a and b fit the following two relations for $CaCl_2$ and $MgCl_2$, respectively:

$$r = a_1 \omega^{18.13} \qquad (10)$$
$$r = a_2 \omega^{11.82}$$

Where:

ω is the angular speed of rotation in rad/s, a_1 and a_2 are constants.

The increase in the rate of corrosion (r) may be due to the fact that the reaction is diffusion-controlled. The diffusion-controlled nature of the reaction was confirmed by the following three facts:

Figure (4-a): Effect of corrosive medium temperature on the steel corrosion at different $MgCl_2$ concentration

Figure (4-b): Effect of corrosive medium temperature on the steel corrosion at different $CaCl_2$ concentration

a) The corrosion rate systematically increases upon increasing the angular speed of rotation. The higher angular speed of rotation reduces the diffusion layer thickness (cf. Fig. 7) which favours the rate of transfer of dissolved oxygen from the solution bulk to the metal surface with a consequent increase in the rate of steel corrosion.

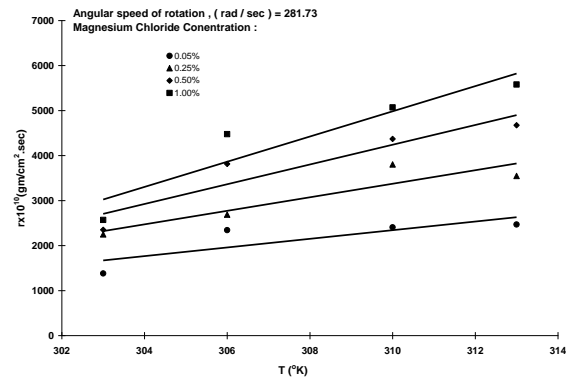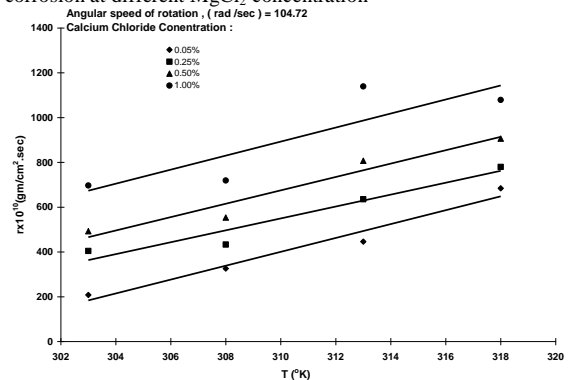(b) The H_2 bubbles evolved at the cathodic areas may generate turbulence in the diffusion layer with a consequent increase in the rate of corrosion.

Figs. 4-a and b show the effect of temperature on the rate of steel corrosion at different
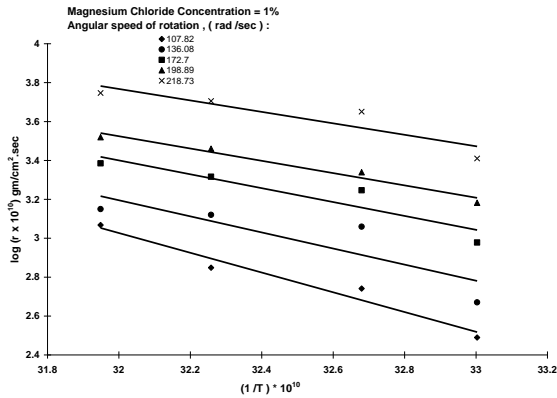
Figure (5-a): Arrhenius plot of the experimental results at different $MgCl_2$ concentration
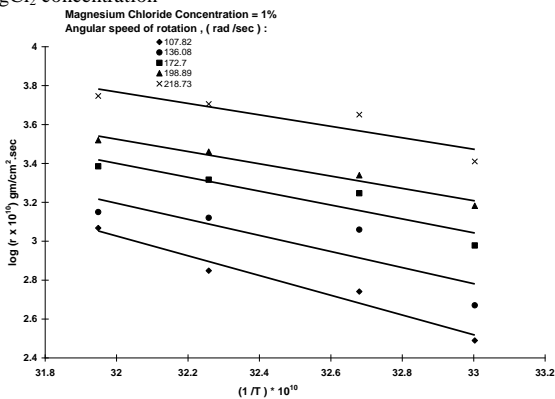
Figure (5-b): Arrhenius plot of the experimental results at different $CaCl_2$ concentration

concentrations of $CaCl_2$ and $MgCl_2$, respectively. Increasing the temperature of the corrosive medium increases the rate of corrosion. This may be ascribed to the increased reaction rate, which might be assisted by the reduced viscosity of the solution, with a consequent increase in the O_2 diffusivity according to the Stocks-Einstein equation [14]:

$$\frac{D\mu}{T} = C \qquad (12)$$

Where:

D = the diffusion coefficient in cm^2 /s, μ = the

solution viscosity in g/cm.s, and C is a constant.

In order to better understand the mechanism of steel corrosion in $CaCl_2$ and $MgCl_2$ solutions, the activation energy was determined by plotting log (r) versus (1/T) according to Arrhenius equation (cf. Figs. 5-a and b):

$$r = A\exp(\frac{-E}{RT}) \qquad (13)$$

Where:

A = pre-exponential factor or frequency factor, R = gas constant = 1.9854×10^{-3} kcal/mol.K and E = activation energy, kcal/mol.

It was found that the activation energy was 5.16 and 8.46 kcal/ mol for $CaCl_2$ and $MgCl_2$, respectively. The low value of the activation energy (< 10 kcal/mol) lends support to the diffusion – controlled mechanism of the reaction under the
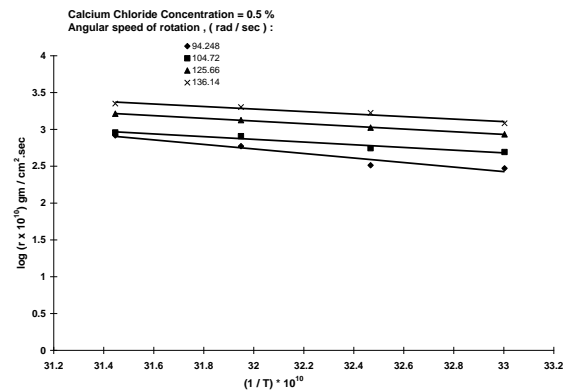
Figure (6): Comparison between the effect of temperature on the rate of steel corrosion at constant (ω) and constant concentration of $CaCl_2$ and $MgCl_2$
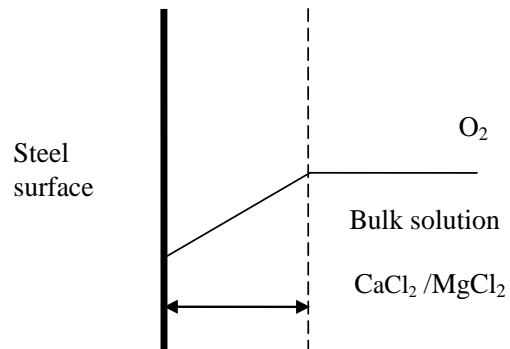
Figure (7): Diffusion layer through which O_2 diffuses from the solution bulk to the steel surface.

present conditions [15-17]. This is in agreement with the previous studies [6, 10, and 13].

Fig. 6 shows a comparison between the effects of temperature on the rate of steel corrosion in $CaCl_2$ and $MgCl_2$ solutions at a constant angular speed of rotation (ω = 136.1 rad/s) and constant salt concentration (0.5 %). It was found that the $CaCl_2$ solution is a more corrosive medium than the $MgCl_2$ solution.

CONCLUSIONS

The effect of the different variables on the rate of steel corrosion in aqueous solutions of CaCl₂ or MgCl₂ can be summarized as follows:

• The rate of steel corrosion increased upon increasing CaCl₂ and/or MgCl₂ concentrations up to a certain level and remained almost constant with further increase in salt concentration.

• The corrosion rate was found to increase with increasing speed of agitation and temperature of the corrosive medium.

• The mechanistic study of the present corrosion process revealed that the process is diffusion-controlled.

• The rate of steel corrosion in aqueous solutions of CaCl₂ is higher than that in MgCl₂ solutions under the same conditions.

• Steel equipments sustain severe corrosion in oil refinery wastewater, especially in the presence of high MgCl₂ and CaCl₂ content.

• Sufficient precautions such as cathodic protection should be taken to protect these equipments.

REFERENCES:

1 T.Y. Chen, R. A. Mohammed, A. I. Bailey et al., *Colloids Surf. A: Physicochemical Eng. Aspects,* **83** (3) 273 (1994).
2 M. Chirinos, D. Graham, I. Layrisse et al., Methods for desalting crude oil [P], US4806231.
3 A. Padron, E. Anez, R. Possamai et al., Crude oil dehydration and desalting system with a higher gravity than 10 degrees API in mixing pipelines [P], US5384039.
4 J. S. Eow, M. Ghadiri, *Chem. Eng. J.,* **85,** 357 (2002).
5 T. L. Prakash, A. U. Malik, *Desalination*, **23**, 215 (1999).
6 H.Uhlig, Corrosion and Corrosion Control, Wiley, New York, 1963.
7 V. N. Erikh, M. G. Rasina, M. G. Rudin, Chemistry and Technology of Petroleum and Gas, Mir, Moscow, 1988.
8 W. L. Nelson, Petroleum Refining Engineering, McGraw Hill, New York, 1987.
9 B. S. Bahl, G. D. Tuli, Essentials of Physical Chemistry, S. Chand, New Delhi, 1976.
10 D. A. Jones, Principles and Prevention of Corrosion, Macmillan, New York, 1992.
11 J. A. Salvato, Environmental Engineering and Sanitation, Wiley-Interscience, 3rd ed., Wiley, New York, 1982.
12 D. Stuckey, A. Hamza, Management of Industrial Wastewater in Developing Nations, Proc. Intern. Symp., Alex, Egypt, Pergamon Press, New York, **316**, 453, 1981.
13 M. G. Fontana, Corrosion Engineering, MsGraw-Hill, New York, 1987.
14 E. L. Cussler (ed.), Diffusion Mass Transfer in Fluid Systems, Cambridge University Press, Cambridge, 2009.
15 O. Levenspiel, Chemical Reaction Engineering, Wiley, New York, 1962.
16 J. M. Smith, Chemical Engineering Kinetics, McGraw-Hill, Inc., New York, 1981.
17 J. Horak, J. Pasek, Design of Industrial Chemical Reactors from Laboratory Data, Heyden & Sons Ltd, London, 1978.

ПРИНУДИТЕЛНА КОНВЕКЦИОННА КОРОЗИЯ НА СТОМАНЕНИ СЪОРЪЖЕНИЯ ВЪВ ВОДНИЯ СЛОЙ В СУРОВ ПЕТРОЛ

С. А. Нозиер, И. А. Алхамед

Катедра инженерна химия и материали, Факултет по инженерство, Университет Крал Абдулазиз, Кралство Саудитска Арабия

(Резюме)

Настоящото проучване разглежда връзката между наличието на някои соли в суровия петрол и на корозията на метални съоръжения в контекста на петролната промишленост. Скоростта на корозия на желязо във вода, съдържаща CaCl₂ и MgCl₂ с концентрации, подобни на тези във водата, присъстваща в суровия петрол, преди обезсоляване е измерена чрез загубата на тегло. Изследваните променливи са концентрацията на CaCl₂, концентрацията на MgCl₂, работната температура и ъгловата скорост на въртене. Установено е, че скоростта на корозия нараства с увеличаване на концентрациите на MgCl₂ и CaCl₂ до определено ниво, след което остава почти постоянна. Увеличаването на ъгловата скорост на въртене благоприятства скоростта на корозия. Установено е, че скоростта на корозия се увеличава с температурата, в съответствие с уравнението на Арениус с активираща енергия от 8,64 и 5,16 ккал/мол съответно за MgCl₂ и CaCl₂, което означава, че корозията на стомана в двата разтвора на MgCl2 и на CaCl2 е дифузионно контролирана реакция при условията на работа.

Separation of gold (III) from ayurvedic medicines and alloys by extraction chromatography

S. Kokate, H. Aher, S. Kuchekar*

P. G. Department of Analytical Chemistry, P. V. P. College, Pravaranagar, At/Po – Loni (Kd), Tal. Rahata, Dist Ahmednagar, 413713, India,

A new method is proposed for the extractive chromatographic separation of gold(III). Gold(III) is extracted from 0.5 mol/L of hydrochloric acid by a silica gel column coated with N-n-octylaniline (liquid anion exchanger), eluted with 0.25 mol/L ammonia and determined by spectrophotometrically as its complex with stannous chloride. The various influencing parameters such as acid concentrations, effect of flow rate of mobile phase and reagent concentration was studied. The method was free from large number of interferences from cations and anions. Proposed method has been applied for analysis of gold(III) from the ayurvedic medicine and synthetic mixtures corresponding to alloys. The reliability of analytical data was verified by statically. The nature of extracted species is $[RR'NH_2^+ AuCl_4^-]_{org.}$

Key words: gold(III), separation, Ayurvedic medicine, alloys

INTRODUCTION

Gold is one of the precious metal. It has wide range of applications as a catalyst in hydrogenation of some organic compounds. The beauty and rarity of gold has led to its use in jewellery, in coinage, as a monetary standard, in jewellery and dentistry. The infrared reflectivity of gold leads to its use in the aeronautics and space industries. The economy of nation depends to a significant extent on the size of its gold reserves. Since many decades every human is having great desire of suvarna i.e. gold. By nourishing the brain cells it improves memory, increases the strength and immunity of the body and improves the pronunciation. It increases blood corpuscles, haemoglobin and improves cardiac functions as well. Gold has low abundance, high prices and wide range of applications hence it is essential to develop an innovative method for its separation is an analytical merits. Reversed phase extraction chromatography (RPEC) is an extremely versatile technique and has been applied successfully for the separation of various metals [1-5]. Literature survey revealed that gold was quantitatively extracted with Bis(2-ethylhexyl) phosphate (HDEHP) [6] from 7-8 mol/L hydrochloric acid and is eluted with 2.0 mol/L hydrochloric acid. Tributylphosphate [7] used as stationary phase towards the column and gold was separated from binary and multicomponent mixtures. The extraction of gold(III) from hydrochloric and hydrobromic acid with 5% tri-iso-octylamine (TIOA) solution in carbon tetrachloride has been studied [8]. The method suffers from interferences of anions like thiocyanate, cyanide, sulphide, sulphite, thiosulphate, EDTA, bromide, nitrite, iodide and silver(I). Separation of gold (III), palladium(II) and platinum(IV) in chromites was achieved by anion exchange chromatography using inductively coupled plasma-atomic emission spectrometry (ICP-AES) [9]. This method suffers from the drawback viz. it requires more elution time and palladium(II) can't be determined. Solid phase extraction of gold(III), platinum(IV) and palladium(II) was carried out using polystyrene-divinylbenzene porous resin (XAD–4) [10]. Platinum(II), palladium(II) and gold(III) were separated by Amberlite XAD-7 resin [11] column gave the recovery of elements greater than 95%. Study was made for the sorption of negative charged sulphate complexes of platinum, palladium, iridium and gold on poly-aniline [12].

Gold has been separated with N-*n*-octylaniline [13, 14] using solvent extraction method but this method requires large amount of solvents. The use of *n*-octylaniline in the extraction of noble metals has been described in the literature [15, 16]. The comparison can be made on the merits of N-*n*-octylaniline relative to *n*-octylaniline as an extractant of noble metal. The extraction depends upon method of preparation of the reagent. Some of the drawbacks of the method are emulsion formation, requirement of more elution time (30 min), higher reagent concentration and need of multiple extractions.

N-n-octylaniline has been used in this laboratory for reversed phase extraction chromatographic

---

* To whom all correspondence should be sent:
 E-mail: shashi17@gmail.com

separation of some platinum group metals [17-20] and coinage metals [21]. The use of this reagent is found to be advantageous as it can be synthesized at low cost, with high yield and of best purity. The present investigation describes its use in quantitative extraction of gold (III) and the development of a rapid and selective method for the separation of gold (III) from Ayurvedic medicine and synthetic mixtures corresponding to alloys.

EXPERIMENTAL

Apparatus

An Elico spectrophotometer model SL-159 with 10 mm path length quartz cell was used for absorbance measurements.

Reagents

The stock solution of gold (III) was prepared by dissolving 1.0 g chloroauric acid (HAuCl$_4$) (Loba Chemie Pvt. Ltd. Mumbai, India) in 1.0 mol/L hydrochloric acid using distilled water, diluted to 250 mL and standardized gravimetrically [22]. A working solution containing 50 μg gold (III) was prepared by further dilution.

Hydrochloric acid was of analytical grade provided by Qualigene fine chemical Pvt. Ltd. (Mumbai, India). Other standard solutions of different metals used for study of effect of foreign ions (Table 1) were prepared by dissolving their salt in dilute hydrochloric acid. The solutions of anions were prepared by dissolving respective sodium salts in distilled water. The stock solution of *N-n*-octylaniline was prepared using method reported by Gardlund [23].

Preparation of anion exchange material

Silica gel (60 –120 mesh) obtained from British Drug House India Ltd., dried at 120 ^{0}C for 2-3 h and stored in desiccators. It was packed in a U tube through which a stream of nitrogen was bubbled though a small Durand bottle containing 20.0 mL dimethyldichlorosilane (DMCS) (Acros Organics, New Jersey, USA). DMCS vapour was continued for 4 h. The silica gel was washed with anhydrous methanol, then dried. A portion of 5.0 g silaned silica gel was soaked with 0.087 mol/L N-n-octylaniline which was previously equilibrated with hydrochloric acid (0.5 mol/L) for 10 min, and then solvent was evaporated to get nearly dried gel. Slurry of coated silica gel in distilled water was prepared by centrifugation at 2000 r/min and was packed into chromatographic column which made from borosilicate glass tube, having bore 8 mm, length 30 cm, fitted with glass-wool plug at the bottom, to give a bed height 6.0 cm. The bed was then covered with a glass wool plug.

General procedure

An aliquot solution containing 50 μg gold (III) was made up to 25.0 mL by adjusting the concentration of hydrochloric acid to 0.5 mol/L. It was passed through the column containing 0.087 mol/L N-n-octylaniline coated with silica gel at a flow rate of 1.0 mL/min. After extraction, gold (III) was eluted with 25.0 mL, 0.25 mol/L ammonia solution. The eluents were evaporated to moist dryness. The residue was dissolved in 5 mL aqua regia and evaporated to moist dryness. Then 2 mL of 2% sodium chloride solution, concentrated hydrochloric acid solutions were added and mother liquor was evaporated again. The procedure of evaporation was repeated to remove the oxides of nitrogen. The residue was dissolve in 0.05 mol/L hydrochloric acid and gold (III) was determined spectrophotometrically by stannous chloride method [24].

RESULTS AND DISCUSSION

Effect of hydrochloric acid concentration on extraction

The effect of hydrochloric acid concentration on the percentage extraction of gold (III) was studied in the range 0.125 to 1.5 mol/L on the column coated with 0.087 mol/L N-n-octylaniline as the stationery phase on hydrophobic silica gel. The extraction of gold (III) was found to be quantitative at 0.5 mol/L hydrochloric acid. Hence, all the extractions were carried out at this concentrations Fig. 1.
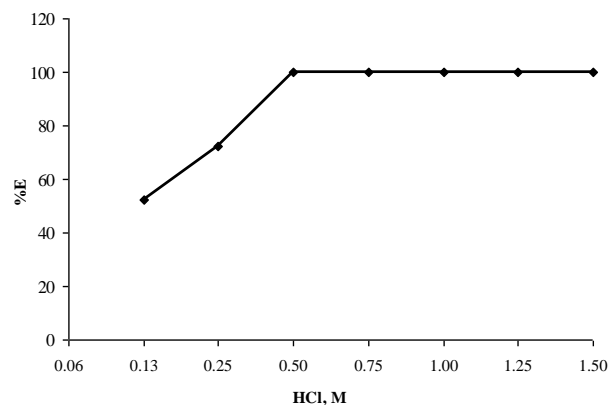

Fig. 1 Extraction of gold (III) as a function of hydrochloric acid concentration

Effect of flow rate

The effect of flow rate on percentage extraction of gold (III) was studied from 0.5 to 3.0 mL/min. It

was observed that the percentage extraction decreases with increase the flow rate. Therefore the flow rate was kept at 1.0 mL/min for further extraction studies.

Effect of N-n-octylaniline concentration

The concentration of *N-n*-octylaniline was varied from 0.022 to 0.110 mol/L while the concentration of hydrochloric acid ranges from 0.125 to 1.25 mol/L for gold (III). It was found that, for quantitative extraction of gold (III), 0.087 mol/L *N-n*-octylaniline was sufficient
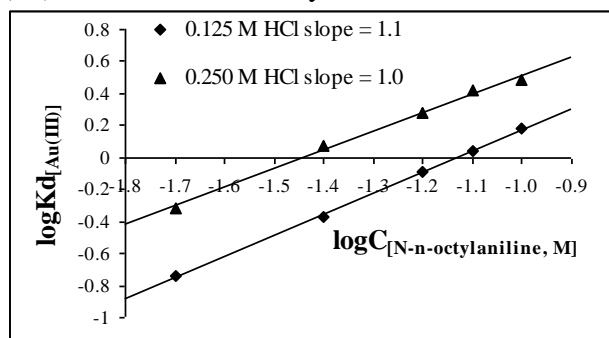
Fig 2. Log-log plot of distribution coffecient versus *N-* in hydrochloric acid media. The percentage extraction of gold (III) increases when the concentration of *N-n*-octylaniline increases. Log-*n*-octylaniline concentration at 0.125 and 0.25 mol/L hydrochloric acid
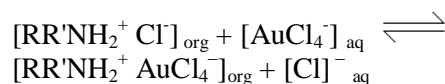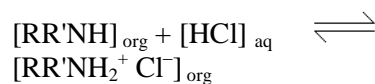
log plot of *N-n*-octylaniline concentration versus distribution coefficient at 0.125 and 0.25 mol/L hydrochloric acid gives slope 1.1 and 1.0 respectively (Fig. 2). The probable composition of extracted species was calculated 1:1 (metal to amine) ratio. The extraction mechanism can be explained as follows

$$[RR'NH]_{org} + [HCl]_{aq} \rightleftharpoons [RR'NH_2^+ Cl^-]_{org}$$

$$[RR'NH_2^+ Cl^-]_{org} + [AuCl_4^-]_{aq} \rightleftharpoons [RR'NH_2^+ AuCl_4^-]_{org} + [Cl]^-_{aq}$$

where
$$R = -C_6H_5 \quad R' = -CH_2(CH_2)_6CH_3$$.

Effect of foreign ions

Various amounts of foreign ions were added to a fixed amount of gold (III) (50 μg) to study the effect of interference according to the recommended procedure. The tolerance limit was set at the amount required to cause ± 1.5% error in the recovery of gold (III), Table 1. It was observed that the method was free from interference from a

Table 1. Effect of foreign ions

Foreign ion	Added	Tolerance limit/μg	Foreign ion	Added	Tolerance limit/μg
Mn(II)	$MnCl_2.6H_2O$	250	Pd(II)	$PdCl_2.xH_2O$	100
V(V)	V_2O_5	400	Pt(IV)	$PtCl_6.xH_2O$	200
U(VI)	$UO2(NO_3)_2.6H_2O$	300	Te(IV)	Na_2TeO_3	200
Tl(III)	$TlNO_3$	400	Ni(II)	$NiCl_2.6H_2O$	300
Zn(II)	$ZnSO_4.7H_2O$	400	Ir(III)	$IrCl_3.xH_2O$	200
Cd(II)	$3CdSO_4.8H_2O$	400	Fe(II)	$FeSO_4 7H_2O$	400
Bi(III)	$Bi(NO_3)_2.5H_2O$	300	Pb(II)	$Pb(NO_3)_2$	250
Ce(IV)	$Ce(SO_4)_2$	400	Os(VIII)	OSO_4	200
Mo(VI)	$(NH_4)_6Mo_7O_{24}.2H_2O$	400	Rh(III)	$RhCl_3.xH_2O$	200
Ag(I)	$AgNO_3$	300	Ru(III)	$RuCl_3.xH_2O$	200
Sr(II)	$Sr(NO_3)_2$	300	EDTA	EDTA(disodium salt)	1000
Sb(III)	Sb_2O_3	300	Tartrate	$C_6H_6O_6$	1000
Mg(II)	$MgCl_2.6H_2O$	250	Malonate	$CH_2(COONa)_2$	1000
Fe(III)	$FeCl_3$	300	Oxalate	$(COOH)_2.2H_2O$	1000
Co(II)	$CoCl_2.6H_2O$	300	Fluoride	NaF	1000
Be(II)	$BeSO_4.4H_2O$	300	Bromide	KBr	1000
Ca(II)	$CoCl_2.6H_2O$	250	H_2O_2	H_2O_2	2.0 ml
Ba(II)	$BaCl_2.H_2O$	250	Iodide	KI	1000
Cu(II)	$CuCl_2.H_2O$	250	Persulfate	$K_2S_2O_8$	1000

Table 2. Separation of gold(III) from synthetic mixtures and alloys. *N-n*-octylaniline: 0.087 mol/L; eluent: 25 mL 0.25 mol/L ammonia; hydrochloric acid 0.5 mol/L; Flow rate 1.0 mL/min.

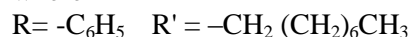| Sample Compositions /μg	Au (III) Certified /μg	Au (III) Found /μg	Mean (*n*=3)	Recovery % (*n*=3)	RSD % (*n*=3)
Cu 49.35; Ag 7.25	43.40	43.35, 43.20, 43.25	43.27	99.7	0.30
Cu 35.00; Ag 5.00	60.0	59.90, 59.95, 59.80	59.88	99.8	0.20

Table 3. Separation of gold(III) from pharmaceutical formulations. *N-n*-octylaniline: 0.087 mol/L; eluent: 25 mL 0.25 mol/L ammonia; Hydrochloric acid 0.5 mol/L; Flow rate 1.0 mL/min.

Sample (Source)	Au(III) Certified value, %	Found/%
Bruhatwat Chintamani (Koral Pharma, Nashik)	0.18	0.15
Vasant Kusumkar (Koral Pharma, Nashik)	0.15	0.13
Suvarna Malini Vasant (Koral Pharma, Nashik)	0.55	0.53
Suvarna Sutshekhar (Koral Pharma, Nashik)	2.13	2.00
Shwas Kas Chintamani (Koral Pharma, Nashik)	1.18	1.15
Suvarna Bhasma (Shree Dhootapapeshwar Ltd, Mumbai)	7.60	7.50

(Average of three determinations)

Table 4. Statistical treatment of the analytical data (*n*=6). Au(III): 50 μg; *N-n*-octylaniline: 0.087 mol/L; eluent: 25 mL 0.25 mol/L ammonia; hydrochloric acid 0.5 mol/L; Flow rate 1.0 mL/min.

Mean (M)	Median (m)	Average deviation (d)	Mean average deviation (D)	Standard deviation (s)	Mean of standard deviation (S)	Coefficient variation (C.V.)
99.3	99.9	0.0004	0.0002	0.095	0.036	0.10%

large number of cations and anions. The only cations showing interference in the method are chromium (VI) and manganese (II) which are strong oxidizing agents. Thiosulphate, thiourea and thiocyanate form very strong complexes with gold (III) because precious metals such as gold, silver, platinum group metals (PGMs) are belong to the soft metals which posses a strong affinity to ligands containing donor type sulphur atom which acts as soft bases.

Analysis of synthetic mixture corresponding to alloys

The proposed method was successfully applied for the analysis of synthetic mixtures corresponding to alloys containing gold (III) i.e. copper-silver-gold alloy. The results of analysis matched with certified values [25], Table 2.

Analysis of gold (III) from ayurvedic samples

Ayurvedic samples containing gold are useful for various chronic disorders, general debility, diseases which deplete immunity, anaemia, mental disorders, respiratory tract disorders etc. The proposed method was successfully applied for the separation of gold (III) from bruhatwat chintamani, vasant kusumkar, suvarna malini vasant, suvarna sutshekhar, shwas kas chintamani and suvarna bhasma. The samples are brought into solution form by wet-oxidation method. Gold (III) was extracted by the proposed method and determined by the standard procedure. The results are in good agreement with certified value calculated by standard calibration curve method Table 3.

Statistical treatment of the analytical data

The evaluation and interpretation of an analytical data is verified by statically. It is measure of performance for analytical procedure. The various criteria used to evaluate the analytical data. The important values obtained were reported in Table 4.

CONCLUSIONS

Proposed method is very simple, selective and reproducible. It is free from the interferences from large number of foreign ions, which are in their states of nature. Low reagent and acid concentration is required for quantitative recovery of gold (III). It is applied for the separation of gold from ayurvedic samples and alloys. Reliability of method verified by stastical treatment analytical data.

REFERENCES

1. B. Mandal, N. Ghosh, *Indian J Chem Sec A*., **47A,** 1041 (2008) .
2. B. Mandal, U. S. Roy, *Indian J Chem Sec A*., **47A,** 1497 (2008).
3. H. R. Aher, S. R. Kuchekar, *Ind J Chem Techno.,* **15,** 403 (2008).
4. M. D. Rokade, P. M. Dhadke, *Indian J Chem Sec A*., **40,** 1243 (2001).
5. M. D. Rokade, J. N. Iyer, P. M. Dhadke, *Chem Environ Res.*, **10,** 101 (2001).
6. LCT. Eusebius, S. M. Khopkar, *Indian J Chem Sec A*., **25A,** 300 (1986).
7. S. N. Bhosale, S. M. Khopkar, *Indian J Chem Sec A.,* **23A,** 705 (1984).
8. M. Y. Mirza, *Talanta*, **27,** 101 (1980).

9. S. C. Kwang, H. L. Chang, J. P. Yeong, S. J. Kih, H. K. Won, *Bull. Korean Chem. Soc.,* **22,** 801 (2001).
10. T. Saitoh, S. Suzuki, M. Hiraide, *J Chromatogra A.*, **1097,** (2005) 179.
11. L. Elci, M. Soylak, E. B. Buyuksekerci, *Anal Sci.,* **19,** 1621 (2003).
12. S. Kumar, R. Verma, B. Venkataramani, V. S. Raju, S. Gangadharan, *Solvent Extr Ion Exch.*, **13,** 1097 (1995).
13. T. N. Lokhande, S. H. Gaikwad, M. A. Anuse, M. B. Chavan, *Annali di Chimica.,* **92,** 615 (2002).
14. S. S. Kolekar, M. A. Anuse, *Gold Bulletin*, **34,** 50 (2001).
15. C. Pohlandt, *Talanta*, **26,** 199 (1979).
16. R. N. Gedye, J. Bozic, P. M. Durbano, B. Williamson, *Talanta*, **36** (1989) 1055.
17. S. J. Kokate, H. R. Aher, S. R. Kuchekar, *Bulgarian Chemical Communications*. **41,** 272 (2009).
18. S. J. Kokate, S. R. Kuchekar, *Chinese Journal of Chromatography*. **27,** 809 (2009).
19. S. J. Kokate, H. R. Aher, S. R. Kuchekar, *Analytical Chemistry an Indian Journal*. **8,** 575 (2009).
20. S. J. Kokate, S. R. Kuchekar, J. *Saudi Chem. Soc.*, **14,** 41 (2010).
21. H. R. Aher, S. R. Kuchekar, *Int J Chem Sci.*, **4,** 157 (2006).
22. N.H. Furman, R.E. Krieger, Standard methods of chemical analysis, Malabar, Florida, **6,** 870 (1962)
23. Z.G. Gardlund,; R.J. Curtis, G.W. Smith, Liquid Crystals and Ordered Fluids. **2,** 541 (1973).
24. E. B. Sandell, Colorimetric Determination of Traces of Metals. B. L. Clarke, P. J. Elving, I. M. Kolthoff, Interscience publishers, New York, **3,** 503 (1965).
25. M. A. Anuse, S. R. Kuchekar, N. A. Mote, M. B. Chavan, *Talanta*, **10,** 1008 (1985).

РАЗДЕЛЯНЕ НА ЗЛАТО (III) ОТ АЮРВЕДИЧНИ ЛЕКАРСТВА И СПЛАВИ ЧРЕЗ ЕКСТРАКЦИОННА ХРОМАТОГРАФИЯ

С. Кокате, Х. Ахер, С. Кучекар*

П.Г. Департамент по аналитична химия, П.В.П. колеж, Праваранагар, Ат/По-Лони(Кд), Тал. Рахата, Окр. Ахмеднагар, 413713, Индия

(Резюме)

Предложен е нов метод за екстракционно хроматографско разделяне на злато (III). Злато (III) се екстрахира от разтвор на 0,5 мол/л солна киселина в колона със силикагел, покрит с N-н-октиланилин (течен анионообменик), елюира се с 0,25 мол/л разтвор на амоняк и се определя спектрофотометрично като комплекс с калаен хлорид. Изучени са различни параметри като концентрация на киселината, ефекта на скоростта на потока на подвижната фаза и концентрацията на реагентите. Методът не се влияе от голям брой аниони и катиони. Предложеният метод е бил приложен за анализ на злато (III) от аюрведическата медицина и синтетични смеси, съответстващи на сплави. Надеждността на аналитичните данни беше проверена статистически. Екстрахираното съединение е $[RR'NH_2^+ AuCl_4^-]_{org}$.

Synthesis and biological activity of 4-chloro-2-hydroxy-N-(5-methylene-4-oxo-2-aryl-thiazolidin-3-yl) benzamide

S. Maheta[1], S.J. Patel*[2]

[1]Emcure Pharmaceuticals, USA
*[2]Unity Dye Chem Pvt. Ltd., Sokhada, Khambhat-388620, INDIA*

4-chloro-2-hydroxy benzoic acid hydrazide (1) undergoes facile condensation with aromatic aldehydes to afford the corresponding 4-chloro-2-hydroxy benzoic acid arylidene hydrazides (2a–h) in good yields. Cyclocondensation of compounds (2a–h) with thioglycolic acid yields 4-chloro-2-hydroxy- N (4-oxo-2-aryl- thiazolidin -3–yl) benzamides (3a–h). These (3a–h) compounds are for the reacted with benzaldehyde in the presence of sodium ethanolate affords, giving 4-chloro-2-hydroxy- N (5-methylene-4-oxo-2-aryl- thiazolidin -3-yl)benzamides (4a–h). The structures of these compounds were established on the basis of analytical and spectral data. All the newly synthesized compounds were evaluated for their antibacterial and antifungal activities.

Key words: 4-chloro-2-hydroxy benzoic acid hydrazide, thiazolidin, antibacterial activity.

INTRODUCTION

Hydrazide and their heterocyclised products display diverse biological activities including antibacterial, antifungicidal, analgesic, anti-inflammatory properties [1–15]. These heterocyclic systems find wide use in medicine, agriculture and industry. One of the hydrazides, 4-chloro-2-hydroxy benzoic acid hydrazide and their condensed products play a vital role in medicinal chemistry [16–18]. 4-Thiazolidinones and its arylidene compounds give good pharmacological properties [19–23]. 4-thiazolidinones are also known to exhibit antitubercular [24], antibacterial [25], antifungal [26] and anticonvulsant activities. Hence, it was thought of interest to merge both of thiazolidinone and 4-chloro-2-hydroxy benzoic acid hydrazide moieties which may enhance the drug activity of compounds to some extent, or they might possess some of the above mentioned biological activities. From this point of view, the objective of the present work is to prepare new derivatives of 4-chloro-2-hydroxy benzoic acid hydrazide containing thiazolidinone moiety. Hence the present communication comprises the synthesis of 4-chloro-2-hydroxy- N (5-methylene-4-oxo-2-aryl- thiazolidin -3-yl) benzamide. The synthetic approach is shown in Scheme 1.
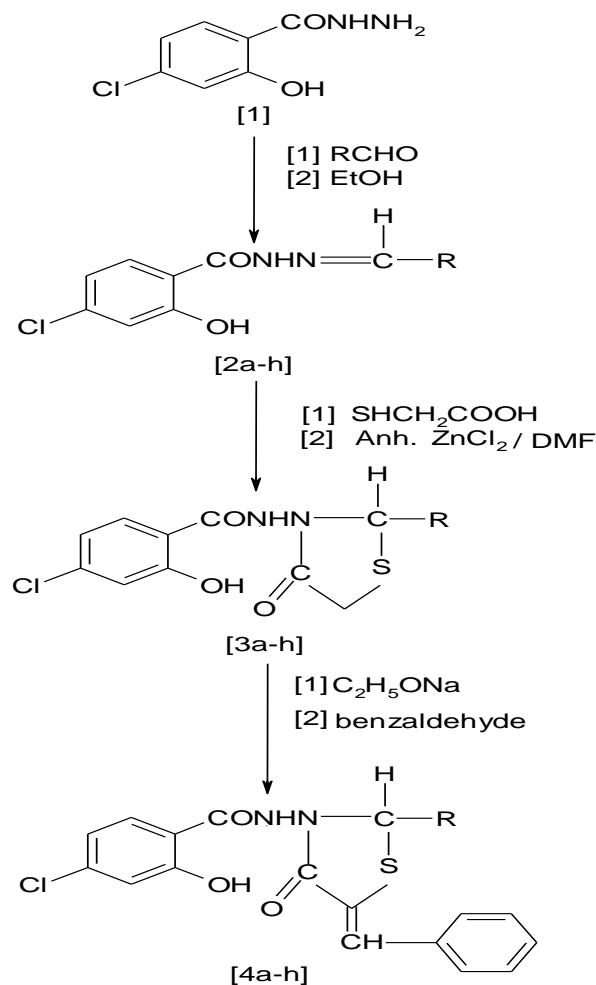
Scheme 1. R = (a) C_6H_5; (b) 4-OCH$_3$-C$_6$H$_4$; (c) 4-OH-C$_6$H$_4$; (d) 2-OH-C$_6$H$_4$; (e) 4-CH$_3$-C$_6$H$_4$; (f) 3,4-CH$_2$O$_2$-C$_6$H$_4$; (g) 4-OH-3-OCH$_3$-C$_6$H$_3$; (h) 3,4-C$_2$H$_5$-C$_6$H$_4$.

---

*To whom all correspondence should be sent:
E-mail: : sumeetcambay@gmail.com

EXPERIMENTAL

Melting points were determined in open capillary tubes and were not corrected. The IR spectra were recorded in KBr pellets on a Nicolet 400D spectrometer and ^{1}H NMR and ^{13}C NMR spectra were recorded in DMSO with TMS as internal standard on a Bruker spectrometer at 400 MHz and 100 MHz, respectively. LC-MS of selected samples taken on LC-MSD-Trap-SL_01046.

Preparation of 4-chlro-2-hydroxy benzoic acid arylidene hydrazide **(2a–h)**

General procedure: An equimolecular mixture of 4-chloro-2-hydroxy benzoic acid hydrazide (1), (0.01mole) and the aromatic aldehydes (a-h) in ethanol (15mL) was refluxed on a water bath for 1-2 h. The solid separated was collected by filtration, dried and recrystallized from ethanol. The yields, melting points and other characterization data of these compounds are given in Table 1.

Table .1 Analytical data and elemental analysis of compounds (2a-h)

Compd.	Molecular formula (Mol.wt.)	Yield	M.P.* ^{0}C	Elemental Analysis					
				%C		% H		%N	
				Found	Calcd.	Found	Calcd.	Found	Calcd.
2a	$C_{14}H_{11}ClN_2O_2$ (274)	85	243	61.18	61.21	3.99	4.04	10.15	10.20
2b	$C_{15}H_{13}ClN_2O_3$ (304)	80	246	59.08	59.12	4.25	4.30	9.14	9.19
2c	$C_{14}H_{11}ClN_2O_3$ (290)	75	240	57.79	57.84	3.77	3.81	9.58	9.64
2d	$C_{14}H_{11}ClN_2O_3$ (290)	81	243	57.78	57.84	3.75	3.81	9.57	9.64
2e	$C_{15}H_{13}ClN_2O_2$ (288)	79	244	62.36	62.40	4.51	4.54	9.64	9.70
2f	$C_{15}H_{11}ClN_2O_4$ (318)	75	247	56.49	56.53	3.44	3.48	8.73	8.79
2g	$C_{15}H_{13}ClN_2O_3$ (320)	77	249	56.14	56.17	3.04	4.09	8.68	8.73
2h	$C_{18}H_{19}ClN_2O_4$ (362)	73	261	59.55	59.59	5.24	5.28	7.68	7.72

* Uncorrected

Table 2. Spectral Data of Compounds (2a-h)

	^{1}H NMR (δ, ppm)							
Compound	Ar-H	-OH	-CONH	-N=CH	-CH$_3$	-OCH$_3$	-OC$_2$H$_5$	-OCH$_2$O- cyclic
2a	6.85-7.84 (m, 8H)	11.70 (s)	11.86 (s)	8.40 (s)	-	-	-	-
2b	6.85-7.80 (m, 8H)	11.79 (s)	11.89 (s)	8.44 (s)	-	3.89 (3H)(s)	-	-
2c	6.88-7.84 (m, 8H)	11.85 (s)	11.88 (s)	8.47 (s)	-	-	-	-
2d	6.86-7.83 (m, 8H)	11.81 (s)	11.84 (s)	8.79 (s)	-	-	-	-
2e	6.85-7.80 (m, 8H)	11.80 (s)	11.91 (s)	8.46 (s)	2.39 (3H) (s)	-	-	-
2f	6.89-7.81 (m, 7H)	11.81 (s)	11.94 (s)	8.45 (s)	-	-	-	6.12, (2H) (s)
2g	6.87-7.84 (m, 7H)	11.76 (s)	11.88 (s)	8.47 (s)	-	3.89 (3H) (s)	-	-
2h	6.88-7.83 (m, 7H)	11.83 (s)	11.98 (s)	8.48(s)	-	-	4.12, 4H, (q) (CH$_2$) 1.34, 6H, (t) (CH$_3$)	-

Table 3. Spectral Data of Compounds (2a-h).

Compound	^{13}C NMR (δ, ppm)						
	Ar-H	-CONH	-N=CH	-OCH$_3$	-OC$_2$H$_5$	-CH3	-OCH$_2$O-cyclic
2a	112.2 -159.6	163.3	146.5	-	-	-	-
2b	113.8 - 159.5	163.4	146.3	55.7	-	-	-
2c	112.2 - 159.2	163.7	146.7	-	-	-	-
2d	112.7 - 159.2	163.9	146.5	-	-	-	-
2e	112.8 - 159.1	163.4	146.9	-	-	21.0	-
2f	113.3 - 160.8	163.6	146.7	-	-	-	102.5
2g	111.9 - 160.1	163-164	147.0	56.8	-	-	-
2h	112 - 160.5	163.8	146.9	-	65.4 (OCH$_2$) 15.2 (CH$_3$)	-	-

Table:-4 Analytical Data and Elemental Analysis of Compounds (3a-h).

Compd	Molecular formula (Mol.wt.)	Yield	M.P.[*] ^{0}C	Elemental Analysis							
				%C		%H		%N		%S	
				Found	Calcd.	Found	Calcd	Found	Calcd	Found	Calcd
3a	C$_{16}$H$_{13}$ClN$_2$O$_3$S (348)	62	218	55.04	55.09	3.64	3.67	7.98	8.03	9.11	9.19
3b	C$_{17}$H$_{15}$ClN$_2$O$_4$S (344)	60	221	53.83	53.90	3.90	3.99	7.32	7.39	8.39	8.46
3c	C$_{16}$H$_{13}$ClN$_2$O$_4$S (364)	59	169	52.64	52.68	3.53	3.59	7.63	7.68	8.74	8.79
3d	C$_{16}$H$_{13}$ClN$_2$O$_4$S (364)	58	147	52.63	52.68	4.54	4.59	7.61	7.68	8.72	8.79
3e	C$_{17}$H$_{15}$ClN$_2$O$_3$S (362)	63	174	56.23	56.27	4.13	4.17	7.68	7.72	8.79	8.84
3f	C$_{17}$H$_{13}$ClN$_2$O$_5$S (392)	57	187	51.92	51.98	3.29	3.34	7.09	7.13	8.13	8.16
3g	C$_{17}$H$_{15}$ClN$_2$O$_5$S (394)	52	162	51.66	51.71	3.79	3.83	7.03	7.10	8.08	8.12
3h	C$_{20}$H$_{21}$ClN$_2$O$_5$S (436)	59	212	54.89	54.98	4.80	4.84	6.38	6.41	7.29	7.34

[*] Uncorrected

Preparation of 4-chloro-2-hydroxy- N-(4-oxo-2-aryl- thiazolidin -3-yl)benzamide **(3a–h)**

General procedure: A mixture 4-chloro-2-hydroxy benzoic acid arylidene hydrazide (2a–h) (0.01 mole) in THF (30mL) and mercapto acetic acid (thioglycolic acid) (0.01 mole) with a pinch of anhydrous ZnCl$_2$ was refluxed for 12 h. The solvent was then removed to get a residue, which was dissolved in benzene and passed through a column of silica gel using benzene: chloroform (8:2; v/v) mixture as eluent. The eluate was concentrated and

the product crystallized from alcohol to give 4-thiazolidinones (3a–h), which were obtained in 50–60% yield. The yields, melting points and other characterization data of these compounds are given in Table 4.

Preparation of 4-chloro-2-hydroxy- N (5-methylene-4-oxo-2-aryl- thiazolidin -3-yl) benzamide **(4a-h)**

Table 5. Spectral Data of Compounds (3a-h)

				^{1}H NMR (δ, ppm)					
Compd.	Ar-H	- CH_2 of the ring	-OH	- CH	-CONH	-CH_3	-OCH_3	-OC_2H_5	-OCH_2O- cyclic
3a	6.70-7.85 (m, 8H)	3.85 (2H) (s)	11.72 (s)	5.90 (S)	11.84 (s)	-	-	-	-
3b	6.72-7.84 (m, 8H)	3.89 (2H) (s)	11.80 (s)	5.94 (S)	11.90 (s)	-	3.90 (3H)(s)	-	-
3c	6.73-7.85 (m, 8H)	3.86 (2H) (s)	11.83 (s)	5.92 (S)	11.88 (s)	-	-	-	-
3d	6.70-7.85 (m, 8H)	3.89 (2H) (s)	11.84 (s)	5.95 (S)	11.86 (s)	-	-	-	-
3e	6.73-7.84 (m, 8H)	3.90 (2H) (s)	11.78 (s)	5.94 (S)	11.98 (s)	2.40 (3H) (s)	-	-	-
3f	6.73-7.85 (m, 7H)	3.88 (2H) (s)	11.83 (s)	5.90 (S)	11.96 (s)	-	-	-	6.10, (2H) (s)
3g	6.72-7.85 (m, 7H)	3.91 (2H) (s)	11.74 (s)	5.93 (S)	11.90 (s)	-	3.90 (3H) (s)	-	-
3h	6.71-7.85 (m, 7H)	3.95 (2H) (s)	11.85 (s)	5.91 (S)	11.95 (s)	-	-	4.10, 4H, (q) (CH_2) 1.34, 6H, (t) (CH_3)	-

Table 6. Spectral Data of Compounds (3a-h)

				^{13}C NMR (δ, ppm)					
Compd.	Ar-H	-CH_2	-CONH	-CH	-CO	-OCH_3	-OC_2H_5	-CH3	-OCH_2O- cyclic
3a	112.4 - 160.5	35.5	165.2	64.5	168.8	-	-	-	-
3b	112.6- 160.8	35.4	164.8	64.8	168.9	55.8	-	-	-
3c	112.3- 160.5	35.8	164.9	64.6	168.5	-	-	-	-
3d	112.8- 159.8	35.6	165.1	64.5	168.7	-	-	-	-
3e	112.5- 160.6	35.5	165.2	64.3	168.6	-	-	21.5	-
3f	112.3- 160.7	35.8	164.5	64.2	168.9	-	-	-	102.8
3g	112.8- 160.8	35.6	165.0	64.0	168.4	55.7	-	-	-
3h	113.0- 160.5	35.4	164.8	64.7	169.0	-	65.1(OCH_2) 14.8 (CH_3)	-	-

Table 7. Analytical Data and Elemental Analysis of Compounds (4a-h)

Compd.	Molecular formula (Mol.wt.)	Yield	M.P. ^{0}C	Elemental Analysis							
				%C		% H		%N		%S	
				Found	Calcd.	Found	Calcd.	Found	Calcd.	Found	Calcd.
4a	C$_{17}$H$_{13}$ClN$_2$O$_3$S (360)	65	225	56.55	56.59	3.59	3.63	7.68	7.76	8.85	8.89
4b	C$_{18}$H$_{15}$ClN$_2$O$_4$S (390)	60	228	55.20	55.31	3.81	3.87	7.10	7.17	8.12	8.20
4c	C$_{17}$H$_{13}$ClN$_2$O$_4$S (376)	65	212	54.12	54.19	3.44	3.48	7.39	7.43	8.45	8.51
4d	C$_{17}$H$_{13}$ClN$_2$O$_4$S (376)	66	215	54.13	54.19	3.43	3.48	7.23	7.43	8.41	8.51
4e	C$_{18}$H$_{15}$ClN$_2$O$_3$S (374)	54	214	57.52	57.68	4.98	4.03	7.38	7.47	8.49	8.55
4f	C$_{18}$H$_{13}$ClN$_2$O$_5$S (404)	57	218	53.32	53.40	3.18	3.24	6.82	6.92	7.86	7.92
4g	C$_{18}$H$_{15}$ClN$_2$O$_5$S (406)	60	215	53.08	53.14	3.68	3.72	6.85	6.89	7.82	7.88
4h	C$_{21}$H$_{21}$ClN$_2$O$_5$S (448)	56	221	56.12	56.18	4.69	4.72	6.20	6.24	7.07	7.14

* Uncorrected

Table 8. Spectral Data of Compounds (4a-h)

Compd.	Ar-H	-OH	-CONH	-CH	-CH$_3$	-OCH$_3$	-OC$_2$H$_5$	-OCH$_2$O- cyclic
								^{1}H NMR (δ, ppm)
4a	6.65-7.80 (m, 8H)	11.72 (s)	11.84 (s)	5.92 (s)	-	-	-	-
4b	6.63-7.78 (m, 8H)	11.80 (s)	11.90 (s)	5.95 (s)	-	3.86 (3H)(s)	-	-
4c	6.70-7.79 (m, 8H)	11.83 (s)	11.87 (s)	5.90 (s)	-	-	-	-
4d	6.65-7.80 (m, 8H)	11.79 (s)	11.85 (s)	5.92 (s)	-	-	-	-
4e	6.71-7.78 (m, 8H)	11.81 (s)	11.93 (s)	5.95 (s)	2.38 (3H) (s)	-	-	-
4f	6.64-7.76 (m, 7H)	11.84 (s)	11.98 (s)	5.91 (s)	-	-	-	6.08, (2H) (s)
4g	6.63-7.80 (m, 7H)	11.85 (s)	11.84 (s)	5.93 (s)	-	3.86 (3H) (s)	-	-
4h	6.64-7.79 (m, 7H)	11.81 (s)	11.96 (s)	5.95 (s)	-	-	4.06, 4H, (q) (CH$_2$) 1.35, 6H, (t) (CH$_3$)	-

An equimolar solution of 4-chloro-2-hydroxy-N-(4-oxo-2-aryl-thiazolidin-3-yl)benzamide (3a–h) and benzaldehyde in dioxane (50mL) in the presence of C$_2$H$_5$ONa were refluxed for about 3 h. The solvent was removed in vacuo. The resulting product was recrystallized from methanol to yield compound (4a–h).

The yields, melting points and other characterization data of these compounds are given in Table 7.

Table 9. Spectral Data of Compounds (4a–h)

Compd	13C NMR (δ, ppm) Ar-H	-C-	-CONH	-CH	-CO	-CH$_2$	-OCH$_3$	-OC$_2$H$_5$	-CH3	-OCH$_2$O- cyclic
4a	112.1 -160.8	140.4	164.9	70.3	168.8	112.9	-	-	-	-
4b	112.7-160.5	140.3	164.7	70.3	168.9	113	56.0	-	-	-
4c	112.3-160.3	140.5	164.5	70.4	168.5	113	-	-	-	-
4d	113.0-160.8	140.5	165.2	70.2	168.7	112.8	-	-	-	-
4e	112.5-160.6	140.0	165.2	70.0	168.6	112.9	-	-	21.6	-
4f	112.6-159.8	140.4	164.8	70.1	168.9	112.6	-	-	-	101.8
4g	112.5-159.5	140.0	165.0	70.2	168.4	112.7	55.5	-	-	-
4h	112.8-160.8	140.3	164.9	70.4	169.0	112.5	-	65.2(OCH$_2$) 15.1 (CH$_3$)	-	-

Table10. Antibacterial Activity of Compounds (3a–h)

Compounds	Gram +Ve Staphylococcus aureus	Bacillus subtilis	Gram –Ve E. coli	Klebsiella promioe
3a	12	12	11	16
3b	15	14	13	18
3c	11	15	17	15
3d	13	13	15	13
3e	16	12	16	12
3f	17	18	18	20
3g	13	13	16	15
3h	18	16	19	19
Tetracycline	22	19	21	23

Table 11. Antifungal Activity of Compounds (3a–h)

Compnds	Zone of Inhibition at 1000 ppm (%) Nigrospora sp.	Aspergillus niger	Botrydepladia thiobromine	Rhizopus nigricum	Fusarium oxyporium
3a	65	62	66	60	68
3b	58	58	65	63	69
3c	67	67	67	67	71
3d	61	62	69	71	64
3e	60	64	63	72	69
3f	62	58	67	63	72
3g	64	69	70	60	68
3h	58	71	72	69	65

Table 12. Antibacterial Activity of Compounds (4a–h)

Compounds	Gram +Ve Staphylococcus aureus	Bacillus subtilis	Gram -Ve E.coli	Klebsiella promioe
4a	12	11	12	10
4b	15	10	11	13
4c	16	18	12	12
4d	10	13	14	15
4e	13	14	12	16
4f	14	12	13	12
4g	18	17	18	19
4h	18	16	19	19
Tetracycline	22	19	21	23

Table 13. Antifungal Activity of Compounds (4a–h)

Compnds	Zone of Inhibition at 1000 ppm (%) Nigrospora sp.	Aspergillus niger	Botrydepladia thiobromine	Rhizopus nigricum	Fusarium oxyporium
4a	68	69	68	50	58
4b	66	61	62	63	65
4c	65	70	61	62	67
4d	61	61	61	68	66
4e	63	62	60	71	62
4f	64	55	67	60	68
4g	69	59	69	56	69
4h	61	64	71	72	65

BIOLOGICAL SCREENING

Antibacterial activities

The antibacterial activities of all the compounds were studied against gram-positive bacteria (*Staphylococcus aureus* and *Bacillus subtilis*) and gram-negative bacteria (*E. coli* and *Klebsiella promioe*) at a concentration of 50μg/mL by agar cup plate method. A methanol system was used as control in this method. Similar conditions using tetracycline as a control was used standard for comparison. The area of inhibition of zone measured in cm. Compounds 3g, 3h, 4g, and 4h were found more toxic for microbes. Other compounds found to be less or moderate active than tetracycline Tables 10 and 12.

Antifungal Activities

The fungicidal activity of all the compounds was studied at 1000 ppm concentration in vitro. Plant pathogenic organisms used were *Nigrospora* sp., *Aspergillus niger, Botrydepladia thiobromine*, and *Rhizopus nigricum, Fusarium oxyporium*. The antifungal activity of all the compounds (3a–h) & (4a–h) were measured on each of these plant pathogenic strains on a potato dextrose agar (PDA) medium. Such a PDA medium contained potato 200g, dextrose 20g, agar 20g and water 1c. Five days old cultures were employed. The compounds to be tested were suspended (1000ppm) in a PDA

medium and autoclaved at 120º C for 15 min. at 15 atm. pressure. These media were poured into sterile Petri plates and the organisms were inoculated after cooling the Petri plates. The percentage inhibition for fungi was calculated after five days using the formula given below:

Percentage of inhibition = 100(X-Y) / X

Where *X* = Area of colony in control plate
Y = Area of colony in test plate

The fungicidal activity displayed by various compounds (3a-h) and (4a-h) is shown in Tables-11 and 13.

RESULTS AND DISCUSSION

It was observed that 4-chloro-2-hydroxy benzoic acid hydrazide (1), on condensation with aromatic aldehydes, yields 4-chloro-2-hydroxy benzoic acid arylidene hydrazides (2a–h). The structures of (2a-h) were confirmed by elemental analysis and IR spectra showing an absorption band at 1620–1640 (C=N), 3030-3080 cm^{-1} (C-H, of Ar.), 3240-3260 cm^{-1} (-OH), 1635–1640 cm^{-1} (C=O of CONH), 3350 – 3500 cm^{-1} (- NH), 2815, 1250 cm^{-1} (-OCH$_3$), 2950, 1370 cm^{-1} (–CH$_3$). The C, H, N analysis data, ^{1}H NMR, and ^{13}C NMR spectral data of all compounds are presented in Tables 1, 2 and 3 respectively.

The structures assigned to 4-chloro-2-hydroxy-N (4-oxo-2-aryl- thiazolidin -3-yl) - benzamides (3a-h) were supported by the elemental analysis and IR spectra showing an absorption bands at 1630–1650cm^{-1} (C=O of thiazolidinone ring), 740 – 750 cm^{-1} (C-S-C of thiazolidinone ring), 3075-3095cm^{-1} (CH$_2$ of thiazolidinone ring), 3030-3080 cm^{-1} (C-H, of Ar.), 3240-3260 cm^{-1} (–OH), 1630 – 1640 cm^{-1} (C=O of CONH), 3350 – 3500 cm^{-1} (- NH). The C, H, N analysis data, ^{1}H NMR, and ^{13}C NMR spectral data of all compounds are presented in Tables 4, 5 and 6 respectively.

The IR spectra of (4a–h) are almost resemble those of the corresponding (3a–h) only discernable difference observed that the new band (but not strong) at 1628cm^{-1} (–C=CH–Ar) is observed in all the spectra of (4a–h) Which might be responsible.

The C, H, N analysis data, ^{1}H NMR, and ^{13}C N-MR spectral data of all compounds are presented in Tables 7, 8 and 9 respectively.

The examination of elemental analytical data reveals that the elemental contents are consistence with the predicted structure shown in Scheme-1. The IR data also direct for assignment of the predicted structure. The final structure of all

compounds is confirmed by LC–MS. LC–MS of 3d and 4f compounds are 378 and 407 respectively.

REFERENCES

1. M.R. Shiradkar, K.K. Murahari, H.R. Gangadasu, T. Suresh, C.C. Kalyan, D. Panchal, R. Kaur, P. Burange, J. Ghogare, V. Mokale, M. Raut, *Bioorg Med. Chem.* **15**, 3997 (2007).
2. Y. Janin, *Bioorg. Med. Chem.* 15, 2479 (2007).
3. E. Gursoy, N. Guzeldemirci-Ulusoy, *Eur. J. Med. Chem.* **42**, 320 (2007).
4. M. R. Rao, K. Hart, N. Devanna and K. B. Chandrasekhar, *Asian J. Chem.* **20**, 1402 (2008).
5. K.B. Kaymakcıoglu, E.E. Oruc, S. Unsalan, F. Kandemirli, N. Shvets, S. Rollas, D. Anatholy, *Eur. J. Med. Chem.* **41**, 1253 (2006).
6. 6. R. Kalsi, M. Shrimali, T. N. Bhalla, J. P. Barthwal, *Indian J. Pharm.* Sci. **41**, 353 (2006).
7. S. Gemma, G. Kukreja, C. Fattorusso, M. Persico, M. Romano, M. Altarelli, L. Savini, G. Campiani, E. Fattorusso, N. Basilico, *Bioorg. Med. Chem. Lett.* **16**, 5384 (2006).
8. D. Sriram, P. Yogeeswari, K. Madhu, *Bioorg. Med. Chem. Lett.* **15**, 4502 (2006).
9. A. Nayyar, R. Jain, *Curr. Med. Chem.* **12**, 1873 (2006).
10. R.M. Fikry, N.A. Ismael, A.A. El-Bahnasawy, A. A. Sayed El-Ahl., Phosphorus Sulfur and Silicon and the related elements, **179**, 1227 (2006).
11. A. Walcourt, M. Loyevsky, D.B. Lovejoy, V.R. Gordeuk, D.R. Richardson, *Int. J. Biochem. Cell Biol.* **36**, 401 (2004).
12. M.G. Mamolo, V. Falagiani, D. Zampieri, L. Vio, E. Banfi , G. Scialino, *Farmaco*, **58**, 631 (2003).
13. N. Terzioglu, A. Gursoy, *Eur. J. Med. Chem.*, **38,** 781 (2003).
14. S.G. Kucukguzel, E.E. Oruc, S. Rollas, F. Sahin, A. Ozbek, *Eur. J. Med. Chem.* **37**, 197 (2002).
15. S. Rollas, N. Gulerman, H. Erdeniz, *Farmaco*, **57**, 171 (2002).
16. L.Q Al-Mawsawi, R. Dayam, L. Taheri, M. Witvrouw, Z. Debyser, N. Neamati, *Bioorg. Med. Chem. Lett.* **17,** 6472 (2007).
17. C. Plasencia, R. Daym, Q. Wang, J. Pinski, T. R. Jr. Burke, D. I. Quinn, N. Neamati, *Mol. Cancer Ther.* **4,** 1105 (2005).
18. H. Zhao, N. Neamati, S. Sunder, H. Hong, S. Wang; G. W. Milne, Y. Pommier, T. R. Burke Jr., *J. Med. Chem.* **40,** 937 (1997).
19. K.C. Asati, S.K. Srivastava, S.D. Srivastava, *Ind. J. Chem.*, **45 (B),** 526 (2006).
20. A. Bishnoi, K. Srivastava. C.K.M. Tripathi, *Ind. J.Chem.,* **45(B)**, 2136 (2006).

21. N.P. Shetgiri, A.D. Chitre, *Ind .J .Chem.* **45(B)**, 1308 (2006).

22. R. Jadav, S. Srivastava, S.D. Srivastava, *Chemistry(an Indian journa)l,* **1**, 95 (2003).

23. S. Srivastava, A. Jain, S. Srivastava, *J. Indian Chem.Soc.*, **83**, 1118 (2006).

24. K.M. Mistry, K.R. Desai, *E- Journal of Chem.*, **1**, 189 (2004).

25. H.S. Patel, H.J. Mistry, *Phosphorous, Sulfur and Silicon & Related Elements*, **179**, 1085 (2004).

26. J.J. Bhatt, B.R. Shah, N.C. Desai, *Ind .J. Chem.*, **33B,** 189 (1994).

СИНТЕЗ И БИОЛОГИЧНА АКТИВНОСТ НА 4-ХЛОРО-2-ХИДРОКСИ- N -(5-МЕТИЛЕНЕ-4-ОКСО-2-АРИЛ-ТИАЗОЛИДИН-3-ИЛ) БЕНЗАМИД

С. Махета[1], С. Дж. Пател[2]

[1]*Емкюър фармацетикалс, САЩ*
[2]*Юнити дай кем ООД, Сокхада, Кхамбхат-388620, Индия*

(Резюме)

Хидразидът на 4-хлоро-2-хидрокси бензоената киселина (1) претърпява лесна кондензация с ароматни алдехиди, за да се получат съответните арилиден хидразиди на 4-хлоро-2-хидрокси бензоената киселина (2a–h) с добри добиви. Циклокондензацията на съединения (2a–h) с тиогликолова киселина дава 4-хлоро-2-хидрокси-N (4-оксо-2-арил-тиазолидин-3-ил) бензамиди (3a–h). Тези съединения (3a–h) реагират с бензалдехид в присъствието на натриев етанолат с получаване на 4-хлоро-2-хидрокси-N (5-метилен-4-оксо-2-арил-тиазолидин-3-ил) бензамиди (4 a–h). Структурите на тези съединения са установени въз основа на аналитични и спектрални данни. Всички новосинтезирани съединения са оценени за тяхната антибактериална и противогъбична активност.

The identity and structure of free radicals in γ-irradiated amino acid derivatives

M. Aydin

Faculty of Education, Adiyaman University, TR 02030-Adiyaman, Turkey

Received July 29, 2010; accepted October 7, 2010

The technique of electron paramagnetic resonance spectroscopy was used to determine the identity and structure of free radicals produced at room temperature by γ-irradiated powders of some biologically important compounds, namely, N-acetyl-L-glutamine, glycine ethyl ester hydrochloride and L-threonine. The paramagnetic species observed in these compounds were identified as $H_2NCOCH_2CH_2\dot{C}(NHCOCH_3)COOH$, $\dot{C}H_2COOCH_2CH_3$ and $CH_3CH(OH)\dot{C}HCOOH$, respectively. The g values and the hyperfine structure constants of the unpaired electron with the environmental protons and the ^{14}N nucleus were determined. The free radicals were stable at room temperature for more than three months. Some spectroscopic properties and suggestions concerning the possible structure of the radicals were also discussed in this study.

Key words: EPR; Free Radicals; γ-Irradiation; Amino Acid Derivatives.

1. INTRODUCTION

Free radicals play an essential role in a variety of chemical and biological processes [1–3]. Electron paramagnetic resonance (EPR) is a highly sensitive spectroscopic technique for examining free radicals [4]. The EPR study of the radicals produced in organic compounds by X-ray and γ-ray irradiation has led to valuable information on the structures of various paramagnetic species [5–12]. The EPR spectrum of γ-irradiated powders of glycyl-L-glutamine has been investigated by Başkan at room temperature and at 150 K [13]. The radiation damage center was attributed to the $H_2NCOCH_2CH_2\dot{C}(NHCOCH_2NH_2)COOH$ radical. Furthermore, in the single crystal of N_α-acetyl-L-glutamine γ-irradiated at room temperature, the free radicals have been identified as $NH_2COCH_2CH_2\dot{C}(NHCOCH_3)COOH$ and $NH_2COCH_2CH_2CH(NHCOCH_3)\dot{C}\bar{O}OH$ [14]. The irradiated single crystals of glycine have been studied by several groups of workers [15-20]. The observed species in these studies were found to be

$NH_3^+\dot{C}HCO\bar{O}$ and $\dot{C}H_2COOH$.

N-acetyl-L-glutamine (NALG), glycine ethyl ester hydrochloride (GEHCl) and L-threonine (LT) are biologically very important amino acid derivatives which play an essential role in metabolic processes. To our knowledge, NALG, GEHCl and LT powders have not been investigated

at room temperature. Therefore it is the goal of this work to identify and check the stabilities of the radical species produced in these amino acid derivatives by the EPR technique.

2. EXPERIMENTAL

The samples used in this study were purchased from Aldrich. Powder samples of the compounds were irradiated with a ^{60}Co γ-ray source (Nordion-Canada model JS 9600) at a rate of 2 kGy/h for a total of 10 h at room temperature. For the EPR measurements of the samples quartz tubes were used. The paramagnetic species generated by γ-irradiation were studied in a Varian model X-band E-109C EPR spectrometer at room temperature. The modulation amplitude was below 5.10^{-2} mT and the microwave power was 2 mW. The g factors were found by comparison with a diphenylpicrylhydrazyl (DPPH) sample with $g = 2.0036$ [21, 22]. The spectrum simulations were made using McKelvey's programs [23].

3. RESULTS AND DISCUSSION

The NALG powder γ-irradiated at room temperature gives the spectrum shown in Fig. 1a. The line resolution of the spectrum is poor. Its thorough examination reveals that it consists of lines of approximate intensity ratio 1:1:3:3:4:4:3:3:1:1. This spectrum exhibits intensity distribution 1:3:4:3:1 because of two β-protons and a ^{14}N nucleus (I=1) with approximately equal coupling constants ($a_\beta = 1.68$ mT and $a_N = 1.46$ mT). Then each of these five lines is subdivided

* To whom all correspondence should be sent: E-mail: maydin@adiyaman.edu.tr
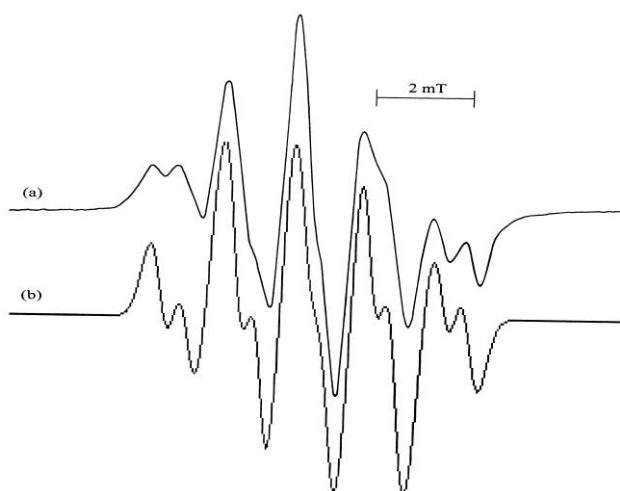
Fig.1. (a) The EPR spectrum of NALG powder γ-irradiated at room temperature, (b) simulation form of the spectrum using a_β = 1.68 mT, a_N = 1.46 mT, a_{NH} = 0.58 mT and linewidth 0.30 mT.
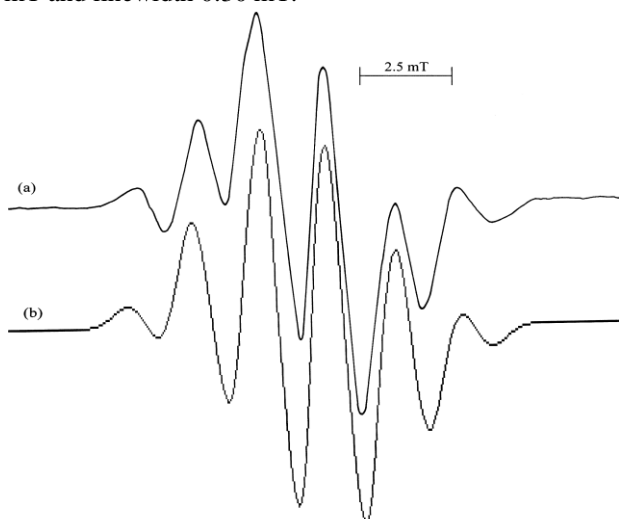
Fig.3. (a) The EPR spectrum of LT powder γ-irradiated at room temperature, (b) simulation form of the spectrum using $a_\alpha = a_{CH} = a_{CH3}$ = 1.80 mT and linewidth 0.58 mT.

into doublets owing to the proton near the adjacent ^{14}N nucleus which is of a splitting of 0.58 mT. According to these findings, the paramagnetic species can be identified as the $H_2NCOCH_2CH\dot{C}(NHCOCH_3)COOH$ radical. The measured g value of this radical is g = 2.0027 ± 0.0005. The spectrum simulated with the above given values agrees with the experiment (Fig.1b). The radical with the obtained hyperfine constants and g value is similar to the radicals observed in the γ-irradiated glycyl-L-glutamine, glycyl-L-glutamine monohydrate and alanyl-L-glutamine powders [13, 24, 25]. It can be stated that γ-irradiation produced free radicals in NALG by loss of the bond of hydrogen atom from the carbon atom bond to the HCOCH_3 and COOH group and the unpaired
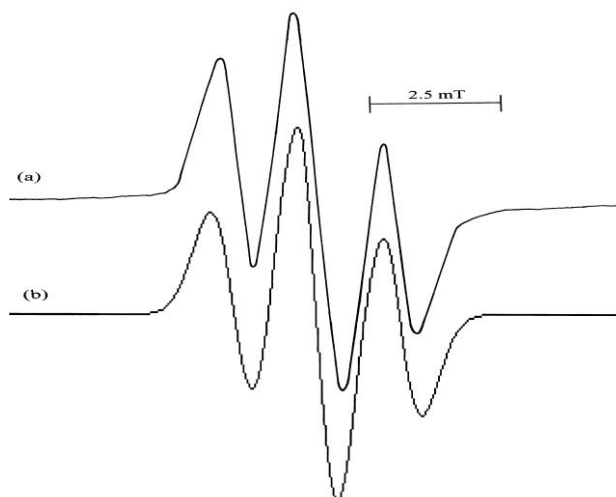
Fig.2. (a) The EPR spectrum of GEHCl powder γ-irradiated at room temperature, (b) simulation form of the spectrum using a_{CH2} = 1.78 mT, and linewidth 0.68 mT.

electron interacts with two β-protons, one NH proton and the ^{14}N nucleus.

The characteristic stable EPR spectrum of the γ-irradiated GEHCl is shown in Fig. 2a. The spectrum consists of three equally spaced (1.78 mT) lines with a relative intensity distribution of 1:2:1. This spectrum belongs to the $\dot{C}H_2COOCH_2CH_3$ radical, hence we suppose that the 1:2:1 ratio of the triplets is due to the interactions of two α-protons which are all magnetically equivalent. The g value of the radical is g = 2.0033 ± 0.0005. A simulation of the GEHCl spectrum is shown in Fig. 2b. A similar EPR spectrum was observed for the γ–irradiated glycine in an aqueous solution at 195 K [26]. The reported hyperfine coupling constant of the two α-protons is 2.10 mT. This value is similar to the hyperfine coupling constant value measured in this study. The measured EPR parameters of the irradiated polycrystalline glycine at room temperature are also in agreement with our results [27, 28]. The identity of the radicals in γ–irradiated glycine has been the object of much debate [15, 29, 30]. It is generally accepted that both $\dot{C}H(NH_2)COOH$ and $\dot{C}H_2COOH$ radicals are present at room temperature in γ–irradiated glycine [31]. According to these results, we can say that the $\dot{C}H_2COOCH_2CH_3$ radical is obtained by the removal of a NH_2 group from the central carbon atom.

Fig.3a presents the EPR spectrum of LT powder γ–irradiated and recorded at room temperature. The spectrum consists of six lines with intensity distribution 1:6:10:10:6:1 with 1.80 mT spacing. The unpaired electron interacts with one α-proton, one CH proton and three CH_3 protons, which are all

magnetically equivalent. According to these results, the radical should be $CH_3CH(OH)\dot{C}HCOOH$. The determined g value is $g = 2.0035 \pm 0.0005$. A spectrum simulated with these values agrees with the experiment and is shown in Fig. 3b. A similar radical was observed for the irradiated single crystal of L-threonine at room temperature and therefore the above interpretations are valid for this compound as well [32]. We can state that this radical produced by γ–irradiation is due to the breakage of a C-NH_2 bond leading to unpaired electron spatially extending through CH_3 and CH groups.

4. CONCLUSION

The γ-irradiated NALG, GEHCl and LT powder samples indicated the inducement of the $H_2NCOCH_2CH_2\dot{C}(NHCOCH_3)COOH$, $\dot{C}H_2COOCH_2CH_3$ and $CH_3CH(OH)\dot{C}HCOOH$ stable radicals, respectively. The identity and the structure of the radicals were determined. It was observed that the EPR parameters of the radicals discussed here are consistent with the literature data.

REFERENCES

1. W. A. Pryor, Ann. *Rev. Physiol.*, **48**, 657 (1986).
2. E. T. Denisov, I. V. Khudyakov, *Chem. Rev.*, **87**, 1313 (1987).
3. D. J. Kieber, N. V. Blough, *Free Radic. Res. Commun.,* **10,** 109 (1990).
4. E. Bozkurt, İ. Kartal, F. Köksal, Y. S. Bozkurt, *Radiat. Phys. Chem.*, **77**, 1005 (2008).
5. W. C. Lin, C. A. Mcdowell, *Can. J. Chem.,* **41**, 9 (1963).
6. E. Sagstuen, E. O. Hole, S. R. Haugedal, W. H. Nelson, *J. Phys. Chem. A*, **101**, 9763 (1997).
7. N. D. Yordanov, R. Mladenova, *Spectrochim. Acta A*, **60**, 1395 (2004).
8. R. Mladenova, N. D. Yordanov, *Bulg. Chem. Commun.*, **39**, 128 (2007).
9. M. Aydın, M. H. Başkan, Y. E. Osmanoğlu, *Braz. J. Phys.*, **39**, 583 (2009).
10. N. D. Yordanov, O. Lagunov, K. Dimov, *Radiat. Phys. Chem.*, **78**, 277 (2009).
11. Y. Karakirova, N. D. Yordanov, *Radiat. Meas.*, **45**, 831 (2010).
12. M. Aydın, Ş. Osmanoğlu, M. H. Başkan, I. Y. Dicle, *J. Mol. Struct.*, **975**, 30 (2010).
13. M. H. Başkan, *Radiat. Eff. Defect. Solids*, **163**, 35 (2008).
14. F. Köksal, Ş. Osmanoğlu, I. Kartal, F. Ucun, *Radiat. Phys. Chem.*, **49**, 537 (1997).
15. J. R. Morton, *J. Am. Chem. Soc.*, **86**, 2325 (1964).
16. M. A. Collins, D. H. Whiffen, *Mol. Phys.*, **10**, 317 (1966).
17. H. C. Box, H. G. Freund, E. E. Budzinski, *J. Am. Chem. Soc.*, **88**, 658 (1966).
18. A. Hedberg, A. Ehrenberg, *J. Chem. Phys.*, **48**, 4822 (1968).
19. J. Sinclair, *J. Chem. Phys.*, **55**, 245 (1971).
20. A. Sanderud, E. Sagstuen, *J. Phys. Chem. B*, **102**, 9353 (1998).
21. N. D. Yordanov, A. Christova, *Appl. Mag. Res.*, **6**, 341 (1994).
22. N. D. Yordanov, *Appl. Mag. Res.*, **10**, 339 (1996).
23. R. D. McKelvey, *J. Chem. Educ.*, **64**, 497 (1987).
24. M. Aydın, Y. E. Osmanoğlu, M.H. Başkan, *Radiat. Eff. Defects Solids*, **163**, 47 (2008).
25. M. Aydın, M. H. Başkan, S. Yakar, F. Ş. Ulak, M. Aydınol, B. Aydınol, M. Büyüm, *Radiat. Eff. Defect. Solids*, **163**, 41 (2008).
26. S. J. Hong, D. E. Holmes, L. H. Piette, J. *Korean Chem. Soc.*, **15**, 256 (1971).
27. A. Müller, P. E. Schambra, E. Pietsch, *Int. J. Rad. Biol.*, **7**, 587 (1964).
28. W. Snipes, J. Schmidt, *Radiat. Res.*, **29**, 194 (1966).
29. D. K. Ghosh, D. H. Whiffen, *J. Chem. Soc.*, **373**, 1869 (1960).
30. R. F. Weiner, W. S. Koski, *J. Am. Chem. Soc.*, **85**, 873 (1963).
31. W. A. Armstrong, W. G. Huımphreys, *Can. J. Chem.*, **45**, 2589 (1967).
32. G. R. Kumar, S. G. Roj, *Adv. Mater. Sci. Eng.*, **49**, 1 (2009).

ИДЕНТИЧНОСТ И СТРУКТУРА НА СВОБОДНИ РАДИКАЛИ В ГАМА-ОБЛЪЧЕНИ ПРОИЗВОДНИ НА АМИНО КИСЕЛИНИ

М. Айдин

Факултет по педагогика, Университет Адияман, TR 02030- Адияман, Турция

(Резюме)

Електронно-парамагнитна резонансна спектроскопия е използвана за определяне на идентичността и структурата на свободните радикали, произведени при стайна температура от гама-облъчени прахове на някои биологично важни съединения, а именно, N-ацетил-L-глутамин, глицин етилов естер хидрохлорид и L-треонин. Парамагнитните частици, наблюдавани в тези съединения са идентифицирани съответно като $H_2NCOCH_2CH_2\dot{C}(NHCOCH_3)COOH$, $\dot{C}H_2COOCH_2CH_3$ и $CH_3CH(OH)\dot{C}HCOOH$. Определени са g-стойностите и константите на свръхфина структура на несдвоения електрон с обкръжаващите протони и ядрото ^{14}N. Свободните радикали са стабилни при стайна температура за повече от три месеца. Някои спектроскопски свойства и предложения относно възможната структура на радикалите също са обсъдени в това изследване.

A modified reaction for the preparation of amidoalkyl naphthols using silica-supported Preyssler nano particles

M.M. Heravi [a], N. Tavakoli-Hoseini [b], F.F. Bamoharram [b]

[a] *Department of Chemistry, School of Sciences, Azzahra University, Vanak, Tehran, Iran*

[b] *Department of Chemistry, Mashhad Branch, Islamic Azad University, Mashhad, Iran.*

An improved green method for the synthesis of amidoalkyl naphthols through one-pot multi-component reaction of aryl aldehyde, β-naphthol and acetamide or acetonitrile (Ritter type reaction) in the presence of silica-supported Preyssler nano particles as effective catalyst is described.

INTRODUCTION

One-pot multi-component reactions (MCRs) by virtue of their convergence, productivity, facile execution and high yield have attracted considerable attention in recent years [1]. There has been tremendous development in three or four component reactions, specially the Bignelli [2], Passerini [3], Ugi [4] and Mannich [5] reactions, which have further led to the renaissance of MCRs. Nevertheless, great efforts have been and still are being made to find new MCRs and improve the already known MCRs. One such reaction is the synthesis of amidoalkyl naphthols. These compounds are generally synthesized in a three-component reaction of aldehydes, urea or amide and β-naphthol in the presence of various catalysts such as montmorillonite K_{10} [6], $Ce(SO_4)_2$ [7], iodine [8], $K_5CoW_{12}O_{40}.3H_2O$ [9], p-TSA [10], $HClO_4$-SiO_2 [11], sulfamic acid [12] and silica-sulfuric acid [13]. Also, recently, Shaterian and co-workers have reported the synthesis of these compounds via a Ritter type reaction using one-pot MCR of aryl aldehydes, β-naphthol and acetonitrile in the presence of $FeCl_3.SiO_2$ as a catalyst [14].

The catalysts based on heteropolyacids have many advantages over liquid acid catalysts. They are not corrosive, environmentally benign, presenting fewer disposal problems. Solid heteropolyacids have attracted much attention in organic synthesis owing to easy work-up procedures, easy filtration, and minimization of cost and waste generation due to reuse and recycling of the catalysts [15]. There have been many attempts to optimize these catalysts. Recently, Keggin nano catalysts have been synthesized [16]. In our attempt to use heteropolyacids as catalysts in organic reactions, we reported that Preyssler type heteropolyacids, $H_{14}[NaP_5W_{30}O_{110}]$, show strong catalytic action [17]. Due to the unique properties of nano particles along with their potential applications in different fields [18], we immobilized $H_{14}[NaP_5W_{30}O_{110}]$ into the SiO_2 nano particles [19] and investigated the catalytic behavior of this new catalyst.

Recently, we submitted a paper on the multi-component synthesis of amidoalkyl naphthols using Brønsted-acidic ionic liquids to the Synthetic Communication Journal. In continuation of our previous works on the applications of reusable acid catalysts in the synthesis of organic compounds [20–23] here we report an improved green method for the synthesis of amidoalkyl naphthols through one-pot multi-component reaction of aryl aldehyde, β-naphthol and acetamide under solvent-free conditions (Method A) or acetonitrile via a Ritter type reaction (Method B) in the presence of silica-supported Preyssler nano particles as a catalyst (Scheme 1).

RESULTS AND DISCUSSION

First, the three-component reaction of aryl aldehyde, β-naphthol, and acetamide was performed in the presence of silica-supported Preyssler nano particles as a catalyst under solvent-free conditions. In all cases, aromatic aldehydes

---

*To whom all correspondence should be sent:
E-mail: : mmh1331@yahoo.com
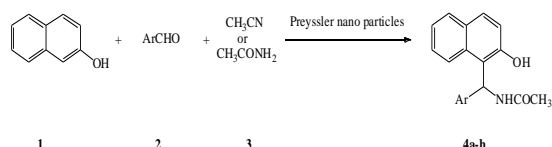
Scheme 1

reacted successfully and gave the products in high yields. It was shown that aromatic aldehydes with electron-withdrawing groups reacted faster than those with electron-releasing groups, as expected (Table 1, Method A).

Next, the synthesis of amidoalkyl naphthols through a Ritter type reaction was investigated. Therefore, a mixture of aryl aldehyde, β-naphthol, and acetonitrile (both reactant and solvent) was heated under reflux in the presence of silica-supported Preyssler nano particles as a catalyst. In all cases, aromatic aldehydes with either electron-donating or electron-withdrawing groups gave the desired products via a Ritter type reaction (Table 1, Method B).

Table 1. Preyssler nano-particles catalyzed synthesis of amidoalkyl naphthols [a]

| Entry	Ar	Method A	Method B	M.P. (°C)	
		time (min)/yield (%)[b]	time (h)/yield (%)[b]	Found (Method A)	Reported
4a	C_6H_5	5/95	8/87	241-242	242-243 [11]
4b	4-ClC_6H_4	4/96	7/90	228-229	230-232 [11]
4c	4-FC_6H_4	4/95	7/88	207-209	210-212 [11]
4d	4-MeC_6H_4	7/88	8/87	220-222	222-223 [14]
4e	4-$MeOC_6H_4$	8/84	8/86	184-185	183-185 [14]
4f	2-$O_2NC_6H_4$	5/91	9/76	180-182	179-182 [14]
4g	3-$O_2NC_6H_4$	4/93	7/91	213-215	212-214 [11]
4h	4-$O_2NC_6H_4$	3/96	7/92	246-248	248-250 [14]

[a] All products were characterized by ^{1}HNMR and IR spectral data and comparison of their melting points with those of authentic samples.
[b] Isolated yields

Although we did not investigate the reaction mechanism, based on the literature report [14], a plausible mechanism for these methods may be adopted, as depicted in scheme 2. As reported in the literature [8–10], the reaction of β-naphthol with aromatic aldehydes in the presence of an acid catalyst is known to give ortho-quinone methides (o – QMs) **I**. The same o – QMs generated *in situ* have reacted either with acetamide or with acetonitrile via intermediate **II** followed by hydrolysis in a Ritter type reaction to give the desired amidoalkyl naphthols.

In conclusion, we have reported herein a new efficient catalyst for the synthesis of amidoalkyl

naphthols through one-pot MCR of aryl aldehyde, β-naphthol and acetamide under solvent-free conditions (Method A) or acetonitrile via a Ritter type reaction (Method B) in the presence of silica-supported Preyssler nano particles as a catalyst. The catalyst can be reused after a simple work-up, a gradual decline of its activity being observed. High yields, shorter reaction times, simplicity of operation and easy work-up are some of the advantages of this protocol.
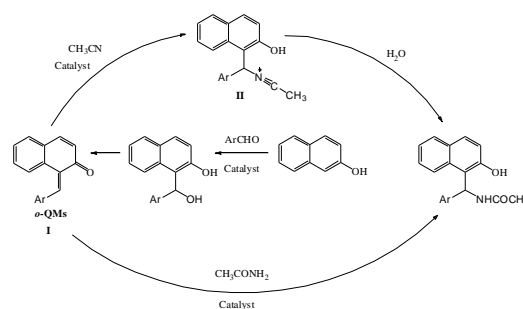
Scheme 2

EXPERIMENTAL

All compounds were known, and their physical and spectroscopic data were compared with those of authentic samples and found to be identical. Melting points were recorded on an electrothermal type 9100 melting point apparatus. The IR spectra were obtained on a 4300 Shimadzu spectrophotometer in KBr disks. The ^{1}H NMR (500 MHz) spectra were recorded on a Bruker DRX500 spectrometer.

Preparation of amidoalkyl naphthols. General procedure.

Method A

A mixture of an aromatic aldehyde (1 mmol), β-naphthol (1 mmol), and acetamide (1.3 mmol) was heated at 90 °C in the presence of silica-supported Preyssler nano particles (0.03 mmol) for the indicated time (Table 1). After completion of the reaction, boiling ethanol was added to the reaction mixture. The catalyst was filtered off and the filtrate was then concentrated and cooled to room temperature. The precipitate was filtered off and recrystallized from aqueous ethanol to give pure amidoalkyl naphthols (Table 1).

Method B

A mixture of an aromatic aldehyde (1 mmol), β-naphthol (1 mmol) and acetonitrile (5 ml) (both reactant and solvent) was heated under reflux in the presence of silica-supported Preyssler nano

particles (0.03 mmol) for the indicated time (Table 1). The reaction progress was monitored by TLC. After completion of the reaction, the reaction mixture was filtered off. The filtrate was then concentrated to afford a solid product, which was purified by re-crystallization from aqueous ethanol (Table 1).

Table 2. Comparison of the efficiency of Preyssler nano particles (fresh and reused) in the synthesis of amidoalkyl naphthols by method A

Entry	Ar	Yield[a], %		
		First use	Second use	Third use
1	C_6H_5	95	93	92
2	$4\text{-}ClC_6H_4$	96	93	91
3	$4\text{-}MeC_6H_4$	88	87	85

[a]Isolated yields

Selected ^1H NMR & IR data

Compound 4a: ^1H NMR (500 MHz, DMSO–d_6, δppm): 1.98 (s, 3H, CH_3), 7.10–7.40 (m, 9H), 7.76 (d, 1H, J = 8.8 Hz), 7.80 (d, 1H, J = 8.0 Hz), 7.84 (br., 1H, NH), 8.43 (d, 1H, J = 8.3 Hz), 9.98 (s, 1H, OH); IR (KBr disc): υ 3400 (NH), 3246 (OH), 1640 cm^{-1} (C=O).

Compound 4b: ^1H NMR (500 MHz, DMSO-d_6, δppm): 1.98 (s, 3H, CH_3), 7.09 (d, 1H, J = 8.1 Hz), 7.15 (d, 2H, J = 8.3 Hz), 7.21 (d, 1H, J = 8.8 Hz), 7.27 (t, 1H, J = 7.3 Hz), 7.30 (d, 2H, J = 8.5 Hz), 7.38 (t, 1H, J = 7.3 Hz), 7.75-7.85 (m, 3H), 8.46 (d, 1H, J = 8.1 Hz), 10.03 (s br., 1H, OH); IR (KBr disc): υ 3392 (NH), 3065 (OH), 1638 cm^{-1} (C=O).

Compound 4g: ^1H NMR (500 MHz, DMSO-d_6, δppm): 2.02 (s, 3H, CH_3), 7.18 (d, 1H, J = 8.0 Hz), 7.22 (d, 1H, J = 8.8 Hz), 7.29 (t, 1H, J = 7.3 Hz), 7.41 (t, 1H, J = 7.4 Hz), 7.50–7.60 (m, 2H), 7.80–7.85 (m, 2H), 7.86 (br, 1H, NH), 8.01 (s, 1H), 8.03–8.07 (m, 1H), 8.61 (d, 1H, J = 8.0 Hz), 10.12 (s, 1H, OH); IR (KBr disc): υ 3375 (NH), 3223 (OH), 1648 (CO), 1524 & 1350 cm^{-1} (NO_2).

Compound 4h: ^1H NMR (500 MHz, DMSO–d_6, δppm): 2.02 (s, 3H, CH_3), 7.18 (d, 1H, J = 7.8 Hz), 7.22 (d, 1H, J = 8.8 Hz), 7.28 (t, 1H, J = 7.3 Hz), 7.35-7.45 (m, 3H), 7.82 (t, 3H, J = 9.3 Hz), 8.13 (d, 2H, J = 8.6 Hz), 8.57 (d, 1H, J = 7.8 Hz), 10.11 (s, 1H, OH); IR (KBr disc): υ 3391 (NH), 3051 (OH), 1640 (C=O), 1523 & 1351 cm^{-1} (NO_2).

Recycling of the catalyst

The catalyst recovered by filtration in method A was dried and reused for three times in reactions. The obtained results are summarized in Table 2. As it is shown, there is no significant loss of activity in using a recycled catalyst in this reaction.

REFERENCES

1. (a) For special issue in MCRs, see *Tetrahedron,* **61**, 11299 (2005); (b) D. J. Ramon, M. Yus, *Angew. Chem., Int. Ed.,* **44**, 1602 (2005).
2. (a) C. O. Kappe, *Eur. J. Med. Chem.,* **35**, 1043 (2000); (b) D. Dallinger, A. Stadler, C. O. Kappe, *Pure Appl. Chem.,* **76**, 1017 (2004).
3. P. R. Krishna, G. Dayaker, P. V. Narasimha Reddy, *Tetrahedron Lett.,* **47**, 5977 (2006).
4. (a) A. Domling, I. Ugi, *Angew. Chem., Int. Ed.,* **39**, 3168 (2000); (b) I. Ugi, B. Werner, A. Domling, *Molecules,* **8**, 53 (2003).
5. M. Arend, B. Westermann, N. Risch, *Angew. Chem., Int. Ed.,* **37**, 1044 (1998).
6. S. Kantevari, S. V. N. Vuppalapati, , L. Nagarapu, *Catal. Commun.,* **8**, 1857 (2007).
7. N. P. Selvam, P. T. Perumal, *Tetrahedron Lett.,* **47**, 7481 (2006).
8. B. Das, K. Laxminarayana, B. Ravikanth, B. R. Rao, *J. Mol. Catal. A: Chem.,* **261**, 180 (2007).
9. L. Nagarapu, M. Baseeruddin, S. Apuri, S. Kantevari, *Catal. Commun.,* **8**, 1729 (2007).
10. M. M. Khodaei, A. R. Khosropour, H. Moghanian, *Synlett.,* 916 (2006).
11. G. Mahdavinia, M. A. Bigdeli, M. M. Heravi, *Chin. Chem. Lett.,* **19**, 1171 (2008).
12. S. B. Patil, P. R. Singh, M. P. Surpur, S. D. Samant, *Ultrason. Sonochem.,* **14**, 515 (2007).
13. G. Srihari, M. Nagaraju, M. M. Murthy, *Helv. Chim. Acta,* **90**, 1497 (2007).
14. H. R. Shaterian, H. Yarahmadi, *Tetrahedron Lett.,* **49**, 1297 (2008).
15. M. M. Heravi, F. Derikvand, A. Haeri, H. A. Oskoie, F. F. Bamoharram, *Synth. Commun.,* **38**, 135 (2008).
16. D. P. Sawant, A. Vinu, N. E. Jacob, F. Lefebvre, S. B. Halligudi, *J. Catal.,* **235**, (2005) 341.
17. M. M. Heravi, S. Sajadi, H. A. Oskooie, R. Hekmat Shoar, F. F. Bamoharram, *Molecules,* **12**, 255 (2007).
18. C. R. Gorla, N. W. Emanetoglu, S. Liang, W. E. Mago, Y. Lu, M. Wraback, H. Shen, *J. Appl. Phys.,* **85**, 2595 (1999).
19. F. F. Bamoharram, M. M. Heravi, M. Roushani, M. R. Toosi, L. Jodeyr, *Green. Chem. Lett and Reviews.,* **2**, 35 (2009).
20. M. M. Heravi, F. K. Behbahani, H. A. Oskooie, F. F. Bamoharram, *Chin. J. Chem.,* **25**, 2150 (2008).
21. M. M. Heravi, Y. S. Beheshtiha, Z. Pirnia, S. Sadjadi, M. Adibi , *Syn. Commun.,* **39** 3663 (2009).
22. M. M. Heravi, F. K. Behbahani, Z. Daroogheha, H. A. Oskooie , *Russ. J. Org. Chem.,* **45**, 1108 (2009).
23. M. M. Heravi, S. Sajadi, S. Sajadi, H. A. Oskooie, R. Hekmat Shoar, F. F. Bamoharram, *S. Afr. J. Chem.,* **62**, 1 (2009).

МОДИФИЦИРАНА РЕАКЦИЯ ЗА ПОЛУЧАВАНЕ НА АМИДОАЛКИЛ НАФТОЛИ С ПОМОЩТА НА ПРАЙСЛЕР НАНОЧАСТИЦИ ВЪРХУ СИЛИЦИЕВ ДИОКСИД

М. М. Херави[a], Н. Таваколи-Хосейни[b], Ф. Ф. Бамохарам[b]

[a] *Катедра по химия, Училище за науки, Университет Азахра, Ванак, Техеран, Иран*
[b] *Катедра по химия, Машхад клон, Ислямски университет Азад, Машхад, Иран.*

(Резюме)

Описан е един подобрен „зелен" метод за синтез на амидоалкил нафтоли чрез „one-pot" многокомпонентна реакция на арил алдехид, β -нафтол и ацетамид или ацетонитрил (реакция тип Ritter) в присъствието на Прайслер наночастици върху силициев диоксид, като ефективен катализатор.

Mass transfer behaviour of a new liquid-liquid rotating screen disc extractor

A.S. Shehata, A.H. Elshazly[*], A.A. Zaatout, G.H. Sedahmed

Chemical Engineering Department, Faculty of Engineering, Alexandria University, Alexandria, Egypt

The mass transfer behaviour of a rotating mesh disc contactor was studied by measuring the rate of mass transfer of acetic acid extraction from toluene solution by water. Variables studied were geometry parameters of the screen disc such as mesh number and wire diameter, rotation speed, physical properties of the solution, axial flow velocity and effect of the number of closely packed screens per disc. For a single rotating screen disc contactor the rate of mass transfer was expressed by the equation:

$$Sh_m = 132.63\, Sc^{0.33}\, \mathrm{Re}_S^{0.25}\, \mathrm{Re}_F^{0.3} \left(\frac{r_h}{d_w} \right)^{-1.38}$$

For rotating multi-screen discs, the mass transfer coefficient decreases by increasing the number of closely packed screens per disc. A comparison between the mass transfer behaviour of a rotating screen disc and a rotating solid disc contactor (RDC) revealed that for a given set of conditions the rate of mass transfer at the rotating screen contactor is higher than that of the rotating disc contactor by a factor of 13.8 – 28.4 depending on the operating conditions. Mechanical power consumption measurements showed that the higher the power consumption, the higher the mass transfer coefficient. Practical applications of the proposed extractor in fields such as pharmaceutical industry, hydrometallurgy, petroleum industry and water treatment were noted.

Key words: Mass transfer, rotating screen disc, solvent extraction, rotating fixed bed.

1. INTRODUCTION

Rotary agitated extraction columns such as the rotating disc contactor (RDC) are more efficient and possess better operational flexibility than conventional sieve plate, packed and spray columns; these advantages have led to the wide use of the RDC in the petroleum industry for furfural and sulfur dioxide extraction, propane deasphalting, solfolane extraction and caprolactum purification [1]. Since its invention by Reman [1, 2] in 1955, a lot of work has been done on various design and operational aspects of the RDC [1–12] such as (i)-dispersed phase holdup along with drop size, which is necessary to calculate the interfacial area per unit volume; (ii)-slip velocity, which is required to estimate the mass transfer coefficient; (iii)-rate of mass transfer and axial dispersion coefficient required to correct the plug flow design. Modified versions of the RDC such as the asymmetric rotating disc extractor (ARD) [13–15], the open turbine rotating disc contactor (OTRDC) [16-19] and the rotating perforated disc contactor (RPDC) [20–26] have been developed. Wang *et al.* [21] demonstrated the superior performance of the modified rotating disc contactor over the traditional RDC. On the other hand, other authors [20] endeavored to expand the application of the RDC in extracting a variety of products such as cutinase [22], bovine serum albumin [23, 24] and trypsin [25]. Cavalcanti *et al.* [26] evaluated the performance of a perforated rotating disc contactor in extracting α-toxin from the fermented broth of *Clostridium perfringens* Type A by an aqueous two-phase system of polyethylene glycol–phosphate salts.

The aim of the present work was to explore the possibility of using rotating horizontal screen discs instead of rotating solid flat discs to make advantage of the high turbulence promoting ability of the screen in order to enhance the rate of mass transfer during extraction. To this end the rate of mass transfer of extraction of acetic acid from toluene (dispersed phase) by water (continuous phase) was chosen, as it has been widely used by different authors to evaluate the performance of extraction equipments. Previous studies on the use of screens to enhance the rate of mass transfer were limited to liquid-solid mass transfer [27–29].

2. EXPERIMENTAL SETUP AND PROCEDURE

2.1. Experimental setup

The apparatus (Figure 1) used in the present work consisted of a stainless steel cylindrical column agitated by rotating horizontal screen discs

---
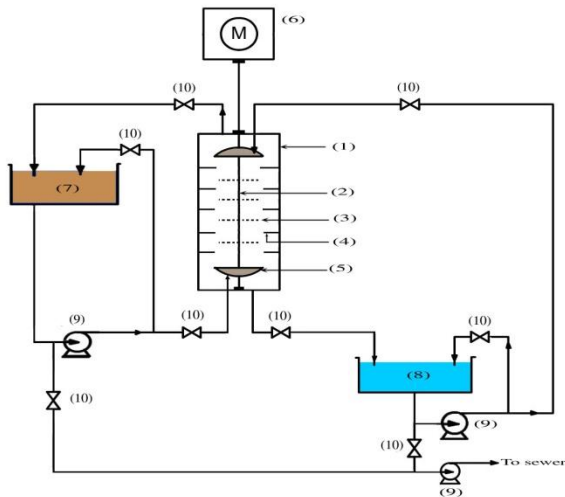
Fig. 1. Experimental setup. 1 - Agitated column; 2 - Rotating shaft; 3 - Rotating screen; 4 - Stator ring; 5 - Liquid distributor; 6 - Variable speed motor; 7 - Light phase storage tank; 8 - Heavy phase storage tank; 9 - Centrifugal pump; 10 - Control valve.
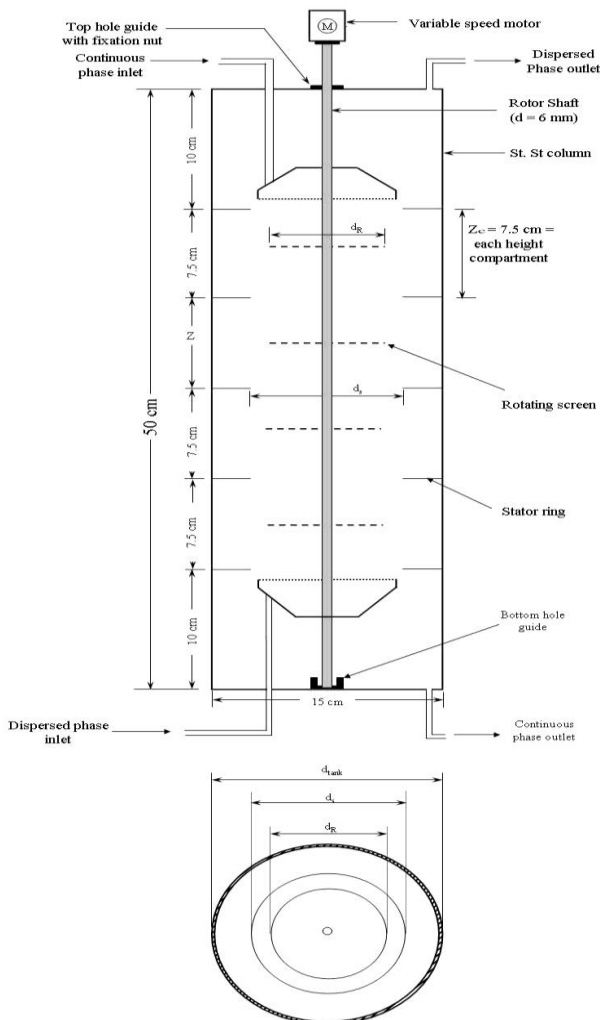
Fig. 2. Cross sectional view of the column

connected to a stainless steel shaft and driven by a digital D.C. (⅓ hp) motor, two glass storage tanks for both heavy phase (water) and light phase

(toluene + acetic acid) and two stainless steel centrifugal pumps for driving liquids through the column. The stainless steel column has dimensions of 15 cm diameter, 50 cm height and 1 mm wall thickness. The column height was divided into four compartments formed by a series of stator rings connected to the column walls with rotating screens centered in each compartment. The dimensions of the column used in the present work conform to the standard dimensions [30] usually employed in designing extraction columns, column dimensions are related to column diameter (d_T) as follows:

Rotor screen diameter, d_R:

$$d_R = 0.5\,(d_T) \qquad (1)$$

Stator ring opening, d_S:

$$d_S = 0.67\,(d_T) \qquad (2)$$

Compartment height, Z_c:

$$Z_c = (0.12 - 0.5)\,(d_T) \qquad (3)$$

Column geometry factor G_f

$$G_f = \left[\left(\frac{Z_c}{d_R} \right)^{0.9} \left(\frac{d_s}{d_R} \right)^{2.1} \left(\frac{d_R}{d_T} \right)^{2.4} \right] \qquad (4)$$

In the present study, Z_c was equal to 0.5 d_T.

Based on the above equations and on the typical preferred ratios of various internal dimensions used by other authors [31], the dimensions of the column internals were selected for the rotating screen extractor column used in the present work as illustrated on Figure 2. The column was fitted with two flanged ends. The stator rings were held in position by welding to the inner column wall and they were placed longitudinally along the inner wall. The stator rings and the rotor screens were made of stainless steel sheet of 2 mm thickness. A stainless steel central shaft of 6 mm diameter holding the rotating screens was mounted through two holes to a guide connected to the lower and upper flanges, and it passes through a copper knob welded to the upper flange in order to support the shaft and prevent vibration during the operation. In addition, the nut was provided with a rubber gasket to prevent solution leakage during rotation of the shaft. The column end cover plates were provided with the necessary pipe connections for the inlet and outlet of the dispersed and continuous phase solutions. Each phase was introduced into the column through a distributor close to the first stator ring from the respective column ends. The exit pipes were flushed with the cover plates on the inside of the column as shown in Figure 2. Each flow circuit of both heavy and light phase consisted

of a 20 L glass storage tank and an ⅓ hp copper centrifugal pump which circulated the solution between the agitated column and the storage tank. The flow rates of both feed and solvent were adjusted by means of a bypass line and a plastic needle valve and were measured by collecting a definite volume of the solution in a definite time using a graduated cylinder and a stopwatch.

The system toluene – acetic acid – water was chosen for this work not only for the availability of materials, but for the availability of literature data on the system and the method of analysis. Toluene

Table 1. Physical properties of the feed solutions used in the present study at 25°C

$C \times 10^3$ mole/cm³	P g/cm³	$\mu \times 10^2$ g/cm.s	$\upsilon \times 10^2$ cm²/s	$D \times 10^5$ cm²/s	$Sc = \dfrac{\upsilon}{D}$
0.1	0.861	0.56	0.6504	2.1	309
0.2	0.862	0.57	0.6613	2.06	320
0.3	0.863	0.58	0.6721	2.03	330
0.4	0.865	0.60	0.6936	1.96	354

was nitration grade with a boiling range of 106 – 110ºC. Acetic acid was A.R. grade, and distilled water was used as a solvent and in preparing all solutions. 10 L of both feed (toluene – acetic acid solution) and solvent (water) were used in each run. The concentrations and the physical properties of the different feed solutions are given in Table 1 at 25ºC.

2.2. Procedure

At the start of each run, the column was first filled with the heavy phase (water) and set at the desired flow rate, and then the speed of the rotor shaft was adjusted to the desired value, which ranged from 350 rpm to 1250 rpm. The light phase (toluene – acetic acid solution) was then introduced at the bottom end of the column and the flow rate was set at the desired value. Four different concentrations of acetic acid in toluene were used: 0.1, 0.2, 0.3 and 0.4 M. The rate of transfer of acetic acid from the organic to the aqueous phase was followed by withdrawing samples of 5 cm³ from the aqueous phase (water) tank at 1 minute intervals for analysis by titrating against 0.1 N fresh sodium hydroxide solution using phenolphthalein as indicator. In all experiments, extraction took place from the toluene to the water and toluene was the dispersed phase.

All experiments were carried out at 25 ± 1ºC. Density and viscosity measurements of the solutions were performed using a density bottle and an Ostwald viscometer, respectively. Acetic acid diffusivity in toluene was obtained from the literature [32, 33] and was corrected for the change in viscosity using the Stokes – Einstein correlation:

$$\frac{D\mu}{T} = \text{constant} \ [\text{g.cm.s}^{-2}.\text{K}^{-1}] \ (5)$$

where: D is the diffusivity of acetic acid, (cm²/s), μ is the solution viscosity, (g/cm.s) and T is the absolute temperature of the solution, (K)

Specifications of the screens used are shown in Table 2 where the screen specific area was calculated in terms of the wire diameter (d_w) and mesh number (N_m) using the method of Armour and Connon [34] as shown below.

Let (a) be the total screen surface area per total

Table 2. Specification of the screens used in the present study

Item	Screen geometry				
1	Mesh number (hole/in.)	10	14	18	22
2	Wire diameter, d_w (cm)	0.071	0.049	0.04	0.035
3	Screen thickness (cm)	0.142	0.098	0.08	0.07
4	Specific area (cm²/cm³)	12.842	17.936	23.14	28.433
5	Screen porosity, ε	0.772	0.78	0.768	0.751

volume of one screen (cm²/cm³), then the value of (a) can be calculated from the equation:

$$a = \pi L N_m^2 \qquad (6)$$

where:

$$L = \sqrt{\frac{1}{N_m^2} + d_w^2}$$

$$(7)$$

d_w = wire diameter, (cm)
N_m = mesh number (number of wires/cm)
The total screen area A_S is given by:

$$A_S = a \, n \, v_s \qquad (8)$$

where: v_s is the volume of a single screen, n is the number of screens per array. In calculating the volume of the screen, the thickness is taken as twice the wire diameter ($2d_w$). In addition, the screen porosity can be calculated from the equation:

$$\varepsilon = 1 - \frac{\pi L N_m^2 d_w}{4} \qquad (9)$$

In the present study five rotation speeds (350, 500, 750, 1000, 1250 r.p.m), screens of mesh number (10, 14, 18, 22 wire/in) were used; the number of closely packed screens per rotating disc was (1, 2, 3, 4, 5, screens/array), the initial concentrations of acetic acid in toluene were (0.1, 0.2, 0.3, 0.4 M) and five flow rates of the heavy phase (water) (79, 146, 174, 205, and 237 cm/s) were used. Mechanical power consumed in rotating the screens was measured experimentally under different conditions by means of a wattmeter. To compare between the performance of the present

rotating screen contactor (RSC) and the rotating disc contactor (RDC), experiments were carried out using a flat disc instead of a screen under different conditions.

3. RESULTS AND DISCUSSION

3.1. Mass Transfer at a Rotating Single Screen:

The volumetric mass transfer coefficient (KA) of the extraction of acetic acid from toluene with water in a batch rotating single screen contactor (Figure 1) was determined under different conditions: different screen rotation speed (r.p.m), different water flow rate (heavy continuous phase), different initial acetic acid concentration in toluene (light dispersed phase) and different mesh number of the rotating screen using the equation:

$$-\frac{dC}{dt} = \frac{KA}{V_s}(C_e - C) \qquad (10)$$

which upon integration yields:

$$\ln\frac{C_o - C_e}{C_e - C} = \left(\frac{KA}{V_s}\right)t \qquad (11)$$

where: C_o, C_e and C are the initial, equilibrium and current concentration of acetic acid in toluene, (mol/cm^3); K is the mass transfer coefficient, (cm/s); V_s is the volume of toluene, (cm^3) and A is the area of mass transfer, (cm^2). For simplicity, equation 11 can be written as:

$$\ln\frac{C_o - C_e}{C_e - C} = \left(\frac{K'}{V_s}\right)t \qquad (12)$$

where: $K' = KA$.

The volumetric mass transfer coefficient K' was calculated from the slope of the straight line obtained by plotting $\ln\dfrac{C_o - C_e}{C_e - C}$ *vs.* time as shown in Figure 3 under different operating conditions. Figures 4 and 5 show that the volumetric mass transfer coefficient increases with increasing the screen rotation speed according to the equation:

$$K' = aN^b \qquad (13),$$

where a and b are constants according to figures 4 and 5; the value of constant b ranges from 0.25 to 0.3.

The increase in the volumetric mass transfer coefficient with increasing screen rotational speed may be ascribed to the increase in the degree of turbulence generated by the rotating screen.
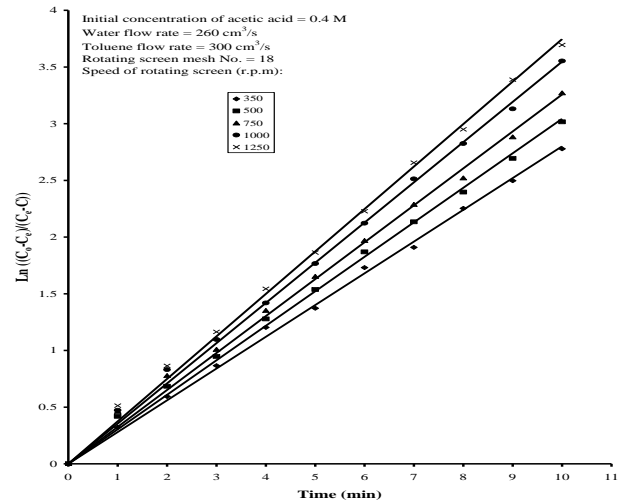

Fig. 3. ln [(C$_o$-C$_e$)/(C-C$_e$)] *vs.* time for different speeds of the rotating screen.

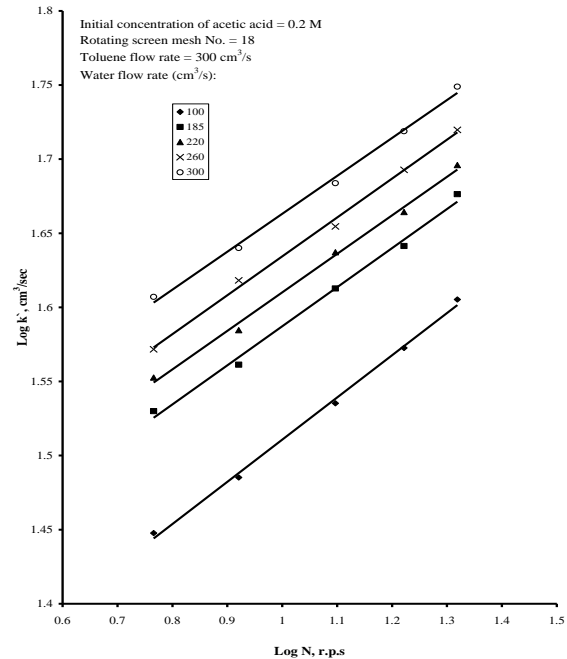**Fig. 4.** log K$^\backslash$ *vs.* log N for different continuous phase flow rates.

Turbulence is generated when the wires of the rotating screen move through the solution because of boundary layer separation in the wake of the moving wires [35]. Turbulence is also generated when the flowing solution penetrates the screen [36, 37]. This turbulence enhances the rate of mass transfer between the organic phase and the aqueous phase via the following effects:

(i) Turbulence reduces the thickness (δ) of both organic phase and aqueous phase diffusion layers around the drop with a consequent increase in the mass transfer coefficient $K = D/\delta$.
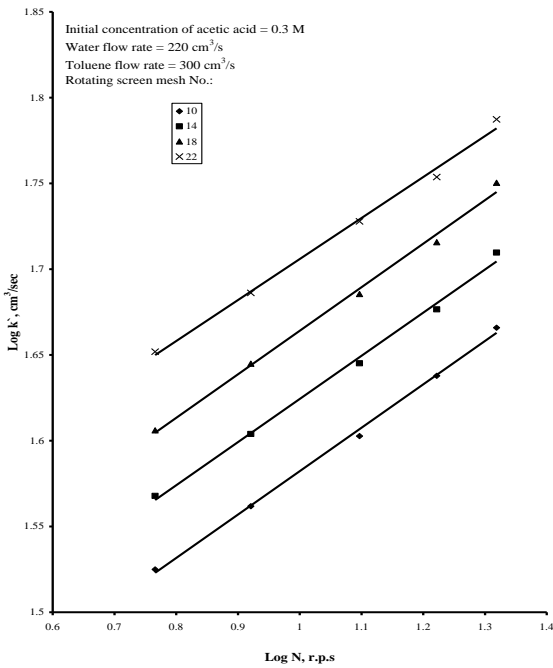
430

Fig. 5. log K$^\backslash$ *vs.* log N for different rotating screen mesh numbers.

(ii) The high shear stress arising from turbulence leads to rapid breakup and coalescence of the dispersed phase drops; the repeated coalescence and re-dispersion of drops enhances the rate of mass transfer through surface renewal [38].

(iii) The high shear stress also exercises drag at the interface between the drops and the continuous phase, this induces internal circulation inside the drops with a subsequent increase in the rate of mass transfer [39]. Whether internal circulation occurs depends on drop diameter and physical properties of the system, internal circulation does not take place when the drops become extremely small, extremely small drops behave as rigid spheres [39].

(iv) Turbulence increases the interfacial mass transfer area A by breaking large dispersed phase drops to the equilibrium size drops according to the equation:

$$A = \frac{6\psi}{d}$$

(14)

where ψ = dispersed phase holdup, and d = drop diameter.

The exponent (b) of equation 13 is less than the value (0.5) predicted from the penetration theory and the hydrodynamic boundary layer theory [38], the present exponent (0.25–0.33) is consistent with the value obtained for mass at stationary cylinders in cross flow at low Re where the velocity exponent ranges from 0.33 to 0.385 for 0.4< Re<40 (Re is based here on screen wire diameter). This similarity

may underline the importance of the role played by the wake formed behind the screen wires as they rotate and are crossed by the axial flow [40]. The value of the exponent is also in a fair agreement with the value 0.358 obtained for the mass transfer at horizontal screens in cross flow [41]. Zaki *et al.* [42] who studied the mass transfer at horizontal vibrating screens found that the mass transfer coefficient increases with the 0.33 power of the vibration velocity. The authors explained this result based on similarity with mass transfer at cylinders in cross flow in the low Re range.

Figure 5 shows that the overall mass transfer coefficient increases by increasing the mesh number of the rotating screens. This may be explained as follows: (i) As the mesh number increases, the number of turbulence promoting wires increases with a consequent increase in the degree of turbulence which enhances the rate of mass transfer as mentioned before; (ii) as the screen opening decreases with increasing mesh number, jets of dispersed phase are formed through each opening as the solution flows across the screen, these jets interact and break down to give turbulence. Finally, this turbulence decays with distance away from the grid [36, 37]. The turbulence generated downstream the screen enhances the volumetric mass transfer coefficient via reducing the diffusion layer thickness and increasing the interfacial area (*A*) as mentioned before.

Figure 4 shows that the volumetric mass transfer coefficient increases by increasing the continuous phase (water) flow rate, which may be ascribed to the turbulence generated downstream of the rotating screen as the axial solution passes through the screen openings [36, 37]. The degree of turbulence generated downstream of the screen increases with increasing axial solution flow rate with a consequent increase in the mass transfer coefficient *K* and the interfacial area *A* as mentioned before.

Figure 6 shows that the rate of mass transfer increases by increasing initial solute (acetic acid) concentration; this can be attributed to the following: (i) As the mesh number increases, the number of turbulence promoting wires increases with a consequent increase in the degree of turbulence which enhances the rate of mass transfer as mentioned before; (ii) as the screen opening decreases with increasing mesh number, jets of dispersed phase are formed through each opening as the solution flows across the screen, these jets

interact and break down to give turbulence. Finally, this turbulence decays with distance away from the grid [36, 37]. The turbulence generated downstream the screen enhances the volumetric mass transfer coefficient via reducing the diffusion layer thickness and increasing the interfacial area (*A*) as mentioned before.

Figure 4 shows that the volumetric mass transfer coefficient increases by increasing the continuous phase (water) flow rate, which may be ascribed to the turbulence generated downstream of the rotating screen as the axial solution passes through the screen openings [36, 37]. The degree of turbulence generated downstream of the screen increases with increasing axial solution flow rate with a consequent increase in the mass transfer coefficient *K* and the interfacial area *A* as mentioned before.

Figure 6 shows that the rate of mass transfer increases by increasing initial solute (acetic acid) concentration; this can be attributed to the following:

As a result of the varying microscopic hydrodynamic conditions around dispersed phase
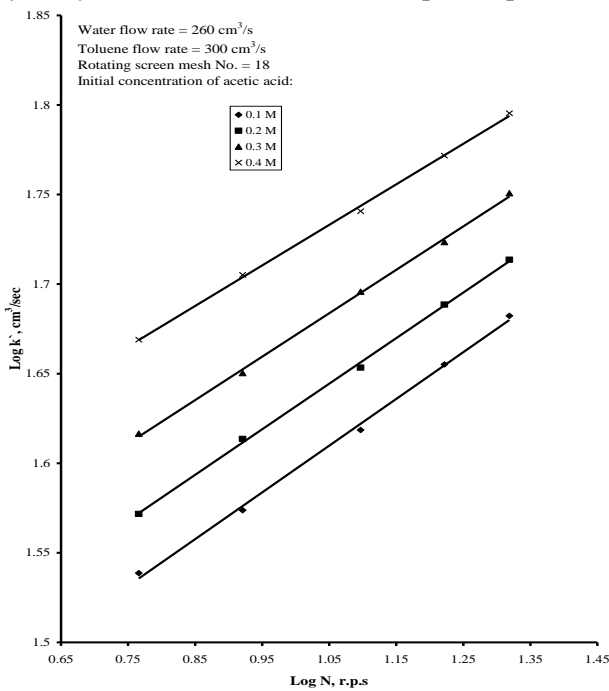
Fig.6. Log K\ *vs.* log N for different initial concentrations of acetic acid.

drop, the rate of mass transfer of acetic acid from the drop surface is not uniform all over the drop surface. This leads to non-uniform concentration of acetic acid at the drop surface. Accordingly, the interfacial tension, which depends on solute concentration, will not be uniform all over the drop surface; surface tension will be high at locations

with low acid concentration and low at locations with high acid concentration. This surface tension gradient gives rise to strong eruptions and interfacial turbulence at the drop surface (Marangoni effect) which enhances the rate of mass transfer [39]. Zhang *et al.* [32] who studied the extraction of acetic acid from water by toluene in a simple cell found that the enhancing effect of a surface tension driven flow increases with increasing acetic acid concentration, which is consistent with the present results.

3.2. Data Correlation

For the present case, dimensional analysis leads to the correlation:
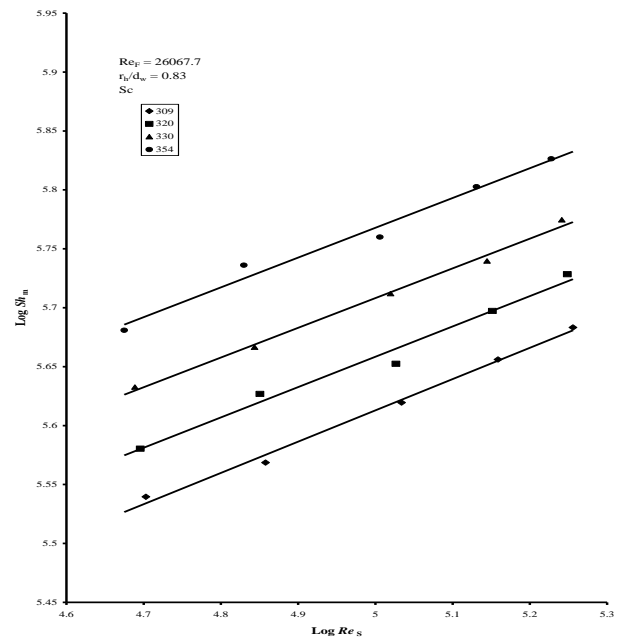
$$Sh = a \, Sc^\alpha \, Re_S^\beta \, Re_F^\gamma \qquad (15)$$

The volumetric mass transfer coefficient will be used instead of the mass transfer coefficient, so a modified Sherwood number Sh_m will be used in the form:

$$Sh_m = \frac{K'}{d_R D} \qquad (16)$$

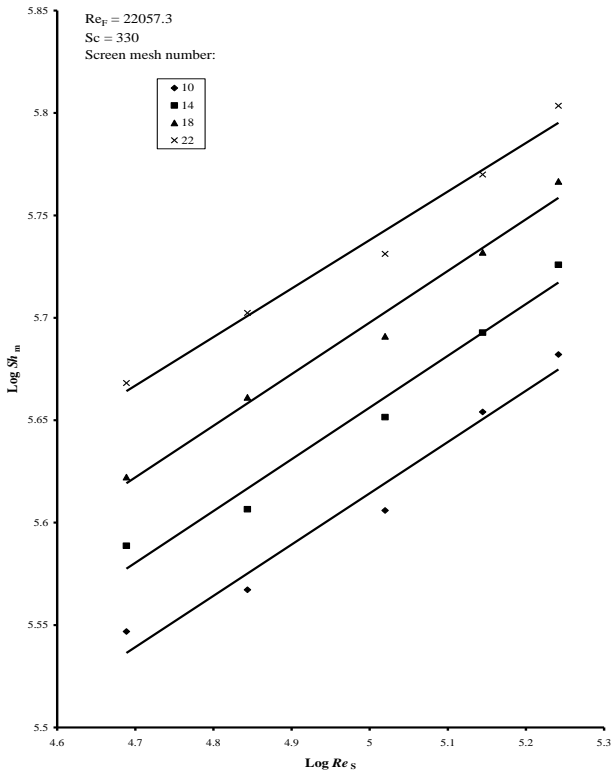Rewriting Eq. (15) in the form:

$$Sh_m = a \, Sc^\alpha \, Re_S^\beta \, Re_F^\gamma \,, \qquad (17)$$

Fig. 7. log Sh_m *vs.* log Re_s for different Sc numbers.

following previous theoretical and experimental studies in mass transfer, the exponent α was fixed at 0.33 [40]. Figures 7 and 8 show the effect of Re_S on Sh_m at different *Sc* and different mesh number respectively. The data fit the equation:
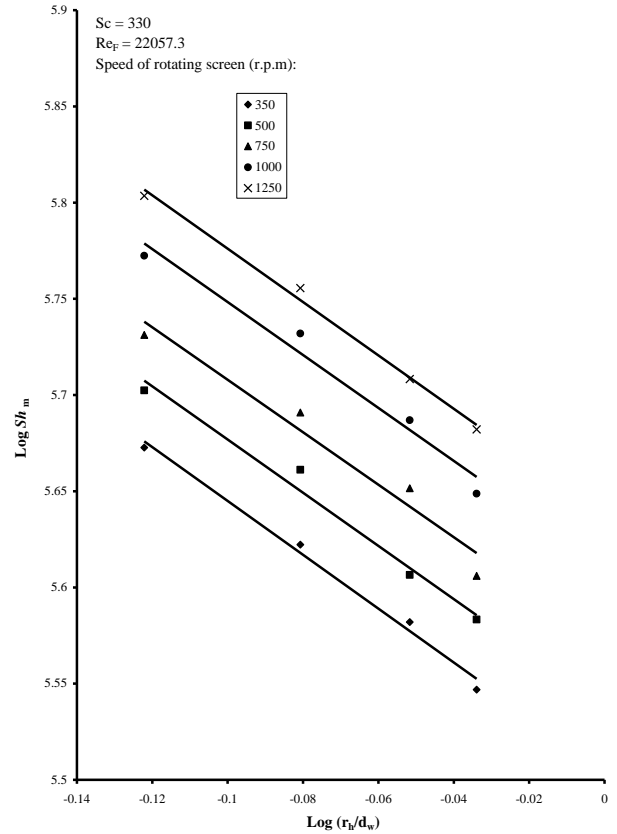
$$Sh_m = a_1 \, Re_S^{0.25} \qquad (18)$$

Fig. 8. log Sh_m *vs.* log Re_s for different screen mesh numbers.
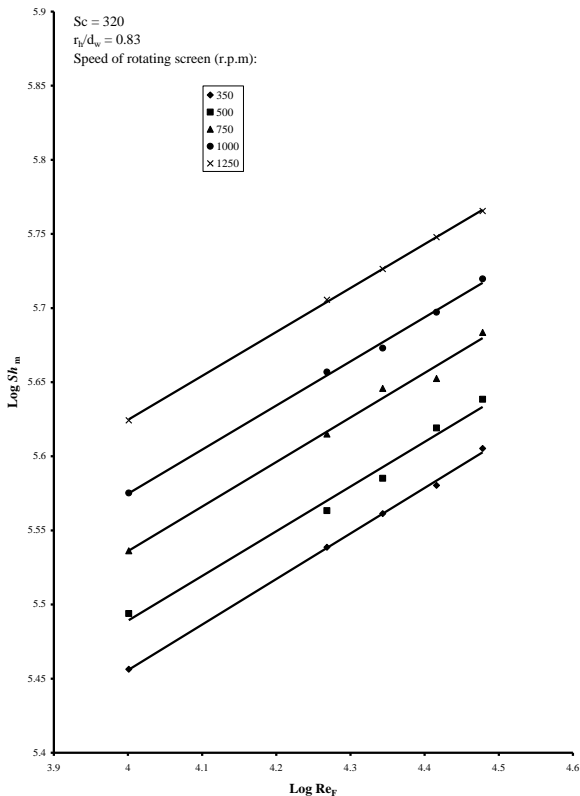
Fig. 9. log Sh_m *vs.* log Re_F for different speeds of rotating screen.

Fig. 10. log Sh_m *vs.* log (r_h/d_w) for different speeds of rotating screen.

Figure 9 shows the effect of Re_F on Sh_m at different rotation speeds, the data fit the equation:

$$Sh_m = a_2\, Re_F^{0.30} \qquad (19)$$

For the screens used in the present work, an extra dimensionless term which accounts for screen geometry should be added to eq. 17.

Screen geometry was expressed in terms of (r_h/d_w) [43] where r_h is the hydraulic radius defined as:

$$r_h = \frac{\varepsilon}{a} \qquad (20)$$

where: ε is the screen porosity, a is the specific screen area (cm^2/cm^3) and d_w is the screen wire diameter. Figure 10 shows the effect of screen geometry (r_h/d_w) on Sh_m at different rotation speeds, the data fit the equation:

$$Sh_m = a_3\left(\frac{r_h}{d_w}\right)^{-1.38} \qquad (21)$$

Accordingly, equation 17 becomes:

$$Sh_m = a\; Sc^{0.33}\, Re_S^{0.25}\, Re_F^{0.30}\left(\frac{r_h}{d_w}\right)^{-1.38} \qquad (22)$$

433
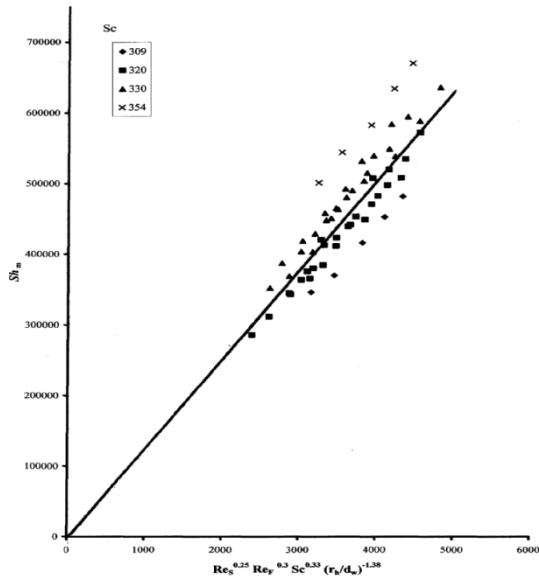
Fig. 11. Overall mass transfer correlation for the extraction of acetic acid from toluene by water using a rotating single screen contactor at different Sc numbers.

Figure 11 shows that the mass transfer data for the transfer of the solute from the dispersed phase to the continuous phase in a rotating single screen extractor under the conditions: $309 < Sc < 354$, $47304 < Re_S < 180176$, $10026 < Re_F < 30078$ and $0.75 < r_h/d_w < 0.92$, fit the equation:

$$Sh_m = 132.63 \, Sc^{0.33} \, Re_S^{0.25} \, Re_F^{0.3} \left(\frac{r_h}{d_w} \right)^{-1.38} \qquad (23)$$

with an average deviation of $\pm$ 14%. The above equation can be used in the design and operation of a rotating screen liquid-liquid extractor.

3.3 Mass Transfer Rate at an Array of Closely Packed Screen

Figures 12 and 13 show the mass transfer behaviour of a rotating bed of closely packed horizontal screens under different conditions. The number of screens per bed ranged from 1 to 5. The results show that the mass transfer coefficient decreases below the value for a single screen with increasing number of screens per bed. These results agree with the finding of Sedahmed *et al.* [27] who studied liquid-solid mass transfer at a rotating fixed bed composed of closely packed screen discs. The mass transfer coefficient decreased below the single screen value increases slightly with increasing the mesh number. The percentage decrease in the rate of mass transfer ranges from 15.6 to 40.6% mainly depending on the bed thickness and the mesh number of the screen. The higher the mesh number of the screen the higher is the percent reduction in
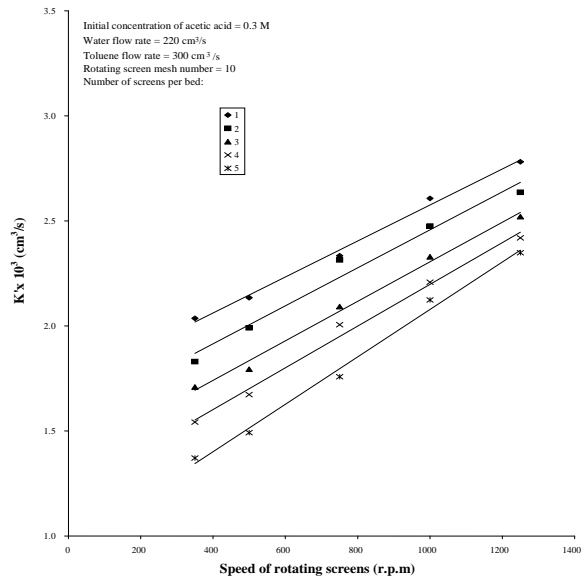
Fig. 12: Volumetric mass transfer coefficient *vs.* speed of rotating screen for different screen numbers per bed.
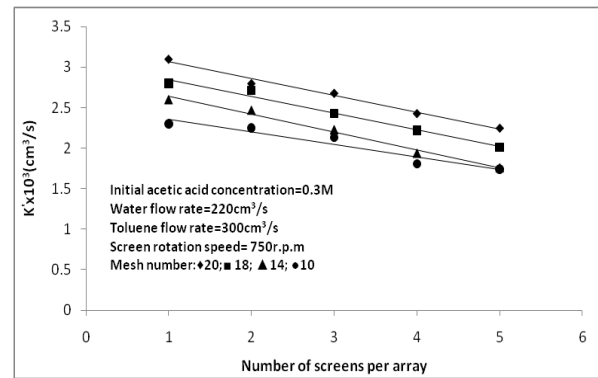
Fig. 13. Volumetric mass transfer coefficient *vs.* number of screens per array for different screen mesh numbers.

the mass transfer coefficient. The decrease in the mass transfer coefficient may be attributed to eddy damping by virtue of the friction between the generated eddies and the wires of the screen matrix.

3.4 Power Consumption

In order to assist in the economic evaluation of the performance of the present work, mechanical power consumed in rotating the screens was measured experimentally under different conditions by means of a wattmeter.

Mechanical power was measured for rotating closely packed arrays with a number of screens ranging from 1 to 5 at different rotational speeds. Figures 14 and 15 show the following results:
1. Power consumption increases with increasing screen rotation speed for all mesh numbers.
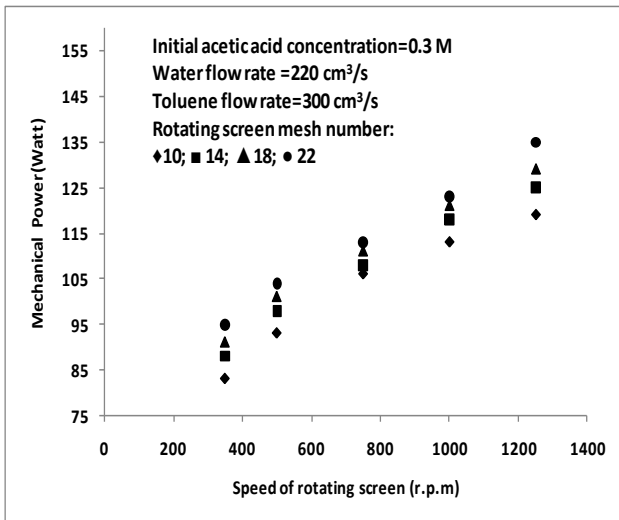2. Power consumption tends to increase with increasing screen mesh number.

Fig. 14. Mechanical power consumption *vs.* speed of rotating screen for different rotating screen mesh numbers.
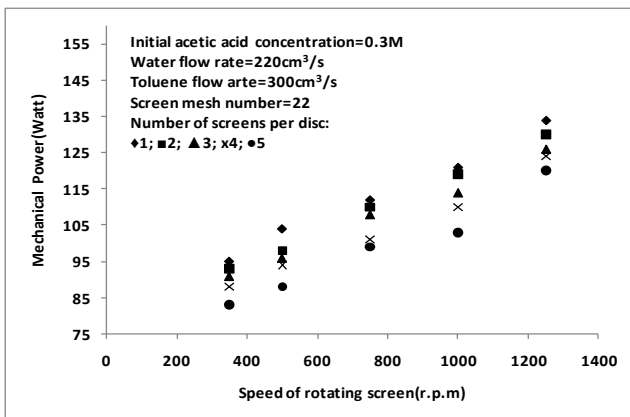

Fig. 15. Mechanical power consumption vs. speed of rotating screen for different screen numbers per bed.

3. Power consumption decreases with increasing the number of screens per array.

The results of power consumption and mass transfer coefficient at a rotating screen are in general consistent with the finding of Calderbank and MooYoung [44] who found that the mass transfer coefficient is proportional to power consumption, i.e., the higher the power consumption the higher the mass transfer coefficient. Figure 16 shows that the rotating screen of mesh number 10 is superior to screens with other mesh numbers because it produces higher mass transfer per unit power consumption.

3.5 Comparison between Rotating Screen Contactor (RSC) and Rotating Disc Contactor (RDC)

It would be of interest to compare the present mass transfer data for rotating screens with that for rotating flat discs. Figure 17 shows that the mass
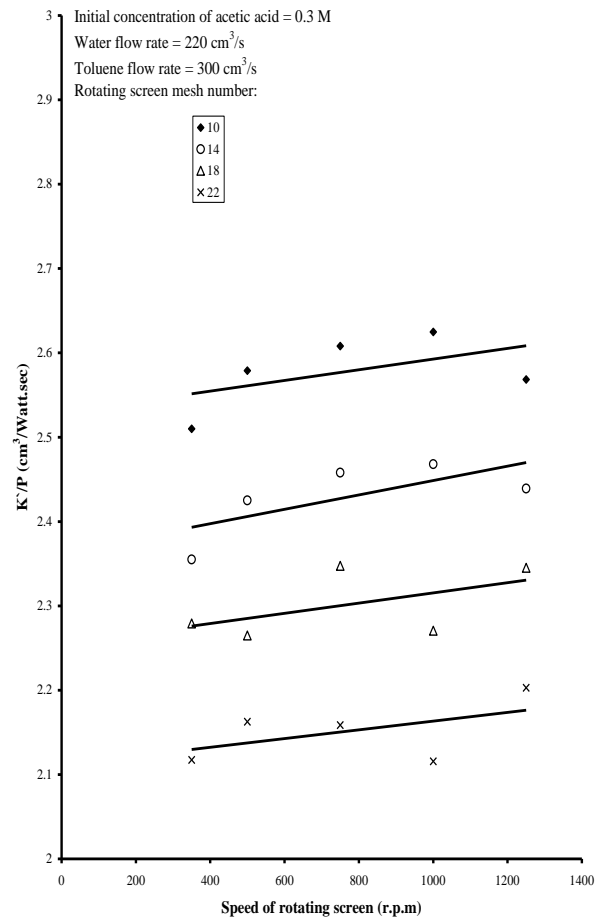

Fig. 16. The ratio $(K^\backslash/P)$ *vs.* speed of rotating screen for rotating screens of different mesh numbers.

transfer coefficients for rotating screens are higher than those for rotating flat discs by an amount ranging from 1379 to 2839% depending on the rotation speed and mesh number of the screen. The above observations can be explained as follows: Both rotating solid discs and screen discs induce an axial flow towards the rotating surface [27, 31]. When the axial flow reaches the solid disc surface it turns to radial flow, but in case of rotating screens part of the axial flow induced by screen rotation turns to radial flow while the other part penetrates the screen in axial direction along with the superimposed net flow. Under such conditions, turbulence can be generated behind the screen wires because of boundary layer separation when the upward moving stream crosses the screen. The presence of eddies downstream of stationary screens in cross flow was revealed by Bourne and Lips [36] who studied the flow behaviour past stationary screens. In addition, turbulence could be also generated when the wires of the rotating screen move through the solution because of boundary layer separation in the wakes of the moving wires. Eddy generation increases the mass transfer coeffi-
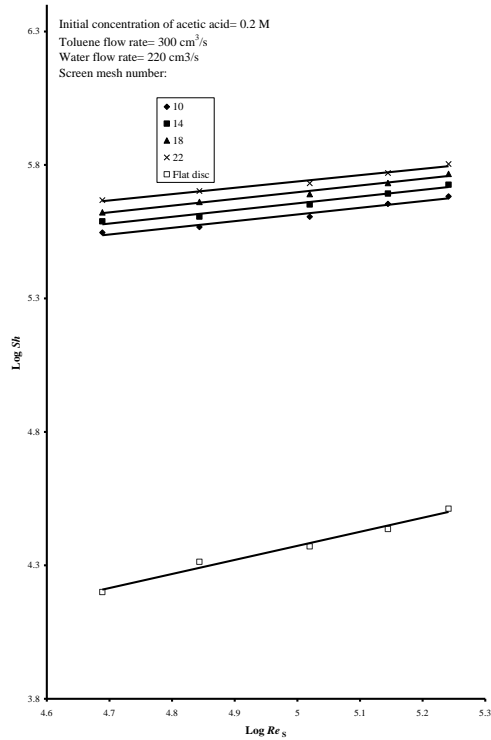
Fig. 17. log Sh *vs.* log Re_s for a rotating flat disc contactor and a rotating screen contactor with different mesh numbers.

cient at rotating screens compared to rotating discs where the radial flow at the disc surface is laminar within the present range of Re_S (47304 < Re_S < 180176)[45].

The superior mass transfer behaviour of a rotating screen contactor compared to the rotating disc contactor shows that the role played by the turbulence generated in the rotating screen contactor outweighs the high degree of axial mixing which characterizes the highly porous screen structure and which tends to reduce the rate of mass transfer.

4. CONCLUSIONS

The present study revealed that the performance of a screen disc extractor is superior to that of an ordinary rotating disc extractor owing to the turbulence promoting ability of rotating screens. The dimensionless mass transfer equation obtained in the present study can be used in the rational design and operation of the suggested rotating screen extractor. Further studies on different solvent extraction systems are needed to confirm the advantages of the present extractor compared to the rotating disc extractor and to validate its mass transfer behaviour under a wider range of operating conditions.

Nomenclature

A	Mass transfer area (cm^2)
A_S	Total screen area (cm^2)
a	Total screen surface area per total volume of one screen (cm^2/cm^3)
C, C_e, C_o	Current concentration, equilibrium concentration and initial acetic acid concentration in toluene (mol/cm^3)
D	Diffusivity (cm^2/s)
d	Drop diameter (cm)
d_R	Rotor screen diameter (cm)
d_S	Stator ring opening (cm)
d_T	Column diameter (cm)
d_w	Wire diameter (cm)
G_f	Column geometry factor
K	Mass transfer coefficient (cm/s)
$K^\backslash$	Volumetric mass transfer coefficient (cm^3/s)
N	Screen rotation speed (r.p.m)
N_m	Mesh number (number of wires/cm)
n	Number of screens per array
T	Absolute temperature of the solution (K)
V	Continuous phase velocity (cm/s)
V_s	Volume of toluene (cm^3)
Z_c	Compartment height (cm)

Dimensionless terms

Re_F	Reynolds number of continuous phase flow ($\rho_c\, V\, d_T/\, \mu_c$)
Re_S	Reynolds number of the rotating screen disc ($\rho_d\, \omega\, d_R^2/\, \mu_d$)
Sc	Schmidt number of dispersed phase ($\mu_d\, /\, \rho_d\, D$)
Sh	Sherwood number ($K\, d_R/D$)
Sh_m	Modified Sherwood number ($K^\backslash/d_R\, D$)
v_s	Volume of single screen (cm^3)

Greek symbols

α, β, γ	Constants
δ	Diffusion layer thickness (cm)
ε	Screen porosity
μ	Viscosity of the solution (g.cm/s)
μ_c	Viscosity of continuous phase (g.cm/s)
μ_d	Viscosity of dispersed phase (g.cm/s)
υ	Kinematic viscosity (cm^2/s)
ρ	Solution density (g/cm^3)
ρ_d	Density of dispersed phase (g/cm^3)
ρ_c	Density of continuous phase (g/cm^3)
ψ	Dispersed phase hold-up
ω	Screen rotational speed (rps)

REFERENCES

1. G.S. Laddha, T.E. Degaleesan, Transport Phenomena in Liquid-Liquid Extraction, McGraw Hill, New York, 1976.
2. W. C. G. Kosters, Rotating-disk Contactor, Handbook of Solvent Extraction Wiley, New York, UK, 1983.
3. W. J. Korchinsky, Rotating Disc Contactor Liquid-Liquid Extraction Equipment, John Wiley and Sons, Chichester, UK, 247, 1994.
4. R. W. Cusack, P. Fremeaux, *Chem. Eng. J.,* 132 (1991).
5. T. Misek, V. Rod, Calculation of Contactors with Longitudinal Mixing, Recent Advance in Solvent Extraction, Pergamon, New York, USA, 197, 1971.
6. M. Amanabadi, H. Bahmanyar, Z. Zarkeshan, M. A. Mousavian, *Chin. J. Chem. Eng.,* **17** (3), 366 (2009).
7. J. C. Godfrey, D. Houlton, K. R. M. Ramlochan, M. J. Slater, *Eng. Res. Des.*, **79** (A2), 156 (2001).
8. A. Kumar, S. Hartland, *Can. J. Chem. Eng*., **70,** 77 (1992).
9. J. Venkataramana, T.E. Degaleesan G.S. Laddha, *Can. J. Chem. Eng.,* **58,** 206 (1980).
10. V.L. Pebalk, N.A. Gromov, M.I. D'yakova, A.E. Kostanyan, *J. Appl. Chem. USSR,* **59,** 1830 (1986).
11. L. Lu, Z. An, Z. Fan, J. Chen, J. *Chem. Ind. Eng. (CHINA)* (English Edition), **1** (2), 44 (1986).
12. S. H. Zhang, X. D. Ni, Y.F. Su, *Can. J. Chem. Eng.,* **59,** 573 (1981).
13. B.D. Kadam, J.B. Joshi, R.N. Patil, *Chem. Eng. Res. Des.*, **87**, 756 (2009).
14. T. Misek, J. Marek, Handbook of Solvent Extraction, Wiley, New York, USA, 1983.
15. T. Misek, *Collect Czech Chem. Commun,* **40**, 1686 (1975).
16. J. W. Zhu, S.H. Zhang, X. K. Zhou, X. X. Chen, Y. F. Su, A. Vogelpohl, *Chem. Eng. Technol.,* **14**, 167 (1991).
17. X. X. Chen, H. T. Wang, K. H. Li, Y. F. Su, *J. Chem. Ind. Eng. (CHINA),* (English Edition), **7**, 28 (1992).
18. X. X. Chen, K. H. Li, Y.F. Su, *Ind. Eng. Chem. Res.* **32,** 453 (1993).
19. X. X. Chen, H. T. Wang, K. H. Li, Y. F. Su, *J. Chem. Ind. Eng. (CHINA),* **44**, 171 (1993).
20. S. Soltanali, Y. Z. Shirkolaee, G. H. Amoabediny, H. Rashedi, A. Sheikhi, P. Chamanrokh, *Chem. Eng. Sci,* **64** (10), 2301 (2009).
21. Y. D. Wang, W. Y. Fei, J. H. Sun, Y. K. Wan, *Chem. Eng. Res. Des.,* **80** (4), 392 (2002).
22. M. T. Cunha, M. J. L. Costa, C. R. C. Calado, L. P. Fonseca, M. R. Aires-Barros J. M. S. Cabral, *J. Biotechnol*., **100,** 55 (2003).
23. E. B. Tambourgi, J.A.F.R. Pereira, *Latin Am. Appl. Res*., **23,** 257 (1993).
24. A. L. F. Porto, L. A. Sarubbo, J. L. Lima-Filho, M. R. Aires-Barros, J. M. S. Cabral, E. B. Tambourgi, *Bioprocess Eng,*. **22,** 215 (2000).
25. L. A. Sarubbo, L. A. Oliveira, A. L. F. Porto, J. L. Lima-Filho, G. M. Campos-Takaki, E.B. Tambourgi, *Biochem. Eng. J.,* **16,** 221 (2003).
26. M. T. H. Cavalcanti, M. G. Carneiro-da-Cunha, I. V. Brandi, T. S. Porto, A. Converti , J. L. Lima Filho, A. L. F. Porto, A. Pessoa, *Chem. Eng. Process.,* **47**, 1771 (2008).
27. G. H. Sedahmed, M. Z. Al-Abd, Y. A. El-Taweel, M. A. Darwish, *Chem. Eng. J.,* **76** (3), 247 (2000).
28. M. M. Zaki, I. Nirdosh, G. H. Sedahmed, *Chem. Eng. J.,* **126** (2-3), 67 (2007).
29. A. H. Abbar, A. H. Sulaymon, M. G. Jalhoom, *Electrochim. Acta,* **53** (4), 1671 (2007).
30. A. S. Philip, Handbook of Separation Techniques for Chemical Engineers, 3rd ed., McGraw Hill, Inc., N.Y., 419, 1997.
31. G. S. Laddha, T. E. Degaleesan, R. Kannappan, *Can. J. Chem. Eng.*, **56** (20), 137 (1978).
32. S. H. Zhnag, Z. M. Wang, Y. F. Su, *Trans IChemE,* **68** (84), 84 (1990).
33. C. R. Wilke, P. Chang, *AIChEJ,* **1**, 264 (1955).
34. J. C. Armour, J. N. Connon, *AIChE J,* **14** (3), 415 (1968).
35. J. G. Knudsen, D. L. Katz, Fluid Dynamics and Heat Transfer, McGraw Hill, N.Y., 1989.
36. J. R. Bourne, M. Lips, *Chem. Eng. J.,* **47** (3), 155 (1991).
37. E. Villermaux, J. Sommeria, Y. Gagne, E. J. Hopfinger, *Eur. J. Mech. B: Fluids*, **10** (4), 427 (1991).
38. D. Glasser, D. R. Arnold, A. W. Bryson and A. M. S. Vieler, *Miner. Sci. Eng*., **8** (1), 23 (1976).
39. T. K. Sherwood, R. L. Pigfood, C. R. Wilke, Mass Trasnfer, McGraw Hill, Inc., N.Y., 1975.
40. F. P. Incropera, D. P. De Witt, Fundamentals of Heat and Mass Transfer, 3rd edn, John Willey & Sons, N.Y., 1995.
41. T. Z. Fahedy, Principles of Electrochemical Reactor Analysis, Elsevier, N.Y., 1985.
42. M. Z. Zaki, Y. A. El-Taweel, A. A. Zaatout, M. Z. El-Abd, G. H. Sedahmed, *J. Electrochem. Soc.,* **138**, 430 (1991).
43. S. Piovano, U. Bohm, *J. Applied Electrochem*., **17** (1), 217 (1987).
44. P. H. Calderbank, M. B. Moo-Young, *Chem. Eng. Sci.,* **16,** 39 (1961).
45. V. G. Levich, Physicochemical Hydrodynamics, Prentice Hall, Englewood Cliffs, N. Y., 1962.

МАСООБМЕННИ ХАРАКТЕРИСТИКИ НА НОВ ЕКСТРАКТОР ТЕЧНОСТ-ТЕЧНОСТ С ВЪРТЯЩИ СЕ ДИСКОВЕ

А. С. Шехата, А. Х. Елшазли[*], А. А. Заатут, Г. Х. Седахмед

Катедра по инженерна химия, Факултет по инженерство, Александрийски университет, Александрия, Египет

(Резюме)

Масообменните характеристики на контактор с въртящи се мрежести дискове са изследвани чрез измерване на скоростта на масопренос на оцетна киселина от разтвор на толуол във вода. Изследваните променливи са геометрични параметри на дисковете като брой на отворите и диаметър на телта, скорост на въртене, физични свойства на разтвора, аксиална скорост на потока и ефект на броя на наредените в пакет мрежи, съставящи един диск. За контактор с единичен въртящ се мрежест диск скоростта на масопренос се определя чрез уравнението:

$$Sh_m = 132.63 \, Sc^{0.33} \, \mathrm{Re}_S^{\,0.25} \, \mathrm{Re}_F^{0.3} \left(\frac{r_h}{d_w} \right)^{-1.38}$$

За въртящи се дискове, съставени от няколко мрежи, коефициентът на масопренос намалява с увеличаване на броя на мрежите в пакет, съставящи диска. Едно сравнение на поведението по отношение на масообмена на въртящ се мрежест диск и въртящ се контактор с плътен диск (КПД), показва, че при дадени условия, скоростта на масопренос при въртящ се мрежест диск е по-висока от тази на контактор с въртящ се плътен диск с фактор от 13.8 - 28.4, в зависимост от условията на работа. Измервания на консумацията на механична енергия показват по-висок коефициент на масопренос, при по-висока консумация на енергия. Отбелязани са практически приложения на предложения екстрактор в области като фармацевтичната промишленост, хидрометалургия, петролната индустрия и обработка на вода.

Synthesis and spectroscopic characterization of piperidine/I$_2$ charge-transfer complex in different chlorinated organic solvents

M.S. Refat[a,b*], O.B. Ibrahim [b], H. Al-Didamony[c], Kh.M. Abou El-Nour[d], L. El-Zayat[a]

[a] Department of Chemistry, Faculty of Science, Port Said, Port Said University, Egypt
[b] Department of Chemistry, Faculty of Science, Taif University, 888 Taif, Kingdom Saudi Arabia
[c] Department of Chemistry, Faculty of Science, Zagazig, Zagazig University, Egypt
[d] Department of Chemistry, Faculty of Science, Ismailia, Suez Canal University, Egypt

The charge-transfer (CT) complex formed between piperidine (Pip) as donor and iodine (I$_2$) as σ-acceptor was studied spectrophotometrically. The synthesis and characterization of the piperidine CT-complex of iodine, $[(Pip)_2]I^+.I_3^-$, was described. This complex was readily prepared by the reaction of Pip with I$_2$ in CHCl$_3$ solvent. Infrared spectra (mid-IR and far-IR), UV-Vis techniques and elemental analyses were used to characterize the piperidine/I$_2$ charge-transfer complex. Benesi-Hildebrand's method and its modifications were applied to the determination of the association constant (K) and the molar absorption coefficient (ε).

Keywords: Charge-transfer, Iodine, Piperidine, Infrared spectra.

1. INTRODUCTION

Charge-transfer complexes are known to take part in many chemical reactions like addition, substitution and condensation [1,2]. These complexes have attracted great attention as non-linear optical materials and electrical conductors [3-6]. Electron donor-acceptor (EDA) interaction is also important in the field of drug-receptor binding mechanism [7], in solar energy storage [8] and in surface chemistry [9] as well as in many biological fields [10]. On the other hand, the EDA reactions of certain π-acceptors have been successfully utilized in pharmaceutical analysis [11]. For these wide applications extensive studies on CT- complexes of π-acceptors have been performed [12].

Piperidine (Formula I) is an organic compound with the molecular formula C$_5$H$_{11}$N. It is a cyclic amine with a six-membered ring. It is a clear liquid with pepper-like odor. The piperidine skeleton is present in numerous natural alkaloids such as piperine, the main active chemical agent in black pepper and relatives, pharmaceutical drugs such as raloxifene.
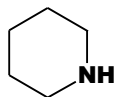
Formula I

The solid charge-transfer complexes formed between iodine and several types of electron donors such as aromatic hydrocarbons, polycyclic amines, mixed oxygen/nitrogen cyclic bases, aromatic/aliphatic amines have been studied and categorized [13-22]. The tri-iodide ion I$_3^-$, penta-iodide ion I$_5^-$, and ennea-iodide ion I$_9^-$ were formed through the reaction of iodine with various donors like metal acetylacetonates [23-25], polyazacyclic [26-28], and crown ethers [29-32]. Some of charge-transfer complexes show very interesting applications in the analysis of some drugs in pure form or in pharmaceutical preparations [33, 34]. The charge-transfer in fullerene-based [35, 36] compounds is currently of great interest since these materials can be utilized as superconductors [37] and to produce non-linear optical activity [38].

2. EXPERIMENTAL

2.1. Materials

All chemicals used throughout this work were Analar or extra pure grade. Piperidine (C$_5$H$_{11}$N), was of analytical reagent grade (Merck reagent). The iodine acceptor was purchased from Aldrich. Stock solutions of piperidine and iodine acceptor were freshly prepared and chloroform of spectroscopic grade (Merck) was used as received.

2.2. Synthesis

[Piperdine]-iodine complex

At room temperature, the solid CT complex of Pip with iodine was prepared by mixing 85.15 mg

(1.0 mmol) of the donor in chloroform (10 mL), a solution of iodine was added (253.81 mg, 1.0 mmol) in the same solvent (10 mL) upon continuous stirring for about 15 min. A dark brown complex was formed, washed several times with small amounts of chloroform, and dried under vacuum over anhydrous calcium chloride; the empirical formula of the complex $[(Pip)_2]I^+.I_3^-$ is $C_{10}H_{22}N_2I_4$ with molecular weight 677.92 g/mol.

2.3. Methods

The electronic spectra of Pip, iodine acceptor and resulting CT complex were recorded in the region of 200-800 nm by using a Jenway 6405 spectrophotometer with quartz cells of 1.0 cm path length. Photometric titration was performed at 25ºC for the reactions of donor with acceptor in chloroform as follow: the concentration of Pip in the reaction mixtures was kept fixed at 5.0×10^{-4} M, while the concentration of acceptor was changed over a wide range from 1:0.25 to 1:4.00. Infrared measurements (KBr discs) of the solid donors, acceptor and CT complexes were carried out on a Bruker FT-IR spectrophotometer over the range of wave numbers 400_3–4000 cm_3^{-1} with 50 scans at 2 cm^{-1} resolution.

3. RESULTS AND DISCUSSION

The results for the elemental analysis of the piperidine charge-transfer complex are shown in Table 1. It can be seen from the table that the

Table 1: Elemental analysis CHN and physical parameters data of the CT-complex formed in the reaction of the Pip with iodine

Complexes (FW)	Mwt.	C%		H%		N%		Physical data	
		Found	Calc.	Found	Calc.	Found	Calc.	Color	mp (ºC)
$[(Pip)_2]I^+.I_3^-$	677.92	17.45	17.70	3.29	3.24	3.99	4.13	Dark brown	< 30
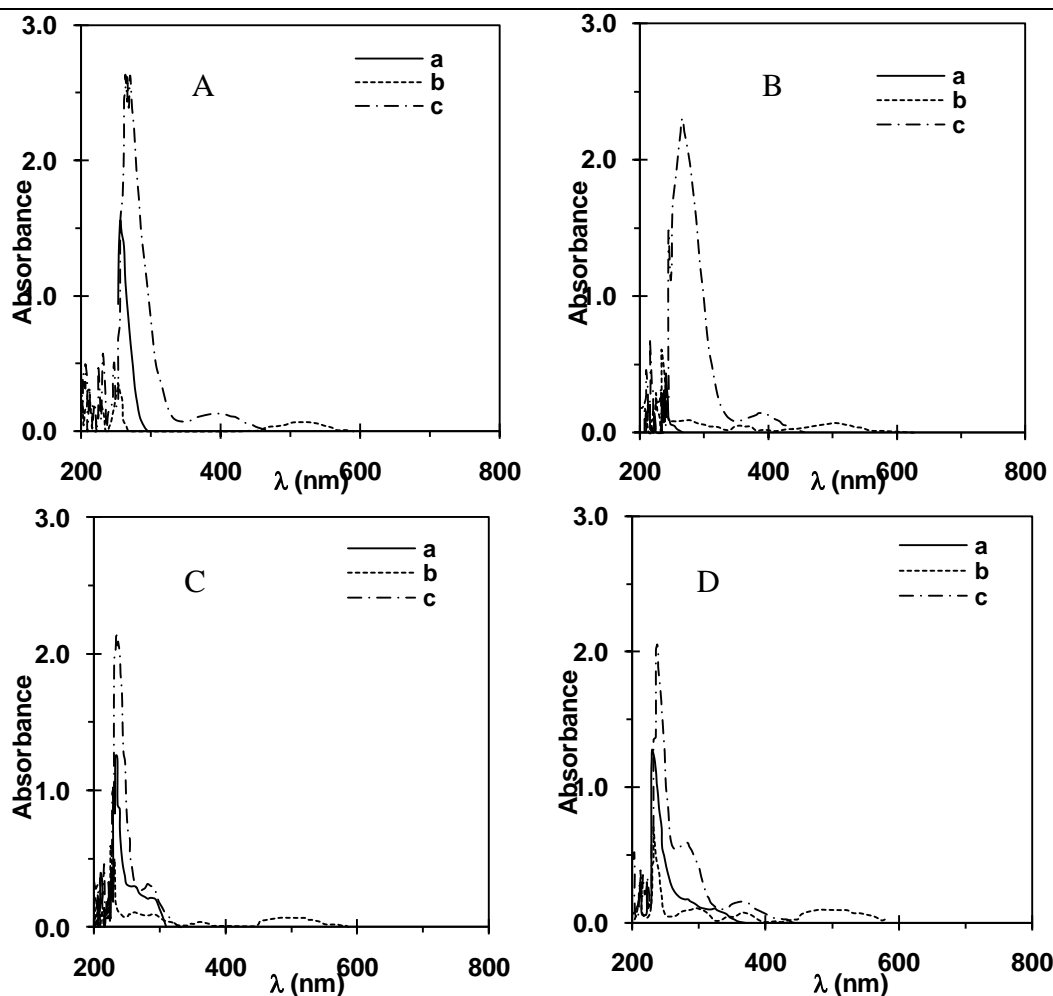
Fig. 1. Electronic absorption spectra of; (A): Pip-iodine reaction in CCl_4, (B): Pip-iodine reaction in $CHCl_3$, (C): Pip-iodine reaction in CH_2Cl_2 and (D): Pip-iodine reaction in 1,2-dichloroethane. (a) = donor (1.0×10^{-4}M), (b) = acceptor (1.0×10^{-4}M) and (c) = CT-complex.
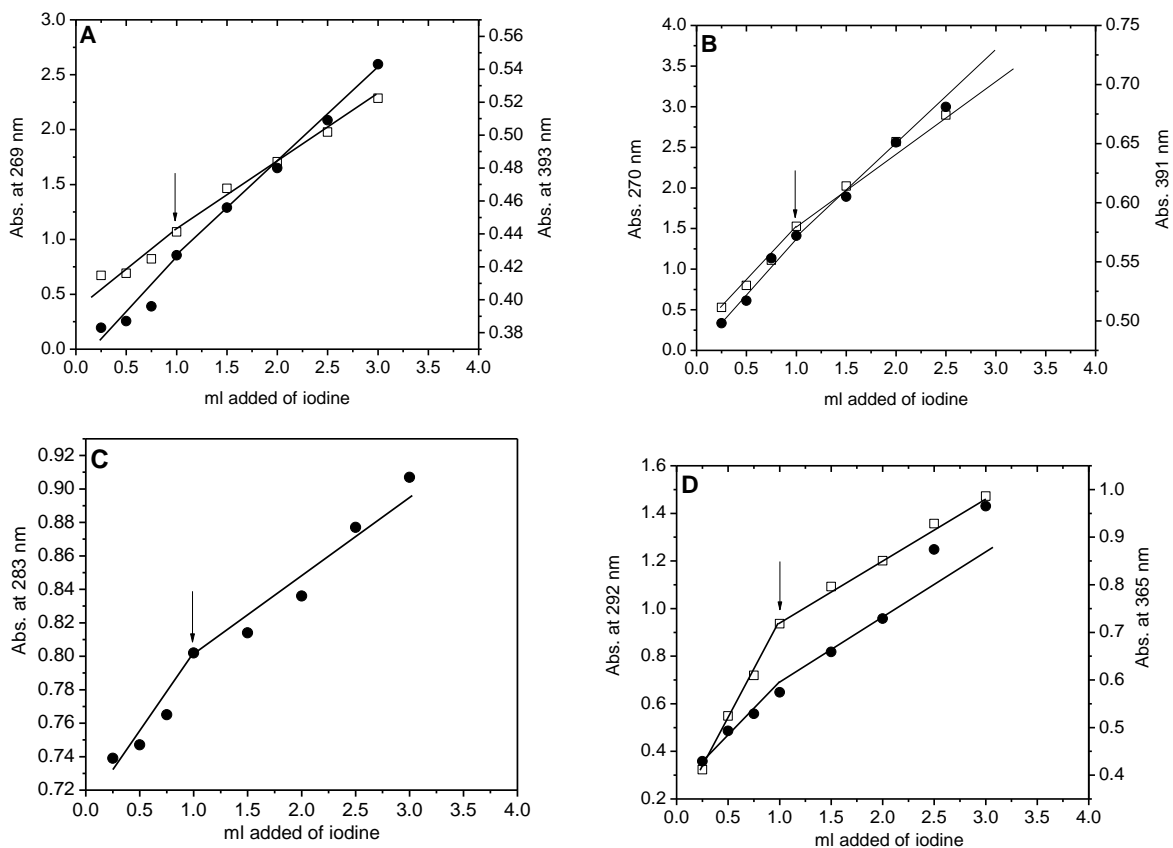
Fig. 2. Photometric titration curves for the Pip-iodine system in various solvents: (A) in CCl_4 at 269 and 393 nm, (B) in $CHCl_3$ at 270 and 391 nm, (C) in CH_2Cl_2 at 283 nm and (D) in 1,2-dichloroethane at 292 and 365 nm.

values found are in agreement with the calculated ones, and the composition of the CT complex is matched with the molar ratios determined from the photometric titration of Pip with the iodine σ-acceptor. All complexes are insoluble in cold and hot water, but easily soluble in DMF and DMSO.

3.1. Electronic absorption spectra of the Pip/iodine system

The electronic (UV-Vis) absorption spectra of the Pip/iodine complex were measured in various solvents such as CCl_4, $CHCl_3$, CH_2Cl_2 and 1,2-dichloroethane. In each solvent the complex was formed by adding X ml of 5.0×10^{-4} M iodine (X = 0.25, 0.50, 0.75, 1.00, 1.50, 2.00, 2.50 and 3.00 ml) to 1.00 ml of 5.0×10^{-4} M Pip. The volume of the mixture in each case was completed to 15 ml for CCl_4, 10 ml for $CHCl_3$, 20 ml for CH_2Cl_2, and 10 ml for 1,2-dichloroethane with the respective solvent. The concentration of Pip in the reaction mixture was kept fixed at 0.33×10^{-4}, 0.50×10^{-4}, 0.25×10^{-4} and 0.50×10^{-4} M in the case of CCl_4, $CHCl_3$, CH_2Cl_2 and 1,2-dichloroethane solvent, respectively, while the concentration of iodine was

varied over the range of 0.0833×10^{-4} M to 1.00×10^{-4} M for Pip/I₂ in CCl_4, from 0.125×10^{-4} M to 1.500×10^{-4} M for Pip/I₂ in $CHCl_3$, from 0.0625×10^{-4} M to 0.7500×10^{-4} for Pip/I₂ in CH_2Cl_2 and from 0.125×10^{-4} M to 1.500×10^{-4} M for Pip/I₂ in 1,2-dichloroethane. These concentrations produce Pip:I₂ ratios in the range from 1:0.25 to 1:3.00. The electronic absorption spectra of the 1:1 Pip:I₂ complexes in CCl_4, $CHCl_3$, CH_2Cl_2 and 1,2-dichloroethane together with those of the reactants I₂ and Pip are shown in Figures 1A, B, C and D, respectively.

The spectra show characteristic absorption bands which are not present in the spectra of the reactants free iodine and Pip. These bands at (393 and 269 nm), (391 and 270 nm), 283 nm and (363 and 292 nm) are assigned to the CT-complex formed by the reaction of Pip with I₂ in the solvents CCl_4, $CHCl_3$, CH_2Cl_2 and 1,2-dichloroethane, respectively. Photometric titration curves based on these characteristic absorption bands are given in Figures 2A, B, C and D.
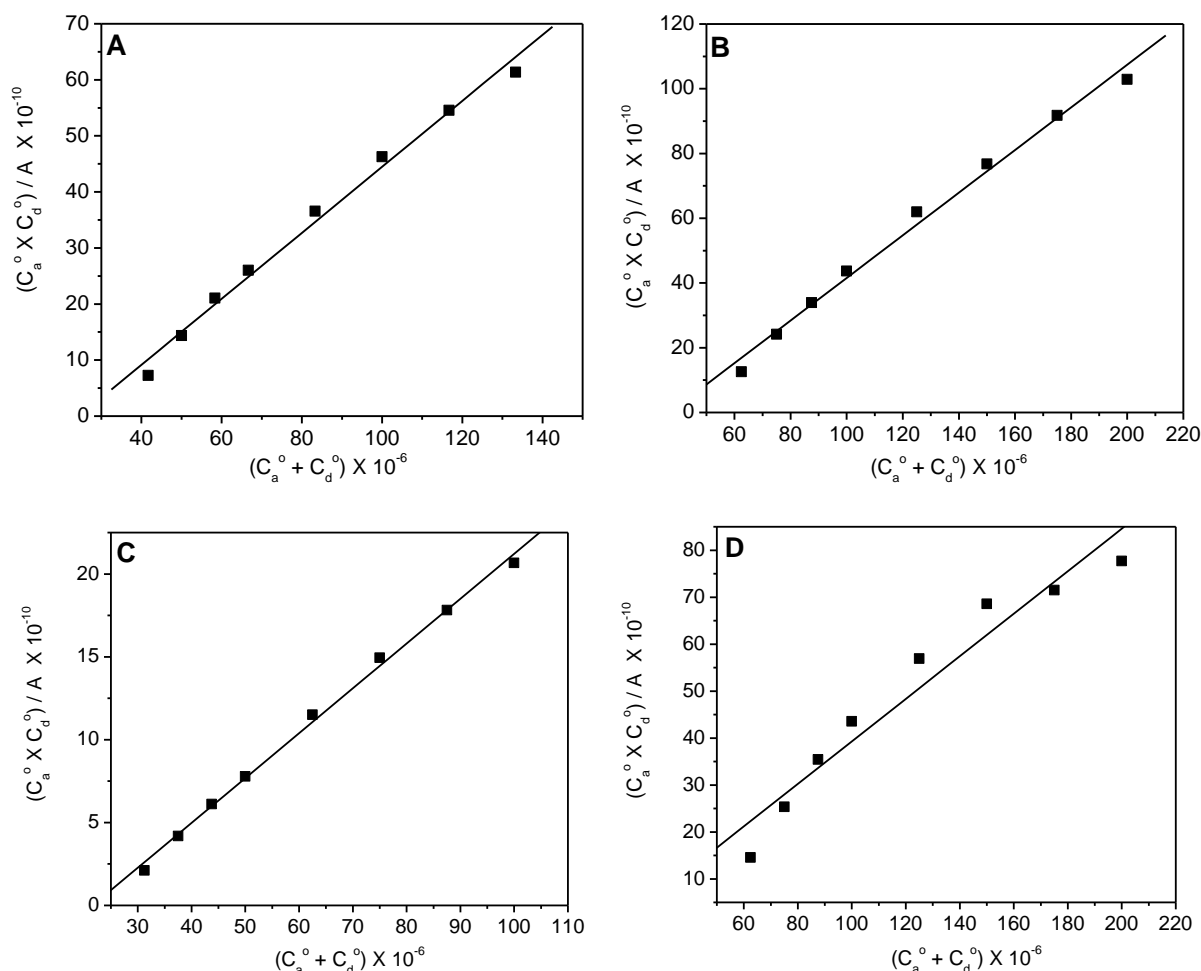
Fig. 3. The plot of $(C_d^o + C_a^o)$ values against $(C_d^o \cdot C_a^o / A)$ values for the Pip-iodine system in various solvents: (A) in CCl_4 at 393 nm, (B) in $CHCl_3$ at 391 nm, (C) in CH_2Cl_2 at 283 nm and (D) in 1,2-dichloroethane at 365 nm.

These photometric titration curves were obtained according to the known methods [39] by plotting absorbance against the X ml added of the iodine σ-acceptor. The equivalence points shown in these curves clearly indicate that the CT complex formed between Pip and iodine is 1:1. The formation of 1:1 complex was also supported by elemental analysis, mid and far infrared spectra.

However, the two absorption bands appearing ≈ 360 and ≈ 290 nm are well known [40-42] to be characteristic for the formation of the tri-iodide ion (I_3^-). Accordingly, the formed complex was formulated as $[(Pip)_2]I^+.I_3^-$.

and A is the absorbance of the definite bands around 290 and 360 nm. From the data obtained C_d^o of Pip, C_a^o of I_2, $(C_a^o + C_d^o)$ and $(C_a^o \cdot C_d^o / A)$ in CCl_4, $CHCl_3$, CH_2Cl_2 and 1,2-dichloroethane were determined. When the $C_a^o \cdot C_d^o / A$ values for each

It was of interest to observe that the solvent has a pronounced effect on the spectral intensities of the formed $[(Pip)_2]I^+.I_3^-$ complex. To study the solvent effect in a quantitative manner, it was necessary to calculate the values of the association constant, K, the molar absorption coefficient ε, and the oscillator strength, f, of the iodine complex in each solvent. The 1:1 modified Benesi-Hildebrand equation [43] was used in the calculations:

$$\frac{C_a^o C_d^o l}{A} = \frac{1}{K\varepsilon} + \frac{C_a^o + C_d^o}{\varepsilon} \qquad (1)$$

where C_a^o and C_d^o are the initial concentrations of the acceptor I_2 and the donor Pip, respectively, solvent are plotted against the corresponding $(C_a^o + C_d^o)$ values, straight lines are obtained with a slope of $1/\varepsilon$ and intercept of $1/k\varepsilon$ as shown in Figures 3A, B, C and D for the reactions in CCl_4, $CHCl_3$, CH_2Cl_2 and 1,2–dichloroethane.

Table 2. Spectrophotometric results for the Pip complex with iodine in different solvents at 25°C and the dielectric constants of the solvents

Solvent	λ_{max} (nm)	E_{CT} (eV)	K (l.mol^{-1})	ε_{max} (l.mol^{-1}.cm^{-1})	f	μ	I_p	D
CCl_4	393	3.16	4.09×10^4	1.70×10^4	6.80	23.80	7.71	2.2
$CHCl_3$	391	3.18	2.71×10^4	1.52×10^4	8.75	27.00	7.73	4.7
CH_2Cl_2	361	3.45	6.97×10^4	1.81×10^4	13.44	31.34	7.96	8.9
$(CH_2)_2Cl_2$	365	3.41	7.52×10^4	2.21×10^4	14.30	33.30	8.08	10.4

Table 3. Infrared frequencies[(a)] (cm^{-1}) and tentative assignments for the Pip donor and the $[(Pip)_2]I^+.I_3^-$ complex.

Pip	$[(Pip)_2]I^+.I_3^-$	Assignments[(b)]
3393 s, br	3445 s, br	ν(N-H)
2938 vs	2949 vs	ν_s(C-H)
2854 ms	2833 mw	ν_{as}(C-H)
2809 mw	2803 mw	
2738 mw	2729	
---	2619 mw	Hydrogen bonding
	2502 mw	
	2401 mw	
	2341 mw	
1627 mw	1617 s	δ_{def}(N-H)
		Ring breathing bands
1542 ms	1582 s	C-H deformation
1447 ms	1455 s	
1417 ms		
1321 mw	1313 w	ν(C-C)
1276 s	1255 w	ν(C-N)
1162 mw	1162 w	
1112 mw	1120 w	
1032 mw	1080 w	
	1027 ms	
948 mw	946 mw	(C-H) bend
861 ms	860 mw	δ_{rock}; NH
806 mw	789 vw	CH_2 rock
737 ms	630 vw	Skeletal vibrations
646 vw		
553 ms	549 ms	CNC deformation
438 mw	433 ms	

(a): s = strong, w = weak, m = medium, sh = shoulder, v = very, br = broad. (b): ν, stretching; δ, bending.

The oscillator strength f was obtained from the approximate formula [44]:

$$f = (4.319 \times 10^{-9})\, \varepsilon_{max} \cdot \nu_{1/2} . \qquad (2)$$

Here $\nu_{1/2}$ is the bandwidth for half-intensity in cm^{-1}. The oscillator strength values together with the corresponding dielectric constants, D, of the solvent used are given in Table 2. The trend of the values in this table reveals several facts.

i) The $[(Pip)_2]I^+.I_3^-$ complex shows high values of both the association constant (K) and the molar absorption coefficient (ε). This high value of K reflects the high stability of the iodine complex as a result of the expected high donation power of Pip, while the high value of ε agrees quite well with the existence of the tri-iodide ion, I_3^-, which is known to have a high absorbance value [40-42].

ii) The values of the oscillator strength, f, increase on increasing the dielectric constant (D) of the solvent. This result could be explained on the basis of competitive solvent interactions with the acceptor [21]. Figure 4 shows the obtained linear relationship between f and D.

iii) The formation constant (K) for the $[(Pip)_2]I^+.I_3^-$ complex shows some variations, Table 2, as the solvent is changed, but no clear relation with solvent properties can be derived.
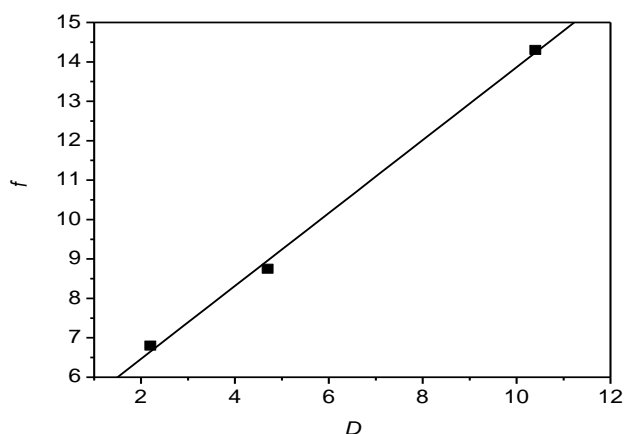
Fig.4. The plot of the oscillator strength f of $[(Pip)_2]I^+.I_3^-$ against the dielectric constant of the solvent D.

Table 4. Fundamental vibrations for some tri-iodide compounds.

Compounds	Assignments*			References
	ν_1	ν_2	ν_3	
KI_3	111	---	143	[44]
CsI_3	103	69	149	[53]
$[Ni(acac)_2]_2I^+.I_3^-$	101	84	132	[25]
$[(Pip)_2]I^+.I_3^-$	102	79	145	Present work

ν_1^*, ν_s (I-I); ν_2, δ (I_3^-); ν_3, ν_{as} (I-I).

Finally, the general mechanism for the formation of the $[(Pip)_2]I^+.I_3^-$ complex is proposed as follows:

$$2Pip + I_2 \rightarrow [Pip]_2I^+.I^-$$
$$[Pip]_2I^+.I^- + I_2 \rightarrow [(Pip)_2]I^+.I_3^-$$
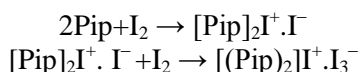
The $[Pip]_2I^+.I^-$ reaction intermediate is analogous to the well known species $[(donor)I]^+.I^-$ formed in the reaction of iodine with many donors [19, 26]. It has characteristic [45] absorption, around 250 nm; see Figures 1A, B, C and D.

The transition dipole moment (μ) of the iodine complex, Table 2, was calculated from the following equation [46]:

$$\mu = 0.0958[\varepsilon_{max} \nu_{1/2} / \nu_{max}]^{1/2} \qquad (3)$$

The ionization potential (I_p) of the free donor was determined from the CT energies of the CT band of its complexes with iodine by using the following relationship [47]:

$$E_{CT} = I_p - 5.2 + 1.5 / (I_p - 5.2) \qquad (4)$$

where E_{CT} is the energy of the charge-transfer of the iodine complex; the energy of the π-σ* or n-σ*

interaction (E_{CT}) is calculated using the following equation [47]:

$$E_{CT} = 1243.667 / \lambda_{CT} \text{ (nm)} \qquad (5)$$

where λ_{CT} is the wavelength of the complexation band.

3.2. Infrared spectra of the Pip-iodine solid complex

The mid infrared spectra of Pip and the formed CT complex, $[(Pip)_2]I^+.I_3^-$, were recorded from KBr discs. These spectra are shown in Figures 5A and B, respectively. The spectral bands are resolved and assigned to their vibrational modes, as given in Table 3. As expected, the bands characteristic for the Pip unit in the $[(Pip)_2]I^+.I_3^-$ CT complex display small changes in band intensities and frequency values. For example, the stretching asymmetry and symmetry of the ν(N-H) vibration occurred at 3393 and 3447 cm^{-1} for free Pip and $[(Pip)_2]I^+.I_3^-$, respectively. There is an increase in the intensity of the δ(N-H) vibration in the case of iodine complex rather than Pip alone as well as a blue shift in the wavenumbers from 1627 cm^{-1}(Pip) to 1617 cm^{-1} (iodine complex). Such changes clearly indicate that the N-H bond in the piperidine donor participates in the complexation process with iodine. On the other hand, the presence of a few bands at 2619, 2502, 2401, and 2341 cm^{-1} could be assigned to the expected hydrogen bonding in the Pip/iodine complex [48]. This fact strongly supports the mode of interaction between Pip and iodine by forming a hydrogen bond between the donor Pip and the iodine acceptor, (N-H---I).

3.3. Far infrared spectra of the Pip-iodine solid complex

The far infrared spectrum of $[(Pip)_2]I^+.I_3^-$ was recorded from Nujol mulls dispersed on polyethylene windows in the region 50-600 cm^{-1} and was focused in the region 50-200 cm^{-1}, as given in Figure 6. The spectrum associated with the $[(Pip)_2]I^+.I_3^-$ complex shows the characteristic bands for the tri-iodide ion, I_3^- at 145, 102 and 79 cm^{-1}. These bands can be attributed to ν_{as}(I-I), ν_s(I-I) and δ(I_3^-), respectively. These three absorption bands do not exist in the spectrum of the donor Pip. However, the I_3^- ion may be linear ($D_{\infty h}$) or non linear (C_{2v}). Group theoretical analysis indicates that the I_3^- ion with C_{2v} symmetry displays three vibrations: ν_s(I-I); A^-_1, ν_{as}(I-I); B_2 and δ(I_3^-); A_1, all infrared active in agreement [40, 49, 50] with the

(A)

(B)
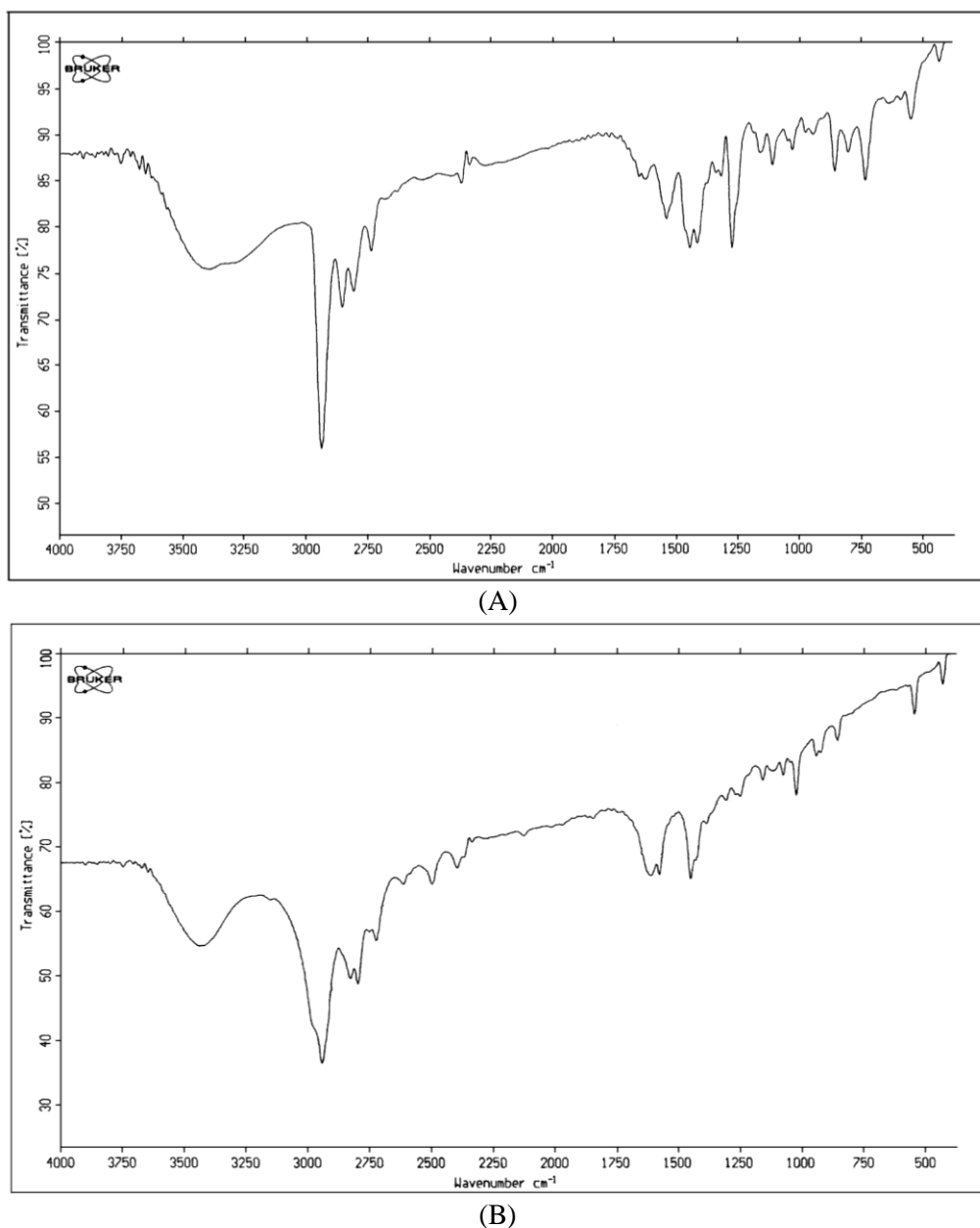
Fig. 5. Infrared spectra of: (A) Pip and (B) the charge-transfer complex, $[(Pip)_2]I^+.I_3^-$.

observed three infrared bands for $[(Pip)_2]I^+.I_3^-$, as shown in Table 4. Accordingly, the formed iodine complex is formulated as $[(Pip)_2]I^+.I_3^-$. The conversion of iodine molecules into polyiodide units is well known in the literature. The formation of I_3^- ions was previously reported [51–53] in the reaction of iodine with various donors such as 4-(dimethylamino) pyridine, 1-aza-15-crown-5,3,6,9,14-tetrathiabicyclo [9.2.1]tetradeca-11,13-diene and nicotine.

3.4. Group theoretical analysis

The geometry of I_3^- in $[(Pip)_2]I^+.I_{33}^-$ may be assigned to one of the two structures: linear structure with ($D_{\infty h}$) symmetry or non-linear structure with (C_{2v}) symmetry. It follows from the

above discussion that the shape of the I_{33}^- ion is non linear and displays C_{2v} symmetry. The three modes of vibrations distributed over the symmetry species $2A_1 + B_2$ should be all infrared active. If the complex is linear, i.e., of $D_{\infty h}$ symmetry, it would give only two infrared bands, which is not the case.

CONCLUSION

The characterization techniques like infrared spectra (mid and far), elemental analysis and electronic spectra confirmed that the piperidine-iodine interaction yields a complex of the formula $[(Pip)_2]I^+.I_{33}^-$. The triiodide ion formed belongs to the C_{2v} point group and the
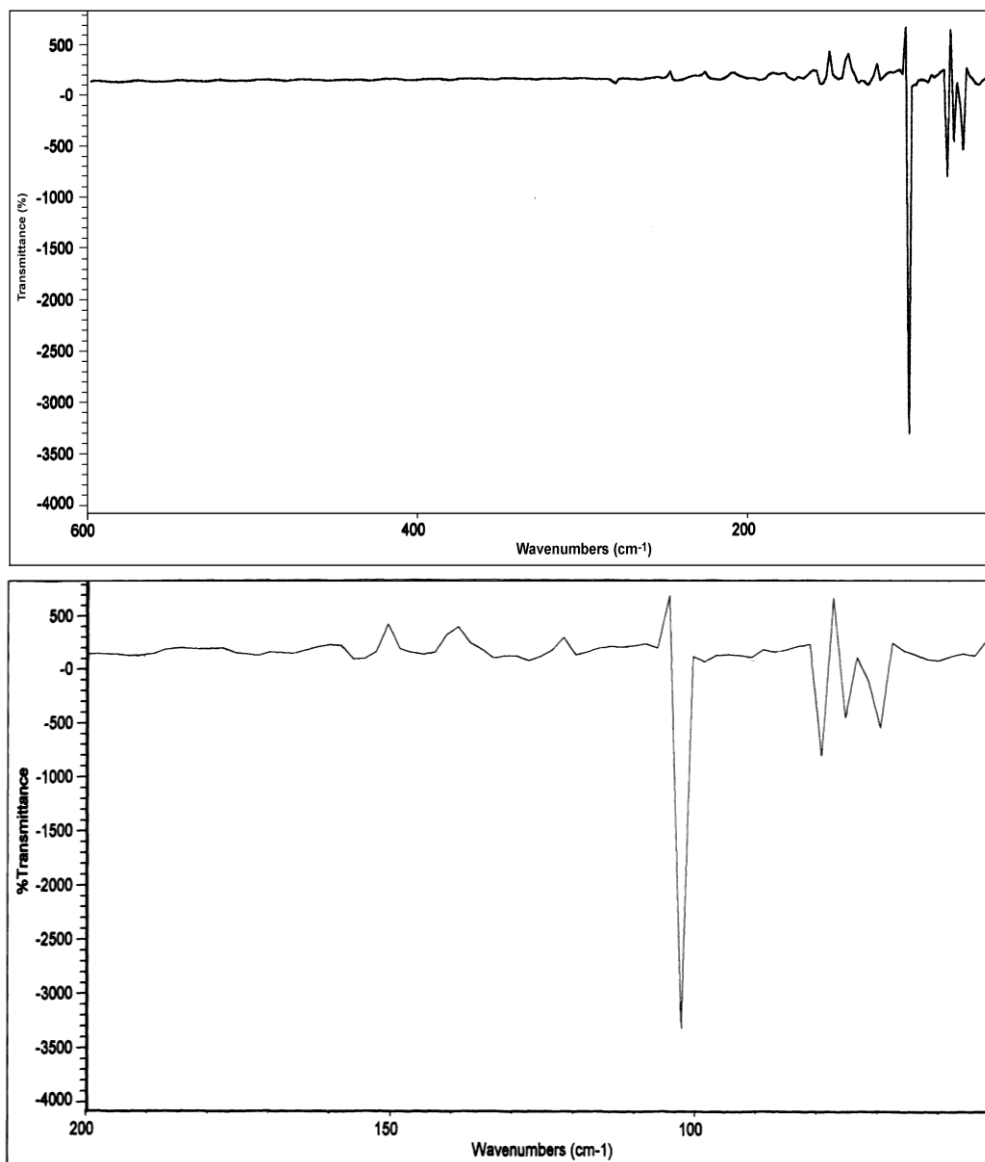
Fig. 6. Far-infrared spectrum of the charge-transfer complex, $[(Pip)_2]I^+.I_3^-$.

far-infrared spectra play an important role for the assignment of I_{33}^-. Some interesting physical data were obtained which throw light on the stability of the piperidine complex. The iodine complex was studied in various solvents like CCl_4, $CHCl_3$, CH_2Cl_2 and 1,2-dichloroethane. It was found that the values of the oscillator strength f increase with the increase in the dielectric constant (D) of the solvent.

REFERENCES

1. A.G. Chapkanov, B. Koleva, M. Arnaudov, I. Petkov, *Chem. Papers*, **62 (3),** 294 (2008).
2. F.P. Fla, J. Palou, R. Valero, C.D. Hall, P. Speers, *JCS Perkin Trans.*, **2**, 1925 (1991).
3. F. Yakuphanoglu, M. Arslan, *Opt. Mater.*, **27**, 29 (2004).
4. F. Yakuphanoglu, M. Arslan, *Solid State Commun.*, **132**, 229 (2004).
5. F. Yakuphanoglu, M. Arslan, M. Kucukislamoglu, M. Zengin, *Sol. Energy*, **79**, 96 (2005).
6. B. Chakraborty, A.S. Mukherjee, B.K. Seal, *Spectrochim. Acta Part A*, **57**, 223 (2001).
7. A. Korolkovas, Essentials of Medical Chemistry, Second ed., Wiley, New York, 1998, Chapter 3.
8. K. Takahashi, K. Horino, T. Komura, K. Murata, *Bull. Chem. Soc. Jpn.*, **66**, 733 (1993).
9. S.M. Andrade, S.M.B. Costa, R. Pansu, *J. Colloid. Interf. Sci.*, **226**, 260 (2000).
10. A.M. Slifkin, Charge-Transfer Interaction of Biomolecules, Academic Press, New York, 1971.
11. F.M. Abou Attia, *Farmaco*, **55**, 659 (2000).
12. K. Basavaiah, *Farmaco*, **59**, 315 (2004).
13. P. Pal, T.N. Misra, J. Phys. D: Appl. Phys., 23, 218 (1990).

14. C.D. Bryan, A.W. Cordes, R.C. Haddon, R.G. Hicks, R.T. Oakley, T.T.M. Palstra, A.S. Perel, S.R. Scottla, Chem. Mater., 6, 508 (1994).

15. G.G. Roberts, D.G. Thomas, J. Phys. C: Solid State Phys., 7, 2312 (1974).

16. H. Kusama, H. Sugihara, Solar Energy Mat. & Solar Cells, 90(7-8), 953 (2006).

17. H.M.A. Salman, M.R. Mahmoud, M.H.M. Abou-El-Wafa, U.M. Rabie, R.H. Crabtree, *Inorg. Chem. Comm.*, **7(11)**, 1209 (2004).

18. N.A. Al-Hashimi, *Spectrochim. Acta Part A*, **60(8-9)**, 2181 (2004).

19. Kh. A. Hassan, *Spectrochim. Acta Part A*, **60(13)**, 3059 (2004).

20. L.I. Bebawy, N. El-Kousy, J.K. Suddik, M. Shokry, *J. Pharm. Biomed. Anal.*, **21(1)**, 133 (1999).

21. M.M. Ayad, *Spectrochim. Acta Part A*, **50(4)**, 671 (1994).

22. E.M. Nour, L. Shahada, *Spectrochim. Acta Part A*, **45(10)**, 1033 (1989).

23. S.M. Teleb, M.S. Refat, *Spectrochim. Acta Part A*, **60(7)**, 1579 (2004).

24. N. Kulevsky, K.N. Butamina, *Spectrochim. Acta.*, **46A**, 79 (1990).

25. E.M. Nour, S.M. Teleb, M.A.F. El-Mosallamy, M.S. Refat, *South Afr. J. Chem.*, **56**, 10 (2003).

26. E.M. Nour, L. Shahada, *Spectrochim. Acta Part A*, **44(12)**, 1277 (1988).

27. L. Shahada, S. Alkaabi, E.M. Nour, *Acta Chim. Hung.*, **127(2)**, 297 (1990).

28. E.M. Nour, S.M. Metwally, M.A.F. El-Mosallamy, Y. Gameel, *Spectrosc. Lett.*, **30**, 1109 (1997).

29. S.R. Salman, S.M. Al-Marsumi, *Spectrochim. Acta Part A*, **49(3)**, 435 (1993).

30. M. Shamsipur, M.H. Mashhadizadeh, *J. Incl. Phenom.*, **38**, 277 (2000).

31. A. Semmani, M. Shamsipur, *J. Chem. Soc., Dalton Trans.*, 2215 (1996).

32. W. Hirsch, J. Greenman, R. Pizer, *Can. J. Chem.*, **71**, 2171 (1993).

33. G.A. Saleh, H.F. Askal, M.F. Radwan, M.A. Omar, *Talanta*, **54(6)**, 1205 (2001).

34. H. Salem, *J. Pharm. Biomed. Anal.*, **29(3)**, 527 (2002).

35. H.W. Kroto, J.R. Heath, S.C. O'Brien, R.F. Smalley, *Nature*, **318**, 162 (1985).

36. E.A. Rohlfing, D.M. Cox, A. Kaldor, *J. Chem. Phys.*, **8**, 13322 (1984).

37. M. Ricco, M. Bisbiglia, R. Derenzi, F. Bolzoni, *Solid State Commun.*, **101**, 413 (1997).

38. F. Kajzar, Y. Okada-Shudo, C. Meritt, Z. Kafafi, *Synth. Methods*, **94**, 91 (1998).

39. D.A. Skoog, Principle of Instrumental Analysis, 3rd edn., Saunders College Publishing, New York, USA, 1985, Chapter 7.

40. W. Kiefer, H.J. Bernstein, *Chem. Phys. Lett.*, **16**, 5 (1972).

41. L. Andrews, E.S. Prochaska, A. Loewenschuss, *Inorg. Chem.*, **19**, 463 (1980).

42. K. Kaya, N. Mikami, Y. Udagawa, M. Ito, *Chem. Phys. Lett.*, **16**, 151 (1972).

43. R. Abu-Eittah, F. Al-Sugeir, *Can. J. Chem.*, **54**, 3705 (1976).

44. H. Tsubomura, R.P. Lang, *J. Am. Chem. Soc.*, **86**, 3930 (1964).

45. I. Harada, J. Tanaka, M.M. Zuno, *J. Phys. Chem.*, **85**, 1789 (1981).

46. R. Rathone, S.V. Lindeman, J.K. Kochi, *J. Am. Chem. Soc.*, **119**, 9393 (1997).

47. G. Briegleb, *Z. Angew. Chem.*, **72**, 401 (1960); G. Briegleb, *Z. Angew. Chem.*, **76**, 326 (1964).

48. L.J. Bellamy, The Infrared Spectra of Complex Molecules, Chapman & Hall, London, 1975.

49. A.G. Maki, R. Forneris, *Spectrochim. Acta*, **23A**, 867 (1967).

50. F.W. Parrett, N.J. Taylor, *J. Inorg. Nucl. Chem.*, **32**, 2458 (1970).

51. U.M. Rabie, *Collect. Czech. Chem. Commun.*, **71(9)**, 1359 (2006).

52. Kh. Hassan, *Spectrochim. Acta Part A*, **60**, 3059 (2004).

53. M.M.A. Hamed, *J. Solution Chem.*, **22(12)**, 1151 (1993).

СИНТЕЗ И СПЕКТРОСКОПСКО ОХАРАКТЕРИЗИРАНЕ НА ПИПЕРИДИН/I$_2$ КОМПЛЕКС С ПРЕНОС НА ЗАРЯД В РАЗЛИЧНИ ХЛОРИРАНИ ОРГАНИЧНИ РАЗТВОРИТЕЛИ

М. С. Рефат[а,б], О. Б. Ибрахим[б], Х. Ал-Дидамони[в], К. М. Абу Ел-Нур[г], Л. Ел-Заят[а]

[а]*Катедра по химия, Факултет на науките, Университет Порт Саид, Порт Саид, Египет*
[б]*Катедра по химия, Факултет на науките, Университет Таиф, Таиф, Кралство Саудитска Арабия*
[в]*Катедра по химия, Факултет на науките, Университет Загазиг, Загазиг, Египет*
[г]*Катедра по химия, Факултет на науките, Университет Суецки канал, Исмаилия, Египет*

(Резюме)

Комплекс с пренос на заряд (ПЗ), образуван между пиперидин (Пип) като донор и йод (I$_2$) като σ-акцептор, е проучен спектрофотометрично. Описан е синтезът и охарактеризирането на пиперидинови ПТ-комплекс на йод, [(Пип)$_2$]I$^+$.I$_3^-$. Този комплекс е получен лесно посредством реакцията на Пип с I$_2$ в CHCl$_3$ като разтворител. Инфрачервена спектроскопия (mid-IR и far-IR), UV-Vis техники и елементен анализ са използвани, за да се характеризира пиперидин/I$_2$ комплекс с пренос на заряд. Методът на Банези-Хилдебранд и негови модификации са приложени за определяне на асоциационната константа (K) и моларния абсорбционен коефициент (ε).

Height of vertical plates with inclined capillary grooves for a redistribution packing layer of packed columns

D. Dzhonova-Atanasova, D. Kolev, N. Kolev

Institute of Chemical Engineering, Bulgarian Academy of Sciences, "Acad. G. Bonchev" Str., Bl.103, 1113 Sofia, Bulgaria

The uniform distribution of the liquid phase over the cross-section of a packed column is a major prerequisite for its effective operation. Regarding various distributor designs, the best uniformity is achieved with devices where the liquid is divided into jets with equal flow-rates. The final liquid redistribution, to obtain uniformity over a cross-section area of the size of a packing element, takes place in the packing itself or in a specially designed redistribution layer. For this purpose a new packing, especially proper for low liquid superficial velocity has been developed and investigated. It consists of parallel vertical polystyrene plates with inclined crossing capillary grooves stamped on them. A computer procedure has been developed for calculating the height of the redistribution layer for a distributor with a given distance between the feed points. The calculated height ensures, with a selected precision, equality of the flow-rates of the liquid phase leaving the capillary grooves. The comparison with other devices shows that for a given degree of uniformity, the new packing is characterized by significantly smaller height.

Key words*: packed columns, liquid distribution, redistribution layer height, capillary grooves, liquid flow-rate, radial liquid spreading coefficient

1. INTRODUCTION

Of all existing packing designs, the packings with vertical walls and especially the honeycomb packings [1-3] are characterized by the lowest pressure drop for a mass transfer unit, but have bad liquid distribution properties. With the purpose to operate as a redistribution layer over a basic layer of this type of packings, a new packing is developed and investigated [4-7]. It consists of vertical polystyrene plates with crossing inclined capillary grooves stamped on their surface, especially proper for low liquid superficial velocity. Changing only the direction of the liquid phase by adding a horizontal component to its velocity vector, it avoids the disadvantage of the existing redistribution packings with inclined walls [8-10] to turn also the direction of the gas flow which leads to increasing of the pressure drop.

The plates can operate as a redistribution layer between the distributor and the main packing and also as a part of the liquid distributor. A scheme of such a device is presented in Fig. 1. The liquid phase leaves the pipes (troughs) (1) of the distributor through orifices perforated in them and runs over plates (2). Here it is regularly distributed by the inclined crossing capillary grooves. From

plates (2) the liquid flows over plates (3) and is regularly distributed by the grooves. The uniform distribution after plates (2) and (3) ensures regular distribution over the whole apparatus cross-section. Fig. 2 is a photograph of a sample plate with stamp inclined grooves.

For implementation of the new device in the industry, it is necessary to have a method for calculation of the height of the plate under which the distribution of the liquid phase will be uniform with a preliminary given precision.

The aim of the present work is to propose a calculation procedure for determination of the height of the new redistribution layer at a given distance between the feed points and degree of uniformity and to compare the new packing design with the existing.

2. CALCULATION PROCEDURE
2.1. Calculation equations

Fig. 3 shows a scheme of the capillary grooves on the surface of the vertical plate between two feed points A and A_1. Here l, m, is distance between the feed points. The liquid from a feed point flows down and is divided into the grooves (shown by arrows). The flow between each two drip points is symmetrical in respect to the axis A'B'. That is why the calculations are performed only for one of the symmetrical parts, i.e. the grooves between lines AB and A'B'.

The proposed procedure for calculation of the flow-rates in each part of the grooves uses the following equations.

1. Equation of the material balance at a crossing point with coordinates x_i, y_j:

$$V_{i,j} + U_{i,j} = V_{i-1,j+1} + U_{i-1,j-1} \qquad (1)$$

where $U_{i,j}$ and $V_{i,j}$ are the outgoing flow-rates in m^3/s in direction from line AB to A'B' and from line A'B' to AB respectively (Fig. 3) at a crossing point with coordinates (x_i, y_j). The beginning of the accepted coordinate system is in the feed point A. The computations are made in discrete points with vertical distance between them $\Delta x = x_i - x_{i-1}$, and horizontal distance $\Delta y = y_j - y_{j-1}$ in m, Fig. 3, in the calculation region AA'B'B, $i = 0 \div m$, $j = 0 \div n$ are current numbers of steps along x and y axis respectively, where m and n are the respective maximal numbers of steps.
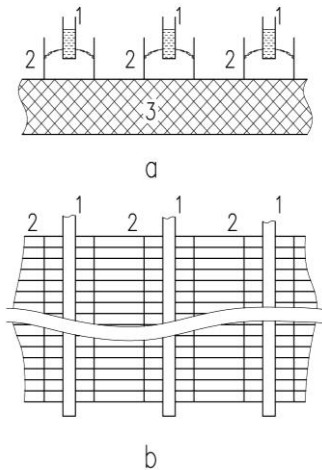
Fig. 1. Liquid phase distributor including plates with inclined crossing grooves. (a) Cross–section view; (b) Above view; (1) Distributing pipes (troughs); (2) Distributor plates with grooves; (3) Redistribution layer plates with grooves.

Fig. 2. Polystyrene packing plate with stamped inclined capillary grooves.

2. Equation for the maximal flow-rate in a capillary groove, just below the drip point A (in Fig. 3), where $i = j = 0$, [7]:

$$Re_{max} = 0.07\, Ga^{0.79}\, (sin\ \alpha)^{0.94}, \qquad (2)$$

where α is the groove inclination angle, Fig. 3; $Re_{max} = U_{max}/vd_h$ is Reynolds number of the flow in the part of the groove just below the feed point; d_h is the hydraulic diameter in m, defined as $d_h = 4ab/(2b+a)$, where a and b are the groove width and depth in m; U_{max} is maximum flow-rate in the parts of the groove just under the feed point, m^3/s; v is kinematic viscosity, m^2/s; $Ga = gd_h^3/v^2$ is Galilei number; g is gravity constant, m/s^2.

3. Equation for the outgoing flow-rates at the crossing points on line AC, where $i = j$ and the flow-rates $V_{i-1,j+1} = 0$, [7]:

$$\frac{U_{i,j}}{U_{i-1,j-1}} = 0.71 Ga^{-0.17\left(\frac{U_{i-1,j-1}}{U_{max}}\right)+0.14(sin\ \alpha)} \times$$
$$\times Re_{i-1,j-1}^{0.38\left(\frac{U_{i-1,j-1}}{U_{max}}\right)-0.31(sin\ \alpha)} \qquad (3)$$

$Re_{i-1,j-1} = \dfrac{U_{i-1,j-1}}{v\, d_h}$ - Reynolds number in the groove

between points (x_{i-1}, y_{j-1}) and (x_i, y_j).

4. Equation for the outgoing flow-rates at the crossing points under line AC, where $i \neq j$ and the flow-rates $V_{i-1,j+1} > 0$:

$$\frac{U_{i,j}}{U_{i-1,j-1} + V_{i-1,j+1}} = 0.5 \Big[0.53 Ga^{0.09(sin\ \alpha)} \times$$
$$\times Re_{i-1,j-1}^{0.06\left(\frac{U_{i-1,j-1}}{U_{max}}\right)} (sin\ \alpha)^{-0.4} \Big]^{\frac{U_{i-1,j-1}-V_{i-1,j+1}}{U_{max}}} \qquad (4)$$

At the boundaries of the calculation region:

1. Initial point A: $U_{0,0} = Q/2$, where Q is flow-rate at a feed point, m^3/s;

2. Axis of symmetry, line AB: $U_{i,0} = V_{i-1,1}$ – perfect deflection;

3. Line CB' $V_{i,n} = U_{i-1,n-1}$ - perfect deflection. To have flow symmetry for the end points next to the column wall, the distance between the plate vertical edge and the closest feed point is equal to $1/2$ AA_1 and the end grooves are stopped.

4. Line AC $i = j$: $V_{i-1,j+1} = 0$, $U_{i,j}$ calculated by Eq. (3).

Inside the boundaries of the calculation region $U_{i,j}$ is calculated by Eq. (4)

Assumptions

1. $Q = 2U_{max}$, i.e the liquid flow-rate at the drip point is chosen equal to the maximum flow-rate the first channel is able to take up according to Eq. (2)

without liquid overspilling. Although the calculation results presented are obtained with this assumption, the proposed calculation procedure gives the possibility to use larger flow-rates at the drip point with overspilling and taking the liquid by the channels situated downwards.

2. Eqs. (3) and (4) are obtained in [7] by processing experimental data for which

$$\frac{U_{i,j}}{U_{max}} \geq 30\% \qquad (5)$$

This ratio is used to characterize the filling up with liquid of the groove cross-section. The smaller is the liquid flow-rate in the groove, the smaller is the degree of its filling up with liquid and the greater the possibility for the liquid to be completely drawn out in the crossing groove. It means that different equations describe the data for different extent of filling up.

3. Eqs. (2) and (3) are proved only for laminar hydrodynamic regime [7].

Variants of plate design

1. To get round the constraint for laminar flow, at turbulent regime conditions the single groove can be replaced by several parallel channels of smaller hydraulic diameter, which ensures laminar regime in each of them.

2. To ensure a greater degree of filling up of the grooves with liquid satisfying Eq. (5), for an industrial packing the dimensions of the groove cross-section can be reduced downstream of a given row of crossing points. At the same time, reduction of the groove depth will reduce the packing pressure drop.

3. To increase the number of the drip points after the redistribution plate, the number of the channels can be redoubled after achieving a given degree of uniformity at a row of crossing points (plate design in Fig. 2). The reduction of the distance between the crossing points at a given inclination of the grooves leads to increasing of the necessary height of the vertical plate for obtaining a prescribed degree of uniformity, which follows from the distribution model of Tour and Lerman [11].

2.2. Steps of the calculation procedure:

1. Input data:
- angle of inclination of the grooves α;
- steps between the crossing points Δy, $\Delta x = \Delta y.tg\, \alpha$;
- groove width and depth, a and b;
- distance between the feed points, l;

- physico-chemical properties of liquid phase;
- flow-rate at the feed point Q dependent on the liquid superficial velocity and the number of the drip points of the distributor per unit of the column cross-section.

2. Calculating the flow-rates $U_{i,j}$ and $V_{i,j}$ successively in each crossing point of a given horizontal row on the plate using their values determined at the previous horizontal row of crossing points $U_{i-1,j-1}$, $V_{i-1,j+1}$, by Eq. (1)-(4) with the relations at the boundaries.

3. When at a certain crossing point condition Eq. (5) is not fulfilled, the groove hydraulic diameter is reduced preserving the ratio between the groove depth and width. The reduced diameter is determined by $d_h' = d_h \left(\dfrac{U'_{max}}{U_{max}} \right)^{0.297}$ following from Eq. (2), where $U'_{max} = U_{i,j}/0.3$, $U_{i,j}$ is the flow-rate at the current point. It is assumed that $d_h = d_h'$ downstream of the current row of crossing points with coordinate x_d, i.e. for $x \geq x_d$ (down the dashed line in Fig. 4). This means that after size reduction the filling up of the channel with the smallest flow-rate will be equal to 30% of the maximal possible.

4. If $Q_{mean} < 30\% U_{max}$, where $Q_{mean} = U_{max}/n$, and for $x_i < x_n$ condition Eq. (5) is not fulfilled, the hydraulic diameter is not changed until $x_i = x_n$ and the calculated height is increased with Δx as many times as these conditions occur.

Step 4 needs some explanation. In the region above C, the point of meeting of the two flows from adjacent feed points, the liquid flows predominantly in the channels along line AC ($x_i = x_n$) and the flow-rates there are much greater than the flow-rates from the rest of the points of a given horizontal row. By the calculation it was found that this condition could be approximately evaluated by the inequality $Q_{mean} < 30\% U_{max}$. So for the channels downstream of such a horizontal row if we reduce the groove cross-section according to step 3, the channel along AC takes in flow-rate much greater than U_{max} (with about 50%). If we decrease the cross-section so as the channel along AC to take in flow-rate equal to U_{max}, the degree of filling up of the channel with the minimal flow-rate is below 30%. Both possibilities result in going out of the range of validity of the equations used. That is why it is accepted that in this case the groove cross-section is unchanged and the results for the redistribution at that row of crossing points are not the actual. Since at the worst the liquid is not redistributed there at all, the calculated plate height should be increased with as many steps as the

451

number of "non-distributing" rows, i.e. the plate height is determined with a small reserve.
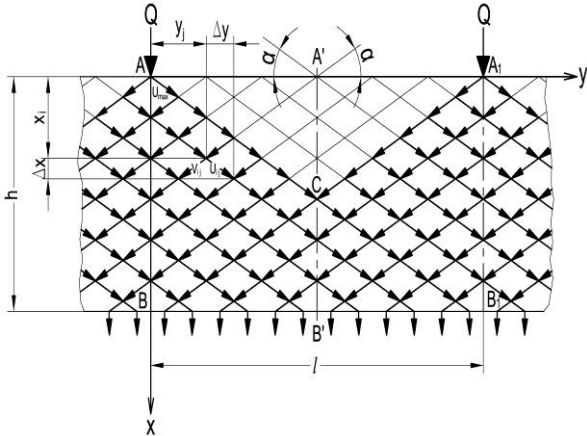
Fig. 3. Liquid spreading in the capillary grooves of a vertical plate. The arrows show the directions of the flows in the grooves. A, A_1 –Feed points; A'B' -Axis of symmetry.

5. Comparing the determined flow-rates from the crossing points of a horizontal row. If they differ more than the prescribed degree of uniformity the vertical coordinate, i.e current plate height, is increased,

$$x_i = x_{i-1} + \Delta x,$$

and step 2 is repeated for the next row of crossing points.

6. The calculation stops (at $i=m$, $x=x_m$) when the flow-rates in all the grooves at a certain horizontal row become practically equal with deviation from the mean value not more than a preliminary chosen percentage (e.g. 5%). The first and the end row of crossing points are located at a distance of $\Delta x/2$ from the plate ends. The design of the plate top and bottom edges ensures the best taking up of the liquid from the drip points above the plate and maximal number of drip points below the plate. According to Fig. 3 the plate height h is determined by

$$h = x_m + \Delta x. \tag{6}$$

Since the grooves distribute the liquid phase only in one vertical plane, the packing layer should comprise two rows of parallel plates, the plates of the second row perpendicular to the first. The packing layer height h_l is calculated by

$$h_l = 2h. \tag{7}$$

This is not valid for the liquid distributor in Fig. 1, where only one layer of redistribution packing is necessary because the plates with inclined grooves included in the distributor construction spread the

liquid in planes perpendicular to the plates of the packing layer below.

3. PACKING LAYER HEIGHT
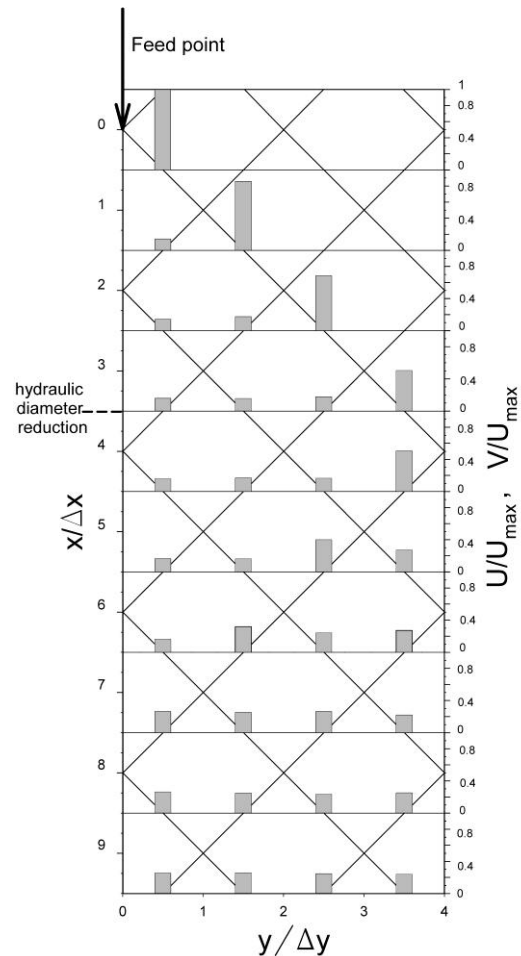
Fig. 4. Flow-rate distribution along a vertical plate with inclined grooves.

Fig. 4 presents the transition to equal flow-rate distribution along a vertical plate with capillary grooves, the bars representing the dimensionless flow-rates from a crossing point $U_{i,j}/U_{max}$ and $V_{i,j}/U_{max}$.

The calculation is performed with the following input data:

- angle of inclination of the grooves $\alpha=45°$;
- steps between the crossing points $\Delta y = 14$ mm;
- groove width and depth 2×2 mm;
- distance between the feed points $l=112$ mm;
- physico-chemical properties of liquid phase, water dynamic viscosity $\mu=1 \times 10^{-3}$ Pa.s and density $\rho=1000$ kg/m^3, (at a temperature of 20ºC);
- flow-rate at the drip point $Q=2U_{max}=3.7 \times 10^{-6}$ m^3/s.

At the horizontal line $x_d/\Delta x=3.5$, Fig. 4, the hydraulic diameter has been reduced from $d_h =2.67$

mm (2×2 mm) to $d_h' = 2.23$ mm (1.67×1.67 mm). The plate height is determined by the horizontal row at which the flow-rates become equal with the prescribed precision of 5% of the mean flow-rate $Q_{mean}=0.462×10^{-6}$ m³/s. As seen from Fig. 4, uniform flow-rates have been achieved at $x_m/\Delta x=9$, so the plate height, Eq. (6), is $h=10\Delta x=140$ mm. The packing layer height, Eq. (7), is

$$h_l=2h=280 \text{ mm}.$$

When using the new redistribution layer under the liquid phase distributor presented in Fig. 1 the layer height is

$$h_l=h=140 \text{ mm}$$

because the first layer of the redistribution packing is replaced by the distributor plates (2) with grooves presented in Fig. 1 as a part of the liquid phase distributor.

Since the new redistribution packing is intended for low liquid superficial velocity and because of the lack of such type of packings operating in similar regimes, it is compared with redistribution packings efficient at higher liquid superficial velocities, inclined Raschig rings [9], block packing of inclined plastic sheets [10] and inclined ceramic honeycomb packing [12].

Table 1 shows the calculated by means of Eq. (7) layer heights for different angles of groove inclination $\alpha = 45^o$, 30° and 15° versus the distance between the feed points, which is divisible by the horizontal distance between the grooves. The results show that the necessary plate height increases with increasing of the feed points distance. The observed exceptions for the plates $\alpha=45^o$ and $\alpha=30^o$ are due to the accepted precision of the calculations in respect to degree of uniformity of the liquid distribution and the circumstance that the height is multiple of the vertical distance between the grooves.

Table 1. Comparison of packing layer heights

Distance between drip points l, m	Packing layer height h_l, m					
	Plates with inclined grooves $\alpha=45^o$	Plates with inclined grooves $\alpha=30^o$	Plates with inclined grooves $\alpha=15^o$	Inclined ceramic Raschig rings, 49.1/41.2 mm, 16° $D=2.85×10^{-3}$ m, [9]	Inclined plastic sheets, 22° $D=1.4×10^{-3}$ m, [10]	Inclined ceramic honeycomb packing 27/50 mm, 24° $D=2.67×10^{-3}$ m [12]
0.0560	0.1960	0.1132	0.0375	0.1067	0.2172	0.1139
0.0840	0.3920	0.1617	0.0450	0.2400	0.4886	0.2562
0.1120	0.2800	0.1455	0.0675	0.4267	0.8687	0.4555
0.1400	0.3360	0.1940	0.0600	0.6667	1.3573	0.7117
0.1680	0.3640	0.2263	0.1050	0.9601	1.9545	1.0248
0.1960	0.3920	0.1940	0.1425	1.3068	2.6603	1.3949

In Table 1 the height of the new packing is compared with the heights of an arranged packing of inclined ceramic Raschig rings with an outside diameter of 49.1 mm, an element height of 41.2 mm and an inclination angle of 16º, [9], a block packing of inclined plastic sheets with an inclination angle of 22º, [10] and an inclined ceramic honeycomb packing with an inscribed circle diameter of 27 mm, an element height of 49 mm and inclination angle of 24º, [12]. The previous investigations [9,10,12] show that just these angles are the optimal for the efficiency of the respective picking. The height ensuring flow uniformity with accuracy 5% of the mean superficial velocity is obtained by the following relation:

$$h = 0.09695\frac{l^2}{D} , \qquad (8)$$

proposed in [13] using the simple model of Kolev [14]. Here D, m, is radial liquid spreading coefficient.

Table 1 shows that the necessary height of the bed of plates with inclined grooves for a given distance between the drip points and liquid flow uniformity is much smaller than the heights of the packings from literature.

It is known, that the increasing of the liquid superficial velocity leads to increasing of the spreading coefficient [10] for the packing with inclined plates and does not affect this coefficient of the packings from [9 and 12]. That is why the value of D for inclined plates is taken for the region

of low superficial velocities, where it does not depend on liquid superficial velocity.

4. PACKING RADIAL SPREADING COEFFICIENT

The radial spreading coefficient of the new packing is determined by Eq. (8) with the calculated heights in Table 1. Table 2 shows that D varies for different distances between drip points, i.e. different superficial velocities, because as expected the applied relation is not adequate. It is based on the assumption that the liquid spreading down a packing bed can be described in terms of rivulets of stable but randomly orientated path through the bed, which is a homogenous medium characterized merely by an empirical radial liquid spreading coefficient. Strictly speaking the random walk hypothesis accepted in [9–12] is inapplicable for arranged packings like these in [9,10,12], and yet it was used there for evaluation and comparison of their spreading ability with other packings. It is especially improper for the present new redistribution packing, where the path of the liquid rivulets is determined by the crossing grooves. That was the reason to develop a principally new method for calculation of the liquid spreading in the packing bed, the purpose of the present work.

Table 2. Radial spreading coefficients of packing of vertical plates with grooves

Distance between drip points	Plates with inclined grooves $\alpha=45^{\circ}$	Plates with inclined grooves $\alpha=30^{\circ}$	Plates with inclined grooves $\alpha=15^{\circ}$
l, m	D, m	D, m	D, m
0.0560	0.001551	0.002686	0.008108
0.0840	0.001745	0.004231	0.015202
0.1120	0.004343	0.008358	0.018017
0.1400	0.005655	0.009795	0.03167
0.1680	0.007517	0.012092	0.02606
0.1960	0.009501	0.019198	0.026136

5. CONCLUSION

A procedure is developed for calculation of the height of the redistribution bed of vertical plates with inclined capillary grooves at given degree of uniformity, distance between the drip points and required design. It uses equations proposed in [6, 7], obtained on the basis of an experimental study of the flow-rates in inclined crossing capillary grooves on vertical plates. On the basis of the investigation the new packing intended for low liquid superficial velocities is evaluated by comparison with other distributor packings showing that the necessary layer height of the proposed packing is much smaller than the heights of the packings from literature.

REFERENCES

1. N. Kolev, K. Winkler, R. Daraktchiev, Z. Brosch, *Chem. Ind.* **8,** 43 (1986) (in Russian).
2. N. Kolev, R. Billet, Kr. Semkov, *Fat Sci. Technol.,* **92**, 291 (1990).
3. N. Kolev, R. Billet, Kr. Semkov, J. Mackowiak, Sv. Nakov, *Fat Sci. Technol.*, **96**, 267 (1994).
4. D. Kolev, N. Kolev, *Festschrift mit Beitragen zur Verfahrens - und Umwelttechnik*, Ruhr-Universität Bochum, 1994, p. 143.
5. N. Kolev, Kr. Semkov, D. Kolev, Bulg. Patent 47679 (1996).
6. D. Kolev, N. Kolev, D. Dzhonova-Atanasova, Tz. Tzvetkov, Abstr. Jubilee Sci. Conf. Int. Partic. - UCTM, Sofia, 2003, p. 197.
7. D. Kolev, D. Dzhonova-Atanasova, N. Kolev, *Chem. Eng. Process.*, **47**, 833 (2008)
8. N. Kolev, R. Daraktschiev, Bulg. Patent. 27123 (1979).
9. R. Daraktschiev, N. Kolev, G. Paskalev, *Verfahrenstechnik*, **15**, 568 (1981).
10. N. Kolev, El. Istatkova, R. Daraktschiev, *Chem. Eng. Process.*, **21**, 77 (1987).
11. R. Tour, F. Lerman, *Trans. Am. Inst. Chem. Engrs.*, **40**, 79 (1944).
12. R. Darakchiev, N.Kolev, S. Nakov, *Chem. Eng. Process.*, **37**, 141 (1998).
13. Kr. Semkov, *Chem. Eng. Sci.*, 46, 1393 (1991)
14. N. Kolev, *Theor. Found. Chem. Eng.*, **16**, 129 (1982) (in Russian).

ВИСОЧИНА НА ВЕРТИКАЛНИ ПЛАСТИНИ С НАКЛОНЕНИ КАПИЛЯРНИ КАНАЛИ ЗА ПРЕРАЗПРЕДЕЛИТЕЛЕН ПЪЛНЕЖЕН СЛОЙ В КОЛОНИ С ПЪЛНЕЖ

Д. Джонова-Атанасова*, Д. Колев, Н. Колев

Институт по инженерна химия, Българска академия на науките, ул. "Акад. Г. Бончев", бл. 103, 1113 София, България

(Резюме)

Равномерното разпределение на течната фаза по напречното сечение на колоната с пълнеж е основна предпоставка за ефективна работа на апарата. Сред съществуващите оросителни устройства най-добра равномерност се постига при тези от тях, които разпределят течността на струйки с равни дебити. Крайното преразпределение до равномерност по напречно сечение с размери от порядъка на пълнежен елемент се осъществява в самия пълнеж или в специално конструиран преразпределителен пълнежен слой. За тази цел е разработен и изследван нов пълнеж, особено подходящ за ниски плътности на оросяване. Той се състои от успоредни вертикални пластини с наклонени пресичащи се капилярни канали, щамповани върху тях. Разработена е компютърна програма за изчисляване на височината на преразпределителния слой при дадено разстояние между точките на оросяване на оросителното устройство. Изчислената височина осигурява, с избрана точност, равенство на дебитите на течната фаза, напускаща капилярните канали. Сравнението със съществуващите устройства показва, че при дадена степен на равномерност новият пълнеж се характеризира със значително по-малка височина.

Pressure drop of vertical plates with inclined capillary grooves for a redistribution packing layer of packed columns

D. Kolev, D. Dzhonova-Atanasova*, N. Kolev

Institute of Chemical Engineering- Bulgarian Academy of Sciences, Acad. G. Bonchev Str., Bl.103, 1113 Sofia, Bulgaria

The uniform distribution of the liquid phase over the cross-section of a packed column is a major prerequisite for its effective operation. Regarding various distributor designs, the best uniformity is achieved with devices, where the liquid is divided into jets with equal flow-rates. The final liquid redistribution, to obtain uniformity over a cross-section area of the size of a packing element, takes place in the packing itself or in a specially designed redistribution layer. For this purpose a new packing, especially proper for low liquid superficial velocity, has been developed and investigated. It consists of parallel vertical polystyrene plates with inclined crossing capillary grooves stamped on their surface. In the present work experimental data for the pressure drop of the new redistribution packing at different gas velocities and liquid superficial velocities have been obtained and compared with data for other packings designed with the same purpose. The results prove that of all compared redistribution packings, the proposed packing is characterized by the lowest pressure drop which is connected with its advantage to change the direction of the liquid phase without changing the direction of the gas phase.

Key words: packed column, pressure drop, liquid distribution, redistribution layer, capillary grooves, comparison.

INTRODUCTION

Of all existing packing designs the packings with vertical walls and especially the honeycomb packings [1-3] are characterized by the lowest pressure drop for a mass transfer unit, but they have bad liquid distribution properties. With the purpose to operate as a redistribution layer over a basic layer of this type of packings, a new packing is developed and investigated [4-6]. It consists of vertical polystyrene plates with crossing inclined capillary grooves stamped on their surface, especially proper for low liquid superficial velocity. Changing only the direction of the liquid phase by adding a horizontal component to its velocity vector, it avoids the disadvantage of the existing redistribution packings with inclined walls [8-10] to turn also the direction of the gas flow which leads to increasing of the pressure drop. The aim of the present work is to investigate the pressure drop of the new packing and to compare it with the respective data for other redistribution packings.

EXPERIMENTAL

For evaluation of the pressure drop of the proposed packing, experiments have been carried out with vertical plates with inclined grooves with a height of the packing elements of 90 mm, a distance between the grooves of 20 mm and groove angle 45°. The grooves are with a square cross-section 2x2 mm with rounded corners formed by stamping on the groove surface. The pressure drop investigations are performed for dry packing and for liquid superficial velocities of 3×10^{-3}- 21.4×10^{-3} $m^3/(m^2 s)$, much higher than the operational regime range of the new packing applicable for superficial velocities one order lower (the values in Table 1) than the minimal experimental superficial velocity. The measurements are obtained in these regimes with the purpose of comparing with the available data for other redistribution packings.

The pressure drop of the packing was measured in a packed column with a cross-section of 175×225 mm at a total height of the packing of 1170 mm. The liquid was regularly distributed by means of a shower type distributor located in an enlargement of the column top.

The results for the pressure drop of a layer 1 m high, $\Delta P/H$, where ΔP, Pa, is layer pressure drop and H, m,- total height of the packing, are given in Fig. 1 and compared to data for the pressure drop of inclined Raschig rings [8]. The geometrical

---

* To whom all correspondence should be sent:
E-mail: dzhonova@.bas.bg

characteristics of the rings are as follows: an outside diameter of 49.1 mm, an element height of 41.2 mm and an inclination angle of 16°. Of all investigated inclined ring packings the described one is characterized by lowest pressure drop for a given degree of redistribution [8]. The lines for the pressure drop of the inclined rings 2', 3', 4' are interpolated from the experimental data in order to compare the pressure drop of the two packings at equal liquid superficial velocities L, m³/(m²s). The original data in [8] are measured for L=0; 2.3x10⁻³; 3.3x10⁻³ and 6.4x10⁻³ m³/(m²s) at the same range of gas velocities w, m/s. It is seen that at a given gas velocity w and liquid superficial velocity L the pressure drop of 1 meter layer of inclined rings is about 40% higher than of the new packing with grooves.
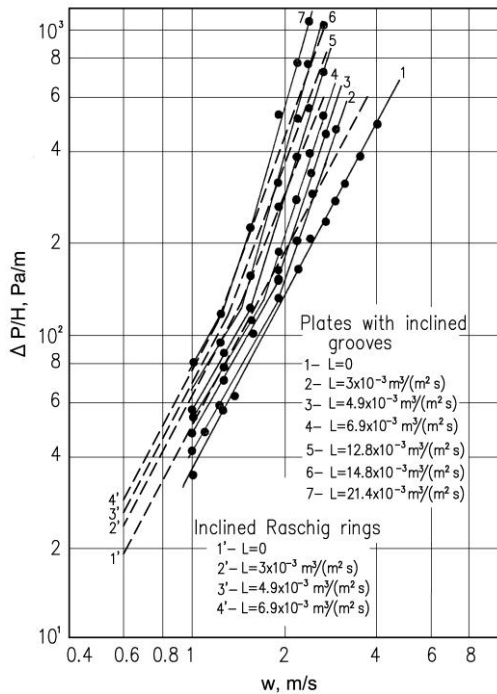
Fig. 1. Pressure drop of plates with inclined grooves and inclined Raschig rings [8] versus the gas velocity at different liquid superficial velocities.

The pressure drop of a redistribution layer with a height h_l ensuring a given degree of uniformity of the liquid superficial velocity is expressed by $\frac{\Delta P}{H} h_l$. The pressure drop of the proposed new redistribution packing layer is compared to the layer pressure drop of the following redistribution packings from literature: arranged packing of inclined ceramic Raschig rings with an outside diameter of 49.1 mm, an element height of 41.2 mm and an inclination angle of 16°, [8], Fig. 2; block packing of inclined plastic sheets with an inclination angle of 22°, [9], Fig. 3; inclined

ceramic honeycomb packing with an inscribed circle diameter of 27 mm, an element height of 49 mm and inclination angle of 24°, [10], Fig. 4. The compared data for each type of packing are chosen for these inclination angles of packing elements which are found to be the optimal for the efficiency of the respective picking.
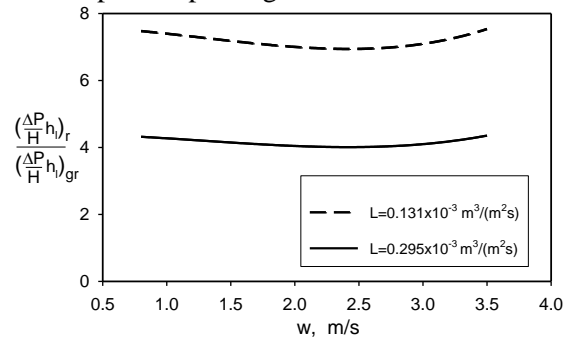
Fig. 2. Ratio of pressure drop of packing layer with inclined Raschig rings [8] to pressure drop of packing layer with grooves $\left(\frac{\Delta P}{H} h_l\right)_r \bigg/ \left(\frac{\Delta P}{H} h_l\right)_{gr}$ versus gas velocity at different values of liquid superficial velocity.
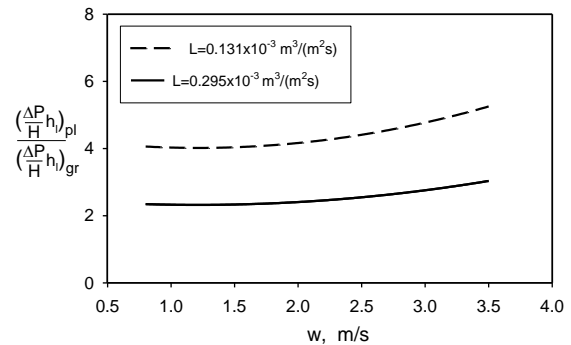
Fig. 3. Ratio of pressure drop of packing layer with inclined plates [9] to pressure drop of packing layer with grooves $\left(\frac{\Delta P}{H} h_l\right)_{pl} \bigg/ \left(\frac{\Delta P}{H} h_l\right)_{gr}$ versus gas velocity at different values of liquid superficial velocity.
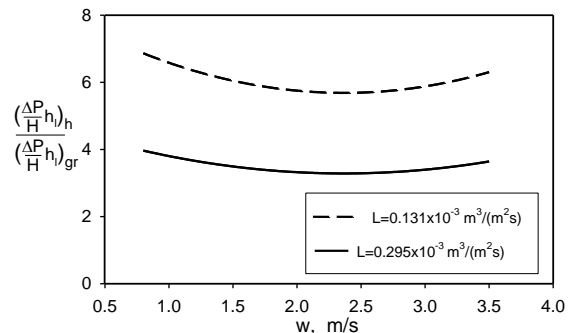
Fig. 4. Ratio of pressure drop of layer with inclined honeycomb packing [10] to pressure drop of packing layer with grooves $\left(\frac{\Delta P}{H} h_l\right)_h \bigg/ \left(\frac{\Delta P}{H} h_l\right)_{gr}$ versus gas velocity at different values of liquid superficial velocity.

457

RESULTS AND DISCUSSION

The heights of the redistribution layers of the compared packings, Table 1, are calculated in [6] at two distances l, m, between the drip points. The liquid superficial velocity is determined as $L=Qn$, where $Q=3.7 \times 10^{-6}$ m^3/s is the maximal flow-rate the grooves under a drip point can take up without liquid overspilling, calculated in [6] for the considered groove sizes, and n is the number of drip points per square meter of the apparatus cross-section determined from the distance between the drip points as $n=1/l^2$. The comparison is performed using the pressure drop experimental data $\Delta P/H$ for dry packing $L=0$, assuming that for these extremely low superficial velocities the error of calculation with the pressure drop for dry packing is negligible.

The heights of the redistribution layer of plates with grooves in Table 1 are half of the heights obtained in [6] for the same distances between drip points. The calculated height necessary for liquid phase regular distribution is doubled in [6] because the crossing grooves distribute the liquid phase only in one vertical plane and the packing layer should comprise two rows of parallel plates, the plates of the second row perpendicular to the first. But this is not valid when the role of first row is performed by the vertical plates with stamped grooves mounted as a part of the liquid phase distributor [6, Fig. 1]. In that case in the redistribution layer only one row of plates is necessary because the upper row of plates included in the distributor construction spread the liquid in planes perpendicular to the row below. Because the distance between the vertical plates in the distributor is significantly greater, than this in the redistribution packing layer, the flow-rate in the distributor grooves should be greater too. That is why to keep similar hydrodynamic regime in these grooves, each of them should be composed of several single parallel channels like those in the redistribution packing layer. It should be mentioned that the pressure drop of the liquid distributor is negligibly low due to its great free cross-section.

The layer heights of the compared packings from the literature [8-10], Table 1, are obtained in [6] by the relation:

$$h = 0.09695 \frac{l^2}{D} \; ,$$

proposed in [11] using the simple model of Kolev [12], where l, m is distance between drip points and D, m, is radial liquid spreading coefficient.

Fig. 2 shows that the pressure drop of a redistribution layer of the proposed packing with grooves $\left(\frac{\Delta P}{H} h_l \right)_{gr}$ for the same degree of uniformity after it and gas velocity is lower over 4 times at $L=0.295 \times 10^{-3}$ m^3/(m^{2}s) and over 7 times at $L=0.131 \times 10^{-3}$ m^3/(m^{2}s) than the pressure drop of a redistribution layer of Raschig rings $\left(\frac{\Delta P}{H} h_l \right)_r$. The indices gr and r denote plates with grooves and rings respectively.

Table 1. Comparison of packing layer heights calculated in [6] ensuring uniform flow-rate distribution as a function of the distance between the drip points.

Distance between drip points l, m	Superficial velocity L m^3/(m^{2}s) $\times 10^3$	Packing layer height h_l, m					
		Plates with inclined grooves 45°	Plates with inclined grooves 30°	Plates with inclined grooves 15°	Inclined Raschig rings, 16° $D=2.85 \times 10^{-3}$ m, [8]	Inclined plastic sheets, 22° $D=1.4 \times 10^{-3}$ m, [9]	Inclined ceramic honeycomb packing 24° $D=2.67 \times 10^{-3}$ m, [10]
0.112	0.295	0.140	0.07275	0.03375	0.4267	0.8687	0.4555
0.168	0.131	0.182	0.11315	0.0525	0.9601	1.9545	1.0248

The results of similar comparison in Figs. 3 and 4 with other redistribution packings from literature are the following:

- The pressure drop of the new redistribution layer is lower over 2 times at L=0.295x10^{-3} m^3/(m^{2}s) and over 4 times at L=0.131x10^{-3} m^3/(m^{2}s) than the pressure drop of a redistribution layer of plate packing, $\left(\dfrac{\Delta P}{H} h_l\right)_{pl}$, Fig. 3. The index pl denotes plate packing.

- The pressure drop of the new redistribution layer is lower over 3 times at L=0.295x10^{-3} m^3/(m^{2}s) and over 6 times at L=0.131x10^{-3} m^3/(m^{2}s) than the pressure drop of a redistribution layer of honeycomb packing $\left(\dfrac{\Delta P}{H} h_l\right)_h$, Fig. 4. The index h denotes honeycomb packing.

CONCLUSION

Experimental data for the pressure drop of a new packing, designed to operate at low liquid superficial velocity as a redistribution layer of a packed bed column, are obtained and a comparison with other redistribution packings from literature is carried out. The results show that at liquid superficial velocity of 0.131x10^{-3} m^3/(m^{2}s) the pressure drop of the proposed new packing layer at the same gas velocity and redistribution degree is over 4 times lower than that of inclined ceramic Raschig rings [8], over 2 times lower than that of inclined plastic plates [9] and over 3 times lower than that of inclined ceramic honeycomb packing [10] when using a usual type of liquid phase distributor.

REFERENCES

1. N. Kolev, K. Winkler, R. Daraktchiev, Z. Brosch, *Chem. Ind.* **8**, 43 (1986) (in Russian).
2. N. Kolev, R. Billet, Kr. Semkov, *Fat Sci. Technol.*, **92**, 291 (1990)
3. N. Kolev, R. Billet, Kr. Semkov, J. Mackowiak, Sv. Nakov, *Fat Sci. Technol.*, **96**, 267 (1994)
4. D. Kolev, N. Kolev, *Festschrift mit Beitragen zur Verfahrens - und Umwelttechnik*, Ruhr-Universität Bochum, 1994, p. 143
5. D. Kolev, D. Dzhonova-Atanasova, N. Kolev, *Chem. Eng. Process.*, **47**, 833 (2008)
6. D. B. Dzhonova-Atanasova, D. N. Kolev, N. N. Kolev, *Bulg. Chem. Commun.*, **43**, No 3, (2011) (accepted for publication)
7. N. Kolev, R. Daraktschiev, Bulg. Patent. 27123 (1979)
8. R. Daraktschiev, N. Kolev, G. Paskalev, *Verfahrenstechnik*, **15**, 568 (1981)
9. N. Kolev, El. Istatkova, R. Daraktschiev, *Chem. Eng. Process.*, **21**, 77 (1987)
10. R. Daraktschiev, N. Kolev, S. Nakov Chem. Eng. Process., 37, 141 (1998)
11. Kr. Semkov, *Chem. Eng.. Sci.*, **46**, 1393 (1991)
12. N. Kolev, *Theor. Found. Chem. Eng.*, **16**, 129 (1982) (in Russian)

ХИДРАВЛИЧНО СЪПРОТИВЛЕНИЕ НА ВЕРТИКАЛНИ ПЛАСТИНИ С НАКЛОНЕНИ КАПИЛЯРНИ КАНАЛИ ЗА ПРЕРАЗПРЕДЕЛИТЕЛЕН ПЪЛНЕЖЕН СЛОЙ В КОЛОНИ С ПЪЛНЕЖ

Д. Колев, Д. Джонова-Атанасова*, Н. Колев

Институт по инженерна химия, Българска академия на науките, ул. "Акад. Г. Бончев", бл. 103, 1113 София, България

(Резюме)

Равномерното разпределение на течната фаза по напречното сечение на колоната с пълнеж е основна предпоставка за ефективна работа на апарата. Сред съществуващите оросителни устройства най-добра равномерност се постига при тези от тях, които разпределят течността на струйки с равни дебити. Крайното преразпределение до равномерност по напречно сечение с размери от порядъка на пълнежен елемент се осъществява в самия пълнеж или в специално конструиран преразпределителен пълнежен слой. За тази цел е разработен и изследван нов пълнеж, особено подходящ за ниски плътности на оросяване. Той се състои от успоредни вертикални пластини с наклонени пресичащи се капилярни канали, щамповани върху тях. В настоящата работа са получени експериментални данни за хидравличното съпротивление на новия преразпределителен пълнеж при различни скорости на газа и плътности на оросяване. Сравнението с данни за други съществуващи пълнежи със същото предназначение доказва, че хидравличното съпротивление на предложеният пълнеж е най-ниско, което се дължи на неговото предимство пред сравняваните преразпределителни пълнежи да променя посоката на течната фаза без да променя посоката на газа.

1,5-diphenylpenta-1,4 dien-3-ones: A novel class of free radical scavengers

Nagaraja Naik*, H. Vijay Kumar, S. Swetha

Department of Studies in Chemistry, University of Mysore, ManasagangotriMysore – 570 006, Karnataka, India

A series of 1,5-diphenylpenta-1,4-dien-3-ones were synthesized by conjugating benzalacetone with different substituted benzaldehydes. The general synthetic strategy employed for the synthesis of the compounds was based on mixed aldol condensation reaction in the presence of strong base. The structures of newly synthesized compounds were characterized by spectral and elemental analysis. Their radical scavenging activity was evaluated through the determination of their abilities to inhibit free radicals using DPPH$^\cdot$ as a stable radical. Ascorbic acid (**AA**) was used as reference antioxidant compound and also the comparative study with the synthesized compounds were done. The compounds that showed potential antioxidant activity based on IC_{50} value from the highest level were: **2e, 2b** and **2a**.

Key words : Benzalacetone, aldehydes and radical scavenging activity

INTRODUCTION

Free radical is an atom or molecule that has one or more unpaired electrons. Theoretically, free radical will be formed if a covalent bond happens to break [1]. Recent evidence [2] suggests that free radicals, which are generated in many bioorganic redox processes, may induce oxidative damage in various components of the body (e.g., lipids, proteins and nucleic acids) and may also be involved in the process leading to the formation of mutations. Furthermore, radical reactions play a significant role in the development of life – limiting chronic diseases such as cancer, hypertension, cardiac infarction, arteriosclerosis, rheumatism, cataracts and others [3]. Oxidative stress seems to be caused by increased production of reactive oxygen species (ROS) and altered cellular redox states [4,5]. ROS are by–products of a variety of pathways of aerobic metabolism. They are unstable and react readily with a wide range of biological substrates such as lipids, DNA and protein resulting in cell damage [6–8].

A series of compounds that can scavenge radicals by trapping, initiating and/or propagating radicals are called as 'antioxidants' [9]. Since the pioneering work on antioxidants by Ingold in the 1980s [10–12] there has been a continuous search for structures with improved or modified antioxidant properties. In recent years, epidemiological studies show that consumption of food with high phenolic content correlates with decreasing cardiovascular diseases [13, 14]. Phenolic compounds may produce their beneficial effect by scavenging free radicals [15, 16]. Study of chemical compounds and their derivatives related with a specific pharmacological activity to find a quantitative structure – activity relationships is very useful for the rational planning of new drugs and have brought many benefits for developing new treatments.

Recently, synthesis of hydroxyl radical scavengers from benzalacetone and its derivatives have been reported [17]. Benzalacetone has a conjugated system and is expected to be easily oxidized [18, 19]. The more the double bond, the easier it will be oxidized. Therefore it is assumed that benzalacetone and its derivatives may show antioxidant activity. With this background, in an effort to develop novel antioxidants of this class, we synthesized a series of benzalacetone derivatives and evaluated their antioxidant activities. The coupling of different aldehydes having different active sites with benzalacetone was introduced to explore the structure-activity relationship.

CHEMISTRY

The general synthetic strategy employed for the preparation of the compounds under study was based on mixed aldol condensation reaction. The starting benzaldehyde (**1**) was treated with acetone in the presence of 10% NaOH at room temperature to get benzalacetone (**2**) (**Scheme 1**). Coupling of benzalacetone with various substituted aldehydes

* To whom all correspondence should be sent:
E-mail: *drnaik_chem@yahoo.co.in*

(hydroxy benzaldehyde, nitro benzaldehyde, trimethoxy benzaldehyde, methoxy benzaldehyde, chloro benzaldehyde, tolualdehyde) using NaOH as base gave respective 1,5-diphenylpenta-1,4-dien-3-ones (**2a–g**) as outlined in **Scheme 2**.
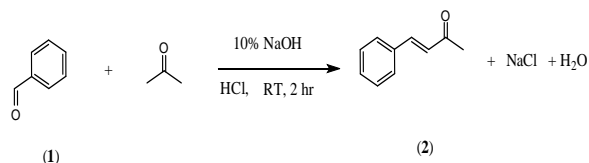
Scheme 1. Reaction protocol for the synthesis of benzalacetone (2)
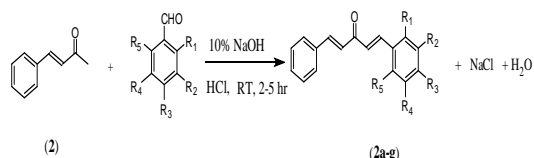
Scheme 2. Reaction pathway for the synthesis of 1,5-diphenylpenta-1,4-dien-3-ones (2a–g).

where the radicals R_i are given in Table 1.

Table 1.

Compound	R_1	R_2	R_3	R_4	R_5
2a	H	H	H	H	H
2b	H	H	OCH_3	H	H
2c	H	OCH_3	OCH_3	OCH_3	H
2d	H	H	Cl	H	H
2e	H	H	OH	H	H
2f	H	H	NO_2	H	H
2g	H	H	CH_3	H	H

EXPERIMENTAL

Materials and Methods

Thin-layer chromatography (TLC) was used to assess the reactions and the purity of the products. The compounds (**2** and **2a–g**) were purified by column chromatography using 9:1 hexane : ethyl acetate. All the reported melting points were taken in open capillaries and are reported uncorrected. IR spectra were recorded in KBr (pellet form) on a Nicolet 5700 FT–IR spectrophotometer and only noteworthy absorption values (cm^{-1}) are listed. ^{1}H NMR spectra were recorded at 500 MHz on Bruker DRX–500MHz spectrometer using CDCl$_3$ as solvent. Mass spectra of the synthesized compound were obtained using a Q-TOF Waters Ultima instrument (No-Q-Tof GAA 082, Water Corporation, Manchester, UK) fitted with an Electron spray ionization (ESI) source. The data acquisition software used was Version 4.0. UV–visible spectrophotometer (Shimadzu 160A) was used for recording the absorbance of the test solutions. All the chemicals were purchased from the Sigma-Aldrich, Himedia, S.d.fine.chem, Rankem, Ranbaxy, E-Merck, India.

Procedure for the synthesis of benzalacetone (2)

To a well stirred solution of benzaldehyde (0.1 mole) and acetone (0.3mole), 2.5 ml of 10% NaOH solution was added drop wise until the solution turned pale yellow. The solution was stirred for 2 hr at room temperature (RT). The progress of the reaction was monitored by using TLC using hexane: ethyl acetate as mobile solvent. After the completion of the reaction, the reaction mixture was treated with dil. HCl until the mixture become slightly acidic. Further, the product was extracted by using diethyl ether. The aqueous layer was removed and the organic layer was washed thrice with triple distilled water and dried over anhydrous sodium sulphate. The solvent was removed by using a rotary evaporator at 35 ºC. The residual portion was distilled under reduced pressure and the fraction boiling at 150–155ºC / 25 mm Hg was collected. The distillate was cooled and the light yellow crystals of benzalacetone separated out.

Yellow solid, Yield (86.3%), M.p. 40-43ºC. IR (KBr) ν_{max} (cm^{-1}): 3053 – 2829.5 (Ar C–H), 1670.9 (C=O); ^{1}H NMR (250 mHz) (CDCl$_3$) δ (ppm): δ 7.3 – 7.6 (m, 5H, Ar-H), 6.6-7.6 (d, 2H, olefinic protons), 2.2 (s, 3H, methylene proton); Mass (m/z %): M$^+$ 146.19; Anal. Calcd. for $C_{10}H_{10}O$: C, 82.16; H, 6.89; O, 10.94%; Found: C,82.13; H,6.87; O, 10.96%

General procedure for the synthesis of substituted 1,5-diphenylpenta-1,4dien-3-ones (2a-g)

To a well stirred solution substituted benzaldehyde (0.01mole) and benzalacetone (0.012 mole), 2.5 ml of 10% NaOH solution was added drop wise. The solution was stirred for 2–5 hr at room temperature (RT). The progress of the reaction was monitored by using TLC using hexane: ethyl acetate as mobile solvent. After the completion of the reaction, the reaction mixture was treated with dil. HCl until the mixture become slightly acidic. Further, the product was extracted by using diethyl ether. The aqueous layer was removed and the organic layer was washed thrice with triple distilled water. The product was obtained by further desolvention in rotary evouporator at 35 ºC.

1,5-diphenylpenta-1,4-dien-3-one, Compound (2a)

Yellow solid, Yield (82.7%), M.p. 108 – 110.5ºC. IR (KBr) ν_{max} (cm^{-1}): 3065 – 2698.5 (Ar

C–H), 1677.9 (C=O); ^{1}H NMR (250 mHz) (CDCl$_3$) δ (ppm): δ 7.3 – 7.6 (m, 10H, Ar-H), 7.0–7.8 (d, 4H, olefinic proton); Mass (m/z %): M$^+$ 234.29; Anal. Calcd. ForC$_{17}$H$_{14}$O: C,87.15; H,6.02; O, 6.83%; Found: C,87.13; H,6.05; O, 6.86%

1-(4-methoxyphenyl)-5-phenylpenta-1,4-

dien-3-one Compound (2b)

Yellow semisolid, Yield (69.48%). IR (KBr) ν$_{max}$ (cm^{-1}): 3045–2789.5 (Ar C–H), 1666.9 (C=O); ^{1}H NMR (250 mHz) (CDCl$_3$) δ (ppm): δ 6.9–7.6 (m, 9H, Ar-H), 7-7.8 (m, 4H, olefinic proton), 3.8 (s, 3H, OCH$_3$); Mass (m/z %): M$^+$ 264.10; Anal. Calcd. for C$_{18}$H$_{16}$O$_2$: C, 81.79; H, 6.10; O, 12.11%; Found: C, 81.77; H, 6.12; O, 12.12%

1-phenyl-5-(3,4,5-trimethoxyphenyl)penta-1,4dien-3-one, Compound (2c)

Yellow solid, Yield (94.71%), M.p. 64-67ºC. IR (KBr) ν$_{max}$ (cm–^{1}): 3051–2811 (Ar C–H), 1670.9 (C=O); ^{1}H NMR (250 mHz) (CDCl$_3$) δ (ppm): δ 6.7-7.6 (m, 7H, Ar-H), 7.0-7.8 (m, 4H, olefinic proton), 3.81 (s, 9H, 3OCH$_3$); Mass (m/z %): M$^+$ 324.14; Anal. Calcd. for C$_{20}$H$_{20}$O$_4$: C,74.06; H,6.21; O,19.73 %; Found: C,74.04; H,6.24; O, 19.71%

1-(4-chlorophenyl)-5-phenylpenta-1,4-dien-3-one, Compound (2d)

Yellow solid, Yield (92.42%), M.p. 70-75^{0}C. IR (KBr) ν$_{max}$ (cm^{-1}): 3100–2729.5 (Ar C–H), 1650.2 (C=O); ^{1}H NMR (250 mHz) (CDCl$_3$) δ (ppm): δ 7.3–7.6 (m, 9H, Ar-H), 7.3–7.8 (m, 4H, Olefinic proton); Mass (m/z %): M$^+$ 268.74; Anal. Calcd. for C$_{17}$H$_{13}$ClO: C,75.98; H,4.88; Cl,13.19; O, 5.95%; Found: C,75.96; H,4.85; Cl,13.20; O, 5.91%

1-(4-hydroxy)-5-phenylpenta-1,4-dien-3-one, Compound (2e)

Yellow semisolid, Yield (70.38%). IR (KBr) ν$_{max}$ (cm^{-1}): 3043–2787.5 (Ar C–H), 3222.4–3500.8 (phenolic-OH); ^{1}H NMR (250 mHz) (CDCl$_3$) δ (ppm): δ 7.3–7.6 (m, 9H, Ar-H), 7.3-7.8 (m, 4H, Olefinic proton), 9.4 (s, 1H, phenolic OH); Mass (m/z %): M$^+$ 250.29; Anal. Calcd. for C$_{17}$H$_{14}$O$_2$: C,81.58; H,5.64; O, 12.78%; Found: C,81.56; H, 5.63; O, 12.75%

Brown solid, Yield (93.39%), M.p. 148–152ºC. IR (KBr) ν$_{max}$ (cm^{-1}): 3003–2729.9 (Ar C–H), 1674.9 (C=O); ^{1}H NMR (250 mHz) (CDCl$_3$) δ

(ppm): δ 7.3–7.6 (m, 9H, Ar-H), 7.3-7.8 (m, 4H, Olefinic proton); Mass (m/z %): M$^+$ 279.09; Anal. Calcd. for C$_{17}$H$_{13}$NO$_3$: C,73.11; H,4.69; N,5.02; O, 17.19%; Found: C,73.14; H,4.71; N, 5.04; O, 17.18%

1-phenyl-5-p-tolylpenta-1,4-dien-3-one, Compound (2g)

Yellow semisolid, Yield (73.71%). IR (KBr) ν$_{max}$ (cm^{-1}): 3033 – 2723.2 (Ar C–H), 1661.9 (C=O); ^{1}H NMR (250 mHz) (CDCl$_3$) δ (ppm): δ 7.3 – 7.6 (m, 9H, Ar-H), 7.3-7.8 (m, 4H, Olefinic proton), 2.3 (s, 3H, methylene proton); Mass (m/z %): M$^+$ 248.32; Anal. Calcd. for C$_{18}$H$_{16}$O: C,87.06; H,6.49; O, 6.44%; Found: C,87.02; H,6.47; O, 6.41%

DPPH RADICAL SCAVENGING ASSAY

The radical scavenging activities of the synthesized compounds were evaluated using a stable free radical, 2,2-diphenyl-1-picrylhydrazyl (DPPH). A number of methods are available for the determination of free radical scavenging activity but the assay employing stable DPPH radical has received most attention owing to its ease of use and its convenience [20]. The solutions of respective compounds were prepared in different concentrations (10, 25, 50, 100, 200 and 500 µM/mL) in methanol and mixed with constant volume of 0.1mM DPPH solution. The absorbance was measured at 517 nm against methanol as blank after the incubation for 20 min. The percentage (%) radical scavenging activity (RSA) was calculated by using the formula,

$$\% \ RSA = [(A_o - A_1)/ A_o] \times 100$$

Where, A_o is the absorbance of the control (blank, without compound) and A_1 is the absorbance of the compound.

RESULTS AND DISCUSSION

In the course of the present research aimed at the development of benzalacetone analogues as a novel class of free radical scavengers, mixed aldol condensation reaction was employed as a method of choice to obtain the target compounds. The synthetic protocol employed for the preparation of the new analogues was based on mixed aldol condensation reaction. Benzaldehyde (**1**) was treated with acetone in the presence of 10% NaOH at room temperature to get benzalacetone (**2**) (**Scheme 1**). Further, coupling of benzalacetone

with various substituted aldehydes using NaOH as base gave respective 1,5-diphenylpenta-1,4-dien-3-ones (**2a–g**) as outlined in **Scheme 2**. ^{1}H NMR, IR, mass spectra and elemental analysis were used to confirm the structure in purity of the newly synthesized compounds.

The IR spectra of benzalacetone and analogues revealed the characteristic absorption of aromatic ketone. The strong bands in the region 1665 – 1648 cm^{-1} were assigned to C=O stretching of the aromatic ring system. In the all the compounds, the aromatic stretching was found at the region of 3100 – 2698 cm^{-1}. On the other hand, in ^{1}H NMR spectra of all 1,5-diphenylpenta-1,4-dien-3-ones (**2a-g**), the aromatic protons appeared at 6.6 – 7.6 ppm as multiplet and all the olefinic protons were appeared at 7.0–7.8 ppm as doublet. Addition to this in compound (**2b**) methoxy proton resonated as singlet at 3.8 ppm. Whereas, nine protons corresponding to three methoxy group in compound (**2c**)were observed as singlet at 3.4 – 3.8 ppm. In compound (**2e**) phenolic –OH proton appeared as singlet at 9.4 ppm and methyl proton was observed as singlet at 2.3 – 3.0 ppm in compound (**2g**). Mass spectra of all synthesized analogues showed M^+ peak in agreement with their molecular formula.

In order to evaluate antioxidant properties of the newly synthesized 1,5–diphenylpenta-1,4-dien-3-ones (**2a–g**) the effects on free radical were examined using DPPH assay according to the Blois method [21]. Their percentage DPPH activity at different concentration is depicted in Figure 1.
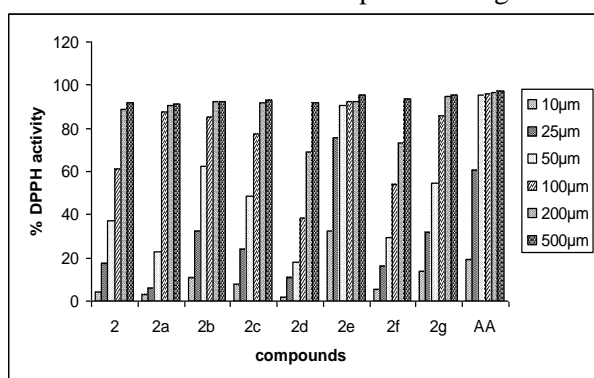
Fig.1. Percentage DPPH activity for the benzalacetone and 1,5-diphenylpenta-1,4-dien-3-ones (**2a–g**) with internal standard (**AA**).

All the synthesized compounds scavenged DPPH radical significantly in a concentration dependent manner. IC_{50} value was calculated by linear regression algorithm and the results were compared with that of internal standard ascorbic acid (**AA**). The respective IC_{50} values of the

synthesized compounds and standard are listed in Table 2.

Table 2. 50% Inhibition of DPPH radical (IC_{50}) by benzalacetone and 1,5-diphenylpenta-1,4-dien-3-ones.

Compound	[a]IC_{50} (μM/mL)
2	62.5±0.65
2a	22.5±0.12
2b	17.5±1.02
2c	52.5±0.97
2d	125±0.43
2e	10±0.64
2f	87.5±0.86
2g	37.5±0.33
AA	22.5±0.21

[a]Each value represents means ± SD (n=3)

Initially, compound (**2a**) showed comparatively good activity. Further, incorporation of different substituents in to the phenolic moiety of compound (**2a**) was done and their influence on radical scavenging activity was studied. The introduction of electron withdrawing groups (NO_2 and Cl) in compounds (**2f**) and (**2d**) significantly reduced the DPPH activity, while that of electron donating groups (OCH_3, OH) in compound (**2e**) and (**2b**) enhanced the activity. On the other hand, compound (**2c**) bearing three methoxy group on the benzene ring exhibits less activity compared to compound (**2b**) having single methoxy group. This might be due to the steric factor and probability of the formation of the intramolecular hydrogen bonding. Incorporation of –OH group in to the benzene ring enhance the RSA exhibiting dominant activity among the analogues. The increasing orders of DPPH activity of newly synthesized compounds are as follows: **2e > 2b > 2a ≥ AA > 2g > 2c > 2 > 2f > 2d**

CONCLUSION

The compounds under study were synthesized by mixed aldol condensation. The radical scavenging activities of newly synthesized compounds were evaluated by using DPPH radical assay. Although most of the compounds synthesized showed considerable inhibition percentages, the compounds (**2e), (2b),** and (**2a**) were the most active. From the present study, conclusion could be drawn that the nature of the substituent on the aromatic ring and the presence of conjugated double bonds played a critical role in exerting the antioxidant activity. The information from the present study may warrant further in-depth biological evaluations.

ABBREVIATIONS

°C = centigrade
min = minute
hr = hour
mL = milli Liter
µM = micro molar
% = percentage
IC_{50} = 50 percent Inhibition concentration
nm = nano meter
mM = milli molar
M= molar
RT = room temperature
AA = Ascorbic acid
DPPH = 2, 2-diphenyl-1-picrylhydrazyl
TLC = Thin layer chromatography
IR= Infrared
^{1}H NMR= proton nuclear magnetic resonance
MP= melting point
KBr= potassium bromide
RSA= radical scavenging activity

REFERENCES

1. S. Atun, R. Arianingrum, S. Handayani, Rudyansyah, M. Garson, *Indonesian J. Chem.,* **7**, 83 (2007)
2. G.C. Yen, H.Y Chen, *J. Agric. Food Chem.,* **43**, 27 (1995)
3. C. Soler–Rivas, J.C. Espin, H.J. Wichers, *Phytochem. Anal.,* **11**, 330 (2000).
4. H. Kaneto, Y. Kajimoto, J. Miyagawa, T. Matsuoka, Y. Fujitani, M. Hori, *Diabetes.,* **48**, 2398 (1999).
5. A. Rudich, A. Tirosh, R. Potashnik, R. Hem, H. Kanety, N. Bashan, *Diabetes.,* **47**, 1562 (1998).
6. B. Halliwell, J.M.C. Gutteridge (1989) In Free Radicals in Biology and Medicine, 2nd ed.; Halliwell, B.; Gutteridge, J. M.C.; Eds.; Oxford University Press, Clarendon: Oxford, pp 1 – 20.
7. M. Roberfroid, P.P. Colderon In Free Radicals and Oxidation Phenomena in Biological Systems; M. Roberfroid, B. Colderon; Eds.; University Of Catholique de Lauvain Brussels: New York, pp **11** (1995).
8. J.M. Braughler, L.A. Duncan, R.L. Chase, *J. Biol. Chem.,* **261**, 10282 (1986)
9. F. Shahidi, P.K.J.P.D. Wanasundara, *Crit. Rev. Food Sci. Nutr.,***32**, 67 (1992).
10. G.W. Burton, K.U. Ingold, *J Am Chem Soc.,* **102**, 7791 (1980)
11. G.W. Burton, K.U. Ingold, *J.Am Chem Soc.,* **103,** 6472 (1981)
12. L.R.C. Barclay, K.U. Ingold, *J Am Chem Soc.,* **103**, 6478 (1981)
13. M.G.L. Hertog, P.M. Sweetnam, A.M. Fehily, P.C. Elwood, D. Kromhout, *Am. J. Clin. Nutr.,* **65**, 1489 (1997).
14. M.I. Gil, F.A. Thomas-Barberan, B. Hess-Pierce, B. M. Holcroft, A.A. Kader., *J. Agr. Food Chem.,* **48**, 4581 (2000).
15. B.N. Ames, *Science.,* **221**,1256 (1983)
16. R. Pulido, L. Bravo, F. Saura-Calixto *J. Agr. Food Chem.,* **48**, 3396 (2000).
17. S. Handayani, S. A. Indyah, *J. Physical Science.,* **19**, 61 (2008).
18. S.Handayani Synthesis of 4'-methoxyflavanon by chalcone isomerization,. Proceeding of the International Seminar on Organic Chemistry, UGM, Yogyakarta (2001).
19. S. Handayani, *Indonesian J. Chem.,* **5**, 22 (2005).
20. A. Abdelnaser, Elzaawely, D.X Tran, K. Haruo, T. Shinkichi, *Food Chem.*, **104**, 1648 (2007).
21. M.S. Blois, *Nature.,* **181**, 1199 (1958).

1,5-ДИФИНИЛПЕНТА-1,4 ДИЕН-3-ОНИ: НОВ КЛАС АНТИОКСИДАНТИ

Н. Найк, Х. Виджай Кумар, С. Света

Департамент за изследвания по химия в Университета на Мисор, Манасаганготри, Мисор 570 006, Индия

(Резюме)

Синтезирани са серия от 1,5 дифенилпента-1,4-диен-3-они чрез свързване на бензалацетон с различни заместени бензалалдехиди. Общата стратегия, приложена за синтеза на съединенията се основава на смесена алдол кондензационна реакция в присъствието на силна база. Структурите на новосинтезираните съединения се характеризират чрез спектрален и елементен анализ. Тяхната антиоксидантна активност е оценена чрез определяне способността им да инхибират свободните радикали, като използват DPPH˙ като стабилен радикал. Аскорбинова киселина (АК) е била използвана като сравнителен антиоксидант, и е извършено сравнително изследване със синтезираните съединения. Съединенията, които показват най-висока потенциална антиоксидантна активност, въз основа на IC_{50} стойностите са: **2e**, **2b** и **2a**.

Short communication

Lifetime of benzyl-*gem*-diacetate in aqueous solution

R. Sanjeev[1]*, V. Jagannadham[2], D. Dhiman[3]

[1]*Department of Chemistry, Osmania University, Hyderabad-500 007, India*
[2]*Department of Chemistry, Mizan-Teppi University, Teppi Campus, Teppi, Ethiopia*
[3]*Lovely Professional University, Phagwara, Punjab (India).*

Conditions for the solvolysis of benzyl-*gem*-diacetate were established and the lifetime of benzyl-*gem*-diacetate was determined.

Key words: Lifetimes, benzyl-*gem*-diacetate, solvolysis.

Solvolysis of benzyl-*gem*-dihalides and benzyl-*gem*-diazides in water were carried out in our laboratory [1, 2] and the mechanism suggested, was as given below.

Scheme 1

X = N₃, Cl, Br, and CH₃COO
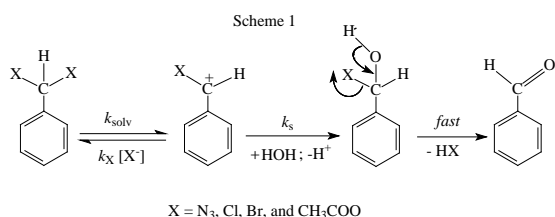
But the solvolysis did not take place at all when X = CH_3COO. Few possible explanations of reluctance of solvolysis or the extraordinary stability of benzyl-*gem*-diacetate in water has been explained in detail in our previous publication [3], based on the arguments of leaving group inability, the nucleophilicity, hydration energies of anions, and the geminal interactions of acetate groups on the ipso carbon. Since the solvolysis of benzyl-*gem*-diacetate did not proceed, (for the reasons stated above), we had resorted to acid catalysis [4].

EXPERIMENTAL

Kinetic studies employed in the present work are similar to our earlier studies [1, 2]. Buffers of pH 6.0, 5.5, 5.0, 4.5, 4.0 and 3.5 were prepared using acetic acid and sodium acetate. Kinetic studies in these buffers were performed and k_{solv} estimated. The concentration of benzyl-*gem*-diacetate in each of the buffer was 0.1 mM and an ionic strength of 0.1M was maintained with KCl in each of the buffer. The stock solution of the compound, benzyl-*gem*-diacetate, was stored in HPLC grade

---

* To whom all correspondence should be sent:
E-mail: rachuru1sanjeev1@rediffmail.com

acetonitrile. All reactions were followed on Kontron uv-visible spectrophotometer and calculations were carried out using Kalaidagraph (USA) software. The chemicals used for this study were acetic acid and sodium acetate (both of analytical grade).

RESULTS AND DISCUSSION:

The kinetic studies at different pH values were carried out. A plot of k_{solv} vs [H⁺] (See Table 1) was plotted and the k_{solv} at zero [H⁺] i.e. in pure water was determined by interpolating the data to zero [H⁺]. The results are shown in Figure 1. Earlier study of benzyl-gem-diacetate [3] demonstrated the reluctance of the compound to undergo solvolysis. In this work, conditions for the solvolysis were established by using different acidic buffer solutions. Kinetic studies were carried out by following the product benzaldehyde.

Table 1. Rate constants for the solvolysis of benzyl-*gem*-diacetate at different pH in aqueous solution.

pH	[H⁺]	k_{solv}/s
3.5	3.16×10^{-4}	1.03×10^{-2}
4.0	1.0×10^{-4}	4.8×10^{-3}
4.5	3.16×10^{-5}	2.28×10^{-3}
5.0	1.0×10^{-5}	1.14×10^{-3}
5.5	3.16×10^{-6}	4.92×10^{-4}
6.0	1.0×10^{-6}	4.62×10^{-4}

Thus the reciprocal of the k_{solv} would give lifetime of the compound in water, which turned out to be 1140 seconds. The mechanism in acid catalyzed path is made known in Scheme 2. As is evident in Scheme 2, the result of protonation leads to the conversion of acetate ion to acetic acid, which is a better leaving group; hence it departs with ease

Fig. 1. Plot of k_{solv} vs. hydrogen ion concentration
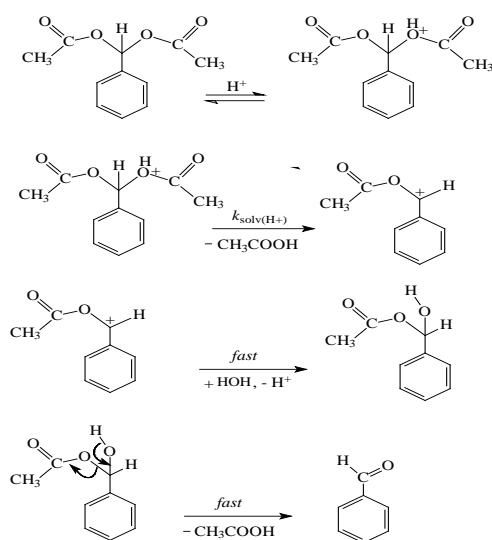
Scheme 2

relative to acetate ion. Therefore it was possible to observe acid catalysis in the reaction.

The lifetime of benzyl-gem-diaceatate was estimated to be 1140 seconds from the interpolation of plot of k_{solv} *vs.* [H$^+$]. This study, i.e. the lifetime determination of benzyl-gem-diacetate, is reported for the first the time. This is the novelty of this piece of work.

REFERENCES

1. R. Sanjeev, V. Jagannadham, *Proc. Indian Acad. Sci. (Chem. Sci.),* **144**, 47 (2002)
2. R. Sanjeev, V. Jagannadham, *Indian J. Chem.*, **41B**, 2150 (2002).
3. V. Jagannadham, R. Sanjeev, D. Annapurna Padmavathi, *Intl. J. Chem. Kin.*, **41**, 554 (2009).
4. D. Dhiman, M. PhD Thesis, Lovely Professional University, Punjab (India), August 2009, pp 26-39.

ПРОДЪЛЖИТЕЛНОСТ НА СЪЩЕСТВУВАНЕТО НА БЕНЗИЛ-*gem*-ДИАЦЕТАТ ВЪВ ВОДНИ РАЗТВОРИ

Р. Санджив[1]*, В. Джаганадхам[2], Д. Дхиман[3]

[1]*Департамент по химия, Университет Османия, Хайдерабад-500 007, Индия*
[2]*Департамент по химия, Университет Мизан-Теппи, Теппи, Етиопия*
[3] *Професионален университет Лъвли, Пхагуара, Пунджаб, Индия.*

(Резюме)

Установени са условията на солволиза на бензил-*gem*-диацетат, като е определена и продължителността на съществуването му.

BULGARIAN CHEMICAL COMMUNICATIONS

Instructions about Preparation of Manuscripts

General remarks: Manuscripts are submitted in English by e-mail or by mail (in duplicate). The text must be typed double-spaced, on A4 format paper using Times New Roman font size 12, normal character spacing. The manuscript should not exceed 15 pages (about 3500 words), including photographs, tables, drawings, formulae, etc. Authors are requested to use margins of 3 cm on all sides. For mail submission hard copies, made by a clearly legible duplication process, are requested. Manuscripts should be subdivided into labelled sections, e.g. **Introduction, Experimental, Results and Discussion**, *etc*.

The title page comprises headline, author's names and affiliations, abstract and key words.

Attention is drawn to the following:

a) **The title** of the manuscript should reflect concisely the purpose and findings of the work. Abbreviations, symbols, chemical formulas, references and footnotes should be avoided. If indispensable, abbreviations and formulas should be given in parentheses immediately after the respective full form.

b) **The author**'s first and middle name initials, and family name in full should be given, followed by the address (or addresses) of the contributing laboratory (laboratories). **The affiliation** of the author(s) should be listed in detail (no abbreviations!). The author to whom correspondence and/or inquiries should be sent should be indicated by asterisk (*).

The abstract should be self-explanatory and intelligible without any references to the text and containing not more than 250 words. It should be followed by key words (not more than six).

References should be numbered sequentially in the order, in which they are cited in the text. The numbers in the text should be enclosed in brackets [2], [5, 6], [9–12], etc., set on the text line. References, typed with double spacing, are to be listed in numerical order on a separate sheet. All references are to be given in Latin letters. The names of the authors are given without inversion. Titles of journals must be abbreviated according to Chemical Abstracts and given in italics, the volume is typed in bold, the initial page is given and the year in parentheses. Attention is drawn to the following conventions:

a) The names of all authors of a certain publications should be given. The use of "*et al.*" in the list of references is not acceptable.

b) Only the initials of the first and middle names should be given.

In the manuscripts, the reference to author(s) of cited works should be made without giving initials, e.g. "Bush and Smith [7] pioneered...". If the reference carries the names of three or more authors it should be quoted as "Bush *et al*. [7]", if Bush is the first author, or as "Bush and co-workers [7]", if Bush is the senior author.

Footnotes should be reduced to a minimum. Each footnote should be typed double-spaced at the bottom of the page, on which its subject is first mentioned.

Tables are numbered with Arabic numerals on the left-hand top. Each table should be referred to in the text. Column headings should be as short as possible but they must define units unambiguously. The units are to be separated from the preceding symbols by a comma or brackets.

Note: The following format should be used when figures, equations, *etc*. are referred to the text (followed by the respective numbers): Fig., Eqns., Table, Scheme.

Schemes and figures. Each manuscript (hard copy) should contain or be accompanied by the respective illustrative material as well as by the respective figure captions in a separate file (sheet). As far as presentation of units is concerned, SI units are to be used. However, some non-SI units are also acceptable, such as °C, ml, l, etc.

The author(s) name(s), the title of the manuscript, the number of drawings, photographs, diagrams, etc., should be written in black pencil on the back of the illustrative material (hard copies) in accordance with the list enclosed. Avoid using more than 6 (12 for reviews, respectively) figures in the manuscript. Since most of the illustrative materials are to be presented as 8-cm wide pictures, attention should be paid that all axis titles, numerals, legend(s) and texts are legible.

The authors are asked to submit **the final text** (after the manuscript has been accepted for publication) in electronic form either by e-mail or mail on a 3.5'' diskette (CD) using a PC Word-processor. The main text, list of references, tables and figure captions should be saved in separate files (as *.rtf or *.doc) with clearly identifiable file names. It is essential that the name and version of the word-processing program and the format of the

text files is clearly indicated. It is recommended that the pictures are presented in *.tif, *.jpg, *.cdr or *.bmp format, the equations are written using "Equation Editor" and chemical reaction schemes are written using ISIS Draw or ChemDraw programme.

The authors are required to submit the final text with a list of three individuals and their e-mail addresses that can be considered by the Editors as potential reviewers. Please, note that the reviewers should be outside the authors' own institution or organization. The Editorial Board of the journal is not obliged to accept these proposals.

EXAMPLES FOR PRESENTATION OF REFERENCES

REFERENCES

1. D. S. Newsome, *Catal. Rev.–Sci. Eng.*, **21**, 275 (1980).
2. C.-H. Lin, C.-Y. Hsu, *J. Chem. Soc. Chem. Commun.*, 1479 (1992).
3. R. G. Parr, W. Yang, Density Functional Theory of Atoms and Molecules, Oxford Univ. Press, New York, 1989.
4. V. Ponec, G. C. Bond, Catalysis by Metals and Alloys (Stud. Surf. Sci. Catal., vol. 95), Elsevier, Amsterdam, 1995.
5. G. Kadinov, S. Todorova, A. Palazov, in: New Frontiers in Catalysis (Proc. 10th Int. Congr. Catal., Budapest, 1992), L. Guczi, F. Solymosi, P. Tetenyi (eds.), Akademiai Kiado, Budapest, 1993, Part C, p. 2817.
6. G. L. C. Maire, F. Garin, in: Catalysis. Science and Technology, J. R. Anderson, M. Boudart (eds), vol. 6, Springer-Verlag, Berlin, 1984, p. 161.
7. D. Pocknell, *GB Patent* 2 207 355 (1949).
8. G. Angelov, PhD Thesis, UCTM, Sofia, 2001.
9. JCPDS International Center for Diffraction Data, Power Diffraction File, Swarthmore, PA, 1991.
10. CA **127**, 184 762q (1998).
11. P. Hou, H. Wise, *J. Catal.*, in press.
12. M. Sinev, private communication.
13. http://www.chemweb.com/alchem/articles/1051611477211.html.

CONTENTS

СЪДЪРЖАНИЕ